# Microscopic description of collective excitations in deformed atomic nuclei

**Bjelčić, Antonio**


University of Zagreb
Faculty of Science
Department of Physics

Antonio Bjelčić

# Microscopic Description of Collective Excitations in Deformed Atomic Nuclei

Doctoral Dissertation

Zagreb, 2022


University of Zagreb,
Faculty of Science,
Department of Physics

Antonio Bjelčić

# Microscopic Description of Collective Excitations in Deformed Atomic Nuclei

Doctoral Dissertation

Supervisor:
prof. dr. sc. Tamara Nikšić

Zagreb, 2022


Sveučilište u Zagrebu,
Prirodoslovno-matematički fakultet,
Fizički odsjek

Antonio Bjelčić

# Mikroskopski opis kolektivnih pobuđenja u deformiranim atomskim jezgrama

Doktorski rad

Mentor:
prof. dr. sc. Tamara Nikšić

Zagreb, 2022

# Abstract

The Quasiparticle Random-Phase Approximation (QRPA) based on the nuclear energy density functionals (EDF) is one of the most widely used theoretical frameworks for describing collective excitations in deformed atomic nuclei. Since the configurational space of quasiparticle excitations can become very large, especially for heavy deformed nuclei, the standard matrix eigendecomposition solution of the QRPA equation is often prohibitive in terms of computational resources. Recently, the Finite Amplitude Method (FAM) with its quasiparticle adaptation (QFAM) has been proposed as a feasible method for solving the QRPA equation. Within this doctoral research, a highly efficient implementation of the QFAM solver based on the relativistic nuclear energy density functionals has been developed, namely the `DIRQFAM` solver in a form of a program package. Due to its efficiency, the developed `DIRQFAM` solver is suitable for describing collective excitations in axially symmetric atomic nuclei with quadrupole deformed ground states. Even heavy systems and systematic large-scale calculations are within reach.

In this dissertation, the implementation of QFAM solver is presented and discussed, together with a new proposed method called the Kernel Polynomial Method (KPM). The KPM method is built on top of QFAM solver and uses QFAM iterations as a means to find the expansion coefficients of the QRPA response function which is expanded in terms of kernel-adjusted Chebyshev polynomials. It is shown that for non-relativistic EDF, the KPM method significantly outperforms the conventional QFAM approach in terms of computational complexity. Two applications of the developed QFAM solver are covered: i) exploration of low-energy response function on multipole excitations in light $\alpha$-conjugate $N = Z$ nuclei, and ii) description of quasiparticle-vibration coupling in deformed systems where QFAM is used to provide the phonon degrees of freedom for Dyson equation.

**Keywords:** Energy density functional, Relativistic mean-field theory, Hartree-Bogoliubov, Relativistic Hartree-Bogoliubov, Quasiparticle Random Phase Approximation, Finite Amplitude Method, Nuclear cluster vibrations, Quasiparticle vibration coupling, Kernel Polynomial Method

**Keywords (in Croatian):** Energijski funkctional gustoće, Relativistička teorija srednjeg polja, Hartree-Bogoliubov, Relativistički Hartree-Bogoliubov, Kvazičestična aproksimacija slučajnih faza, Metoda konačnih amplituda, Vibracije nukleonskih grozdova, Kvazičestica-fonon vezanje, Kernel Polynomial metoda

# Contents

# List of Abbreviations and Notations

**Abbreviations**

DD-ME – Density-dependent meson-exchange

DD-PC – Density-dependent point-coupling

EDF – Energy density functional

GMRES – Generalized minimal residual method

HO – Harmonic oscillator

KPM – Kernel Polynomial Method

QFAM – Quasiparticle Finite Amplitude Method

qPVC – Quasiparticle vibration coupling

QRPA – Quasipartcile Random Phase Approximation

RHB – Relativistic Hartree-Bogoliubov

RMF – Relativistic mean-field

RPA – Random Phase Approximation

**Notations**

$\boldsymbol{\alpha}, \beta$ – $4 \times 4$ matrices $\boldsymbol{\alpha} = \begin{bmatrix} 0 & \boldsymbol{\sigma} \\ \boldsymbol{\sigma} & 0 \end{bmatrix}$ and $\beta = \begin{bmatrix} I & 0 \\ 0 & -I \end{bmatrix}$.

$\chi_{m_s}(1/2)$ – Spin part of the wave-function: $\chi_{m_s=+1/2} = \begin{bmatrix} 1 \\ 0 \end{bmatrix}, \chi_{m_s=-1/2} = \begin{bmatrix} 0 \\ 1 \end{bmatrix}$.

$\mathrm{diag}[x]$ – Diagonal matrix $\mathrm{diag}[x]_{i,j} = \delta_{i,j} x_i$ with vector $x$ on diagonal.

$\overrightarrow{F}$ – Isovector function $\overrightarrow{F} = F(\boldsymbol{r}, t)\overrightarrow{\tau}$.

$A^*$ – For matrix $A$, $A^*$ denotes element-wise conjugation $(A^*)_{i,j} = A^*_{i,j}$.

$A^\dagger$ – For matrix $A$, $A^\dagger$ denotes conjugate transpose $(A^\dagger)_{i,j} = A^*_{j,i}$.

$A^T$ – For matrix $A$, $A^T$ denotes transposition $(A^T)_{i,j} = A_{j,i}$.

$X_{\mu\nu} \sim X$ – Vector $X$ is obtained by vectorizing the matrix $X_{\mu\nu}$.

# Chapter 1

# Introduction

Modern theory of quantum chromodynamics (QCD) is capable to successfully describe and experimentally validate the inter-nucleon strong nuclear interaction and thus nuclear physics can be naively classified as a specific subbranch of QCD theory. However, it turns out that such fully *ab-initio* calculations starting from the most fundamental principles are far from feasible in nuclear physics. Even the simplest nuclear systems are challenging to tackle owed to the tremendous complexity of nuclear force. Today, complex medium-heavy and heavy nuclear systems can be studied almost exclusively within the framework of effective models which use fundamental theory as a microscopic guide when constructing effective interaction models. The most successful approach in that direction is the well established Energy density functional theory (EDF) used in various branches of physics where quantum many-body problem is encountered.

One of the most challenging problems of modern theoretical nuclear physics is construction and parameterization of effective energy density functional which would reproduce the experimental data with high degree of accuracy across the entire chart of nuclides. Such universal EDF could then be credibly utilized in various researches and applications where experimental data are not available, such as problem of element synthesis within stars in nuclear astrophysics, or theoretical predictions of exotic excitation modes which would then guide experiments towards experimental validation.

Response of the nucleus when subjected to external perturbation can reveal significant information about its structure. Once the EDF is constructed and fully defined, one should in principle be able to calculate such response theoretically. For theoretical study of such collective excitations in atomic nuclei one often uses the Random Phase Approximation (RPA) extended to the Hartree-Bogoliubov framework. The main goal of this dissertation is to present and discuss the implementation of such RPA solver together with the results of some of its applications.

This dissertation is logically divided into six parts. In the first part, theoretical background regarding the EDF and RPA framwework is reviewed. Second part presents in detail the implementation of RPA solver based on the Finite Amplitude Method (FAM) in form of `DIRQFAM` software package. Third part, which can be read independently from other parts, presents the Kernel Polynomial Method (KPM), a novel method which starts from existing FAM implementation and uses it to calculate the full RPA response function by expanding it in terms of kernel-adjusted Chebyshev polynomials. The performance and efficiency of KPM com-

pared to conventional QFAM approach is evaluated and discussed. Fourth part presents and discusses the results obtained using the DIRQFAM solver when applied on calculating the multipole response of light $\alpha$-conjugated $N = Z$ nuclei, where significant modes residing in low-energy region are linked to $\alpha$ cluster vibrations. Fifth part contains the formalism and application of DIRQFAM code for extraction of phonon vertex functions used to construct the quasiparticle-vibration coupling (qPVC) self-energy. After solving the associated Dyson equation, obtained fragmentation of quasiparticle spectra and spectroscopic factors are calculated for selected light and super-heavy deformed nuclei. Finally, the last part concludes the dissertation and contains the technical details regarding the DIRQFAM solver and KPM method in a form of extensive appendix.

# Chapter 2

# Theoretical framework

In this Chapter, first the covariant density functionals based on point-coupling and meson-exchange interaction are introduced together with the relativistic Hartree-Bogoliubov framework used to theoretically describe the nuclear ground state. Regarding the theoretical introduction, Ref. [1] is followed. On top of that, Quasiparticle Random Phase Approximation is introduced with Quasiparticle Finite Amplitude Method (QFAM) as a viable method for solving the QRPA equation.

## 2.1 Covariant density functional theory

Energy density functional (EDF) provide an accurate description of ground-state properties and collective excitations of atomic nuclei, from relatively light systems to superheavy nuclei, and from the valley of $\beta$ stability to the particle drip-lines. The basic implementation of EDF is in terms of self-consistent mean-field models in which an EDF is constructed as a functional of one-body nucleon density matrices. This approach is analogous to Kohn-Sham density functional theory (DFT), that enables a description of complex quantum many-body system in terms of a universal EDF. Self-consistent mean-field models effectively map the many-body problem onto a one-body problem, and the exact EDF (which exists according to the Kohn-Sham theorem) is approximated and modelled by simple functionals of powers and gradients of ground-state nucleon densities and currents [3, 4, 5, 6].

A particular class of self-consistent mean-field models are those based on relativistic (covariant) energy density functionals. These models have been successfully applied to the analyses of a variety of nuclear structure phenomena and the level of accuracy against experimental data has reached a level comparable to the state-of-the-art non-relativistic Hartree-Fock-Bogoliubov (HFB) approach based on popular Skyrme functionals or Gogny effective interactions. In this work, we focus only on even-even open-shell nuclei with axially symmetric and parity preserved shape, and with possible quadrupole deformation.

In conventional quantum hadronodynamics, a nucleus is desribed as a system of Dirac nucleons coupled to exchange mesons through an effective Lagrangian. The isoscalar-scalar $\sigma$ meson, the isoscalar-vector $\omega$ meson and the isovector-vector $\rho$ meson build the minimal set of meson fields that is necessary for a description of bulk and single-particle nuclear properties.

An isoscalar-scalar field $\sigma$ mediates the medium-range attraction between nucleons. It is an effective field whose origin lies in many complex effects, for example

two-pion resonances and QCD combinations of quark-antiquark pairs and gluons. An isoscalar-vector field $\omega$ is introduced to model the short range repulsion. And finally the isospin dependence of the nuclear force is taken into account by a isovector-vector field $\rho$. In principle one should also include one-pion exchange in the formulation of the Lagrangian, as it is the basic ingredient of the nuclear force. However it does not enter at the classical Hartree level because it leads to a parity-breaking field, which has not been observed in nuclei. However, as already stated, two-pion exchange is included in a phenomenological way within the $\sigma$ field. The electromagnetic interaction is also taken into account by including the photon field. In following subsection, the meson-exchange formalism is introduced.

### 2.1.1 Meson-exchange models

The meson-exchange model is defined by the Lagrangian density $\mathcal{L}$ given by:

$$\mathcal{L} = \mathcal{L}_N + \mathcal{L}_m + \mathcal{L}_{int}. \tag{2.1}$$

$\mathcal{L}_N$ denotes the Lagrangian of the free nucleon:

$$\mathcal{L}_N = \bar{\psi}(\mathrm{i}\gamma^\mu \partial_\mu - m)\psi, \tag{2.2}$$

where $m$ is the bare nucleon mass and $\psi$ denotes the Dirac spinor. $\mathcal{L}_m$ is the Lagrangian of the free meson fields and electromagnetic field:

$$\begin{aligned}\mathcal{L}_m = &-\frac{1}{2}\partial_\mu\sigma\partial^\mu\sigma - \frac{1}{2}m_\sigma^2\sigma^2 - \frac{1}{2}\Omega_{\mu\nu}\Omega^{\mu\nu} + \frac{1}{2}m_\omega^2\omega_\mu\omega^\mu \\ &- \frac{1}{4}\overrightarrow{R}_{\mu\nu}\cdot\overrightarrow{R}^{\mu\nu} + \frac{1}{2}m_\rho^2\overrightarrow{\rho}_\mu\cdot\overrightarrow{\rho}^\mu - \frac{1}{4}F_{\mu\nu}F^{\mu\nu},\end{aligned} \tag{2.3}$$

with the corresponding meson masses $m_\sigma, m_\omega, m_\rho$ and $\Omega^{\mu\nu}$, $\overrightarrow{R}^{\mu\nu}$, $F^{\mu\nu}$ are field tensors:

$$\Omega^{\mu\nu} = \partial^\mu\omega^\nu - \partial^\nu\omega^\mu, \tag{2.4}$$

$$\overrightarrow{R}^{\mu\nu} = \partial^\mu\overrightarrow{\rho}^\nu - \partial^\nu\overrightarrow{\rho}^\mu, \tag{2.5}$$

$$F^{\mu\nu} = \partial^\mu A^\nu - \partial^\nu A^\mu. \tag{2.6}$$

Arrows denote isovectors and boldface symbols are used for vectors in ordinary space. The minimal set of interaction terms is constrained in $\mathcal{L}_{int}$:

$$\mathcal{L}_{int} = -g_\sigma\bar{\psi}\psi\sigma - g_\omega\bar{\psi}\gamma^\mu\psi\omega_\mu - g_\rho\bar{\psi}\overrightarrow{\tau}\gamma^\mu\psi\cdot\overrightarrow{\rho}_\mu - e\frac{1+\tau_3}{2}\bar{\psi}\gamma^\mu\psi A_\mu, \tag{2.7}$$

with the couplings $g_\sigma, g_\omega, g_\rho$ and $e$.

From the Lagrangian density, one can easily obtain the Hamiltonian density (for details see Ref. [7]) which for the static case reads:

$$\begin{aligned}\mathcal{H}(\boldsymbol{r}) = &\sum_i^A \psi_i^\dagger(\boldsymbol{\alpha}\cdot\boldsymbol{p} + \beta m)\psi_i \\ &+ \frac{1}{2}\left[|\nabla\sigma|^2 + m_\sigma^2\sigma^2\right] - \frac{1}{2}\left[|\nabla\omega|^2 + m_\omega^2\omega^2\right] - \frac{1}{2}\left[|\nabla\rho|^2 + m_\rho^2\rho^2\right] - \frac{1}{2}|\nabla A|^2 \\ &+ \left[g_\sigma\rho_s\sigma + g_\omega j_\mu\omega^\mu + g_\rho\overrightarrow{j}_\mu\cdot\overrightarrow{\rho}^\mu + ej_p^\mu A_\mu\right].\end{aligned} \tag{2.8}$$

We also introduce the isoscalar-scalar density, the isoscalar-vector current, the isovector-vector current and the electromagnetic current:

$$\rho_s(\boldsymbol{r}) = \sum_{i=1}^{A} \bar{\psi}_i(\boldsymbol{r})\psi_i(\boldsymbol{r}), \tag{2.9}$$

$$j^{\mu}(\boldsymbol{r}) = \sum_{i=1}^{A} \bar{\psi}_i(\boldsymbol{r})\gamma^{\mu}\psi_i(\boldsymbol{r}), \tag{2.10}$$

$$\overrightarrow{j}^{\mu}(\boldsymbol{r}) = \sum_{i=1}^{A} \bar{\psi}_i(\boldsymbol{r})\overrightarrow{\tau}\gamma^{\mu}\psi_i(\boldsymbol{r}), \tag{2.11}$$

$$j_p^{\mu}(\boldsymbol{r}) = \sum_{i=1}^{Z} \bar{\psi}_i(\boldsymbol{r})\gamma^{\mu}\psi_i(\boldsymbol{r}), \tag{2.12}$$

where the summation is performed only over occupied obrits in the Fermi sea of positive energy states, i.e. the *no-sea* approximation is used. By integrating the Hamiltonian density (2.8) over the $\boldsymbol{r}$-space, we obtain the total energy which depends on the Dirac spinors and the meson fields:

$$E_{RMF}[\psi, \bar{\psi}, \sigma, \omega^{\mu}, \overrightarrow{\rho}^{\mu}, A^{\mu}] = \int d\boldsymbol{r}\mathcal{H}(\boldsymbol{r}). \tag{2.13}$$

Already in the earliest applications of the relativistic mean-field framework, it was realized, however, that this simple model with interaction terms only linear in the meson fields does not provide a quantitative description of the complex nuclear system. Therefore, an effective density dependence was introduced by replacing the quadratic $\sigma$-potential with a quartic one [8]. Of course, implementation of the covariant density functional with non-linear meson coupling has no direct physical meaning. Therefore, it seems more natural to follow the idea of Brockmann and Toki [9] and use density-dependent couplings. Coupling constants $g_\sigma, g_\omega$ and $g_\rho$ are assumed to be vertex functions of Lorentz-scalar bilinear forms of the nucleon operators. In most applications the meson-nucleon couplings are functions of the vector density $\rho_v = j^0$. Brockmann and Toki derived the density dependence of the coupling constants in an *ab-initio* calculation from the relativistic Brueckner-Hartree-Fock calculation in the infinite nuclear matter. Since there are no free parameters in this model, the results of such calculation are not very precise. Therefore, a phenomenological *ansatz* is introduced for the density-dependence of the couplings with parameters adjusted to the experimental data in finite nuclei [10, 11, 12, 13].

The single-nucleon Dirac equation is derived by variation of the energy density functional (2.13) with respect to $\bar{\psi}$:

$$\hat{h}_D\psi_i = \epsilon_i\psi_i, \tag{2.14}$$

with the Dirac Hamiltonian:

$$\hat{h}_D = \begin{bmatrix} \Sigma^0 + \Sigma_R^0 + (\Sigma_s + m) & \boldsymbol{\sigma}\cdot(\boldsymbol{p} - \boldsymbol{\Sigma}) \\ \boldsymbol{\sigma}\cdot(\boldsymbol{p} - \boldsymbol{\Sigma}) & \Sigma^0 + \Sigma_R^0 - (\Sigma_s + m) \end{bmatrix}. \tag{2.15}$$

The nucleon self-energies are defined by the following expressions:

$$\Sigma_s = g_\sigma(\rho_v)\sigma, \tag{2.16}$$

$$\Sigma^\mu = g_\omega(\rho_v)\omega^\mu + g_\rho(\rho_v)\overrightarrow{\tau}\cdot\overrightarrow{\rho}^\mu + e\frac{1+\tau_3}{2}A^\mu. \tag{2.17}$$

The density dependece of the vertex functions $g_\sigma(\rho_v), g_\omega(\rho_v)$ and $g_\rho(\rho_v)$ produces the *rearrangement* contribution to the vector self-energy:

$$\Sigma_R^0 = g'_\sigma(\rho_v)\rho_s\sigma + g'_\omega(\rho_v)\rho_v\omega^0 + g'_\rho(\rho_v)\overrightarrow{j^0}\cdot\overrightarrow{\rho^0}. \tag{2.18}$$

The variation of the energy density functional (2.13) with respect to the meson fields leads to the Helmholtz equation for the meson fields:

$$\left[-\triangle + m_\sigma^2\right]\sigma = -g_\sigma(\rho_v)\rho_s, \tag{2.19}$$

$$\left[-\triangle + m_\omega^2\right]\omega^\mu = g_\omega(\rho_v)j^\mu, \tag{2.20}$$

$$\left[-\triangle + m_\rho^2\right]\overrightarrow{\rho^\mu} = g_\rho(\rho_v)\overrightarrow{j^\mu}, \tag{2.21}$$

and to the Poisson equation for the electromagnetic field:

$$-\triangle A^\mu = ej_p^\mu. \tag{2.22}$$

Because of the charge conservation, only the third component of the isovector $\rho$-meson contributes. In the ground-state solution for an even-even nucleus, there are no currents (time-reversal invariance) and the corresponding spatial components of the meson-fields vanish $\mathbf{\Sigma} = \mathbf{0}$. The Dirac equation takes a simple form that includes only the vector potential $V(\boldsymbol{r})$ and the effective mass $M^*(\boldsymbol{r}) = m + g_\sigma(\rho_v)\sigma$:

$$\left\{-\mathbf{i}\boldsymbol{\alpha}\cdot\boldsymbol{\nabla} + \beta M^*(\boldsymbol{r}) + V(\boldsymbol{r})\right\}\psi_i(\boldsymbol{r}) = \epsilon_i\psi_i(\boldsymbol{r}). \tag{2.23}$$

The vector potential reads:

$$V(\boldsymbol{r}) = g_\omega(\rho_v)\omega^0 + \tau_3 g_\rho(\rho_v)\rho^0 + e\frac{1+\tau_3}{2}A^0 + \Sigma_R^0, \tag{2.24}$$

and the rearrangement contribution is:

$$\Sigma_R^0 = g'_\sigma(\rho_v)\rho_s\sigma + g'_\omega(\rho_v)\omega^0 + g'_\rho(\rho_v)\rho_{tv}\rho^0. \tag{2.25}$$

$\rho_{tv}$ denotes the isovector density, i.e. the difference between the proton and neutron vector density.

The density depedence of the meson-nucleon couplings is parameterized in a phenomenological way. The coupling of the $\sigma$-meson and $\omega$-meson to the nucleon field reads:

$$g_i(\rho_v) = g_i(\rho_{sat})f_i(x), \quad \text{for } i = \sigma, \omega, \tag{2.26}$$

where the functions $f_i(x)$ are defined as:

$$f_i(x) = a_i\frac{1+b_i(x+d_i)^2}{1+c_i(x+d_i)^2}, \text{for } x = \rho_v/\rho_{sat}. \tag{2.27}$$

Table 2.1: DD-ME2 parameter set for the density-dependent meson-exchange relativistic energy functional.

| DD-ME2 parameter set | | |
|---|---|---|
| Parameter | Value | Unit |
| $m_\sigma$ | 550.1238 | [MeV/$c^2$] |
| $m_\omega$ | 783.0000 | [MeV/$c^2$] |
| $m_\rho$ | 763.000 | [MeV/$c^2$] |
| $g_\sigma(\rho_{sat})$ | 10.5396 | |
| $g_\omega(\rho_{sat})$ | 13.0189 | |
| $g_\rho(\rho_{sat})$ | 3.6836 | |
| $a_\sigma$ | 1.3881 | |
| $b_\sigma$ | 1.0943 | |
| $c_\sigma$ | 1.7057 | |
| $d_\sigma$ | 0.4421 | |
| $a_\omega$ | 1.3893 | |
| $b_\omega$ | 0.9240 | |
| $c_\omega$ | 1.4620 | |
| $d_\omega$ | 0.4775 | |
| $a_\rho$ | 0.5647 | |
| $\rho_{sat}$ | 0.1520 | [fm$^{-3}$] |

$\rho_{sat}$ denotes the baryon density at saturation in symmetric nuclear matter. The eight real parameters in Eq. (2.27) are not independent. The five constraints:

$$f_i(1) = 1, \quad f''_\sigma(1) = f''_\omega(1), \quad f''_i(0) = 0, \tag{2.28}$$

reduce the number of independent parameters to three. Three additional parameters in the isoscalar channel are: $g_\sigma(\rho_{sat}), g_\omega(\rho_{sat})$ and the $m_\sigma$-the mass of the phenomenological $\sigma$-meson. For the $\rho$-meson coupling, the functional form of the density dependence is suggested by a Dirac-Brueckner calculation of asymmetric nuclear matter [14]:

$$g_\rho(\rho_v) = g_\rho(\rho_{sat})e^{-a_\rho(x-1)}. \tag{2.29}$$

The isovector channel is parameterized by $g_\rho(\rho_v)$ and $a_\rho$. For the masses of the $\omega$ and $\rho$ mesons the free values are used. The eight independent parameters (seven coupling parameters and the mass of the $\sigma$ meson) are adjusted to reproduce empirical properties of symmetric and asymmetric nuclear matter, binding energies, charge radii and neutron radii of spherical nuclei. In this work, the very successful density-dependent meson-exchange relativistic energy density functional DD-ME2 is used [13]. In Table 2.1 we list all the parameters which fully define the DD-ME2 meson-exchange functional.

We notice that since the meson masses are relatively large compared to the energy scale encountered in nuclear interactions, by expanding the finite range meson propagators into a zero-range coupling plus gradient corrections we can approximate the meson-exchange model by a point-coupling one. In the following subsection such point-coupling models are introduced.

### 2.1.2 Point-coupling models

Point-coupling models represent an alternative formulation of the self-consistent relativistic mean-field framework [15, 16, 17, 18, 19]. Similar to the finite range relativistic density functional approach, the density-dependent point-coupling (DD-PC) functionals consider an effective Lagrangian for nuclear mean-field calculations at the Hartree level with *no-sea* approximation. Instead of modelling the interaction by the exchange of mesons, in DD-PC the model consists in four, six and eight fermion point couplings (contact interactions) together with derivative terms representing, respectively, two, three and four-body forces and the finite ranges of the corresponding mesonic interactions. In many applications, however, the three and four-body forces can be modelled by density dependent two-body coupling constants whose dependence is given by *ansatz*. In fact, DD-PC functionals are closely related to finite range relativistic functionals. Expanding the finite range meson propagators into a zero-range coupling plus gradient corrections we can link both. For example, for the $\sigma$-meson the corresponding vertex can be approximated by:

$$\frac{g_\sigma^2}{-\triangle + m_\sigma^2}\rho_s \approx \frac{g_\sigma^2}{m_\sigma^2}\rho_s + \frac{g_\sigma^2}{m_\sigma^4}\triangle\rho_s, \tag{2.30}$$

where the differential operator $-\triangle + m_\sigma^2$ originates from mesonic Klein-Gordon equation.

An effective Lagrangian that includes the isoscalar-scalar, isoscalar-vector and isovector-vector four-fermion contact interactions reads:

$$\begin{aligned}\mathcal{L} = &\bar{\psi}(\mathrm{i}\gamma_\mu\partial^\mu - m)\psi - \frac{1}{2}\alpha_S(\rho_v)(\bar{\psi}\psi)(\bar{\psi}\psi)\\ &- \frac{1}{2}\alpha_V(\rho_v)(\bar{\psi}\gamma^\mu\psi)(\bar{\psi}\gamma_\mu\psi) - \frac{1}{2}\alpha_{TV}(\rho_v)(\bar{\psi}\overrightarrow{\tau}\gamma^\mu\psi)(\bar{\psi}\overrightarrow{\tau}\gamma_\mu\psi)\\ &- \frac{1}{2}\delta_S(\partial_\nu\bar{\psi}\psi)(\partial^\nu\bar{\psi}\psi) - e\frac{1+\tau_3}{2}\bar{\psi}\gamma^\mu A_\mu\psi + \frac{1}{4}F^{\mu\nu}F_{\mu\nu}.\end{aligned} \tag{2.31}$$

The derivative term in Eq. (2.31) accounts for leading effects of finite-range interactions that are crucial for a quantitative description of nuclear density distribution, e.g. nuclear radii. Similar interactions can be included in each isospace-space channel, but in practice data only constrain a single derivative term, for instance: $\delta_S(\partial_\nu\bar{\psi}\psi)(\partial^\nu\bar{\psi}\psi)$. Similar to DD-ME Lagrangian (2.3), the couplings $\alpha_S, \alpha_V$ and $\alpha_{TV}$ of the interaction terms in Eq. (2.31) are functions of isovector density $\rho_v = j^0$. Lagrangian density (2.31) yields the Hamiltonian density and the EDF for the point-coupling model:

$$\begin{aligned}E_{RMF}[\psi,\bar{\psi},A^\mu] &= \int d\boldsymbol{r}\mathcal{H}(\boldsymbol{r})\\ &= \sum_{i=1}^{A}\int d\boldsymbol{r}\psi_i^\dagger(\boldsymbol{\alpha}\cdot\boldsymbol{p} + \beta m)\psi_i + \frac{1}{2}\int d\boldsymbol{r} j_p^\mu A_\mu\\ &\quad + \frac{1}{2}\int d\boldsymbol{r}\left[\alpha_S\rho_s^2 + \alpha_V j_\mu j^\mu + \alpha_{TV}\overrightarrow{j_\mu}\cdot\overrightarrow{j^\mu} + \delta_S\rho_s\triangle\rho_s\right].\end{aligned} \tag{2.32}$$

Again, the variation of the EDF $E_{RMF}[\psi,\bar{\psi},A^\mu]$ with respect to the Dirac spinors $\bar{\psi}$ leads to the Dirac equation with single-particle Hamiltonian $\hat{h}_D$ having the same

form as in Eq. (2.15):

$$\hat{h}_D = \begin{bmatrix} \Sigma^0 + \Sigma^0_R + (\Sigma_s + m) & \boldsymbol{\sigma} \cdot (\boldsymbol{p} - \boldsymbol{\Sigma}) \\ \boldsymbol{\sigma} \cdot (\boldsymbol{p} - \boldsymbol{\Sigma}) & \Sigma^0 + \Sigma^0_R - (\Sigma_s + m) \end{bmatrix}. \tag{2.33}$$

Variation with respect to photon field $A^\mu$ yields Poisson equation (2.22). The nucleon self-energies are defined by the following expressions:

$$\Sigma_s = \alpha_S(\rho_v)\rho_s + \delta_S \triangle \rho_s, \tag{2.34}$$

$$\Sigma^\mu = \alpha_V(\rho_v) j^\mu + \alpha_{TV}(\rho_v) \overrightarrow{\tau} \cdot \overrightarrow{j^\mu} + e\frac{1+\tau_3}{2} A^\mu. \tag{2.35}$$

The density dependence of the vertex function $\alpha_S, \alpha_V$ and $\alpha_{TV}$ produces the *rearrangement* contribution to the vector self-energy:

$$\Sigma^0_R = \frac{1}{2}\left(\alpha'_S(\rho_v)\rho_s^2 + \alpha'_V(\rho_v)\rho_v^2 + \alpha'_{TV}(\rho_v)\rho_{tv}^2\right). \tag{2.36}$$

In this work, a specific parameterization *ansatz* for the functional form of the coupling vertex functions:

$$\alpha_S(\rho_v) = a_S + (b_S + c_S x)e^{-d_S x}, \tag{2.37}$$

$$\alpha_V(\rho_v) = a_V + b_V e^{-d_V x}, \tag{2.38}$$

$$\alpha_{TV}(\rho_v) = b_{TV} e^{-d_{TV} x}, \tag{2.39}$$

with $x = \rho_v/\rho_{sat}$, where $\rho_{sat}$ denotes the nucleon density at saturation in symmetric nuclear matter.

Recently developed parameter set of the point-coupling interaction DD-PC1 [18] is used in this work. In Table 2.2 we list all the parameters which fully define the DD-PC1 point-coupling functional. The DD-PC1 parameters were adjusted simultaneously to infinite and semi-infinite nuclear matter properties and to the binding energies of 64 axially symmetric deformed nuclei in the mass region $A \approx 150-180$ and $A \approx 230-250$. The resulting energy density functional DD-PC1 has been further tested in calculations of binding energies, charge radii, deformation parameters, neutron skin thickness, and excitation energies of giant monopole and dipole resonances in Ref. [18].

## 2.2 Relativistic EDF theory with pairing

Relativistic energy density functionals have successfully been employed in studies of properties of ground and excited states in spherical and deformed nuclei. For a quantitative analysis of open-shell nuclei it is necessary to consider also pairing correlations. Pairing has often been taken into account in a very phenomenological way in the Bardeen–Cooper–Schrieffer (BCS) model with the monopole pairing force, adjusted to the experimental odd–even mass differences. In many cases, however, this approach presents only a poor approximation. The physics of weakly-bound nuclei, in particular, necessitates a unified and self-consistent treatment of mean-field and pairing correlations. This has led to the formulation and

| DD-PC1 parameter set | | |
|---|---|---|
| Parameter | Value | Unit |
| $a_S$ | $-10.0462$ | [fm$^2$] |
| $b_S$ | $-9.1504$ | [fm$^2$] |
| $c_S$ | $+6.4273$ | [fm$^2$] |
| $d_S$ | $+1.3724$ | |
| $a_V$ | $+5.9195$ | [fm$^2$] |
| $b_V$ | $+8.8637$ | [fm$^2$] |
| $d_V$ | $+0.6584$ | |
| $b_{TV}$ | $+1.8360$ | [fm$^2$] |
| $d_{TV}$ | $+0.6403$ | |
| $\delta_S$ | $-0.8149$ | [fm$^4$] |
| $\rho_{sat}$ | $+0.1520$ | [fm$^{-3}$] |

Table 2.2: DD-PC1 parameter set for the density-dependent point-coupling relativistic energy functional.

development of the relativistic Hartree–Bogoliubov (RHB) model [7, 20], which represents a relativistic extension of the conventional Hartree–Fock–Bogoliubov framework.

### 2.2.1 Relativistic Hartree-Bogoliubov model

The RHB model provides a unified description of particle-hole ($ph$) and particle-particle ($pp$) correlations on a mean-field level by using two average potentials: the self-consistent mean field $\hat{h}$ that encloses all the long range $ph$ correlations, and a pairing field $\hat{\Delta}$ which sums up the $pp$-correlations.

The ground state of a nucleus is described by a generalized Slater determinant $|\Phi\rangle$ that represents the vacuum with respect to independent quasiparticles. The quasiparticle operators $\hat{\alpha}_\mu, \hat{\alpha}^\dagger_\mu$ are defined by the unitary Bogoliubov transformation of the single-nucleon creation and annihilation operators:

$$\hat{\alpha}^\dagger_\mu = \sum_k \left( U_{k,\mu} \hat{c}^\dagger_k + V_{k,\mu} \hat{c}_k \right), \tag{2.40}$$

where the index $k$ refers to the original basis (configurational space), e.g. an oscillator basis or the coordinates $(\boldsymbol{r}, s, \tau)$ in space, spin and isospin. In addition, for the relativistic case, the index $d \in \{f, g\}$ will denote the large and small components of the corresponding Dirac spinor respectively. Columns of Bogoliubov matrices $U$ and $V$ are the Hartree-Bogoliubov wave functions determined by the variational principle. In the presence of pairing, the single-particle density matrix is generalized by two densities [21]: the normal density $\hat{\rho}$ matrix and the pairing tensor $\hat{\kappa}$ defined as:

$$\hat{\rho}_{k,k'} = \langle \Phi | \hat{c}^\dagger_{k'} \hat{c}_k | \Phi \rangle, \tag{2.41}$$

$$\hat{\kappa}_{k,k'} = \langle \Phi | \hat{c}_{k'} \hat{c}_k | \Phi \rangle. \tag{2.42}$$

The RHB energy density functional thus depends on both densities:

$$E_{RHB}[\hat{\rho}, \hat{\kappa}] = E_{RMF}[\hat{\rho}] + E_{pair}[\hat{\kappa}], \tag{2.43}$$

where $E_{RMF}[\hat{\rho}]$ is the RMF-functional defined by Eq. (2.13) or (2.32), and the pairing part of the RHB functional reads:

$$E_{pair}[\hat{\kappa}] = \frac{1}{4}\sum_{k_1,k_1'}\sum_{k_2,k_2'}\hat{\kappa}^*_{k_1,k_1'}\langle k_1,k_1'|V^{pp}|k_2,k_2'\rangle_a\hat{\kappa}_{k_2,k_2'}. \tag{2.44}$$

$\langle k_1,k_1'|V^{pp}|k_2,k_2'\rangle_a$ are the (antisymmetrized) matrix elements of the two-body pairing interaction:

$$\langle k_1,k_1'|V^{pp}|k_2,k_2'\rangle_a = \langle k_1,k_1'|V^{pp}|k_2,k_2'\rangle - \langle k_1,k_1'|V^{pp}|k_2',k_2\rangle. \tag{2.45}$$

The columns of Bogoliubov matrices $U_\mu, V_\mu$ are obtained by the variational principle of $E_{RHB}$ which yields the RHB eigenvalue equation:

$$\begin{bmatrix}\hat{h}_D - m - \lambda & \hat{\Delta} \\ -\hat{\Delta}^* & -\hat{h}_D^* + m + \lambda\end{bmatrix}\begin{bmatrix}U_\mu \\ V_\mu\end{bmatrix} = E_\mu\begin{bmatrix}U_\mu \\ V_\mu\end{bmatrix}. \tag{2.46}$$

In the relativistic case, the self-consistent mean-field corresponds to the single-nucleon Dirac Hamiltonian $\hat{h}_D$ of Eqs. (2.15) or (2.33). $m$ is the nucleon mass, and the chemical potential $\lambda$ is determined as a Lagrange multiplier by the particle number subsidiary condition such that the expected value of the particle number operator in the ground state equals the given number of nucleons. The pairing field reads:

$$\hat{\Delta}_{k_1,k_1'} = \frac{1}{2}\sum_{k_2,k_2'}\langle k_1,k_1'|V^{pp}|k_2,k_2'\rangle_a\hat{\kappa}_{k_2,k_2'}. \tag{2.47}$$

The colum vectors in the eigenvalue problem Eq. (2.46) denote the quasiparticle wave functions, and $E_\mu$ are the quasiparticle energies. The dimension of the RHB matrix equation is two times the dimension of the corresponding Dirac eigenvalue matrix equation (2.14). Therefore, for each eigenvector $(U_\mu, V_\mu)$ with positive quasiparticle energy $E_\mu > 0$, there exists an eigenvector $(V_\mu^*, U_\mu^*$ with negative quasiparticle energy $-E_\mu$. Since the baryon quasiparticle operators satisfy fermion commutation relations, the levels $E_\mu$ and $-E_\mu$ cannot be occupied simultaneously, that is, one chooses either the positive or the negative eigenvalue and the corresponding eigenvector.

In the Hartree–Fock case, the choice of positive or negative value of the quasiparticle energy means that the level is either occupied or empty. For the non-relativistic HFB the ground state represents the minimum of the energy surface and, to form a vacuum with respect to all quasiparticles, one chooses only the positive quasiparticle energies, which defines the quasiparticle vacuum $|\Phi\rangle$:

$$\hat{\alpha}_\mu|\Phi\rangle = 0, \quad \text{for } E_\mu > 0. \tag{2.48}$$

The single-particle density $\hat{\rho}$ and pairing tensor $\hat{\kappa}$ that correspond to this state can be expressed in terms of the quasiparticle wave functions:

$$\hat{\rho}_{k,k'} = \sum_{E_\mu>0} V^*_{k,\mu}V_{k',\mu}, \tag{2.49}$$

$$\hat{\kappa}_{k,k'} = \sum_{E_\mu>0} V^*_{k,\mu} U_{k',\mu}. \tag{2.50}$$

In the relativistic case one finds solutions in the Dirac sea (usually called negative energy solutions and denoted by the index $a$ - antiparticles), and solutions above the Dirac sea (usually called positive energy solutions and denoted by the index $p$ - particles). In the Dirac equation without pairing they can easily be distinguished by the sign of the corresponding eigenvalues. For the RHB equations (2.46) this is no longer the case but, because of the large gap between the Dirac sea and the Fermi sea (by at least 1000 MeV), one can easily distinguish the levels in the Dirac sea $|E_a|>$ 1200 MeV, from those above the Dirac sea. The *no-sea approximation* here means that we have to choose solutions with positive quasiparticle energies $E_p > 0$ for the states above the Dirac sea, and solutions with negative quasiparticle energies $E_a < 0$ for all levels in the Dirac sea.

### 2.2.2 Separable pairing interaction

Pairing correlations in nuclei are restricted to an energy window of a few MeV around the Fermi level, and their scale is well separated from the scale of binding energies, that are in the range from several hundred to thousand MeV. There is no empirical evidence for any relativistic effect in the nuclear pairing field $\hat{\Delta}$ and, therefore, a hybrid RHB model with a non-relativistic pairing interaction can be formulated. For a general two-body interaction, the matrix elements of the relativistic pairing field read:

$$\hat{\Delta}_{k_1 d_1, k'_1 d'_1} = \frac{1}{2} \sum_{k_1 d_1, k'_1 d'_1} \langle k_1 d_1, k'_1 d'_1 | V^{pp} | k_2 d_2, k'_2 d'_2 \rangle_a \hat{\kappa}_{k_2 d_2, k'_2 d'_2}. \tag{2.51}$$

The indices $d_1, d'_1, d_2, d'_2$ refer to the large and small components of the quasiparticle Dirac spinor:

$$U_\mu = \begin{bmatrix} f^{(U)}_\mu \\ i g^{(U)}_\mu \end{bmatrix}, \quad V_\mu = \begin{bmatrix} f^{(V)}_\mu \\ i g^{(V)}_\mu \end{bmatrix}. \tag{2.52}$$

In practical application of the RHB model, only the large components of the spinors $U_\mu$ and $V_\mu$ are used to build the pairing tensor $\hat{\kappa}$. The resulting pairing field reads:

$$\hat{\Delta}_{k_1 f_1, k'_1 f'_1} = \frac{1}{2} \sum_{k_1 f_1, k'_1 f'_1} \langle k_1 f_1, k'_1 f'_1 | V^{pp} | k_2 f_2, k'_2 f'_2 \rangle_a \hat{\kappa}_{k_2 f_2, k'_2 f'_2}. \tag{2.53}$$

Other components: $\hat{\Delta}_{fg}, \hat{\Delta}_{gf}$ and $\hat{\Delta}_{gg}$ can be safely omitted [22].

In order to reduce the computational effort, a separable form of the pairing force has been introduced for RHB calculations in spherical and deformed nuclei [23, 24, 25]. The force is separable in momentum space, and is completely determined by two parameters that are adjusted to reproduce the pairing gap of the Gogny force in symmetric nuclear matter. The gap equation in the $^1S_0$ channel reads:

$$\Delta(k) = -\int_0^\infty \frac{k'^2 dk'}{2\pi^2} \langle k | V^{^1S_0} | k' \rangle \frac{\Delta(k')}{2E(k')}, \tag{2.54}$$

and the pairing force is separable in momentum space:

$$\langle k|V^{^1S_0}|k'\rangle = -Gp(k)p(k'). \tag{2.55}$$

By assuming a simple Gaussian *ansatz* $p(k) = e^{-a^2k^2}$, the two parameters $G$ and $a$ have been adjusted to reproduce the density dependence of the gap at the Fermi surface, calculated with a Gogny force. For the D1S parameterization [26] of the Gogny force, the following values were determined: $G = 728$ MeV fm$^3$ and $a = 0.6442$ fm. When the pairing force equation (2.55) is transformed from momentum to coordinate space, it takes the form:

$$V^{pp}(\boldsymbol{r}_1, \boldsymbol{r}_2, \boldsymbol{r}_1'\boldsymbol{r}_2') = -G \cdot \frac{1}{2}(1 - \hat{P}_\sigma) \cdot \delta^3(\boldsymbol{R} - \boldsymbol{R}') \cdot P(\boldsymbol{r})P(\boldsymbol{r}'), \tag{2.56}$$

where $\frac{1}{2}(1 - \hat{P}_\sigma)$ is the spin exchange term, $\boldsymbol{R} = \frac{1}{2}(\boldsymbol{r}_1 + \boldsymbol{r}_2)$ and $\boldsymbol{r} = \boldsymbol{r}_1 - \boldsymbol{r}_2$ denote the center-of-mass and the relative coordinates respectively, and $P(\boldsymbol{r})$ is the Fourier transform of the $p(k)$ function:

$$P(\boldsymbol{r}) = \frac{1}{(4\pi a^2)^{3/2}} e^{-\boldsymbol{r}^2/4a^2}. \tag{2.57}$$

The pairing force has a finite range and, because of the presence of the factor $\delta^3(\boldsymbol{R} - \boldsymbol{R}')$, it preserves translational invariance. Even though $\delta^3(\boldsymbol{R} - \boldsymbol{R}')$ implies that this force is not completely separable in coordinate space, the corresponding antisymmetrized $pp$ matrix elements $\langle k_1 k_2|V^{pp}|k_1' k_2'\rangle_a$ can be represented as a sum of a finite number of separable terms in the harmonic oscillator basis. Details are given in [23, 24, 25].

### 2.2.3 Numerical implementation of the RHB model

For nuclei with spherical symmetry the RHB equation in coordinate space reduces to a simple set of radial integro-differential equations. In the case of deformed nuclei, however, the solution of integro-differential equations in coordinate space presents a numerically intensive and time-consuming task. For an efficient implementation of the RHB model in this work a method proposed by Vautherin [27] is used, that combines the configurational and coordinate space representations.

The RHB equation is solved in the configurational space of harmonic oscillator wave functions with appropriate symmetry, whereas the densities are computed in coordinate space. The method can be applied to spherical, axially and non-axially deformed nuclei. The RHB eigenvalue problem in configurational space of harmonic oscillator reads [17]:

$$\begin{bmatrix} \mathcal{A} - \lambda I & \mathcal{B} & \Delta_{ff} & 0 \\ \mathcal{B}^T & \mathcal{C} - \lambda I & 0 & 0 \\ \Delta_{ff} & 0 & -\mathcal{A} + \lambda I & -\mathcal{B} \\ 0 & 0 & -\mathcal{B}^T & -\mathcal{C} + \lambda I \end{bmatrix} \begin{bmatrix} f^{(U)} \\ g^{(U)} \\ f^{(V)} \\ g^{(V)} \end{bmatrix} = E \begin{bmatrix} f^{(U)} \\ g^{(U)} \\ f^{(V)} \\ g^{(V)} \end{bmatrix}. \tag{2.58}$$

The diagonalization of the RHB matrix equation yields the wave functionals in configurational space. The resulting density matrix is computed in configurational

space:

$$\begin{bmatrix} \hat{\rho}_{k,k'} & \hat{\rho}_{k,\tilde{k}'} \\ \hat{\rho}_{\tilde{k},k'} & \hat{\rho}_{\tilde{k},\tilde{k}'} \end{bmatrix} = \begin{bmatrix} \sum_\mu f_k^{(V_\mu)*} f_{k'}^{(V_\mu)} & \mathrm{i}\sum_\mu f_k^{(V_\mu)*} g_{\tilde{k}'}^{(V_\mu)} \\ -\mathrm{i}\sum_\mu g_{\tilde{k}}^{(V_\mu)*} f_{k'}^{(V_\mu)} & \sum_\mu g_{\tilde{k}}^{(V_\mu)*} g_{\tilde{k}'}^{(V_\mu)} \end{bmatrix}, \tag{2.59}$$

where $k$ and $\tilde{k}$ denote the indices of an expansion of the large and small components of the Dirac spinor in the oscillator basis. The density matrix is then transformed to the coordinate space, and the resulting vector and scalar densities are used to calculate the potentials.

The map of the energy surface as a function of quadrupole deformation parameters is obtained by solving the RHB equation with constraints on mass quadrupole moments of a given nucleus. The method of quadratic constraints uses an unrestricted variation of the function:

$$\langle \hat{H} \rangle + c_2(\langle \hat{Q}_2 \rangle - q_2)^2, \tag{2.60}$$

where $\langle \hat{H} \rangle$ is the total energy and $\langle \hat{Q}_2 \rangle$ denotes the expectation value of the mass quadrupole moment operator. $q_2$ is the constrained value of the multipole moment and $c_2$ is the corresponding stiffness constant. Augmented Lagrangian method [28] is used to push the system in a state with constrained value of quadrupole moment.

In this work, we focus exclusively on axially deformed nuclei with constrained quadrupole moment. We introduce a convenient dimensionless deformation parameter $\beta$ which uniquely defines the quadrupole deformation of axially symmetric nucleus $\rho_v(\boldsymbol{r}) = \rho_v(r_\perp, z)$ as:

$$\beta = \frac{4\pi}{3}\frac{1}{AR_0^2}\int \rho_v(\boldsymbol{r})|\boldsymbol{r}|^2 Y_{20}(\theta,\varphi)d\boldsymbol{r}, \tag{2.61}$$

for $R_0 = 1.2A^{1/3}$ fm. For illustration, $\beta \sim 0$ corresponds to nearly spherical nuclei, $\beta \sim 0.2 - 0.5$ correspond to typical deformation encountered in ground state of nuclei, while $\beta \sim 1$ correspond to very deformed configurations. Parameter $\beta$ will be used throughout this work as a quantitative measure of quadrupole deformation in axially symmetric systems.

RHB solver DIRHB [1] implements DD-PC1 and DD-ME2 energy density functionals and separable pairing interaction for axially deformed systems with a possible constraint of quadrupole deformaton. In the iterative procedure that leads to the self-consistent solution, the intermediate solutions are combined by using the Broyden's mixing procedure [29]. DIRHB solver is used as a starting point of this work since it calculates the ground state properties on top of which collective excitations can be studied. In the following section, a theoretical framework for calculating the nuclear response in presence of a weak external perturbation is presented as an extension of the RHB model.

## 2.3 Quasiparticle Finite Amplitude Method

In the formalism of supermatrices introduced by Valatin [30], the RHB functions are determined by the Bogoliubov transformation which relates the original basis of particle creation and annihilation operators $c_k$, $c_k^\dagger$ (e.g. an oscillator basis) to

the quasiparticle basis $\alpha_\mu$, $\alpha_\mu^\dagger$[1]:

$$\begin{pmatrix} c \\ c^\dagger \end{pmatrix} = \mathcal{W} \begin{pmatrix} \alpha \\ \alpha^\dagger \end{pmatrix} \qquad \text{with} \qquad \mathcal{W} = \begin{pmatrix} U & V^* \\ V & U^* \end{pmatrix}, \tag{2.62}$$

where $\mathcal{W}$ denotes the matrix of unitary Bogoliubov transformation. In this notation a single-particle operator can be represented in a matrix form:

$$F = \frac{1}{2} \begin{pmatrix} \alpha^\dagger & \alpha \end{pmatrix} \mathcal{F} \begin{pmatrix} \alpha \\ \alpha^\dagger \end{pmatrix} + \text{const}, \tag{2.63}$$

with:

$$\mathcal{F} = \begin{pmatrix} F^{11} & F^{20} \\ -F^{02} & -(F^{11})^T \end{pmatrix}. \tag{2.64}$$

In particular, for the generalized density $\mathcal{R}$:

$$\mathcal{R} = \mathcal{W}^\dagger \begin{pmatrix} \rho & \kappa \\ -\kappa^* & 1-\rho^* \end{pmatrix} \mathcal{W}, \tag{2.65}$$

where the density matrix and pairing tensor read: $\rho = V^* V^T$ and $\kappa = V^* U^T$. The RHB Hamiltonian is given by a functional derivative of a given energy density functional with respect to the generalized density:

$$\mathcal{H} = \frac{\delta E[\mathcal{R}]}{\delta \mathcal{R}} = \mathcal{W}^\dagger \underbrace{\begin{pmatrix} h & \Delta \\ -\Delta^* & -h^* \end{pmatrix}}_{H} \mathcal{W}. \tag{2.66}$$

The evolution of the quasiparticle operator $\alpha_\mu(t)$ subject to time-dependent external perturbation $F(t)$ is determined by the equation:

$$i\partial_t \alpha_\mu(t) = [H(t) + F(t), \alpha_\mu(t)]. \tag{2.67}$$

For a weak harmonic external field:

$$F(t) = \eta(F(\omega)e^{-i\omega t} + F^\dagger(\omega)e^{+i\omega t}), \tag{2.68}$$

characterized by the small real parameter $\eta$, the $F(\omega)$ operator reads:

$$F(\omega) = \frac{1}{2} \sum_{\mu\nu} F^{20}_{\mu\nu} \alpha^\dagger_\mu \alpha^\dagger_\nu + F^{02}_{\mu\nu} \alpha_\nu \alpha_\mu. \tag{2.69}$$

The $F^{11}_{\mu\nu}$ term that would appear in the previous equation does not contribute in linear response and thus can be safely omitted. The external harmonic field $F(t)$ induces a small-amplitude oscillations of the $\alpha_\mu(t)$ operator around the ground-state solution with the same energy:

$$\alpha_\mu(t) = (\alpha_\mu + \delta\alpha_\mu(t))\, e^{iE_\mu t}. \tag{2.70}$$

[1] In the following, the Roman alphabet characters will denote the particle basis states, while the Greek will denote the quasiparticle basis states.

$E_\mu$ denotes the quasiparticle energies (as introduced in Section 2.2.1). The oscillating part of the $\alpha_\mu(t)$ operator is expanded in terms of quasiparticle creation operators[2]:

$$\delta\alpha_\mu(t) = \eta \sum_\nu \alpha^\dagger_\nu \left( X_{\nu\mu}(\omega) e^{-i\omega t} + Y^*_{\nu\mu}(\omega) e^{+i\omega t} \right). \tag{2.71}$$

Coefficients $X_{\mu\nu}(\omega)$ and $Y_{\mu\nu}(\omega)$ are referred to as the forward and backward QRPA amplitudes respectively. The oscillations of the density matrix and the pairing tensor produce the induced oscillating fields in the single-particle Hamiltonian $h(t) = h_0 + \delta h(t)$ and the pairing field $\Delta(t) = \Delta_0 + \delta\Delta(t)$. $h_0$ and $\Delta_0$ denote the ground state values. The Hamiltonian $H(t)$ can also be decomposed into static and oscillating terms:

$$H(t) = H_0 + \delta H(t) = H_0 + \eta \left[ \delta H(\omega) e^{-i\omega t} + \delta H^\dagger(\omega) e^{+i\omega t} \right]. \tag{2.72}$$

The $\delta H(\omega)$ operator is decomposed in quasiparticle basis as:

$$\delta H(\omega) = \frac{1}{2} \sum_{\mu\nu} \delta H^{20}_{\mu\nu}(\omega) \alpha^\dagger_\mu \alpha^\dagger_\nu + \delta H^{02}_{\mu\nu}(\omega) \alpha_\nu \alpha_\mu. \tag{2.73}$$

By inserting Eqs. (2.70-2.73) into the equation of motion Eq. (2.67), and retaining only linear terms in $\eta$, we obtain the QFAM equations:

$$\left(E_\mu + E_\nu - \omega\right) X_{\mu\nu}(\omega) + \delta H^{20}_{\mu\nu}(\omega) = -F^{20}_{\mu\nu}, \tag{2.74}$$

$$\left(E_\mu + E_\nu + \omega\right) Y_{\mu\nu}(\omega) + \delta H^{02}_{\mu\nu}(\omega) = -F^{02}_{\mu\nu}. \tag{2.75}$$

We notice that $\delta H^{20}_{\mu\nu}(\omega)$ and $\delta H^{02}_{\mu\nu}(\omega)$ depend on the induced fields $\delta h(\omega), \delta\Delta(\omega)$, which in turn depend on the induced densities, i.e., on the amplitudes $X_{\mu\nu}(\omega)$ and $Y_{\mu\nu}(\omega)$. Therefore, Eqs. (2.74-2.75) represent a set of non-linear equations that can be solved self-consistently. The expansion of $\delta H^{20}_{\mu\nu}(\omega)$ and $\delta H^{02}_{\mu\nu}(\omega)$ in terms of $X_{\mu\nu}(\omega)$ and $Y_{\mu\nu}(\omega)$:

$$\delta H^{20}_{\mu\nu}(\omega) = -(E_\mu + E_\nu) X_{\mu\nu}(\omega) + \sum_{\mu'<\nu'} A_{\mu\nu,\mu'\nu'} X_{\mu'\nu'}(\omega) + B_{\mu\nu,\mu'\nu'} Y_{\mu'\nu'}(\omega), \tag{2.76}$$

$$\delta H^{02}_{\mu\nu}(\omega) = -(E_\mu + E_\nu) Y_{\mu\nu}(\omega) + \sum_{\mu'<\nu'} B^*_{\mu\nu,\mu'\nu'} X_{\mu'\nu'}(\omega) + A^*_{\mu\nu,\mu'\nu'} Y_{\mu'\nu'}(\omega), \tag{2.77}$$

leads to the conventional QRPA equation:

$$\left( \begin{bmatrix} A & B \\ B^* & A \end{bmatrix} - \omega \begin{bmatrix} I & 0 \\ 0 & -I \end{bmatrix} \begin{bmatrix} X(\omega) \\ Y(\omega) \end{bmatrix} \right) = - \begin{bmatrix} F^{20} \\ F^{02} \end{bmatrix}. \tag{2.78}$$

where the vectorized matrix notation is used. In order to prevent that the QRPA solutions diverge in the vicinity of the QRPA eigenfrequency, one adds a small imaginary part $\gamma$ to the excitation energy $\omega \to \omega + i\gamma$.

These equations contain second derivatives ($A$ and $B$ matrices) of the density functional $E[\mathcal{R}]$ with respect to $\mathcal{R}$ as matrix elements. For deformed nuclei in

[2]We notice that including the annihilation operators in the expansion would not alter the density matrix or the pairing tensor.

particular, the number of two-quasiparticle configurations $(\mu, \nu)$, i.e. the size of matrices $A$ and $B$, can become very large and the evaluation of matrix elements requires a considerable, and in many cases prohibitive, numerical effort. Even if the matrix elements are calculated, the direct solution of the QRPA equation by matrix diagonalization is even more prohibitive in terms of computational cost. In many cases this has prevented systematic applications of the conventional QRPA method to studies of the multipole response of medium-heavy and heavy deformed nuclei.

In order to use the stationary RHB code as a starting point for the evaluation of the $\mathcal{H}(\mathcal{R})$, the generalized density should be transformed back to the original single-particle basis by using the Bogoliubov transformation:

$$\alpha_\mu(t) = \sum_k \left( U^*_{k\mu}(t) c_k + V^*_{k\mu}(t) c^\dagger_k \right). \tag{2.79}$$

Eqs. (2.70) and (2.71) lead to the following expressions for the $U(t)$ and $V(t)$ coefficients:

$$U_{k\mu}(t) = U_{k\mu} e^{-iE_\mu t} + \eta e^{-iE_\mu t} \sum_\nu \left( V^*_{k\nu} Y_{\nu\mu}(\omega) e^{-i\omega t} + V^*_{k\nu} X^*_{\nu\mu}(\omega) e^{+i\omega t} \right), \tag{2.80}$$

$$V_{k\mu}(t) = V_{k\mu} e^{-iE_\mu t} + \eta e^{-iE_\mu t} \sum_\nu \left( U^*_{k\nu} Y_{\nu\mu}(\omega) e^{-i\omega t} + U^*_{k\nu} X^*_{\nu\mu}(\omega) e^{+i\omega t} \right). \tag{2.81}$$

$V_{k\mu}$ and $U_{k\mu}$ denote the stationary Bogoliubov coefficients. The induced density matrix $\rho(t) = V^*(t) V^T(t)$ reads:

$$\rho(t) = V^* V^T + \eta \left( \delta\rho(\omega) e^{-i\omega t} + \delta\rho^\dagger(\omega) e^{+i\omega t} \right), \tag{2.82}$$

with:

$$\delta\rho(\omega) = U X(\omega) V^T + V^* Y^T(\omega) U^\dagger. \tag{2.83}$$

The induced pairing tensor $\kappa(t) = V^*(t) U^T(t)$ reads:

$$\kappa(t) = V^* U^T + \eta \left( \delta\kappa^{(+)}(\omega) e^{-i\omega t} + \delta\kappa^{(-)}(\omega) e^{+i\omega t} \right), \tag{2.84}$$

with:

$$\delta\kappa^{(+)}(\omega) = U X(\omega) U^T + V^* Y^T(\omega) V^\dagger \tag{2.85}$$

and

$$\delta\kappa^{(-)}(\omega) = V^* X^\dagger(\omega) V^\dagger + U Y^*(\omega) U^T. \tag{2.86}$$

It should be noted that although $\delta\rho(\omega)$ matrix is not necessarily hermitian, the matrices $\delta\kappa^{(+)}(\omega)$ and $\delta\kappa^{(-)}(\omega)$ are still antisymmetric. The induced single-particle Hamiltonian:

$$\delta h(t) = \eta \left( \delta h(\omega) e^{-i\omega t} + \delta h^\dagger(\omega) e^{+i\omega t} \right), \tag{2.87}$$

is linearized explicitly in the coordinate space, while the induced pairing field reads:

$$\delta\Delta(t) = \eta \left( \delta\Delta^{(+)}(\omega) e^{-i\omega t} + \delta\Delta^{(-)}(\omega) e^{+i\omega t} \right), \tag{2.88}$$

with

$$\delta\Delta^{(\pm)}_{lm}(\omega) = \frac{1}{2}\sum_{pq} \bar{v}_{lmpq}\delta\kappa^{(\pm)}_{pq}(\omega). \tag{2.89}$$

$\bar{v}_{lmpq}$ are the antisymmetrized matrix elements of the pairing interaction introduced earlier in Section 2.2.1.

The induced Hamiltonian components in quaiparticle basis $\delta H^{20}(\omega)$ and $\delta H^{02}(\omega)$ are calculated by transforming back to the quasiparticle basis via unitary Bogoliubov transformation:

$$\delta\mathcal{H}(\omega) = \mathcal{W}^\dagger \begin{pmatrix} \delta h(\omega) & \delta\Delta^{(+)}(\omega) \\ -\delta\Delta^{(-)}(\omega)^* & -\delta h^T(\omega) \end{pmatrix} \mathcal{W}. \tag{2.90}$$

The explicit expressions for $\delta H^{20}(\omega)$ and $\delta H^{02}(\omega)$ read:

$$\begin{aligned} \delta H^{20}(\omega) =& + U^\dagger \delta h(\omega) V^* - V^\dagger \delta h^T(\omega) U^* \\ &+ U^\dagger \delta\Delta^{(+)}(\omega) U^* - V^\dagger [\delta\Delta^{(-)}(\omega)]^* V^*, \end{aligned} \tag{2.91}$$

$$\begin{aligned} \delta H^{02}(\omega) =& - V^T \delta h(\omega) U + U^T \delta h^T(\omega) V \\ &- V^T \delta\Delta^{(+)}(\omega) V + U^T [\delta\Delta^{(-)}(\omega)]^* U. \end{aligned} \tag{2.92}$$

The transition strength function $S(f,\omega)$ is defined as:

$$S(f,\omega) = \sum_{\mu<\nu} F^{20}_{\mu\nu}(\omega)^* X_{\mu\nu}(\omega) + F^{02}_{\mu\nu}(\omega)^* Y_{\mu\nu}(\omega), \tag{2.93}$$

while the response function is defined as:

$$\frac{dB}{d\omega}(f,\omega) = -\frac{1}{\pi}\,\mathrm{Im}\, S(f,\omega). \tag{2.94}$$

One can show that one can alternatively calculate the response function as:

$$\frac{dB}{d\omega}(f,\omega) = -\frac{1}{\pi}\,\mathrm{Im}\left[f^\dagger \delta\rho(\omega)\right], \tag{2.95}$$

where $\delta\rho(\omega)$ denotes the induced density matrix and $f_{kl}$ are the matrix elements of the operator $F(\omega)$ in the single-particle basis:

$$F(\omega) = \sum_{kl} f_{kl} c^\dagger_k c_l. \tag{2.96}$$

# Chapter 3

# QFAM implementation

In this Chapter, a QFAM implementation is presented for a specific choice of energy density functionals, pairing interaction, configurational basis, imposed axial symmetry and for a certain class of excitation operators. Ref. [2] is followed. In conjunction with this section, Appendix A is referenced as an extensive supplement throughout the Chapter for technical details.

## 3.1 QFAM solver - **DIRQFAM**

### 3.1.1 Harmonic oscillator simplex-y basis

In this section we first briefly describe the single-particle basis of eigenfunctions of a single-particle Hamiltonian for an axially symmetric deformed harmonic oscillator (HO) potential:

$$V_{osc}(z, r_\perp) = \frac{1}{2} m\omega_z^2 z^2 + \frac{1}{2} m\omega_\perp^2 r_\perp^2, \tag{3.1}$$

used in the ground-state calculations. $(z, r_\perp, \varphi)$ denote the standard cylindrical coordinates:

$$x = r_\perp \cos\varphi, \quad y = r_\perp \sin\varphi, \quad z = z. \tag{3.2}$$

Imposing volume conservation, the two oscillator frequencies $\hbar\omega_z$ and $\hbar\omega_\perp$ can be expressed in terms of a deformation parameter $\beta_0$:

$$\hbar\omega_z = \hbar\omega_0 e^{-\sqrt{\frac{5}{4\pi}}\beta_0}, \quad \hbar\omega_\perp = \hbar\omega_0 e^{\frac{1}{2}\sqrt{\frac{5}{4\pi}}\beta_0}. \tag{3.3}$$

The corresponding oscillator length parameters are:

$$b_z = \sqrt{\frac{\hbar}{m\omega_z}}, \quad b_\perp = \sqrt{\frac{\hbar}{m\omega_\perp}}. \tag{3.4}$$

$b_\perp^2 b_z = b_0^3$ because of the volume conservation. The basis is now determined by the two constants $\hbar\omega_0$ and $\beta_0$. Current implementation uses the following estimate for the HO frequency: $\hbar\omega_0 = 41A^{1/3}$ MeV originating from classical nuclear shell-model. The eigenfunctions of the deformed harmonic oscillator potential are labeled by the set of quantum numbers:

$$|\alpha\rangle = |n_z n_r \Lambda m_s\rangle, \tag{3.5}$$

where $n_z, n_r \in \mathbb{N}_0$, are the number of nodes in the $z$ and $r_\perp$ directions, respectively. $\Lambda \in \mathbb{Z}$ and $m_s \in \{\pm\frac{1}{2}\}$ are projections of the orbital angular momentum and spin on the intrinsic $z$-axis, respectively. Making use of the dimensionless variables:

$$\xi = z/b_z, \quad \eta = r_\perp^2/b_\perp^2, \tag{3.6}$$

the harmonic oscillator eigenvectors read:

$$|\alpha\rangle = |n_z n_r \Lambda m_s\rangle = \phi_{n_z}(z, b_z)\phi_{n_r}^{\Lambda}(r_\perp, b_\perp)\frac{e^{i\Lambda\varphi}}{\sqrt{2\pi}}\chi_{m_s}(s), \tag{3.7}$$

where:

$$\phi_{n_z}(z, b_z) = b_z^{-1/2}\mathcal{N}_{n_z}H_{n_z}(\xi)e^{-\xi^2/2}, \tag{3.8}$$

$$\phi_{n_r}^{\Lambda}(r_\perp, b_\perp) = b_\perp^{-1}\mathcal{N}_{n_r}^{\Lambda}\sqrt{2}\eta^{|\Lambda|/2}L_{n_r}^{|\Lambda|}(\eta)e^{-\eta/2}. \tag{3.9}$$

$H_{n_z}(\xi)$ and $L_{n_r}^{|\Lambda|}(\eta)$ denote the Hermite and associated Laguerre polynomials, respectively. The normalization factors are:

$$\mathcal{N}_{n_z} = (\sqrt{\pi}2^{n_z}n_z!\,)^{-1/2} \quad \text{and} \quad \mathcal{N}_{n_r}^{\Lambda} = (n_r!\,/(n_r + |\Lambda|)!\,)^{1/2}. \tag{3.10}$$

The large and small components of a Dirac spinor are expanded independently in terms of the oscillator eigenfunctions:

$$f_\mu(\boldsymbol{r}, m_s, t_z) = \sum_{\substack{\text{Shell}(\alpha)\leq N_{\text{shells}} \\ \Omega=\Lambda+m_s>0}} f_\alpha^{(\mu)}|\alpha\rangle\chi_{t_z}(t), \tag{3.11}$$

$$g_\mu(\boldsymbol{r}, m_s, t_z) = \sum_{\substack{\text{Shell}(\tilde{\alpha})\leq N_{\text{shells}}+1 \\ \tilde{\Omega}=\tilde{\Lambda}+\tilde{m}_s>0}} g_{\tilde{\alpha}}^{(\mu)}|\tilde{\alpha}\rangle\chi_{t_z}(t). \tag{3.12}$$

To avoid the appearance of spurious states, the quantum numbers $\alpha$ and $\tilde{\alpha}$ are chosen in such a way that the corresponding shell they belong to: $\text{Shell}(\alpha) = n_z + 2n_r + |\Lambda|$ and $\text{Shell}(\tilde{\alpha}) = \tilde{n}_z + 2\tilde{n}_r + |\tilde{\Lambda}|$, are not larger than $N_{\text{shells}}$ and $N_{\text{shells}}+1$ for the large and small components, respectively. Due to the time-reversal symmetry of the ground state solution, only positive eigenvalues $\Omega = \Lambda+m_s > 0$ of the $J_z$ symmetry operator are retained in the expansion. Notice that the size of the truncated HO basis basis, i.e. the total number of vectors used in the expansion (and consequently the size of matrices in RHB equation (2.46)), depend only on the number of shells $N_{\text{shells}}$.

The HO basis states are used to build the eigenfunctions of the simplex-y operator $S_y = Pe^{-i\pi J_y}$, where $P$ denotes the parity operator[1]. One can easily verify that the following combinations are eigenstates of the $S_y$ operator with

[1]Recall that the parity operator acting on Dirac spinors is given by $\gamma^0$ matrix.

eigenvalues $s = +i$ and $s = -i$:

$$|n_z n_r \Lambda;\ s = +i\rangle = \frac{1}{\sqrt{2}} \left( i|n_z n_\perp \Lambda \uparrow\rangle + |n_z n_r - \Lambda \downarrow\rangle \right), \tag{3.13}$$

$$|n_z n_r \Lambda;\ s = -i\rangle = \frac{1}{\sqrt{2}} \left( |n_z n_\perp \Lambda \uparrow\rangle + i|n_z n_r - \Lambda \downarrow\rangle \right). \tag{3.14}$$

Furthermore, these states are related by the time-reversal operator $T$:

$$T|n_z n_r \Lambda;\ s = \pm i\rangle = \mp |n_z n_r \Lambda;\ s = \mp i\rangle. \tag{3.15}$$

Due to the time-reversal symmetry of the ground state solution, for each solution with $\Omega > 0$, there is a degenerate time-reversed solution with $\Omega < 0$. These two states can be used to construct the eigenstates of the RHB Hamiltonian that are simultaneously also the eigenfunctions of the simplex-y operator. The HO basis states used to expand the ground state quasiparticle spinors are ordered in the following way: basis states with $\Omega > 0$ are listed first followed by their time-reversed pairs. The simplex-y HO basis states used in the QFAM calculations are ordered into two blocks: basis states with $s = +i$ are listed first followed by the $s = -i$ pairs of states. By ordering the single-quasiparticle states in the same manner, the Bogoliubov matrices $U$ and $V$ acquire the following block structure:

$$U = \begin{pmatrix} u & 0 \\ 0 & u^* \end{pmatrix}, \quad V = \begin{pmatrix} 0 & -v^* \\ v & 0 \end{pmatrix}. \tag{3.16}$$

Appendix A.1 provides the transformation formula of Bogoliubov $U$ and $V$ matrices obtained from ground state solution in HO basis to the HO simplex-y basis.

### 3.1.2 QFAM iteration

In order to solve QFAM Eqs. (2.74) and (2.75), the QFAM amplitudes are expanded in a basis of the eigenstates of the axially symmetric harmonic oscillator and the simplex-y operator. In the following we will refer to this basis as the simplex-y harmonic oscillator (simplex-y HO) basis.

First let us assume that we have the induced single-particle Hamiltonian $\delta h(\omega)$ and pairing fields $\delta\Delta^{(\pm)}(\omega)$. Then, following Eq. (2.90) we can directly compute the induced Hamiltonian $\delta H^{20}_{\mu\nu}(\omega)$ and $\delta H^{02}_{\mu\nu}(\omega)$. After that, the QFAM equations (2.74) and (2.75) yield the QFAM amplitudes $X_{\mu\nu}(\omega)$ and $Y_{\mu\nu}(\omega)$ if the excitation operator is specified, i.e. $F^{20}_{\mu\nu}(\omega)$ and $F^{02}_{\mu\nu}(\omega)$ are known. Once the QFAM aplitudes are computed, Eq. (2.83), (2.85) and (2.86) yield the induced density matrix $\delta\rho(\omega)$ and pairing tensor $\delta\kappa^{(\pm)}(\omega)$ in HO simplex-y basis. As will be shown in the following sections, induced density matrix can be used to calculate the induced densities and currents in coordinate space which will define the induced potentials of the used EDF. These induced potentials, on the other hand, can be used to find the induced single-particle Hamiltonian $\delta h(\omega)$ by numerical integration. Also, the induced pairing tensor can be used to directly compute the induced pairing fields $\delta\Delta^{(\pm)}(\omega)$.

This completes a full circle, which is referred to as the QFAM iteration. In the end of QFAM iteration, we want to obtain the same induced single-particle

Hamiltonian $\delta h(\omega)$ and pairing fields $\delta\Delta^{(\pm)}(\omega)$ from the beginning of the QFAM iteration, up to a certain numerical accuracy. In that case, we have found the self-cosistent solution which satisfies the QFAM equations and can easily calculate the response function $\frac{dB}{d\omega}(F,\omega)$ for that specific energy $\omega$ and specific external perturbation $F$. By repeating the process for many $\omega$, we obtain the response function profile point-wise. In the following sections, we will describe in detail how each step in QFAM iteration is calculated.

Notice however that unlike the conventional matrix QRPA approach where once the QRPA matrix is diagonalized, one can readily find the response function of an arbitrary external perturbation $F$, here in QFAM one has to predefine the operator $F$. The current version of the `DIRQFAM` solver supports the electric isoscalar and isovector multipole operators, defined as:

$$f^{IS}_{JK} = \sum_{i=1}^{A} f_{JK}(\boldsymbol{r}_i), \quad f^{IV}_{JK} = \sum_{i=1}^{Z} f_{JK}(\boldsymbol{r}_i) - \sum_{i=1}^{N} f_{JK}(\boldsymbol{r}_i). \tag{3.17}$$

The summations in the expression for the $f^{IV}_{JK}$ operator run over protons and neutrons, respectively. In general, the operator $f_{JK}(\boldsymbol{r})$ is given by:

$$f_{JK}(\boldsymbol{r}) = |\boldsymbol{r}|^J Y_{JK}(\theta,\varphi). \tag{3.18}$$

However, for the monopole excitations, the operator is defined as $f_{00}(\boldsymbol{r}) = |\boldsymbol{r}|^2$, while for the isovector dipole excitation ($D_K = rY_{1K}$, $K = 0, \pm 1$), the following definition is employed:

$$D_K = e\frac{NZ}{A}\left[\frac{1}{Z}\sum_{i=1}^{Z} D_K(\boldsymbol{r}_i) - \frac{1}{N}\sum_{i=1}^{N} D_K(\boldsymbol{r}_i)\right]. \tag{3.19}$$

Since for an even-even axially symmetric nucleus the operators $f_{JK}$ and $f_{J-K}$ produce identical strength functions, in the code we employ the operator:

$$f^{(+)}_{JK} = \frac{f_{JK} + (-1)^K f_{J-K}}{\sqrt{2+2\delta_{K,0}}} \tag{3.20}$$

and assume $K \geq 0$. `DIRQFAM` supports operators up to $0 \leq J \leq 5$ and $0 \leq K \leq J$.

### 3.1.3 Induced single-particle Hamiltonian and pairing field

The induced single-particle Dirac Hamiltonian is obtained by calculating the functional derivative of the Dirac Hamiltonian $h_D$ with respect to the density. For DD-PC1 single-particle Hamiltonian given in Eq. (2.33), the functional derivative reads:

$$\delta h_D = \begin{pmatrix} \delta V + \delta S & -\boldsymbol{\sigma}\cdot\delta\boldsymbol{\Sigma} \\ -\boldsymbol{\sigma}\cdot\delta\boldsymbol{\Sigma} & \delta V - \delta S \end{pmatrix}, \tag{3.21}$$

where $\delta S = \delta\Sigma_s$, $\delta V = \delta\Sigma^0 + \delta\Sigma^0_R$ and $\delta\boldsymbol{\Sigma}$ denote the induced scalar, time-like and space-like components of the induced vector potential, respectively. The detailed

expressions for $\delta\Sigma_s$, $\delta\Sigma^0$, $\delta\Sigma^0_R$ and $\delta\boldsymbol{\Sigma}$ are listed below.

$$\delta\Sigma_s = \left\{\alpha'_S(\rho^0_v)\rho^0_s\right\}\delta\rho_v + \left\{\alpha_S(\rho^0_v)\right\}\delta\rho_s + \delta_S\triangle\delta\rho_s, \tag{3.22}$$

$$\delta\Sigma^0 = \left\{\alpha'_V(\rho^0_v)\rho^0_v + \alpha_V(\rho^0_v) + \tau_3\alpha'_{TV}(\rho^0_v)\rho^0_{tv}\right\}\delta\rho_v \tag{3.23}$$

$$+ \left\{\tau_3\alpha_{TV}(\rho^0_v)\right\}\delta\rho_{tv} + \frac{1+\tau_3}{2}\delta V_C, \tag{3.24}$$

$$\delta\Sigma^0_R = \frac{1}{2}\left\{\alpha''_S(\rho^0_v)(\rho^0_s)^2 + \alpha''_V(\rho^0_v)(\rho^0_v)^2 + \alpha''_{TV}(\rho^0_v)(\rho^0_{tv})^2\right\}\delta\rho_v$$

$$+ \left\{\alpha'_S(\rho^0_v)\rho^0_s\right\}\delta\rho_s + \left\{\alpha'_V(\rho^0_v)\rho^0_v\right\}\delta\rho_v + \left\{\alpha'_{TV}(\rho^0_v)\rho^0_{tv}\right\}\delta\rho_{tv}, \tag{3.25}$$

$$\delta\boldsymbol{\Sigma} = \left\{\alpha_V(\rho^0_v)\right\}\delta\boldsymbol{j}_v + \left\{\tau_3\alpha_{TV}(\rho^0_v)\right\}\delta\boldsymbol{j}_{tv} + \frac{1+\tau_3}{2}\delta\boldsymbol{V}_C. \tag{3.26}$$

$\rho^0_s$, $\rho^0_v$ and $\rho^0_{tv}$ denote the isoscalar-scalar, isoscalar-vector and isovector-vector ground state densities. We notice that the expression for $\delta\boldsymbol{\Sigma}$ is simplified considerably due to the fact that the single-nucleon currents vanish in the time-reversal invariant ground-state.

In the case of DD-ME2 single-particle Hamiltonian $h_D$ given in Eq. (2.15), the induced potentials are listed below.

$$\delta\Sigma_s = \left[g_\sigma(\rho_v)\right]_{gs}\delta\sigma + \left[g'_\sigma(\rho_v)\sigma\right]_{gs}\delta\rho_v, \tag{3.27}$$

$$\delta\Sigma^0 = \left[g_\omega(\rho_v)\right]_{gs}\delta\omega^0 + \left[g'_\omega(\rho_v)\omega^0\right]_{gs}\delta\rho_v + \tau_3\left[g_\rho(\rho_v)\right]_{gs}\delta\rho^0$$

$$+ \tau_3\left[g'_\rho(\rho_v)\rho^0\right]_{gs}\delta\rho_v + \frac{1+\tau_3}{2}\delta V_C, \tag{3.28}$$

$$\delta\Sigma^0_R = \left(\left[g''_\sigma(\rho_v)\rho_s\sigma\right]_{gs} + + \left[g''_\omega(\rho_v)\rho_v\omega^0\right]_{gs} + \left[g''_\rho(\rho_v)\rho_{tv}\rho^0\right]_{gs}\right)\delta\rho_v$$

$$+ \left[g'_\sigma(\rho_v)\sigma\right]_{gs}\delta\rho_s + \left[g'_\omega(\rho_v)\omega^0\right]_{gs}\delta\rho_v + \left[g'_\rho(\rho_v)\rho^0\right]_{gs}\delta\rho_{tv}$$

$$+ \left[g'_\sigma(\rho_v)\rho_s\right]_{gs}\delta\sigma + \left[g'_\omega(\rho_v)\rho_v\right]_{gs}\delta\omega^0 + \left[g'_\rho(\rho_v)\rho_{tv}\right]_{gs}\delta\rho^0, \tag{3.29}$$

$$\delta\boldsymbol{\Sigma} = \left[g_\omega(\rho_v)\right]_{gs}\delta\boldsymbol{\omega} + \tau_3\left[g_\rho(\rho_v)\right]_{gs}\delta\boldsymbol{\rho} + \frac{1+\tau_3}{2}\delta\boldsymbol{V}_C. \tag{3.30}$$

The value of function given in bracket $[\cdot]_{gs}$ denotes the ground state value of that function. The induced meson fields are obtained by solving the Klein-Gordon equations:

$$\left[-\triangle + m^2_\sigma\right]\delta\sigma = -\left[g_\sigma(\rho_v)\right]_{gs}\delta\rho_s - \left[g'_\sigma(\rho_v)\rho_s\right]_{gs}\delta\rho_v, \tag{3.31}$$

$$\left[-\triangle + m^2_\omega\right]\delta\omega^0 = \left[g_\omega(\rho_v)\right]_{gs}\delta\rho_v + \left[g'_\omega(\rho_v)\rho_v\right]_{gs}\delta\rho_v, \tag{3.32}$$

$$\left[-\triangle + m^2_\rho\right]\delta\rho^0 = \left[g_\rho(\rho_v)\right]_{gs}\delta\rho_{tv} + \left[g'_\rho(\rho_v)\rho_{tv}\right]_{gs}\delta\rho_v, \tag{3.33}$$

$$\left[-\triangle + m^2_\omega\right]\delta\boldsymbol{\omega} = \left[g_\omega(\rho_v)\right]_{gs}\delta\boldsymbol{j}, \tag{3.34}$$

$$\left[-\triangle + m^2_\rho\right]\delta\boldsymbol{\rho} = \left[g_\rho(\rho_v)\right]_{gs}\delta\boldsymbol{j}_{tv}. \tag{3.35}$$

The time-like and space-like components of the induced Coulomb fields are calculated by solving the Poisson equation:

$$-\triangle\delta V_C = e^2\delta\rho_p \quad \text{and} \quad -\triangle\delta\boldsymbol{V}_C = e^2\delta\boldsymbol{j}_p, \tag{3.36}$$

where $\delta\rho_p$ and $\delta\boldsymbol{j}_p$ denote the induced proton density and current. The procedure of solving the Klein-Gordon and the Poisson equations in cylindrical coordinates is described in Appendix A.2, Appendix A.3 and Appendix A.4.

In conclusion, if the induced densities and currents are known in coordinate space, one can easily evaluate the induced potentials defining the induced single-particle Hamiltonian $\delta h(\omega)$. However, we need the matrix $\delta h(\omega)$ in HO simplex-y configurational space, rather than in coordinate space. Regarding that step, Appendix A.5 contains the technical details of obtaining $\delta h(\omega)$ in configurational space from coordinate representation.

For completeness, in Appendix A.6 we provide technical details regarding the calculation of the induced pairing field $\delta\Delta^{(\pm)}(\omega)$ once the induced pairing tensor $\delta\kappa^{(\pm)}(\omega)$ is known.

Now that we have shown how to obtain $\delta h(\omega)$ and $\delta\Delta^{(\pm)}(\omega)$ once the induced currents and densities as well as induced pairing tensor are known, in Appendix A.8 we show how to calculate the QFAM amplitudes $X_{\mu\nu}(\omega), Y_{\mu\nu}(\omega)$ and then, using the QFAM Eqs. (2.74) and (2.75) how to find the induced density matrix $\delta\rho(\omega)$ and induced pairing tensor.

### 3.1.4 Induced currents and densities

In this section we explain the method used for calculating the induced densities and currents, acting as the source terms for the induced potentials, using the induced density matrix $\delta\rho(\omega)$. In Appendix A.9 we provide a detailed list of the expressions for induced densities and currents calculated in the simplex-y harmonic oscillator (HO) basis. For example, the induced isoscalar-vector density $\delta\rho_v(\boldsymbol{r},\omega)$ in coordinate space is given as $\delta\rho_v(\boldsymbol{r},\omega) = \delta\rho_v(z, r_\perp, \omega)\cos K\varphi$, where the separated angular part is given by:

$$\delta\rho_v(z,r_\perp,\omega) = \frac{1}{2\pi}\sum_{\substack{\alpha_1,\alpha_2 \\ |\Lambda_1-\Lambda_2|=K \\ d_1=d_2}} \left(\delta\rho_1(\omega)+\delta\rho_2(\omega)\right)_{\alpha_1,\alpha_2}\phi_{n_{z_1}}(z)\phi_{n_{z_2}}(z)\phi^{|\Lambda_1|}_{n_{r_1}}(r_\perp)\phi^{|\Lambda_2|}_{n_{r_2}}(r_\perp). \tag{3.37}$$

Notice that (after symmetrization) all induced densities and currents in coordinate space can be written as:

$$\delta S(z,r_\perp,\omega) = \sum_{\alpha_1,\alpha_2} A_{\alpha_1,\alpha_2}(\omega)\phi_{n_{z_1}}(z)\phi_{n_{z_2}}(z)\phi^{|\Lambda_1|}_{n_{r_1}}(r_\perp)\phi^{|\Lambda_2|}_{n_{r_2}}(r_\perp), \tag{3.38}$$

where $A_{\alpha_1,\alpha_2}(\omega)$ is block upper triangular matrix. Detailed definition of the index $\alpha = (d, n_z, n_r, \Lambda)$ can be found in Appendix A.9. Block structure of the $A_{\alpha_1,\alpha_2}(\omega)$ matrix depends on the excitation multipolarity $K$, e.g. for $K = 0$ one obtains block diagonal matrix. For higher values of the multipolarity $K$, the block structure of the $A_{\alpha_1,\alpha_2}(\omega)$ matrix is more complicated, but one can always deduce it thus making the multiplication with matrix $A_{\alpha_1,\alpha_2}(\omega)$ much less time consuming. This block structure in simplex-y basis originates from the ground state solution in which the RHB equation can be split in independent angular momentum $\Omega = \Lambda + m_s$ and parity $\pi$ blocks since the nuclear interactions don't connect two states from different $\Omega^\pi$ blocks. One can show that this block structure can be inherited in

QFAM part of the calculation even in simplex-y basis. `DIRQFAM` solver essentially addresses only the non-trivial $\Omega^\pi$ blocks.

The source terms $\delta S(z^{i_{GH}}, r_\perp^{i_{GL}}, \omega)$ should be evaluated on the Gaussian quadrature grid points $\boldsymbol{r}^{i_G} = (z^{i_{GH}}, r_\perp^{i_{GL}})$. This is because we actually need them only to evaluate the induced potentials (as described in Section 3.1.3) which are then used to evaluate the induced single-particle Hamiltonian $\delta h(\omega)$ by means of numerical integration (as explained in Appendix A.5). Thus, it suffices to find $\delta S(z^{i_{GH}}, r_\perp^{i_{GL}}, \omega)$.

In principle, one could implement the sum in Eq. (3.38) directly by arranging the loops in some convenient order. However, it is more efficient to define the matrix:

$$\boldsymbol{\Phi}_{(\alpha,i_G)} = \phi_{n_z}(z^{i_{GH}})\phi_{n_r}^{|\Lambda|}(r_\perp^{i_{GL}}), \tag{3.39}$$

which is unchanged throughout QFAM iterations. Then the Eq. (3.38) can be written as:

$$\delta S(\boldsymbol{r}^{i_G}, \omega) = \operatorname{diag}\left[\boldsymbol{\Phi}^T A(\omega)\boldsymbol{\Phi}\right], \tag{3.40}$$

where diag$[\cdot]$ denotes the diagonal of a matrix. Since the HO basis functions $\phi_{n_z}(z)$ and $\phi_{n_r}^{|\Lambda|}(r_\perp)$ contain Hermite and Laguerre polynomials, which both satisfy recursive relations, rows of the matrix $\boldsymbol{\Phi}$ are linearly dependent. Consequently, the rank of the matrix $\boldsymbol{\Phi}$ is relatively low in comparison to its full rank.

For example, if HO simplex-y basis with $N_{\text{shells}} = 16$ is used, matrix $\boldsymbol{\Phi}$ has $1 \leq \alpha \leq 2109$ rows, while the rank of $\boldsymbol{\Phi}$ is only 171. Therefore, if $1 \leq i^G \leq 3200$ quadrature points are used, $\boldsymbol{\Phi}$ can be preprocessed via singular value decomposition and be written as a product:

$$\boldsymbol{\Phi} = \boldsymbol{U}_{\boldsymbol{\Phi}}\boldsymbol{V}_{\boldsymbol{\Phi}}, \tag{3.41}$$

where $\boldsymbol{U}_{\boldsymbol{\Phi}}$ is $2109 \times 171$ matrix, while $\boldsymbol{V}_{\boldsymbol{\Phi}}$ is $171 \times 3200$ matrix. Matrices $\boldsymbol{U}_{\boldsymbol{\Phi}}, \boldsymbol{V}_{\boldsymbol{\Phi}}$ are calculated and stored in the QFAM initialization phase, and are used during the QFAM iterations as a means to find the source terms on a Gaussian quadrature grid:

$$\delta S(\boldsymbol{r}^{i_G}, \omega) = \operatorname{diag}\left[\boldsymbol{V}_{\boldsymbol{\Phi}}^T \left(\boldsymbol{U}_{\boldsymbol{\Phi}}^T A(\omega)\boldsymbol{U}_{\boldsymbol{\Phi}}\right)\boldsymbol{V}_{\boldsymbol{\Phi}}\right]. \tag{3.42}$$

$A(\omega)\boldsymbol{U}_{\boldsymbol{\Phi}}$ is a product of a block-matrix $A(\omega)$ and *tall-and-skinny* matrix $\boldsymbol{U}_{\boldsymbol{\Phi}}$, while $\boldsymbol{U}_{\boldsymbol{\Phi}}^T A(\omega)\boldsymbol{U}_{\boldsymbol{\Phi}}$ turns out to be a relatively small matrix, in our example $171 \times 171$ matrix. Then if we select the $i_G$th column of a matrix $\boldsymbol{V}_{\boldsymbol{\Phi}}$, i.e. the vector $v_{i_G} = \boldsymbol{V}_{\boldsymbol{\Phi}}(:, i_G)$, the value $\delta S(\boldsymbol{r}^{i_G}, \omega)$ is calculated as a bilinear form with a small matrix $\boldsymbol{U}_{\boldsymbol{\Phi}}^T A(\omega)\boldsymbol{U}_{\boldsymbol{\Phi}}$ for each quadrature point as:

$$\delta S(\boldsymbol{r}^{i_G}, \omega) = v_{i_G}^T \left(\boldsymbol{U}_{\boldsymbol{\Phi}}^T A(\omega)\boldsymbol{U}_{\boldsymbol{\Phi}}\right) v_{i_G}. \tag{3.43}$$

Thus, utilizing the low-rank property of the matrix $\boldsymbol{\Phi}$, we have managed to write Eq. (3.38) in terms of basic linear algebra matrix operations. Taking advantage of a highly optimized libraries which provide basic linear algebra operations, the proposed method proved to be more efficient as compared to the straightforward loop implementation.

### 3.1.5 Generalized minimal residual method

In previous sections we have show how to perform a single QFAM iteration starting from the induced single-particle Hamiltonian $\delta h(\omega)$ and induced pairing field $\delta\Delta^{(\pm)}(\omega)$. At the end of QFAM iteration, we want to obtain the same values of $\delta h(\omega)$ and $\delta\Delta^{(\pm)}(\omega)$ as the ones we have started with, i.e. we want to obtain self-consistency of QFAM Eqs. (2.74,2.75), and in this section we explain the method used to achieve it.

#### Method description and convergence

The generalized minimal residual method (GMRES) is an iterative method for numerical solution of an indefinite non-Hermitian system of $m$ linear equations $Ax = b$ with invertible $A$, where only mapping $x \mapsto Ax$ is required. It is assumed that the dimension $m$ of matrix $A$ is huge leading to massive memory requirements. In the $n$th iteration, GMRES approximates the solution $x_n$ by a vector in a Krylov subspace with minimal residual norm. The Arnoldi iteration is used to find this vector $x_n$. More precisely, for the initial guess $x_0$ and initial residual $r_0 = b - Ax_0$, the $n$th Krylov subspace for this problem is:

$$K_n = \text{span}\left\{r_0, Ar_0, A^2r_0, \ldots, A^{n-1}r_0\right\}. \tag{3.44}$$

The Arnoldi iteration is used to find orthonormal vectors $Q_n = [q_1, q_2, \ldots, q_n]$ which form a basis for $K_n$, where the first Arnoldi vector is $q_1 = r_0/\|r_0\|$. GMRES searches the vectors $x_n \in K_n$ in the Krylov spaces and thus it can be written as $x_n = x_0 + Q_n y_n$, for $y_n \in \mathbb{C}^n$, which is found by minimizing the residual norm (Euclidean norm is assumed $\|x\| = \sqrt{x^\dagger x}$):

$$\|r_n\| = \|b - Ax_n\| = \|b - Ax_0 - AQ_n y_n\| = \|r_0 - AQ_n y_n\|. \tag{3.45}$$

The Arnoldi process also produces an $(n+1) \times n$ upper Hessenberg matrix $H_n$ such that $AQ_n = Q_{n+1}H_n$. Using that, Eq. (3.45) can be written as:

$$\|r_n\| = \|\|r_0\|q_1 - Q_{n+1}H_n y_n\| = \|Q_{n+1}(\|r_0\|e_1 - H_n y_n)\| = \|\|r_0\|e_1 - H_n y_n\|, \tag{3.46}$$

where we used that fact that the Euclidean norm is unitary invariant. Therefore, minimizing $\|r_n\|$ is a linear least squares problem with $(n+1) \times n$ matrix $H_n$ and vector $\|r_0\|e_1 \in \mathbb{C}^{n+1}$. To summarize, GMRES method performs the following steps in the $n$th iteration:

1. Using $H_{n-1}$ and $Q_{n-1}$, calculate $H_n$ and $Q_n = [Q_{n-1}, q_n]$ with the Arnoldi iteration.

2. Find $y_n$ which minimizes the residual norm $\|r_n\|$.

3. If the relative residual error $\frac{\|b-Ax_n\|}{\|b\|} = \frac{\|r_n\|}{\|b\|}$ is below the desired tolerance, calculate $x_n = x_0 + Q_n y_n$. Otherwise, continue with the described process.

Notice that we need only the mapping $x \mapsto Ax$ in order to perform Arnoldi iterations. The GMRES method relies on the assumption that after a small number of iterations (small in comparison to the to matrix dimension $m$), the vector $x_n$ is already a good approximation of the solution $x$.

Suppose that matrix $A$ can be diagonalized $A = V \operatorname{diag}[\lambda]_{\lambda\in\sigma(A)} V^{-1}$. Then one can prove the following relation [31]:

$$\frac{\|r_n\|}{\|r_0\|} \leq \kappa_2(V) \inf_{p\in\mathbb{P}_n} \max_{\lambda\in\sigma(A)} |p(\lambda)|, \tag{3.47}$$

where $\mathbb{P}_n$ is a set of polynomials of a maximal degree $n$ with $p(0) = 1$, and $\kappa_2(V)$ is the condition number of $V$. This suggests that if the matrix $A$ is close to normality ($\kappa_2(V) \sim 1$), and the spectrum $\sigma(A)$ is localized, we can expect fast convergence of the GMRES method. More details on the GMRES method and its implementation can be found in Ref. [31].

### Illustrative example

We will now show a typical case of matrix spectrum $\sigma(A)$, where one obtains fast convergence of the GMRES method. In Fig. 3.1 we plot the spectrum $\sigma(A)$ of the

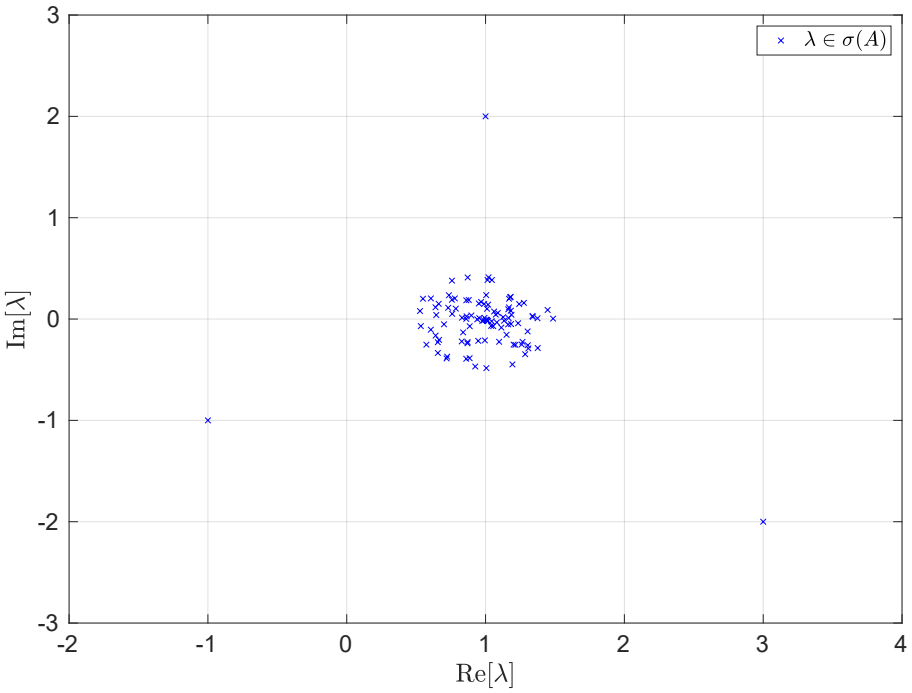


Figure 3.1: Spectrum $\sigma(A)$ of the matrix $A$ with large cluster of eigenvalues contained within a circle $|\lambda - 1| \leq \frac{1}{2}$, and few eigenvalues located far away from the cluster.

matrix $A$ with large cluster of eigenvalues contained within a circle $|\lambda - 1| \leq \frac{1}{2}$, and few eigenvalues ($\lambda_1 = 3 - 2\mathbf{i},\ \lambda_2 = 1 + 2\mathbf{i},\ \lambda_3 = -1 - \mathbf{i}$) located far away from the cluster. For $n \geq 3$, let us consider the following polynomials:

$$p_n(\lambda) = (1 - \lambda)^{n-3} \frac{(\lambda_1 - \lambda)(\lambda_2 - \lambda)(\lambda_3 - \lambda)}{\lambda_1\lambda_2\lambda_3}. \tag{3.48}$$

One can easily verify that $p_n \in \mathbb{P}_n$, i.e. $p_n(0) = 1$. Let us define a constant $C_{\lambda_1,\lambda_2,\lambda_3}$ as follows:

$$C_{\lambda_1,\lambda_2,\lambda_3} = \max_{|\lambda-1|\leq\frac{1}{2}} \left| \frac{(\lambda_1-\lambda)(\lambda_2-\lambda)(\lambda_3-\lambda)}{\lambda_1\lambda_2\lambda_3} \right|. \tag{3.49}$$

Then the following relation holds:

$$\max_{\lambda\in\sigma(A)} |p_n(\lambda)| \leq \max_{|\lambda-1|\leq\frac{1}{2}} |p_n(\lambda)| \leq C_{\lambda_1,\lambda_2,\lambda_3} \max_{|\lambda-1|\leq\frac{1}{2}} |1-\lambda|^{n-3} \leq \frac{C_{\lambda_1,\lambda_2,\lambda_3}}{2^{n-3}}. \tag{3.50}$$

If the initial guess vector $x_0$ is simply set to a null vector $x_0 = 0$, then according to Eq. (3.47), the rate of decay of the relative residual error is at least exponentially fast:

$$\frac{\|r_n\|}{\|b\|} \sim \frac{1}{2^n}. \tag{3.51}$$

In practice, one usually obtains even faster convergence rate as compared to the rate that we have just estimated theoretically. One can repeat the same argument given here for a spectrum $\sigma(A)$ which is mostly contained a circle $|\lambda - 1| \leq \frac{1}{2}$ but now for the case of a spectrum $\sigma(A)$ mostly contained within an ellipse centered at 1 which doesn't contain the origin. Again, one can show [31] that even then the convergence is exponential.

### Application of the GMRES method for solving the QFAM equations

Recall that we are solving the QFAM equations:

$$(E_\mu + E_\nu - \omega_\gamma) X_{\mu\nu}(\omega_\gamma) = -\left(F^{20}_{\mu\nu}(\omega_\gamma) + \delta H^{20}_{\mu\nu}(\omega_\gamma)\right), \tag{3.52}$$

$$(E_\mu + E_\nu + \omega_\gamma) Y_{\mu\nu}(\omega_\gamma) = -\left(F^{02}_{\mu\nu}(\omega_\gamma) + \delta H^{02}_{\mu\nu}(\omega_\gamma)\right), \tag{3.53}$$

for a given complex frequency $\omega_\gamma = \omega + i\gamma$. $F^{20}_{\mu\nu}(\omega_\gamma)$ and $F^{02}_{\mu\nu}(\omega_\gamma)$ correspond to the external field, while $H^{20}_{\mu\nu}(\omega_\gamma)$ and $H^{02}_{\mu\nu}(\omega_\gamma)$ depend on the induced single-particle Hamiltonian $\delta h_{kl}(\omega_\gamma)$ and pairing fields $\delta\Delta^{(+)}_{kl}(\omega_\gamma)$, $\left(\delta\Delta^{(-)}_{kl}(\omega_\gamma)\right)^*$ which in turn depend on the induced densities, i.e., on the QFAM amplitudes $X_{\mu\nu}(\omega_\gamma)$ and $Y_{\mu\nu}(\omega_\gamma)$. We denote the induced single-particle Hamiltonian and the pairing field by the symbol $\boldsymbol{x}(\omega_\gamma)$, i.e.,

$$\boldsymbol{x}(\omega_\gamma) = \left\{\delta h_{kl}(\omega_\gamma), \delta\Delta^{(+)}_{kl}(\omega_\gamma), \left(\delta\Delta^{(-)}_{kl}(\omega_\gamma)\right)^*\right\}. \tag{3.54}$$

Furthermore, $\boldsymbol{x}_i(\omega_\gamma)$ denotes the value calculated in the $i$th QFAM iteration. The goal is to obtain the same self-consistent value $\boldsymbol{x}_i(\omega_\gamma) = \boldsymbol{x}_{i+1}(\omega_\gamma)$ in two consecutive iterations, up to the given error tolerance.

The input for the $i$th QFAM iteration are the values induced single-particle Hamiltonian and pairing field from the previous iteration and the following trans-

formations are performed:

$$\boldsymbol{x}_i(\omega_\gamma) \xrightarrow{1.} \left\{\delta H^{20}_{\mu\nu}(\omega_\gamma), \delta H^{02}_{\mu\nu}(\omega_\gamma)\right\} \xrightarrow{2.} \left\{X_{\mu\nu}(\omega_\gamma), Y_{\mu\nu}(\omega_\gamma)\right\} \xrightarrow{3.}$$
$$\left\{\delta\rho_{kl}(\omega_\gamma), \delta\kappa^{(\pm)}_{kl}(\omega_\gamma)\right\} \xrightarrow{4.} \left\{\delta\rho(\boldsymbol{r},\omega_\gamma), \delta\boldsymbol{j}(\boldsymbol{r},\omega_\gamma), P^{(\pm)}_{N_z,N_r}(\omega_\gamma)\right\} \xrightarrow{5.} \boldsymbol{x}_{i+1}(\omega_\gamma). \quad (3.55)$$

Notice that steps 1., 3., 4. and 5. are linear transformations. For example, step 1. is a linear transformation performed by multiplying with Bogoliubov unitary matrix $\mathcal{W}$, while the numerical integration in step 5. can also be written as a linear transformation. Only step 2. is affine transformation which is actually the QFAM equation:

$$X_{\mu\nu}(\omega_\gamma) = -\left(F^{20}_{\mu\nu}(\omega_\gamma) + \delta H^{20}_{\mu\nu}(\omega_\gamma)\right)/(E_\mu + E_\nu - \omega_\gamma), \quad (3.56)$$

$$Y_{\mu\nu}(\omega_\gamma) = -\left(F^{02}_{\mu\nu}(\omega_\gamma) + \delta H^{02}_{\mu\nu}(\omega_\gamma)\right)/(E_\mu + E_\nu + \omega_\gamma). \quad (3.57)$$

If we set the residual interaction to zero, i.e., $\delta H^{20}_{\mu\nu}(\omega_\gamma) = \delta H^{02}_{\mu\nu}(\omega_\gamma) = 0$, and perform steps 2., 3., 4., and 5., we obtain the free response value $\boldsymbol{x}_{\text{free}}(\omega_\gamma)$. Hence, the QFAM iteration (3.55) can be written as:

$$\boldsymbol{x}_{i+1}(\omega_\gamma) = \mathbb{T}(\omega_\gamma)\boldsymbol{x}_i(\omega_\gamma) + \boldsymbol{x}_{\text{free}}(\omega_\gamma), \quad (3.58)$$

where $\mathbb{T}(\omega_\gamma)$ is a matrix describing the linear transformation induced by residual interaction which is ignored in free response. Size of the vector $\boldsymbol{x}(\omega_\gamma)$, and consequently the order of matrix $\mathbb{T}(\omega_\gamma)$, tends to be extremely large as the dimension of the configuration space increases. E.g. with only $N_{\text{shells}} = 10$ oscillator shells used in the expansion of the Dirac spinors, the size of the vector $\boldsymbol{x}(\omega_\gamma)$ is $\approx 10^5$, while for $N_{\text{shells}} = 20$ oscillator shells the size is $\approx 2 \times 10^6$. Despite its size, the vector $\boldsymbol{x}_{\text{free}}(\omega_\gamma)$ is easy to calculate, while the calculation of the matrix $\mathbb{T}(\omega_\gamma)$ can be prohibitively time consuming. However, the QFAM iteration (3.58) can be recognized as a means of calculating the mapping $\boldsymbol{x} \mapsto (\mathbb{I} - \mathbb{T}(\omega_\gamma))\,\boldsymbol{x}$, for finding the self-consistent solution:

$$(\mathbb{I} - \mathbb{T}(\omega_\gamma))\,\boldsymbol{x}(\omega_\gamma) = \boldsymbol{x}_{\text{free}}(\omega_\gamma). \quad (3.59)$$

It turns out that the spectrum of the residual interaction matrix $\mathbb{T}(\omega_\gamma)$ contains relatively small number of eigenvalues far from zero. This is because, for a given excitation operator, the residual interaction tends to excite only a mall subset of particle-hole pairs. Hence, the eigenvalues of the matrix $\mathbb{I} - \mathbb{T}(\omega_\gamma)$ are clustered around 1, with relatively small number of the eigenvalues scattered around the complex plane away from 1. Motivated by the illustrative example shown previously, this situation is well suited for the GMRES method. In Appendix A.10 we include details regarding the performance and convergence benchmark of GMRES on realistic examples when compared to conventionally used Broyden's method [29].

### 3.1.6 Nucleon localization function

In this section we give a detailed derivation of the nucleon localization function firstly introduced in Ref. [32]. We start with a Hermitian density matrix $\hat{\rho} = \hat{\rho}^\dagger$

and define[2]:

$$\rho^q_{\sigma,\sigma'}(\boldsymbol{x},\boldsymbol{x}') = \sum_{\alpha_1,\alpha_2} \hat{\rho}^q_{\alpha_1,\alpha_2}(\sigma,\sigma')\phi^*_{\alpha_2}(\boldsymbol{x}',\sigma')\phi_{\alpha_1}(\boldsymbol{x},\sigma), \tag{3.60}$$

together with:

$$\rho^q_\sigma(\boldsymbol{x}) = \rho^q_{\sigma,\sigma}(\boldsymbol{x},\boldsymbol{x}), \tag{3.61}$$

where $\sigma$ denotes the spin index. Notice that, because $\hat{\rho}$ is hermitian, $\rho^q_\sigma(\boldsymbol{x})$ is real. The probability of finding two nucleons with the same spin $\sigma$ and isospin $q$ at spatial locations $\boldsymbol{x}$ and $\boldsymbol{x}'$ is given by:

$$P^q_\sigma(\boldsymbol{x},\boldsymbol{x}') = \rho^q_\sigma(\boldsymbol{x})\rho^q_\sigma(\boldsymbol{x}') - \left|\rho^q_{\sigma,\sigma}(\boldsymbol{x},\boldsymbol{x}')\right|^2. \tag{3.62}$$

On the other hand, the conditional probability of finding a nucleon with spin $\sigma$ and isospin $q$ at point $\boldsymbol{x}'$ when we know that another nucleon with the same spin and isospin is located at point $\boldsymbol{x}$ is given by the following expression:

$$R^q_\sigma(\boldsymbol{x},\boldsymbol{x}') = \frac{P^q_\sigma(\boldsymbol{x},\boldsymbol{x}')}{\rho^q_\sigma(\boldsymbol{x})} = \rho^q_\sigma(\boldsymbol{x}') - \frac{\left|\rho^q_{\sigma,\sigma}(\boldsymbol{x},\boldsymbol{x}')\right|^2}{\rho^q_\sigma(\boldsymbol{x})}. \tag{3.63}$$

We fix the isospin value $q$ and for simplicity omit the corresponding index in the following discussion. Because we are interested in the localization aspects, it is sufficient to consider only the local short-range behavior of the conditional probability, which one can obtain by performing a spherical averaging of $P_\sigma(\boldsymbol{x},\boldsymbol{x}')$ over a shell of radius $\delta$ about the point $\boldsymbol{x}$:

$$\langle P_\sigma(\boldsymbol{x},\boldsymbol{x}')\rangle_{\mathrm{AVG}(\boldsymbol{x},\delta)} = \frac{1}{4\pi\delta^2}\int_{S(\boldsymbol{x},\delta)} P_\sigma(\boldsymbol{x},\boldsymbol{x}')dS_{\boldsymbol{x}'}. \tag{3.64}$$

We seek the limiting case $\delta \to 0^+$. First we consider a Taylor expansion over variable $\boldsymbol{x}'$ around $\boldsymbol{x}$:

$$\begin{aligned}\left|\rho_{\sigma,\sigma}(\boldsymbol{x},\boldsymbol{x}')\right|^2 &= \rho_\sigma(\boldsymbol{x})^2 + \sum_{i=1}^{3}\partial'_i\left|\rho_{\sigma,\sigma}(\boldsymbol{x},\boldsymbol{x}')\right|^2\Big|_{\boldsymbol{x}'=\boldsymbol{x}}(x'_i - x_i) + \\ &+ \frac{1}{2}\sum_{i,j=1}^{3}\partial'_i\partial'_j\left|\rho_{\sigma,\sigma}(\boldsymbol{x},\boldsymbol{x}')\right|^2\Big|_{\boldsymbol{x}'=\boldsymbol{x}}(x'_i - x_i)(x'_j - x_j) + \mathcal{O}(||\boldsymbol{x}' - \boldsymbol{x}||^3).\end{aligned} \tag{3.65}$$

One can trivially calculate the following spherical averages:

$$\langle(x'_i - x_i)\rangle_{\mathrm{AVG}(\boldsymbol{x},\delta)} = 0 \quad \text{and} \quad \big\langle(x'_i - x_i)(x'_j - x_j)\big\rangle_{\mathrm{AVG}(\boldsymbol{x},\delta)} = \delta_{i,j}\frac{\delta^2}{3}. \tag{3.66}$$

Using that, we obtain:

$$\Big\langle\left|\rho_{\sigma,\sigma}(\boldsymbol{x},\boldsymbol{x}')\right|^2\Big\rangle_{\mathrm{AVG}(\boldsymbol{x},\delta)} = \rho_\sigma(\boldsymbol{x})^2 + \frac{\delta^2}{6}\nabla^2_{\boldsymbol{x}'}\left|\rho_{\sigma,\sigma}(\boldsymbol{x},\boldsymbol{x}')\right|^2\Big|_{\boldsymbol{x}'=\boldsymbol{x}} + \mathcal{O}(\delta^3), \tag{3.67}$$

[2]See Appendix D, Eq. (D.8) of Ref. [21].

and similarly:

$$\langle \rho_\sigma(\boldsymbol{x}') \rangle_{\mathrm{AVG}(\boldsymbol{x},\delta)} = \rho_\sigma(\boldsymbol{x}) + \frac{\delta^2}{6} \nabla^2_{\boldsymbol{x}'} \rho_\sigma(\boldsymbol{x}') \big|_{\boldsymbol{x}'=\boldsymbol{x}} + \mathcal{O}(\delta^3). \tag{3.68}$$

Using the Hermitian property of the density matrix $\hat{\rho}$ and formula $\nabla^2(fg) = g\nabla^2 f + f\nabla^2 g + 2\nabla f \cdot \nabla g$, it is straightforward to obtain:

$$\nabla^2_{\boldsymbol{x}'} \left| \rho_{\sigma,\sigma}(\boldsymbol{x}, \boldsymbol{x}') \right|^2 \Big|_{\boldsymbol{x}'=\boldsymbol{x}} = \rho_\sigma(\boldsymbol{x}) \left( \nabla^2 \rho_\sigma(\boldsymbol{x}) - 2 \sum_{\alpha_1,\alpha_2} \hat{\rho}_{\alpha_1,\alpha_2}(\sigma,\sigma) \nabla \phi^*_{\alpha_2}(\boldsymbol{x},\sigma) \cdot \nabla \phi_{\alpha_1}(\boldsymbol{x},\sigma) \right)$$
$$+ 2 \left| \sum_{\alpha_1,\alpha_2} \hat{\rho}_{\alpha_1,\alpha_2}(\sigma,\sigma) \phi_{\alpha_1}(\boldsymbol{x},\sigma) \nabla \phi^*_{\alpha_2}(\boldsymbol{x},\sigma) \right|^2, \tag{3.69}$$

where the norm of a complex vector in the last term is $|v|^2 = |v_1|^2 + |v_2|^2 + |v_3|^2$. Inserting Eqs. (3.67), (3.68) and (3.69) into the spherical average of Eq. (3.62) and dividing by $\rho_\sigma(\boldsymbol{x})$, we obtain:

$$\langle R_\sigma(\boldsymbol{x}, \boldsymbol{x}') \rangle_{\mathrm{AVG}(\boldsymbol{x},\delta)} = D_\sigma(\boldsymbol{x}) \frac{\delta^2}{3} + \mathcal{O}(\delta^3), \tag{3.70}$$

where $D_\sigma(\boldsymbol{x})$ is defined as:

$$D_\sigma(\boldsymbol{x}) = \sum_{\alpha_1,\alpha_2} \hat{\rho}_{\alpha_1,\alpha_2}(\sigma,\sigma) \nabla \phi^*_{\alpha_2}(\boldsymbol{x},\sigma) \cdot \nabla \phi_{\alpha_1}(\boldsymbol{x},\sigma)$$
$$- \frac{1}{\rho_\sigma(\boldsymbol{x})} \left| \sum_{\alpha_1,\alpha_2} \hat{\rho}_{\alpha_1,\alpha_2}(\sigma,\sigma) \phi^*_{\alpha_2}(\boldsymbol{x},\sigma) \nabla \phi_{\alpha_1}(\boldsymbol{x},\sigma) \right|^2, \tag{3.71}$$

and $\rho_\sigma(\boldsymbol{x})$ reads:

$$\rho_\sigma(\boldsymbol{x}) = \sum_{\alpha_1,\alpha_2} \hat{\rho}_{\alpha_1,\alpha_2}(\sigma,\sigma) \phi^*_{\alpha_2}(\boldsymbol{x},\sigma) \phi_{\alpha_1}(\boldsymbol{x},\sigma). \tag{3.72}$$

Notice that $D_\sigma(\boldsymbol{x})$ is real. In particular, if we insert $\hat{\rho}_{\alpha_1,\alpha_2}(\sigma,\sigma) = \delta_{\alpha_1,\alpha_2}$ into Eq. (3.71), we obtain the same result as given in Eq. (4) of Ref. [32]. Finally, we define the nucleon localization function as:

$$\mathcal{C}_\sigma(\boldsymbol{x}) = \left[ 1 + \left( \frac{D_\sigma(\boldsymbol{x})}{\tau^\sigma_{\mathrm{TF}}(\boldsymbol{x})} \right)^2 \right]^{-1}, \tag{3.73}$$

where the Thomas-Fermi kinetic energy density:

$$\tau^\sigma_{\mathrm{TF}}(\boldsymbol{x}) = \frac{3}{5} (6\pi)^{2/3} \rho^{5/3}_\sigma(\boldsymbol{x}), \tag{3.74}$$

acts as a natural scaling. The extreme case of ideal metallic bonding is realized for homogeneous matter where $\mathcal{C}_\sigma(\boldsymbol{x}) \sim 1/2$ , a value that signals a region with a nearly homogeneous Fermi gas as is typical for metal electrons, nuclear matter,

or neutron stars. The opposite regime is space regions where exactly one single-particle wave function contributes. Such a situation yields $D_\sigma(\boldsymbol{x}) \sim 0$, as it is not possible to find another spin-like state in the vicinity, and consequently $\mathcal{C}_\sigma(\boldsymbol{x}) \sim 1$, which signals localization.

In our case, the induced density matrix is block diagonal and each block corresponds to the simplex-y quantum number $s = \pm\mathrm{i}$:

$$\hat{\rho}(t) = \begin{bmatrix} \underbrace{vv^\dagger}_{\rho_0} & 0 \\ 0 & (vv^\dagger)^T \end{bmatrix} + \eta e^{-\mathrm{i}\omega t} \begin{bmatrix} \delta\rho_1(\omega) & 0 \\ 0 & \delta\rho_2(\omega) \end{bmatrix} + \eta e^{+\mathrm{i}\omega t} \begin{bmatrix} \delta\rho_1^\dagger(\omega) & 0 \\ 0 & \delta\rho_2^\dagger(\omega) \end{bmatrix} + \mathcal{O}(\eta^2). \tag{3.75}$$

Thus, up to the linear order in $\eta$, the density matrix $\hat{\rho}^\dagger(t) = \hat{\rho}(t)$ is indeed Hermitian. Simplex-y is conserved quantum number with values $s = \pm\mathrm{i}$, and thus instead of the spin index $\sigma$ in previous equations, we use the simplex-y index $s$. Since we are not interested in states with specific values of the simplex-y quantum number, we perform averaging over the simplex-y quantum number when inserting the simplex-y blocks from Eq. (3.75):

$$\begin{aligned} \hat{\rho}(s = +\mathrm{i}, s = +\mathrm{i}) &= \rho_0 + \eta e^{-\mathrm{i}\omega t}\delta\rho_1(\omega) + \eta e^{+\mathrm{i}\omega t}\delta\rho_1^\dagger(\omega) + \mathcal{O}(\eta^2), \\ \hat{\rho}(s = -\mathrm{i}, s = -\mathrm{i}) &= \rho_0^T + \eta e^{-\mathrm{i}\omega t}\delta\rho_2(\omega) + \eta e^{+\mathrm{i}\omega t}\delta\rho_2^\dagger(\omega) + \mathcal{O}(\eta^2), \end{aligned} \tag{3.76}$$

into the Eq. (3.71). Further details regarding the implementation of $\mathcal{C}(\boldsymbol{x})$ function are given in Appendix A.11. To summarize, the nucleon localization function (after the simplex averaging) can be written as:

$$\mathcal{C}(\boldsymbol{x}, t) = \mathcal{C}^0(z, r_\perp) + 2\eta\,\mathrm{Re}\left[e^{-\mathrm{i}\omega t}\delta\mathcal{C}(z, r_\perp, \omega)\right]\cos K\varphi + \mathcal{O}(\eta^2), \tag{3.77}$$

where $\mathcal{C}^0(\boldsymbol{x}) = \mathcal{C}^0(z, r_\perp)$ is the ground state nucleon localization function.

### 3.1.7 Contour integration techniques

Although QFAM approach represents a very economical approach to the standard QRPA problem, it does not provide direct access to the QRPA eigenfrequencies $\Omega_i$. However, in Ref. [33] a method based on the contour integration in the complex plane has been proposed that allows one to extract the QRPA transition matrix elements and eigenfrequencies from the QFAM calculation. In this section we provide only a brief overview and for detailed derivation we refer the reader to Ref. [33]. The starting point is the explicit connection between the QFAM strength function (2.93) and the smeared QRPA strength function derived in [34]:

$$S(\hat{f}, \omega_\gamma) = -\sum_i \left( \frac{|\langle i|\hat{F}|0\rangle|^2}{\Omega_i - (\omega + \gamma\mathrm{i})} + \frac{|\langle 0|\hat{F}|i\rangle|^2}{\Omega_i + (\omega + \gamma\mathrm{i})} \right), \tag{3.78}$$

where $\langle i|\hat{F}|0\rangle$ and $\langle 0|\hat{F}|i\rangle$ are transition matrix elements. They are equal for Hermitian external perturbation $\hat{F}$, which is often the case. Similar connection can be established for the response (2.94) function, which can be written as a

weighted sum of Lorentzians folded with smearing parameter $\gamma$ and centered at QRPA eigenfrequencies $\Omega_i$:

$$\frac{dB(\hat{f},\omega_\gamma)}{d\omega} = -\frac{1}{\pi}\,\mathrm{Im}\,S(\hat{f},\omega_\gamma) = \frac{\gamma}{\pi}\sum_i\left(\frac{|\langle i|\hat{F}|0\rangle|^2}{(\omega-\Omega_i)^2+\gamma^2} - \frac{|\langle 0|\hat{F}|i\rangle|^2}{(\omega+\Omega_i)^2+\gamma^2}\right). \tag{3.79}$$

The discrete QRPA transition strength can be calculated by employing the Cauchy integral formula:

$$|\langle i|\hat{F}|0\rangle|^2 = \frac{1}{2\pi\mathrm{i}}\oint_{C_i} S(\hat{f},\omega_\gamma)d\omega_\gamma, \tag{3.80}$$

where $C_i$ is a closed positively-oriented simple loop in complex plane that only encloses the $i$th positive first-order QRPA pole $\Omega_i$. On the other hand, if the contour $C$ in its interior $\mathrm{Int}\,C$ has other poles, the following relation holds:

$$\sum_{\Omega_i\in\mathrm{Int}\,C}|\langle i|\hat{F}|0\rangle|^2 = \frac{1}{2\pi\mathrm{i}}\oint_{C} S(\hat{f},\omega_\gamma)d\omega_\gamma. \tag{3.81}$$

As a first step one should run the QFAM calculation for sufficiently small smearing $\gamma$, and obtain a response profile $\frac{dB(\hat{f},\omega_\gamma)}{d\omega}$ providing a fair estimate for the locations of the QRPA poles $\Omega_i$ with significant transition probabilities $|\langle i|\hat{F}|0\rangle|^2$. After that, a contour integration of the strength function (3.81) with carefully selected contour $C_i$ can be used to obtain the desired transition matrix elements. In principle, we can select any closed simple loop $C_i$, but for practical reasons we use a circle:

$$\omega_\gamma(\varphi) = \omega_0 + \omega_R e^{\mathrm{i}\varphi}, \tag{3.82}$$

centered at $\omega = \omega_0$ with radius $\omega_R$. The center and radius of the contour can easily be estimated from the response function profile in order that the contour encircles the desired pole $\Omega_i$. Integral in Eq. (3.81) is numerically evaluated using a simple Newton-Cotes second order formula (Simpson's rule) with a given number of quadrature points.

The presented method of extracting the QRPA transition matrix elements and eigenfrequencies can be validated by comparing the calculated value with the results obtained by using the QRPA code that explicitly constructs and diagonalizes the QRPA matrix. As an example, we select spherical $^{16}$O isotope because the available QRPA code [35] works for nuclei with spherically symmetric ground state. For the excitation operator we use the isoscalar octupole operator $r^3Y_{3,0}$. The calculation is performed by using the DD-ME2 energy density functional and large (small) components of the Dirac spinors are expanded in $N_{\mathrm{shells}} = 6(7)$ oscillator shells. In Fig. 3.2 we show the QFAM response function calculated by using $\gamma = 0.05$ MeV smearing parameter. Approximate positions of the QRPA eigenfrequencies $\Omega_i$ are evident and red circles denote the choices for the integration contours.

In Tab. 3.1 we show the results of the contour integration. First two columns are the QRPA eigenfrequencies and transition probabilities obtained by explicitly diagonalizing the QRPA matrix. Third column contains the results of the QFAM

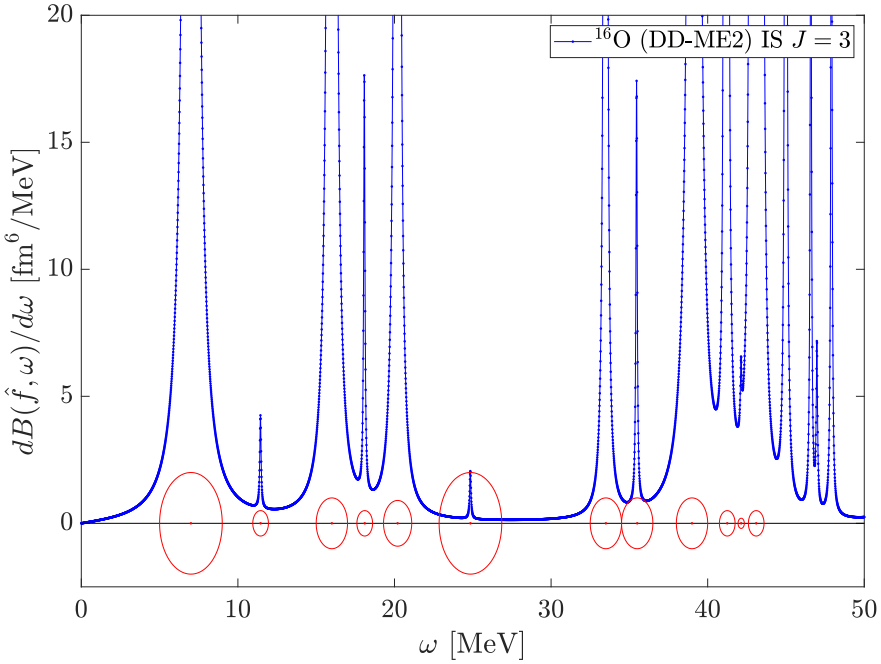


Figure 3.2: Isoscalar octupole response of $^{16}$O, using DD-ME2 parameterization and $N_{\text{shells}} = 6$ oscillator shells for spinor expansion. Smearing $\gamma = 0.05$ MeV is used. Approximate positions of dominant eigenfrequencies $\Omega_i$ are evident. Circles schematically illustrate possible countours for integration.

contour integration with 20 quadrature points while in the fourth column we list the results of contour integration with 50 quadrature points. The GMRES solver tolerance is set very low $\varepsilon = 10^{-9}$ in order to unambiguously check the convergence with respect to the number of quadrature points along the contour. We notice an excellent agreement between the direct QRPA approach and the QFAM calculation, especially since these calculations are entirely different. Furthermore, third and fourth column demonstrate that 20 quadrature points are enough for sufficient precision. Notice that QFAM transition probabilities have to be multiplied by the factor $2J + 1$, because spherical systems have the same response for all $|K| \leq J$.

For illustration of the contour $C$ containing several eigenfrequencies, we used a circle centered at 43.1 MeV with radius of 0.5 MeV. There are two eigenfrequencies contained in that circle, namely $\Omega_i = 42.82$ MeV and $\Omega_i = 43.38$ MeV with transition matrix elements $|\langle i|\hat{F}|0\rangle|^2 = 402.9829$ [fm$^6$] and $|\langle i|\hat{F}|0\rangle|^2 = 511.1528$ [fm$^6$] respectively. The QFAM contour integration method (with 50 quadrature points) gives $\frac{1}{2\pi \mathrm{i}} \oint_C S(\hat{f}, \omega_\gamma) d\omega_\gamma = 914.3587$ [fm$^6$] compared to $402.9829 + 511.1528 = 914.1357$ [fm$^6$], which is consistent with Eq. (3.81).

There are methods [33] which can be used to calculate the QRPA eigenfrequencies $\Omega_i$ via contour integration. However, in practice, once we have the transition matrix element $|\langle i|\hat{F}|0\rangle|^2$, the corresponding eigenfrequency $\Omega_i$ can be well estimated by fitting the Lorentz curve to the corresponding part of the response

Table 3.1: Comparions of transition matrix elements $|\langle i|\hat{F}|0\rangle|^2$ [fm$^6$] corresponding to Fig. 3.2 calculated by direct QRPA approach (second column) and QFAM contour integration method (third and fourth column). In third(fourth) column 20(50) quadrature points are used. First column contains the QRPA eigenfrequencies $\Omega_i$ [MeV].

| $\Omega_i$ | QRPA $\|\langle i\|\hat{F}\|0\rangle\|^2$ | QFAM $\|\langle i\|\hat{F}\|0\rangle\|^2$ | QFAM $\|\langle i\|\hat{F}\|0\rangle\|^2$ |
|---|---|---|---|
| 6.99207 | 3792.643 | 3786.191892 | 3786.190079 |
| 11.44044 | 4.025732 | 4.027805908 | 4.027805187 |
| 16.00261 | 1411.010 | 1410.827509 | 1410.823246 |
| 18.07308 | 18.13698 | 18.16427984 | 18.16384591 |
| 20.17490 | 695.1176 | 695.7697558 | 695.7685455 |
| 24.84325 | 2.073040 | 2.124316957 | 2.076412219 |
| 33.47279 | 290.0444 | 290.0960090 | 290.0886744 |
| 35.46012 | 18.41065 | 18.51968657 | 18.43513546 |
| 39.13158 | 2410.897 | 2410.598750 | 2410.565647 |
| 41.22860 | 253.4163 | 269.2637591 | 269.2620168 |
| 42.13009 | 2.739089 | 2.749169122 | 2.748494819 |

function since in the vicinity of the $\Omega_i$ pole we have:

$$\frac{dB(\hat{f},\omega_\gamma)}{d\omega} \approx |\langle i|\hat{F}|0\rangle|^2 \frac{\gamma/\pi}{(\omega-\Omega_i)^2+\gamma^2}. \tag{3.83}$$

We have validated this approach in practice. Also, one can show [33] that countour integrals of QFAM amplitudes $X_{\mu\nu}(\omega_\gamma)$ and $Y_{\mu\nu}(\omega_\gamma)$ can also yield the QRPA eigenamplitudes $X^i_{\mu\nu}$ and $Y^i_{\mu\nu}$ corresponding to QRPA eigenfrequency $\Omega_i$ as:

$$X^i_{\mu\nu} = \langle i|\hat{F}|0\rangle^{-1} \frac{1}{2\pi\mathrm{i}} \oint_{C_i} X_{\mu\nu}(\omega_\gamma) d\omega_\gamma, \tag{3.84}$$

$$Y^i_{\mu\nu} = \langle i|\hat{F}|0\rangle^{-1} \frac{1}{2\pi\mathrm{i}} \oint_{C_i} Y_{\mu\nu}(\omega_\gamma) d\omega_\gamma, \tag{3.85}$$

where we assumed that the excitation operator $\hat{F}$ is Hermitian. Thus, in conclusion, even though QFAM approach doesn't have direct access to the eigenvalues $\Omega_i$ and eigenvectors $X^i_{\mu\nu}, Y^i_{\mu\nu}$ of the QRPA matrix, one can circumvent this problem and obtain them even with QFAM approach by utilizing the described contour integration techniques.

### 3.1.8 Elimination of the translational spurious mode

In the QRPA calculations, sometimes one encounters zero-energy modes known as the Nambu-Goldstone (NG) modes. The NG modes originate from the broken symmetries on the mean-field level of the calculation: translational symmetry, rotational symmetry and particle-number (gauge) symmetry. Since the NG modes do not represent physical excitations, they are also referred to as spurious modes.

Although the zero-energy modes and the physical modes should be decoupled exactly within the random phase approximation, in practice there is always some

mixing mostly due to the finite size of the oscillator basis used in the calculation. Other numerical inaccuracies also contribute to the mixing of the spurious and physical modes, but their contribution is less pronounced in comparison to the finite size of the basis. For example, the finite size of the harmonic oscillator basis certainly violates the translational invariance thus causing admixtures of the zero-energy mode within the physical modes.

The method proposed in [36] to separate the spurious response related to the breaking of the translation symmetry from the physical response is implemented in `DIRQFAM` solver. We have verified that the method proposed in Ref. [36] removes such unphysical admixtures. For completeness, here the implementation of the method for elimination of the translational spurious mode is described.

The phonon operator is given by:

$$\hat{O}^{\dagger} = \frac{1}{2}\sum_{\mu,\nu} X_{\mu\nu}\hat{\alpha}^{\dagger}_{\mu}\hat{\alpha}^{\dagger}_{\nu} - Y_{\mu\nu}\hat{\alpha}_{\nu}\hat{\alpha}_{\mu}, \tag{3.86}$$

while the center of mass and total momentum operators in quasiparticle basis read:

$$\hat{R} = \frac{1}{2}\sum_{\mu,\nu} R^{20}_{\mu\nu}\hat{\alpha}^{\dagger}_{\mu}\hat{\alpha}^{\dagger}_{\nu} + R^{02}_{\mu\nu}\hat{\alpha}_{\nu}\hat{\alpha}_{\mu}, \tag{3.87}$$

$$\hat{P} = \frac{1}{2}\sum_{\mu,\nu} P^{20}_{\mu\nu}\hat{\alpha}^{\dagger}_{\mu}\hat{\alpha}^{\dagger}_{\nu} + P^{02}_{\mu\nu}\hat{\alpha}_{\nu}\hat{\alpha}_{\mu}. \tag{3.88}$$

Because the operators $\alpha_\mu$ and $\alpha_\nu$ anticommute, the $X$ and $Y$ matrices are antisymmetric: $X^T = -X$ and $Y^T = -Y$. Furthermore, since the operators $\hat{R}$ and $\hat{P}$ are Hermitian, the following relations hold: $R^{02} = (R^{20})^*, P^{02} = (P^{20})^*$. The self-consistent solution $\hat{O}^{\dagger}_{(\mathrm{calc})}$ contains both the physical solution $\hat{O}^{\dagger}_{(\mathrm{phys})}$ as well as the admixtures of the spurious modes:

$$\hat{O}^{\dagger}_{(\mathrm{calc})} = \hat{O}^{\dagger}_{(\mathrm{phys})} + \lambda_R\hat{R} + \lambda_P\hat{P}. \tag{3.89}$$

Since the physical modes should be orthogonal to the spurious mode, we require:

$$\langle\Phi|\left[\hat{O}^{\dagger}_{(\mathrm{phys})},\hat{R}\right]|\Phi\rangle = 0 \quad \text{and} \quad \langle\Phi|\left[\hat{O}^{\dagger}_{(\mathrm{phys})},\hat{P}\right]|\Phi\rangle = 0. \tag{3.90}$$

Previous equations allow us to calculate the $\lambda_R$ and $\lambda_P$ coefficients:

$$\lambda_R = +\frac{\langle\Phi|\left[\hat{O}^{\dagger}_{(\mathrm{calc})},\hat{P}\right]|\Phi\rangle}{\langle\Phi|\left[\hat{R},\hat{P}\right]|\Phi\rangle} \quad \text{and} \quad \lambda_P = -\frac{\langle\Phi|\left[\hat{O}^{\dagger}_{(\mathrm{calc})},\hat{R}\right]|\Phi\rangle}{\langle\Phi|\left[\hat{R},\hat{P}\right]|\Phi\rangle}. \tag{3.91}$$

Using the anticommutation relation $\left\{\alpha^{\dagger}_{\mu},\alpha_{\nu}\right\} = \delta_{\mu\nu}$, one can easily evaluate:

$$\langle\Phi|\left[\hat{O}^{\dagger}_{(\mathrm{calc})},\hat{R}\right]|\Phi\rangle = \frac{1}{2}\,\mathrm{Tr}\left[X^{(\mathrm{calc})}\left(R^{20}\right)^* + Y^{(\mathrm{calc})}R^{20}\right], \tag{3.92}$$

$$\langle\Phi|\left[\hat{O}^{\dagger}_{(\mathrm{calc})},\hat{P}\right]|\Phi\rangle = \frac{1}{2}\,\mathrm{Tr}\left[X^{(\mathrm{calc})}\left(P^{20}\right)^* + Y^{(\mathrm{calc})}P^{20}\right], \tag{3.93}$$

$$\langle\Phi|\left[\hat{R},\hat{P}\right]|\Phi\rangle = \mathrm{i}\,\mathrm{Im}\left[\mathrm{Tr}\left[(R^{20})^{\dagger}\frac{1}{2}\left(P^{20}-\left(P^{20}\right)^{T}\right)\right]\right]. \tag{3.94}$$

Notice that if we used a complete harmonic oscillator basis, the following relation would hold: $\langle\Phi|\left[\hat{R},\hat{P}\right]|\Phi\rangle = \mathrm{i}$. However, in practical calculations harmonic oscillator basis is truncated which yields a correction term in Eq. (3.94). Of course, as one increases the number of oscillator shells in the basis, the value of $\langle\Phi|\left[\hat{R},\hat{P}\right]|\Phi\rangle$ approaches $\mathrm{i}$. Once the scalars $\lambda_R$ and $\lambda_P$ are evaluated, Eq. (3.89) yields the corrected values for QFAM amplitudes:

$$X^{(\mathrm{phys})}_{\mu\nu} = X^{(\mathrm{calc})}_{\mu\nu} - \lambda_R R^{20}_{\mu\nu} - \lambda_P P^{20}_{\mu\nu}, \tag{3.95}$$

$$Y^{(\mathrm{phys})}_{\mu\nu} = Y^{(\mathrm{calc})}_{\mu\nu} + \lambda_R \left(R^{20}_{\mu\nu}\right)^{*} + \lambda_P \left(P^{20}_{\mu\nu}\right)^{*}. \tag{3.96}$$

In Appendix A.12 further technical details regarding the implementation of the translational spurious mode removal in `DIRQFAM` solver is described.

## 3.2 Structure of the **DIRQFAM** code

The programming language of the `DIRQFAM` code is Fortran and the user should provide an implementation of the BLAS [37] and LAPACK [38] (version 3.1. or higher) linear algebra libraries. The main program calls various subroutines that read the data and perform the computation. The execution essentially consists of three parts. The first part starts the program, initializes and generates all the relevant information and allocate the arrays. The second part of the code carries out the self-consistent ground-state computation [1]. The third part of the code performs the computation of the multipole response built upon the ground state. Most of the subroutines related to this part of the code are specified in details in Ref. [2]. The current version of the code is `DIRQFAM v2.0.0`, and the latest tested version is always available at GitHub repository:

**https://github.com/abjelcic/DIRQFAM**.

The program offers a simple interface via input text file `dirqfam.dat` and outputs the calculated values in output text files. In the following, we describe the input and output parameters.

### 3.2.1 Input data

The input data can be divided into two parts: i) input related to the ground state calculation, ii) input related to the QFAM calculation. The input data needed by the ground state part of the code includes:

- Number of oscillator shells used in the expansion of nucleon spinors (`n0f`). In the current implementation of the code `n0f` should be even.
- Number of Gauss-Hermite nodes (`NGH`).
- Number of Gauss-Laguerre nodes (`NGL`).

- $\beta$-deformation parameter of the harmonic oscillator basis (`beta0`). We recommend that the user chooses the value that is close to the actual deformation of the considered atomic nucleus.

- $\beta$-deformation parameter for the initial Woods-Saxon potentials (`betai`). We recommend that the user chooses the value that is close to the actual deformation of the considered atomic nucleus.

- The starting parameter for the potentials (`inin`). If the parameter `inin` is set to 1, the code starts from a default Woods-Saxon potentials predefined in the code. If the parameter `inin` is set to 0, the initial potentials are read from the file `dirhb.wel`.

- The starting parameter for the pairing field (`inink`). If `inink` is set to 1, the code starts with the diagonal pairing field with equal matrix elements `delta0`. If `inink` is set to 0, the initial pairing matrix elements are read from the file `dirhb.del`.

- The nuclide to be computed: the element name (`nucnam`) followed by the mass number (`nama`). If the element name has only one character, it should begin with an underscore, e.g. `_C 12 _O 16, _U 238`.

- Neutron and proton initial pairing gaps (`delta0`).

- Acronym of the parameter set of the selected energy density functional (`parname`). Current implementation of the code supports DD-PC1 effective interaction.

- The quadrupole constraint control parameter `icstr`. If `icstr` is set to 0, the quadrupole constraint is not included, and the parameters `betac` and `cqad` are not used. If `icstr` is set to 1, then `betac` denotes the constrained value of the quadrupole deformation.

- Constrained value of the $\beta$-deformation parameter (`betac`).

- Stiffness constant for the quadrupole constraint (`cqad`). The default value is 0.1, but if the iteration starts diverging it should be reduced.

The input parameters used to calculate multipole response include:

- Calculation type (`calculation_type`) flag. Value `0`: Free response is calculated for a given range of energies. Value `1`: Self-consistent response is calculated for a given range of energies. Value `2`: Self-consistent response is calculated for a given energy and various data are printed. Value `3`: Self-consistent solution is calculated along a circular contour and the contour integral is calculated.

- Coulomb interaction flag (`include_coulomb`). If set to `0/1`, the Coulomb interaction is omitted/included in both the ground state and the QFAM calculation.

- Pairing interaction flag (`include_pairing`). If set to `0/1`, the pairing interaction is omitted/included in both the ground state and the QFAM calculation.

- Number of Gauss-Hermite (`NGH`) nodes in the $z > 0$ direction and number of Gauss-Laguerre (`NGL`) nodes in the $r_\perp$ direction. One should use at least:

$$\texttt{NGH} \geq \max\left\{N_{\text{shells}}+1, N_{\text{shells}}^{(\text{mesons})}\right\}, \texttt{NGL} \geq \max\left\{2(N_{\text{shells}}+1), N_{\text{shells}}^{(\text{mesons})}\right\}, \tag{3.97}$$

  where $N_{\text{shells}}$ is the number of HO shells (`n0f`) used for Dirac spinor expansion and $N_{\text{shells}}^{(\text{mesons})}$ is the number of HO shells (`n0b`) used for the expansion of meson fields. We recommend fixing these values to `NGH=25` and `NGL=50`, since one rarely uses more than `n0f=24` and `n0b=50` shells.

- The smearing width $\gamma$ (in MeV) used in the QFAM calculation (`gamma_smear`).

- Solver tolerance (`selfConsistencyTolerance`). Relative residual error tolerance $\varepsilon$ for GMRES solver. We recommend using the value of `1.e-6`, which has shown to give the strength function accurate up to 5 most significant digits.

- Maximum number of Arnoldi vectors (`NoArnoldiVectors`) used by the GMRES solver. This is the limit on the number of QFAM solver steps. We recommend using the value of `70`. If the GMRES solver fails to satisfy the relative residual error tolerance, we recommend increasing this value, however keep in mind that this means larger memory consumption of the program.

- $J$ (`J_multipole`) and $K$ (`K_multipole`) multipolarity values that define the multipole excitation operator $\hat{f}_{J,K}$. In the current implementation of the code their values are restricted to $0 \leq J \leq 5$, $0 \leq K \leq J$.

- The isospin (`Isospin`) value that determines whether the excitation is isoscalar (value `0`) or isovector (value `1`).

- Parameters that control the starting point (`omega_start`), the ending point (`omega_end`) and the increment (`delta_omega`) of the energy range over which the response is calculated. Relevant only if the calculation type flag is set to `0` or `1`.

- The energy (`omega_print`) for which the self-consistent solution is calculated if the calculation type is set to `2`.

- Parameters for the contour integration if the calculation type is set to `3`. The contour is a circle centered at `omega_center` (in MeV) with radius `omega_radius` (in MeV). Number of integration points used for contour integration is determined by the `NoContourPoints` parameter.

### 3.2.2 Output data

The output is divided into two parts. Output file `dirhb.out`, located in the `output/GS_output` folder contains the information related to the ground state calculation (detailed description can be found in Ref. [1]). The output files relevant for the QFAM calculation are located in the `output/QFAM_output` folder. The calculated strength function is written to the `strength.out` file.

If the calculation type flag is set to `2`, several additional output files are generated. Files `rhov_neut.out` and `rhov_prot.out` contain the ground state neutron/proton vector density and the induced neutron/proton vector density for the selected energy value `omega_print`. The values printed in these files, $\rho_v^0(z, r_\perp)$ and $\delta\rho_v(z, r_\perp, \omega)$, are suitable for visualisation of the time dependent density:

$$\rho_v(\boldsymbol{r}, t) = \rho_v^0(z, r_\perp) + 2\eta \mathrm{Re}\left[e^{-\mathrm{i}\omega t}\delta\rho_v(z, r_\perp, \omega)\right] \cos K\varphi + \mathcal{O}(\eta^2), \tag{3.98}$$

where superscript 0 denotes the ground state density. $\eta$ denotes small real parameter quantifying deviation of the system from the ground state imposed by external perturbation (for precise definition see Eq. (2.68)). Files `jr_neut.out`, `jr_prot.out`, `jz_neut.out`, `jz_prot.out`, `jphi_neut.out` and `jphi_prot.out` contain the $r_\perp$, $z$ and $\varphi$ components of the induced neuron/proton current for the selected energy value $\omega$ (`omega_print`). The values printed in these files, $\delta j_z(z, r_\perp, \omega)$, $\delta j_\perp(z, r_\perp, \omega)$, $\delta j_\varphi(z, r_\perp, \omega)$, are suitable for visualisation of the time dependent currents:

$$j_z(\boldsymbol{r}, t) = 2\eta \mathrm{Re}\left[e^{-\mathrm{i}\omega t}\delta j_z(z, r_\perp, \omega)\right] \cos K\varphi + \mathcal{O}(\eta^2), \tag{3.99}$$

$$j_\perp(\boldsymbol{r}, t) = 2\eta \mathrm{Re}\left[e^{-\mathrm{i}\omega t}\delta j_\perp(z, r_\perp, \omega)\right] \cos K\varphi + \mathcal{O}(\eta^2), \tag{3.100}$$

$$j_\varphi(\boldsymbol{r}, t) = 2\eta \mathrm{Re}\left[e^{-\mathrm{i}\omega t}\delta j_\varphi(z, r_\perp, \omega)\right] \sin K\varphi + \mathcal{O}(\eta^2). \tag{3.101}$$

Furthermore, nucleon localization functions for neutrons and protons are printed into files `nuclocfunc_neut.out` and `nuclocfunc_prot.out`. More precisely, the printed values $\mathcal{C}^0(z, r_\perp)$ and $\delta\mathcal{C}(z, r_\perp, \omega)$, allow one to reconstruct the time-dependent localtization function as defined in Eq. (3.77). Finally, QFAM quantities in configurational space are also printed out. Files `U_neut.out`, `U_prot.out`, `V_neut.out` and `V_prot.out` contain the ground state Bogoliubov $U$ and $V$ matrices in simplex-y HO basis for neutrons and protons, while files `qpenergy_neut.out` and `qpenergy_prot.out` contain the ground state quasiparticle energies $E_\mu$ for neutrons and protons. QFAM amplitudes $X_{\mu\nu}(\omega)$ and $Y_{\mu\nu}(\omega)$ are printed in files `X_neut.out`, `X_prot.out`, `Y_neut.out` and `Y_prot.out`. The matrix elements of the induced Hamiltonian in the quasiparticle basis $\delta H^{20}_{\mu\nu}(\omega), \delta H^{02}_{\mu\nu}(\omega)$ and $\delta H^{11}_{\mu\nu}(\omega)$ are printed in files `dH20_neut.out`, `dH20_prot.out`, `dH02_neut.out` and `dH02_prot.out`, `dH11_neut.out` and `dH11_prot.out`. Detailed description of the simplex-y HO basis is provided in the file `basis.out`.

If the calculation type flag is set to `3`, the file `strength.out` contains strength function and the result of the contour integration.

Table 3.2: Memory consumption of the DIRQFAM program and the execution time per QFAM iteration for a given number of shells in HO basis.

| $N_{\text{shells}}$ | Memory [GB] | Time [s] |
|---|---|---|
| 10 | 0.42 | 0.24 |
| 12 | 0.68 | 0.49 |
| 14 | 1.11 | 0.99 |
| 16 | 1.77 | 1.82 |
| 18 | 2.83 | 3.23 |
| 20 | 4.40 | 5.52 |
| 22 | 6.65 | 8.97 |
| 24 | 11.1 | 14.1 |

### 3.2.3 Performance benchmark

We present the results of a benchmark calculation performed on Intel® Xeon® Platinum 8280 @ 2.70 GHz machine. BLAS and LAPACK are provided via Intel® oneAPI Math Kernel Library and the benchmark is performed on a single thread. We select the isoscalar $J = 2$, $K = 2$ excitation with Gaussian quadrature grid: NGH $= 25$, NGL $= 50$. The DD-PC1 parameterization of the Lagrangian is used and 70 Arnoldi vectors stored in the memory are used by the GMRES solver. In Table 3.2 we give the memory consumption of the program and the execution time per QFAM iteration for a given number of shells $N_{\text{shells}}$ in HO basis.

In order to estimate the total time needed to calculate the response function, we need an estimate of number of QFAM iterations for GMRES solver to find the self-consistent solution of QFAM equations for each energy $\omega$, and the number of energies at which the response function is sampled. If we estimate the number of QFAM iterations needed to solve the QFAM equations for single energy to be around $\approx 50$, and take around $\approx 200$ energies $\omega$, total CPU time required for a heavy nucleus with $N_{\text{shells}} = 20$ shells is around: $50 \times 200 \times 5.52$ s $= 15.3$ hours. When properly parallelized on e.g. 6 independent computing cores, we see that one can obtain the response function of heavy deformed nucleus within around 3 hours, even when personal desktop computer is used. This efficiency opens the door for a possible large-scale systematic calculations.

## 3.3 Illustrative calculations

### 3.3.1 Spherical test

We perform the fully self-consistent calculation of the $J = 2$, ($K = 0$, $K = 1$, $K = 2$) response built on top of the spherically constrained $\beta = 0$ configuration of the $^{84}$Zr isotope. Due to the Wigner-Eckart theorem, spherical nuclei should exhibit the strength function response invariant to the quantum number $K$ for the fixed value of the angular momentum $J$. In Tab. 3.3 we display the results of this calculation thus demonstrating the agreement within 7 most significant digits in the strength response function. Same result is obtained for other values of $J$. We have confirmed that for spherical nuclei and for $1 \leq J \leq 5$, all responses $0 \leq K \leq J$ are equal up to 7 most significant digits. We notice that if the

Table 3.3: Isoscalar quadrupole response in the spherical configuration of the $^{84}$Zr atomic nucleus. Calculation was performed in a space of $N_{\text{shells}} = 10$ harmonic oscillator shells with dense Gaussian mesh: NGH = 48, NGL = 48. The GMRES tolerance parameter was decreased to $\varepsilon = 10^{-8}$ in order to improve the level of agreement between various $K$ quantum numbers.

| Energy [MeV] | $S(f,\omega)$ [fm$^4$MeV$^{-1}$] | | |
|---|---|---|---|
| | $K=0$ | $K=1$ | $K=2$ |
| 5 | **31.5919**694917 | **31.5919**710786 | **31.5919**715257 |
| 10 | **24.7155**86321 | **24.7155**875415 | **24.7155**892845 |
| 15 | **107.0087**945746 | **107.0087**760979 | **107.0087**950602 |
| 20 | **39.7574**98943 | **39.7574**764571 | **39.7574**725327 |
| 25 | **8.9181**104468 | **8.9181**111725 | **8.9181**102475 |
| 30 | **3.184910**253 | **3.184910**6081 | **3.184910**2773 |
| 35 | **1.334428**3637 | **1.334428**3202 | **1.334428**2347 |
| 40 | **0.78188**53950 | **0.78188**86118 | . **0.78188**85252 |

Coulomb interaction is ignored, one can obtain even better agreement because Coulomb interaction is notoriously difficult to integrate very accurately due to the logarithmic singularity of the Coulomb potential.

### 3.3.2 Response of heavy deformed nucleus

For illustration, we select heavy deformed open-shell $^{240}$Pu nucleus with ground state deformation $\beta = 0.28$ and calculate its isovector quadrupole $J = 2$ response show in Fig. 3.3. DD-PC1 parameterization is used and the Dirac spinors are expanded in basis of $N_{\text{shells}} = 20$ oscillator shells. This large number of oscillator shells is sufficient to achieve reasonable convergence even with such large system. We notice that since the isotope has prolate ellipsoidal shapes ($\beta > 0$), isovector giant resonance peak is shifted to higher energies as $K$ increases. Also, we notice a strong peak in $K = 1$ response which can be traced back to the corresponding spurious rotational mode.

The full response was obtained within 12 hours using personal desktop computer. Such performance is order(s) of magnitude better than direct matrix approach. E.g. in Refs. [39, 40, 41], matrix approach to QRPA is implemented for axially symmetric deformed systems using the same relativistic EDF as in this work. However, such $J = 2$ calculation of $^{240}$Pu nucleus would be simply too time consuming. Thus, the DIRQFAM solver opens a door for systematic study even for heavy deformed nuclei.

### 3.3.3 Response dependence on deformation

In this illustrative calculation, we select $^{20}$Ne isotope with deformed ground state $\beta = 0.55$ and calculate its octupole $J = 3, K = 0$ response with DD-ME2 parameterization of EDF. Ground state of $^{20}$Ne is well studied [103] and its density exhibits cluster structures at the outer end of the symmetry axis with density peaks of 0.2 fm$^{-3}$ and an oblate deformed core, reminiscent of a quasimolecular $\alpha - ^{12}\text{C} - \alpha$ structure. As deformation $\beta$ increases, the $\alpha$ clusters in density become

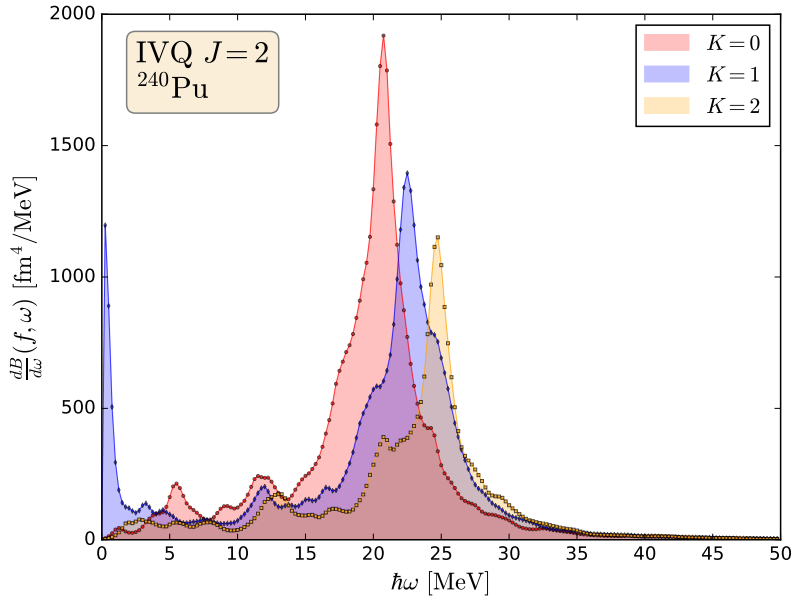


Figure 3.3: Isovector quadrupole $J = 2$ response of heavy deformed open-shell $^{240}$Pu nucleus with ground state deformation $\beta = 0.28$. In calculations, DD-PC1 EDF is used, smearing $\gamma = 0.5$ MeV and the Dirac spinors are expanded in basis of $N_{\text{shells}} = 20$ oscillator shells. Strong $K = 1$ peak at approximately zero energy correspond to spurious rotational mode.

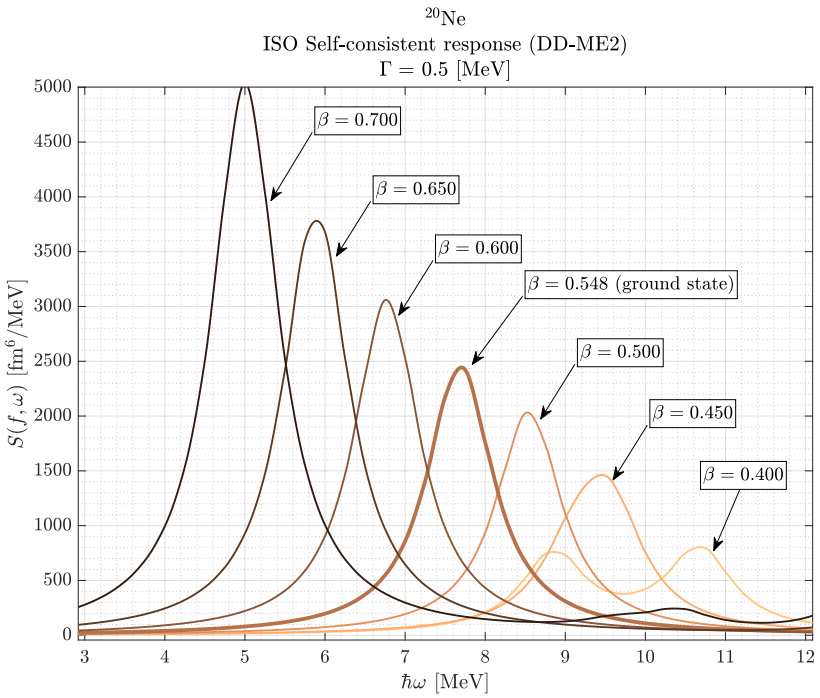


Figure 3.4: Isoscalar octupole $J = 3, K = 0$ response of $^{20}$Ne nucleus, for various constrained deformation $\beta$. Calculation is performed using $N_{\text{shells}} = 16$ oscillator shells, DD-ME2 parameterization of EDF and smearing $\gamma = 0.5$ MeV. As deformation increases, the most significant peak increases in amplitude and shifts to lower energies.

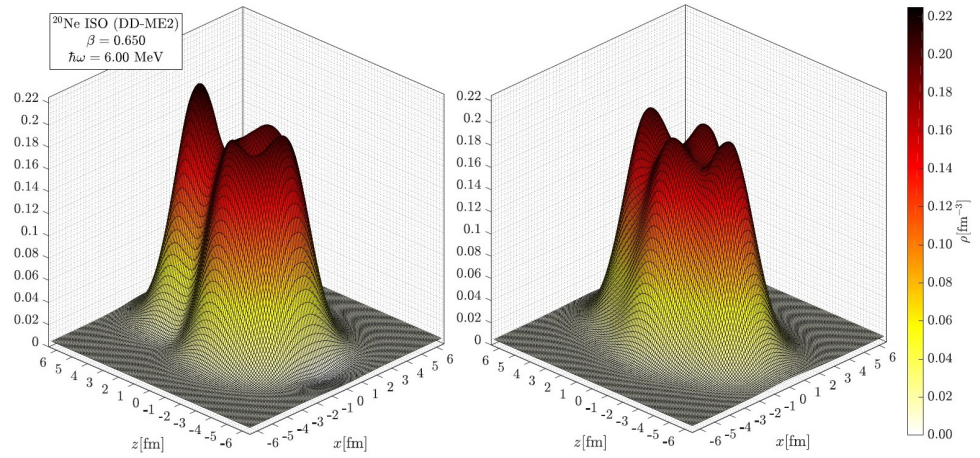


Figure 3.5: Density projection on $x-z$ plane of deformed $\beta = 0.65$ configuration of $^{20}$Ne isotope for octupole excitation of energy $\omega = 6$ MeV. Left figure shows density at quarter-period moment $T/4$, where $T = 2\pi/\omega$ is the period of oscillation, and the right figure shows the density at half-period moment $T/2$.

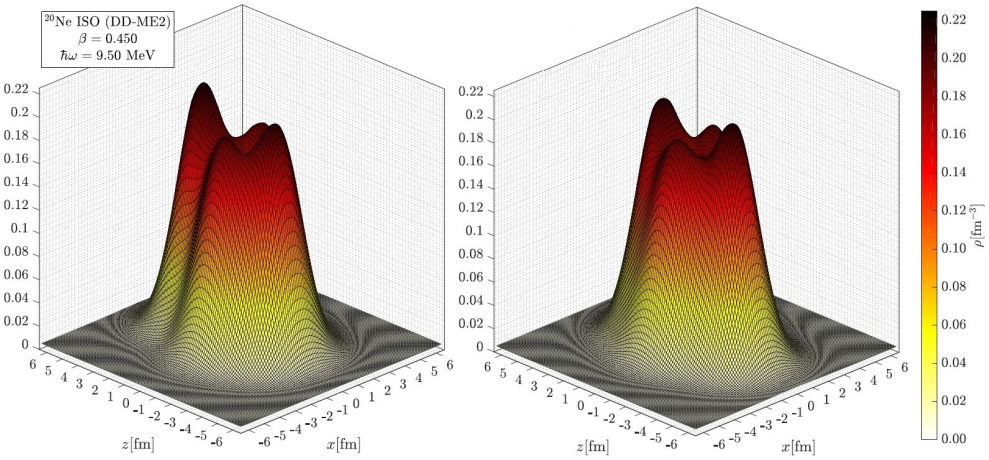


Figure 3.6: Same as Fig. 3.5 but with deformation $\beta = 0.45$ and $\omega = 9.5$ MeV.

even more distinct. In Fig. 3.4 we show octupole $J = 3, K = 0$ response of $^{20}$Ne when deformation is increased from $\beta = 0.4$ to $\beta = 0.7$. We expect, as calculations confirm in Fig. 3.4, that increased deformation yield stronger octupole response.

If we select a slightly more deformed $\beta = 0.65$ configuration compared to its ground state $\beta = 0.55$, and calculate its time-dependent density $\rho_v(\boldsymbol{r}, t)$ (see Eq. (3.98)) at peak excitation energy of $\omega = 6$ MeV, we obtain the density profile shown in Fig. 3.5. On the other hand, if we repeat the same procedure, but for a slightly less deformed $\beta = 0.45$ configuration and at peak excitation energy of $\omega = 9.5$ MeV, the obtained density profile is shown in Fig. 3.6. We conjecture that the increased deformation makes $\alpha$ particle more distinct and the oscillation resembles to $\alpha$ particle oscillating between a $^{16}$O core. Therefore, from this naive picture where we only consider the visual resemblance of density oscillation, this low-energy octupole peak is probably linked to cluster oscillation in a form of $\alpha - {}^{16}\mathrm{O}$. Similar result is obtained for monopole $J = 0$ oscillation, but now with cluster substructure resembling $\alpha - {}^{12}\mathrm{C} - \alpha$. Microscopic study of this phenomena is covered in Chapter 5.

# Chapter 4

# Kernel Polynomial Method

In this Chapter, which can be read independently of others, we present an implementation of the algorithm based on the expansion of the response function in terms of the Chebyshev polynomials in conjunction with the Kernel Polynomial Method (KPM) for very efficient calculation of the QRPA response function. Several test calculations are performed in order to asses the applicability and feasibility of this algorithm. We follow Ref. [34].

## 4.1 Quasiparticle Random Phase Approximation

The $X_{\mu\nu}(\omega)$ and $Y_{\mu\nu}(\omega)$ QRPA amplitudes are calculated by solving the linear response QRPA equation:

$$\left( \begin{bmatrix} A & B \\ B^* & A^* \end{bmatrix} - \omega \begin{bmatrix} \mathbf{I} & \mathbf{0} \\ \mathbf{0} & -\mathbf{I} \end{bmatrix} \right) \begin{bmatrix} X(\omega) \\ Y(\omega) \end{bmatrix} = - \begin{bmatrix} F^{20}(\omega) \\ F^{02}(\omega) \end{bmatrix}, \tag{4.1}$$

where $X(\omega), Y(\omega), F^{20}(\omega), F^{02}(\omega)$ are the corresponding vectorized matrices. Furthermore, the left-hand side of Eq. (4.1) leads to the QRPA eigenvalue equation when the right-hand side is set to zero:

$$\begin{bmatrix} A & B \\ B^* & A^* \end{bmatrix} \begin{bmatrix} X^i \\ Y^i \end{bmatrix} = \Omega_i \begin{bmatrix} \mathbf{I} & \mathbf{0} \\ \mathbf{0} & -\mathbf{I} \end{bmatrix} \begin{bmatrix} X^i \\ Y^i \end{bmatrix}. \tag{4.2}$$

The QRPA matrices $A$ and $B$ are calculated from second variational derivative of the energy density functional $\mathcal{E}$ with respect to the density matrix and pairing tensor. The matrix formulation of the QRPA problem becomes computationally very demanding, especially for applications to deformed atomic nuclei. The reason is the large number of quasiparticle states involved in the calculations which makes the dimension of the QRPA matrix rather large. This means that one first has to calculate large number of matrix elements and subsequently diagonalize huge QRPA matrix. Since neither of these two tasks is feasible in large-scale calculations involving deformed nuclei, a number of efficient methods to solve the QRPA problem have been formulated [42, 43]. Among them the finite-amplitude method (FAM), first proposed in Ref. [36], has proved very successful in numerous applications [44, 45, 46, 47, 48, 49, 50, 51, 52, 53]. Within the framework of the finite-amplitude method, one can avoid explicit construction and diagonalization

of the QRPA matrix and instead iteratively solve the linear response problem:

$$(E_\mu + E_\nu - \omega)\, X_{\mu\nu}(\omega) + \delta H^{20}_{\mu\nu}(\omega) = -F^{20}_{\mu\nu}(\omega), \tag{4.3}$$
$$(E_\mu + E_\nu + \omega)\, Y_{\mu\nu}(\omega) + \delta H^{02}_{\mu\nu}(\omega) = -F^{02}_{\mu\nu}(\omega). \tag{4.4}$$

$\delta H^{20}_{\mu\nu}(\omega)$ and $\delta H^{02}_{\mu\nu}(\omega)$ are the matrix elements of the induced HFB Hamiltonian in the quasiparticle basis. In principle, by expanding the $\delta H^{20}_{\mu\nu}(\omega)$ and $\delta H^{02}_{\mu\nu}(\omega)$ in terms of the amplitudes $X_{\mu\nu}(\omega)$ and $Y_{\mu\nu}(\omega)$, one could show that Eqs. (4.1) and (4.3-4.4) are equivalent. In order to avoid divergencies at the positions of the QRPA poles $\Omega_i$, the frequency in Eqs. (4.3-4.4) is set complex, i.e., $\omega \to \omega + \mathrm{i}\gamma$. Small imaginary part $\gamma$ corresponds to the smearing width. By employing the $X_{\mu\nu}(\omega)$ and $Y_{\mu\nu}(\omega)$ amplitudes, we can calculate the response function:

$$\frac{dB(\hat{F},\omega)}{d\omega} = -\frac{1}{\pi}\,\mathrm{Im}\, S(\hat{F},\omega), \tag{4.5}$$

with strength function defined as:

$$S(\omega,\hat{F}) = \sum_{\mu<\nu} \left(F^{20}_{\mu\nu}(\omega)^* X_{\mu\nu}(\omega) + F^{02}_{\mu\nu}(\omega)^* Y_{\mu\nu}(\omega)\right). \tag{4.6}$$

For a more complete description of the finite amplitude method for solving the quasiparticle random phase approximation we refer the reader to Ref. [46] and references cited therein. Furthermore, in this work we will assume that the excitation operators $F^{20}_{\mu\nu}(\omega), F^{02}_{\mu\nu}(\omega)$ do not depend on the frequency $\omega$, i.e. $F^{20}_{\mu\nu}(\omega) = F^{20}_{\mu\nu}$ and $F^{02}_{\mu\nu}(\omega) = F^{02}_{\mu\nu}$. In practical calculations this assumption is virtually always fulfilled.

### 4.1.1 Properties of the QRPA matrix

Before we formally state the problem, we would like to collect some well known technical results related to the properties of the QRPA matrices [21, 54]. If the QRPA matrix $\begin{bmatrix} A & B \\ B^* & A^* \end{bmatrix}$ is positive-definite, which corresponds to a minimum in the energy surface of the HFB solution, then there exist positive eigenfrequencies $\Omega_i > 0$ and QRPA amplitudes $X^i, Y^i \in \mathbb{C}^n$ which are the generalized eigenpair of the QRPA matrix:

$$\begin{bmatrix} A & B \\ B^* & A^* \end{bmatrix} \begin{bmatrix} X^i \\ Y^i \end{bmatrix} = \Omega_i \begin{bmatrix} X^i \\ -Y^i \end{bmatrix}, \tag{4.7}$$

with generalized normalization and closure relations:

$$\sum_{\mu=1}^{n} (X^i_\mu)^* X^j_\mu - (Y^i_\mu)^* Y^j_\mu = \delta_{i,j} \quad \text{and} \quad \sum_{i=1}^{n} X^i_\mu (X^i_\nu)^* - (Y^i_\mu)^* Y^i_\nu = \delta_{\mu,\nu}. \tag{4.8}$$

The detailed proof of the previous statement is included in the Appendix B.1 as Proposition 1. Next, we give a straightforward but useful result related to the polynomial $P \in \mathbb{C}[x]$ with complex coefficients evaluated at a matrix: $\begin{bmatrix} \mathbf{I} & \mathbf{0} \\ \mathbf{0} & -\mathbf{I} \end{bmatrix} \begin{bmatrix} A & B \\ B^* & A^* \end{bmatrix}$.

**Lemma 1.** *Let* $\begin{bmatrix} A & B \\ B^* & A^* \end{bmatrix} \in \mathbb{C}^{2n\times 2n}$ *be a positive-definite QRPA matrix and* $X, Y \in \mathbb{C}^{n\times n}$ *QRPA amplitudes matrices. Furthermore, let* $\Omega \in \mathbb{R}^{n\times n}$ *be a diagonal matrix containing the QRPA eigenfrequencies. Then for any polynomial* $P \in \mathbb{C}[x]$ *the following equation holds:*

$$P\left(\begin{bmatrix} \mathbf{I} & \mathbf{0} \\ \mathbf{0} & -\mathbf{I} \end{bmatrix}\begin{bmatrix} A & B \\ B^* & A^* \end{bmatrix}\right) = \begin{bmatrix} X & Y^* \\ Y & X^* \end{bmatrix}\begin{bmatrix} P(+\Omega) & \mathbf{0} \\ \mathbf{0} & P(-\Omega) \end{bmatrix}\begin{bmatrix} X & Y^* \\ Y & X^* \end{bmatrix}^{-1}. \tag{4.9}$$

*Proof.* Equation (B.5) shows that the matrix $\begin{bmatrix} X & Y^* \\ Y & X^* \end{bmatrix}$ is invertible. Therefore, Eq. (B.4) can be written as:

$$\begin{bmatrix} \mathbf{I} & \mathbf{0} \\ \mathbf{0} & -\mathbf{I} \end{bmatrix}\begin{bmatrix} A & B \\ B^* & A^* \end{bmatrix} = \begin{bmatrix} X & Y^* \\ Y & X^* \end{bmatrix}\begin{bmatrix} +\Omega & \mathbf{0} \\ \mathbf{0} & -\Omega \end{bmatrix}\begin{bmatrix} X & Y^* \\ Y & X^* \end{bmatrix}^{-1}, \tag{4.10}$$

which immediately yields Eq. (4.9). □

Finally, we recall two elementary facts which will be useful.

**Lemma 2.** *Let* $A \in \mathbb{C}^{n\times n}$ *be a complex symmetric matrix, i.e.* $A^T = A$. *Then for any* $x \in \mathbb{C}^n$ *there holds:*

$$\mathrm{Im}\left[x^\dagger A x\right] = x^\dagger \,\mathrm{Im}[A] x. \tag{4.11}$$

*Proof.* Writing $A = A_r + A_i\mathbf{i}$, for $A_r, A_i \in \mathbb{R}^{n\times n}$ real symmetric and $x = x_r + x_i\mathbf{i}$ for $x_r, x_i \in \mathbb{R}^n$, one trivially sees:

$$\mathrm{Im}\left[x^\dagger A x\right] = x_r^T A_i x_r + x_i^T A_i x_i + x_r^T A_r x_i - x_i^T A_r x_r, \tag{4.12}$$

$$x^\dagger \,\mathrm{Im}[A] x = x^\dagger A_i x = x_r^T A_i x_r + x_i^T A_i x_i + \left(x_r^T A_i x_i - x_i^T A_i x_r\right)\mathbf{i}. \tag{4.13}$$

Since $A_r^T = A_r$ and $A_i^T = A_i$, there holds: $x_r^T A_r x_i = x_i^T A_r x_r$ and $x_r^T A_i x_i = x_i^T A_i x_r$, which yields Eq. (4.11). □

**Lemma 3.** *Let* $f : [-1, +1] \to \mathbb{R}$ *be continuous function,* $a > 0$ *and let* $\Omega \in \langle -a, +a\rangle$. *Then there holds:*

$$\lim_{\gamma\to 0^+} \int_{-a}^{+a} f\left(\omega/a\right) \frac{\gamma/\pi}{(\omega-\Omega)^2+\gamma^2} d\omega = f\left(\Omega/a\right). \tag{4.14}$$

*Proof.* Follows from a restricted version of $\delta(x) = \lim_{\gamma\to 0^+} \frac{\gamma/\pi}{x^2+\gamma^2}$ to $[-a, +a]$ domain. □

### 4.1.2 Problem statement

Next, we give a detailed description of the problem that we would like to solve in this paper. Suppose we have $A, B \in \mathbb{C}^{N_p\times N_p}$ satisfying $A^\dagger = A$, $B^T = B$, such that the QRPA matrix:

$$\begin{bmatrix} A & B \\ B^* & A^* \end{bmatrix} \in \mathbb{C}^{2N_p\times 2N_p}, \tag{4.15}$$

is positive-definite. Furthermore, let us suppose that two vectors $F^{20}, F^{02} \in \mathbb{C}^{Np}$ are given. For $\omega \in \mathbb{R}$ and $\gamma > 0$ we denote the complex frequency $\omega_\gamma = \omega + \gamma\mathbf{i}$ in the upper complex plane. Let the vectors $X(\omega_\gamma), Y(\omega_\gamma) \in \mathbb{C}^{N_p}$ be the solution of the following linear system:

$$\left( \begin{bmatrix} A & B \\ B^* & A^* \end{bmatrix} - \omega_\gamma \begin{bmatrix} \mathbf{I} & \mathbf{0} \\ \mathbf{0} & -\mathbf{I} \end{bmatrix} \right) \begin{bmatrix} X(\omega_\gamma) \\ Y(\omega_\gamma) \end{bmatrix} = - \begin{bmatrix} F^{20} \\ F^{02} \end{bmatrix}. \tag{4.16}$$

We define the strength function $S : \mathbb{R} + \mathbb{R}^+\mathbf{i} \to \mathbb{C}$ as:

$$S(\omega_\gamma) := \begin{bmatrix} F^{20} \\ F^{02} \end{bmatrix}^\dagger \begin{bmatrix} X(\omega_\gamma) \\ Y(\omega_\gamma) \end{bmatrix}. \tag{4.17}$$

Our task is to calculate the response function $\frac{dB}{d\omega} : \mathbb{R} \to \mathbb{R}$ defined as:

$$\frac{dB(\omega)}{d\omega} := \lim_{\gamma \to 0^+} \frac{-1}{\pi} \operatorname{Im}[S(\omega_\gamma)]. \tag{4.18}$$

First, we will show that the strength is well defined, i.e. that a matrix in Eq. (4.16) is invertible for any $\omega_\gamma$. Later, it will be clear that the limit in Eq. (4.18) exists in the weak-* topology as a limit of sequence of distributions. According to the Proposition 1, there exist $X, Y \in \mathbb{C}^{N_p \times N_p}$ and $\Omega = \operatorname{diag}[\Omega_i]_{i=1}^{N_p} \in \mathbb{R}^{N_p \times N_p}$ such that $\Omega_i > 0$ for all $i = 1, \ldots, N_p$ and:

$$\begin{bmatrix} \mathbf{I} & \mathbf{0} \\ \mathbf{0} & -\mathbf{I} \end{bmatrix} \begin{bmatrix} A & B \\ B^* & A^* \end{bmatrix} = \begin{bmatrix} X & Y^* \\ Y & X^* \end{bmatrix} \begin{bmatrix} +\Omega & \mathbf{0} \\ \mathbf{0} & -\Omega \end{bmatrix} \begin{bmatrix} X & Y^* \\ Y & X^* \end{bmatrix}^{-1}, \tag{4.19}$$

$$\begin{bmatrix} X & Y^* \\ Y & X^* \end{bmatrix}^{-1} = \begin{bmatrix} \mathbf{I} & \mathbf{0} \\ \mathbf{0} & -\mathbf{I} \end{bmatrix} \begin{bmatrix} X & Y^* \\ Y & X^* \end{bmatrix}^\dagger \begin{bmatrix} \mathbf{I} & \mathbf{0} \\ \mathbf{0} & -\mathbf{I} \end{bmatrix}. \tag{4.20}$$

Thus, one can easily see that for any $\omega_\gamma$ in the upper complex plane, the matrix:

$$\begin{aligned} \begin{bmatrix} A & B \\ B^* & A^* \end{bmatrix} - \omega_\gamma \begin{bmatrix} \mathbf{I} & \mathbf{0} \\ \mathbf{0} & -\mathbf{I} \end{bmatrix} = \begin{bmatrix} \mathbf{I} & \mathbf{0} \\ \mathbf{0} & -\mathbf{I} \end{bmatrix} \begin{bmatrix} X & Y^* \\ Y & X^* \end{bmatrix} \times \\ \times \begin{bmatrix} +\Omega - \omega_\gamma \mathbf{I} & \mathbf{0} \\ \mathbf{0} & -\Omega - \omega_\gamma \mathbf{I} \end{bmatrix} \begin{bmatrix} X & Y^* \\ Y & X^* \end{bmatrix}^{-1} \end{aligned} \tag{4.21}$$

is invertible, rendering $S(\omega_\gamma)$ well defined with formula:

$$\begin{aligned} S(\omega_\gamma) = - \left( \begin{bmatrix} X & Y^* \\ Y & X^* \end{bmatrix}^\dagger \begin{bmatrix} F^{20} \\ F^{02} \end{bmatrix} \right)^\dagger \begin{bmatrix} (\Omega - \omega_\gamma \mathbf{I})^{-1} & \mathbf{0} \\ \mathbf{0} & (\Omega + \omega_\gamma \mathbf{I})^{-1} \end{bmatrix} \times \\ \times \left( \begin{bmatrix} X & Y^* \\ Y & X^* \end{bmatrix}^\dagger \begin{bmatrix} F^{20} \\ F^{02} \end{bmatrix} \right). \end{aligned} \tag{4.22}$$

According to Lemma 2, one immediately obtains:

$$-\frac{1}{\pi}\,\mathrm{Im}[S(\omega_\gamma)] = \left(\begin{bmatrix} X & Y^* \\ Y & X^* \end{bmatrix}^\dagger \begin{bmatrix} F^{20} \\ F^{02} \end{bmatrix}\right)^\dagger \begin{bmatrix} \frac{\gamma/\pi}{(\omega-\Omega)^2+\gamma^2} & \mathbf{0} \\ \mathbf{0} & \frac{-\gamma/\pi}{(\omega+\Omega)^2+\gamma^2} \end{bmatrix} \times \\ \times \left(\begin{bmatrix} X & Y^* \\ Y & X^* \end{bmatrix}^\dagger \begin{bmatrix} F^{20} \\ F^{02} \end{bmatrix}\right), \tag{4.23}$$

where it is now clear that the limit of distributions in Eq. (4.18) exists, i.e. the response function $\frac{dB(\omega)}{d\omega}$ is well defined distribution on $\mathbb{R}$.

In direct implementations, the QRPA matrix is constructed explicitly and subsequently diagonalized by solving Eq. (4.19). The resulting matrices $X$, $Y$ and $\Omega$ are used to calculate the strength according to Eq. (4.22) for arbitrary smearing parameter $\gamma > 0$. The main advantage of this approach is that one can use the calculated matrices $X$, $Y$ and $\Omega$ to find the response for arbitrary excitation operator $\hat{F}$. This is analogous to solving the linear system of equations $\mathbf{A}x = b$, in the case when we know the spectral decomposition: $\mathbf{A} = \mathbf{S}\mathbf{\Lambda}\mathbf{S}^{-1}$. Then for any right-hand side vector $b$, one can easily find the solution: $x = \mathbf{S}\mathbf{\Lambda}^{-1}\mathbf{S}^{-1}b$. However, because this approach is computationally prohibitive for deformed atomic nuclei due to the large dimension of the QRPA matrix (4.15), in practice one often solves the system of linear equations (4.16) for preselected excitation operator $\hat{F}$ and smearing parameter $\gamma > 0$. In this case, one only obtains the shape profile $(\omega, S(\omega_\gamma))$ of the strength function $S(\omega_\gamma)$, but for most applications this is quite satisfactory.

A very successful approach for solving the linear response problem is the finite amplitude method, described at the beginning of this section. When solving the linear system Eq. (4.16) for fixed frequency $\omega_\gamma$, one usually uses an iterative solver which does not require the access to the full QRPA matrix, but rather only requires the access to the linear mapping:

$$\begin{bmatrix} x \\ y \end{bmatrix} \mapsto \begin{bmatrix} A & B \\ B^* & A^* \end{bmatrix} \begin{bmatrix} x \\ y \end{bmatrix}, \quad \text{for given} \quad x, y \in \mathbb{C}^{N_p}. \tag{4.24}$$

This mapping, equivalent to the FAM equations (4.3-4.4), can actually be constructed without explicit calculation of the residual nuclear interaction (i.e. without explicit construction of $A$ and $B$ matrices), which makes the FAM method convenient in practical implementations. Since the main goal of this paper is to improve the performance of the existing FAM solvers, we will only assume the access to the mapping (4.24). We will show that one can obtain an accurate approximation to the response function $\frac{dB(\omega)}{d\omega}$ in fewer number of FAM iterations. The proposed method is easy to implement in the existing FAM solvers with minimum additional effort.

## 4.2 Implementation of the kernel polynomial method for calculating the QRPA response function

### 4.2.1 Chebyshev expansion

First, we assume that all QRPA eigenfrequencies $(\pm\Omega_i)_{i=1}^{N_p}$ are contained in the finite interval $\langle -\Omega_b, +\Omega_b\rangle$. The parameter $\Omega_b > 0$ is referred to as the bounding frequency. Next, we fix the smearing parameter $\gamma > 0$, and since the set of Chebyshev polynomials:

$$T_n(x) = \cos(n \arccos(x)),\ x \in [-1, +1],\ n \in \mathbb{N}_0, \tag{4.25}$$

form an orthonormal basis, we expand the function $\frac{-1}{\pi}\,\mathrm{Im}[S(\omega_\gamma)]$ for $\omega \in \langle -\Omega_b, +\Omega_b\rangle$ as the following Chebyshev series:

$$\frac{-1}{\pi}\,\mathrm{Im}[S(\omega_\gamma)] = \frac{2/\pi}{\sqrt{\Omega_b^2 - \omega^2}} \sum_{n=0}^{+\infty} \mu_n^{(\gamma)} T_n\left(\frac{\omega}{\Omega_b}\right), \tag{4.26}$$

where $\mu_n^{(\gamma)} \in \mathbb{R}$ are the expansion coefficients. Using the orthogonality of the Chebyshev polynomials:

$$\int_{-1}^{+1} \frac{T_n(x) T_m(x)}{\sqrt{1-x^2}} dx = \frac{\pi}{2}(1 + \delta_{n,0})\delta_{m,n}, \quad m, n \in \mathbb{N}_0, \tag{4.27}$$

one easily obtains the formula for the expansion coefficients:

$$\mu_n^{(\gamma)} = \frac{1}{1 + \delta_{n,0}} \int_{-\Omega_b}^{+\Omega_b} \frac{-1}{\pi}\,\mathrm{Im}[S(\omega_\gamma)] T_n\left(\frac{\omega}{\Omega_b}\right) d\omega. \tag{4.28}$$

From Eq. (4.23) and using (4.20) we easily see:

$$-\frac{1}{\pi}\,\mathrm{Im}[S(\omega_\gamma)] = \begin{bmatrix} F^{20} \\ F^{02} \end{bmatrix}^\dagger \begin{bmatrix} X & Y^* \\ Y & X^* \end{bmatrix} \begin{bmatrix} \frac{\gamma/\pi}{(\omega-\Omega)^2+\gamma^2} & \mathbf{0} \\ \mathbf{0} & \frac{\gamma/\pi}{(\omega+\Omega)^2+\gamma^2} \end{bmatrix} \times \\ \times \begin{bmatrix} X & Y^* \\ Y & X^* \end{bmatrix}^{-1} \begin{bmatrix} F^{20} \\ -F^{02} \end{bmatrix}, \tag{4.29}$$

and thus, according to Lemma 3, the following equation holds:

$$\lim_{\gamma\to 0^+} \mu_n^{(\gamma)} = \frac{1}{1 + \delta_{n,0}} \begin{bmatrix} F^{20} \\ F^{02} \end{bmatrix}^\dagger \begin{bmatrix} X & Y^* \\ Y & X^* \end{bmatrix} \begin{bmatrix} T_n\left(+\frac{\Omega}{\Omega_b}\right) & \mathbf{0} \\ \mathbf{0} & T_n\left(-\frac{\Omega}{\Omega_b}\right) \end{bmatrix} \times \\ \times \begin{bmatrix} X & Y^* \\ Y & X^* \end{bmatrix}^{-1} \begin{bmatrix} F^{20} \\ -F^{02} \end{bmatrix}, \tag{4.30}$$

which after using Lemma 1 transforms to:

$$\begin{aligned}\mu_n &:= \lim_{\gamma\to 0^+} \mu_n^{(\gamma)} \\ &= \frac{1}{1+\delta_{n,0}} \begin{bmatrix} F^{20} \\ F^{02} \end{bmatrix}^\dagger T_n\left(\frac{1}{\Omega_b}\begin{bmatrix} \mathbf{I} & \mathbf{0} \\ \mathbf{0} & -\mathbf{I} \end{bmatrix}\begin{bmatrix} A & B \\ B^* & A^* \end{bmatrix}\right)\begin{bmatrix} \mathbf{I} & \mathbf{0} \\ \mathbf{0} & -\mathbf{I} \end{bmatrix}\begin{bmatrix} F^{20} \\ F^{02} \end{bmatrix}. \end{aligned} \tag{4.31}$$

If we truncate the series (4.26) up to $2N_{\mathrm{it}}+1 \in \mathbb{N}$ coefficients, after taking the limit $\gamma \to 0^+$, one obtains the approximate expression for the response function:

$$\frac{dB(\omega)}{d\omega} \approx \frac{2/\pi}{\sqrt{\Omega_b^2-\omega^2}} \sum_{n=0}^{2N_{\mathrm{it}}} \mu_n T_n\left(\frac{\omega}{\Omega_b}\right), \text{ for } \omega \in \langle -\Omega_b, +\Omega_b\rangle, \tag{4.32}$$

where the coefficients $\mu_n \in \mathbb{R}$ are defined in Eq. (4.31). Notice that $\mu_n \in \mathbb{R}$ are indeed real because one can easily see that matrices:

$$T_n\left(\frac{1}{\Omega_b}\begin{bmatrix} \mathbf{I} & \mathbf{0} \\ \mathbf{0} & -\mathbf{I} \end{bmatrix}\begin{bmatrix} A & B \\ B^* & A^* \end{bmatrix}\right)\begin{bmatrix} \mathbf{I} & \mathbf{0} \\ \mathbf{0} & -\mathbf{I} \end{bmatrix} \in \mathbb{C}^{2N_p\times 2N_p}, \tag{4.33}$$

are Hermitian. Let us define a sequence of vectors $(|\alpha_n\rangle)_{n\in\mathbb{N}_0} \subseteq \mathbb{C}^{2N_p}$ as:

$$|\alpha_n\rangle := T_n\left(\frac{1}{\Omega_b}\begin{bmatrix} \mathbf{I} & \mathbf{0} \\ \mathbf{0} & -\mathbf{I} \end{bmatrix}\begin{bmatrix} A & B \\ B^* & A^* \end{bmatrix}\right)\begin{bmatrix} \mathbf{I} & \mathbf{0} \\ \mathbf{0} & -\mathbf{I} \end{bmatrix}\begin{bmatrix} F^{20} \\ F^{02} \end{bmatrix}. \tag{4.34}$$

Using $T_0(x) = 1$ and $T_1(x) = x$, the first two terms $|\alpha_0\rangle, |\alpha_1\rangle \in \mathbb{C}^{2N_p}$ are equal to:

$$|\alpha_0\rangle := \begin{bmatrix} F^{20} \\ -F^{02} \end{bmatrix} \quad \text{and} \quad |\alpha_1\rangle := \frac{1}{\Omega_b}\begin{bmatrix} \mathbf{I} & \mathbf{0} \\ \mathbf{0} & -\mathbf{I} \end{bmatrix}\begin{bmatrix} A & B \\ B^* & A^* \end{bmatrix}\begin{bmatrix} F^{20} \\ -F^{02} \end{bmatrix}, \tag{4.35}$$

while the Chebyshev recursion: $T_n(x) = 2xT_{n-1}(x) - T_{n-2}(x)$, for $n \geq 2$, can be used to find other terms $|\alpha_n\rangle$ for $n \geq 2$, recursively:

$$|\alpha_n\rangle = \frac{2}{\Omega_b}\begin{bmatrix} \mathbf{I} & \mathbf{0} \\ \mathbf{0} & -\mathbf{I} \end{bmatrix}\begin{bmatrix} A & B \\ B^* & A^* \end{bmatrix}|\alpha_{n-1}\rangle - |\alpha_{n-2}\rangle. \tag{4.36}$$

Since there holds:

$$\mu_n = \frac{1}{1+\delta_{n,0}}\begin{bmatrix} F^{20} \\ F^{02} \end{bmatrix}^\dagger |\alpha_n\rangle, \quad \text{for} \quad n \in \mathbb{N}_0, \tag{4.37}$$

we can initialize the coefficients $\mu_0, \mu_1$ and use recursion (4.36) to find the higher coefficients $\mu_n$, $n \geq 2$, i.e. as we calculate the $n$th vector $|\alpha_n\rangle$, we can calculate the $n$th coefficient $\mu_n$. However, we can do better utilizing two identities:

$$T_{2n}(x) = 2T_n(x)T_n(x) - 1 \quad \text{and} \quad T_{2n-1}(x) = 2T_{n-1}(x)T_n(x) - x. \tag{4.38}$$

Then, one can easily show using Hermitian property of matrices (4.33) that there holds:

$$\mu_{2n-1} = 2\langle\alpha_{n-1}|\begin{bmatrix} \mathbf{I} & \mathbf{0} \\ \mathbf{0} & -\mathbf{I} \end{bmatrix}|\alpha_n\rangle - \mu_1, \quad n \in \mathbb{N}, \tag{4.39}$$

$$\mu_{2n} = 2\langle\alpha_n| \begin{bmatrix} \mathbf{I} & \mathbf{0} \\ \mathbf{0} & -\mathbf{I} \end{bmatrix} |\alpha_n\rangle - 2\mu_0, \quad n \in \mathbb{N}. \tag{4.40}$$

Thus, if we initialize $|\alpha_0\rangle, |\alpha_1\rangle \in \mathbb{C}^{2N_p}$ and $\mu_0, \mu_1 \in \mathbb{R}$, during the recursion (4.36) for each new $|\alpha_n\rangle$ we can obtain two coefficients $\mu_{2n-1}$ and $\mu_{2n}$. Notice that for calculation of $|\alpha_0\rangle, |\alpha_1\rangle, \ldots, |\alpha_{N_{\text{it}}}\rangle$, we need to evaluate the mapping:

$$\begin{bmatrix} x \\ y \end{bmatrix} \mapsto \begin{bmatrix} A & B \\ B^* & A^* \end{bmatrix} \begin{bmatrix} x \\ y \end{bmatrix}, \tag{4.41}$$

exactly $N_{\text{it}}$ times, which will yield the coefficients $\mu_0, \mu_1, \ldots, \mu_{2N_{\text{it}}}$ required in the expansion (4.32).

### 4.2.2 Kernel polynomial method

It is well known and can be seen from Eq. (4.29) that the response function $\frac{dB(\omega)}{d\omega}$ can be written as a sum of weighted delta functions centered at eigenfrequencies $\pm\Omega_i$. Experience shows that a simple truncation of Chebyshev series (4.32) leads to poor precision and oscillatory behaviour, also known as Gibbs oscillations, near points where the expanded function is singular or discontinuous which in this case is near QRPA poles $\pm\Omega_i$. This problem has been studied in details [55] and a common procedure to damp Gibbs oscillations relies on the modification of the coefficients in the Chebyshev expansion:

$$f(x) \approx \frac{2/\pi}{\sqrt{1-x^2}} \sum_{n=0}^{N-1} \mu_n T_n(x), \quad x \in \langle -1, +1 \rangle, \tag{4.42}$$

with a simple transformation of expansion coefficients: $\mu_n \to \mu_n g_n^{(N)}$, for an appropriate coefficients: $g_0^{(N)}, g_1^{(N)}, \ldots, g_{N-1}^{(N)}$, called the kernel coefficients. One can represent this transformation as a convolution of $f(x)$ with an appropriate kernel $K_N(x, y)$. Details can be found in Ref. [55] and here we only introduce three kernels which are most relevant for our work.

First we would like to present the Jackson kernel, designed to minimize the kernels root mean square (RMS) width. The Jackson kernel is defined as:

$$g_n^{(N)}(\text{Jackson}) := \frac{(N-n+1)\cos\left(\frac{\pi n}{N+1}\right) + \sin\left(\frac{\pi n}{N+1}\right)\cot\left(\frac{\pi}{N+1}\right)}{N+1}. \tag{4.43}$$

One can show that if one expands the delta function $\delta(x)$ in Chebyshev series (4.42), i.e. calculates the coefficients $\mu_n$ corresponding to $f(x) = \delta(x)$, followed by modifying the coefficients $\mu_n$ with Jackson kernel: $\mu_n \to \mu_n g_n^{(N)}(\text{Jackson})$, then the obtained kernel-modified Chebyshev approximation (RHS of Eq. (4.42)) visually resembles to a Gaussian $\frac{1}{\sqrt{2\pi}\sigma} e^{-\frac{x^2}{2\sigma^2}}$ of width $\sigma = \frac{\pi}{N}$. In Figure 4.1, we plot a Gaussan of width $\sigma = \frac{\pi}{N}$, for $N = 64$, together with Jackson kernel-modified Chebyshev approximation of delta function of order $N = 64$. We also plot the kernel-unmodified Chebyshev approximation of delta function as a reference. We can see that KPM reduces the Gibbs oscillations, and the Jackson kernel-modified approximation resembles to a Gaussian of an appropriate width.

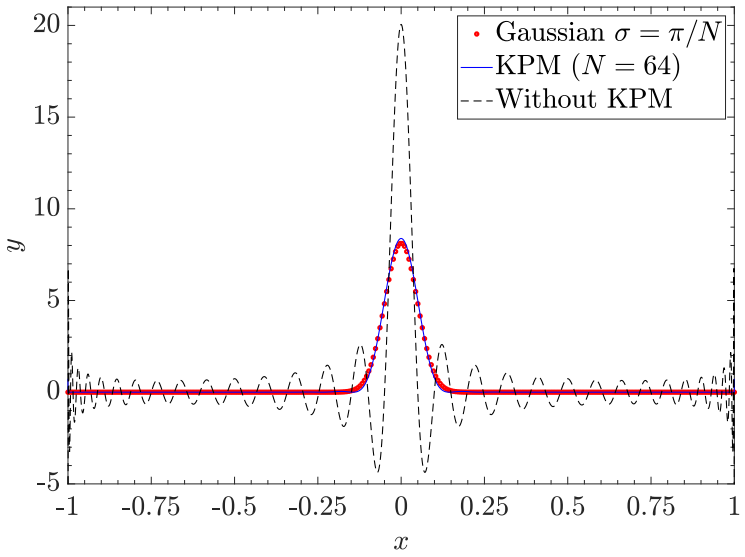


Figure 4.1: Gaussian function of width $\sigma = \pi/N$, for $N = 64$ (red circles) compared to Jackson kernel-modified Chebyshev approximation of delta function of order $N = 64$ (blue solid curve). For reference, kernel-unmodified Chebyshev approximation of delta function of order $N = 64$ is also shown (black dashed curve). Figure taken from Ref. [34].

Second kernel that we present is the Lorentz kernel defined as:

$$g_n^{(N)}(\text{Lorentz}) := \frac{\sinh\left(\lambda(1 - n/N)\right)}{\sinh\left(\lambda\right)}, \tag{4.44}$$

where the value of the free parameter $\lambda > 0$ should be chosen to ensure a satisfactory compromise between good resolution (small values of the parameter $\lambda$) and sufficient damping (large values of the parameter $\lambda$). Depending on the application, the value of the $\lambda$ parameter is usually chosen between values 1 and 5. In this case, if one expands the delta function as in Eq. (4.42), i.e. calculates the coefficients $\mu_n$ corresponding to $f(x) = \delta(x)$, followed by modifying the coefficients $\mu_n$ with Lorentz kernel: $\mu_n \to \mu_n g_n^{(N)}(\text{Lorentz})$, then the obtained kernel-modified Chebyshev approximation visually resembles to a Lorentzian $\frac{\gamma/\pi}{x^2+\gamma^2}$ with smearing parameter $\gamma = \frac{\lambda}{N}$. For example, if one selects $\lambda = 5$, the two functions: the Lorentzian having width $\gamma = \frac{\lambda}{N}$ and a Chebyshev expanded delta function with kernel-modified expansion coefficients, are virtually identical. In Figure 4.2 we fix $N = 64$, and show Lorentzians of width $\gamma = \frac{\lambda}{N}$ together with Lorentz kernel-modified Chebyshev approximations of delta function of order $N$, as parameter $\lambda$ is swept through the values $\lambda = 1, 2, 3, 4, 5$. We notice that larger value of $\lambda$ gives better damping of the Gibbs oscillations and gives better resemblance to an approriate Lorentzian, however, for a fixed Chebyshev approximation order $N$, smaller values of $\lambda$ yield higher peaks and better resolution in terms of width. Thus, the value $\lambda = 1.5$ seems like a good compromise between the two. In Figure 4.3, we fix $\lambda = 1.5$ parameter, and show Lorentzians of width $\gamma = \frac{\lambda}{N}$ together with Lorentz kernel-modified Chebyshev approximations of delta function of order $N$,

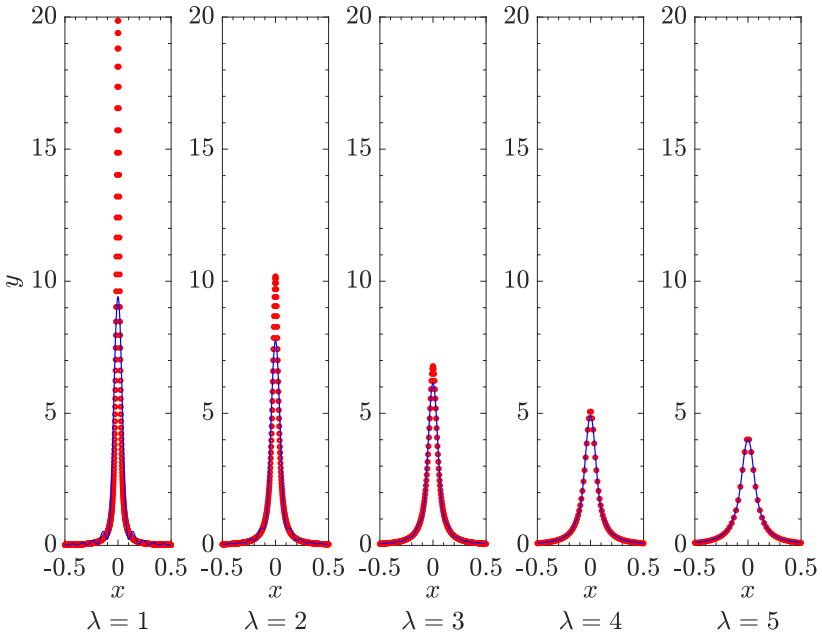


Figure 4.2: Lorentzians of width $\gamma = \frac{\lambda}{N}$ (red circles) together with Lorentz kernel-modified Chebyshev approximations od delta function of order $N$ (blue solid curves), for a fixed value of $N = 64$ when the parameter $\lambda$ is swept from values $\lambda = 1$ to $\lambda = 5$. Figure taken from Ref. [34].

as the order parameter $N$ is swept through the values $N = 16, 32, 64, 128, 256$. Thus, for values of $\lambda$ parameter below $\lambda < 4$ the resemblance with Lorentzian is less pronounced, however the relation $\gamma = \frac{\lambda}{N}$ still approximatelly holds, but has to be taken only indicatively. Important remark to notice is that once the Chebyshev expansion coefficients $\mu_n$ are obtained (as explained in the previous subsection) one can easily choose and experiment with various kernel coefficients since they are selected *a posteriori*.

Notice that trivial transformation: $\mu_n \to 1 \cdot \mu_n$, can also be viewed as an action of constant kernel:

$$g_n^{(N)}(\text{Dirichlet}) := 1, \tag{4.45}$$

which is usually called the Dirichlet kernel.

In conclusion, the main goal is to damp Gibbs oscillations encountered when expanding a delta function in Chebyshev series (4.42), by simply multiplying the expansion coefficients $\mu_n$ with the kernel coefficient $g_n^{(N)}$, where the choice of the coefficients $g_n^{(N)}$ depends on the particular application. For example, if we want a rapidly decreasing expansion, a good choice is to use the Jackson kernel. On the other hand, if the expanded function displays the Breit-Wigner shape, such as the response function $\frac{dB(\omega)}{d\omega}$, one should use the Lorentz kernel.

### 4.2.3 Evaluation of Chebyshev series

Suppose we have calculated the coefficients $\mu_0, \mu_1, \ldots, \mu_{2N_{\text{it}}}$ in Eq. (4.32) and multiplied them with an appropriate kernel coefficients $g_n^{(2N_{\text{it}}+1)}$. We wish to evaluate

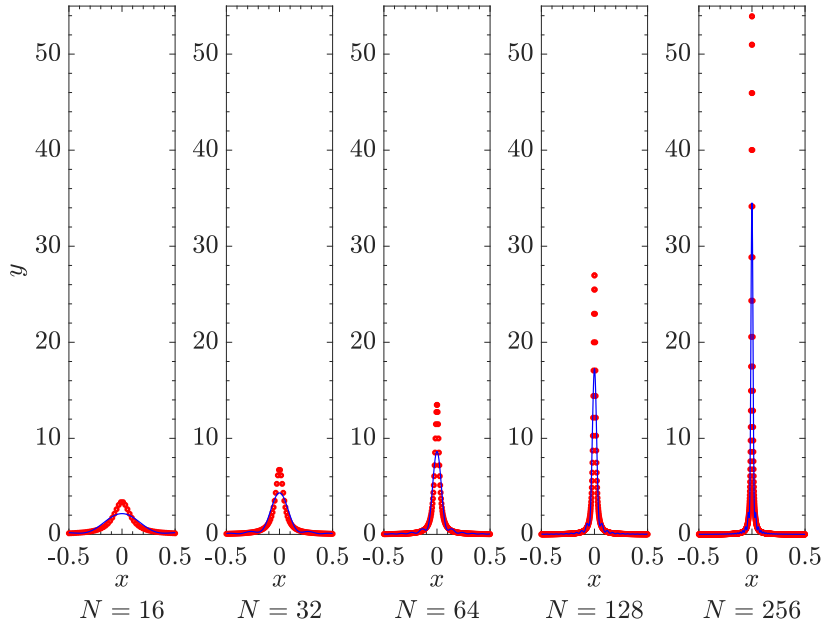


Figure 4.3: Lorentzians of width $\gamma = \frac{\lambda}{N}$ (red circles) together with Lorentz kernel-modified Chebyshev approximations of delta function of order $N$ (blue solid curves), for a fixed value of kernel parameter $\lambda = 1.5$ when the order $N$ is swept through the values $N = 16, 32, 64, 128, 256$. Figure taken from Ref. [34].

the series (4.32) on a frequency grid $(\omega_k)_{k=1}^{N_e} \subseteq \langle -\Omega_b, +\Omega_b \rangle$ having $N_e$ points for e.g. plotting or numerical integration purpose. We can use the well known Clenshaw algorithm [56], but if we do not insist on a specific frequency grid such as uniform grid, it is better to use the Chebyshev nodes:

$$\omega_k = \Omega_b \cos\left(\frac{\pi}{N_e}\left(k - \frac{1}{2}\right)\right), \quad k = 1, 2, \ldots, N_e. \tag{4.46}$$

Let us assume that $N_e > N_{\mathrm{it}}$, which is in practice always true since we usually evaluate the series on a very dense grid $N_e \gg N_{\mathrm{it}}$. In that case we can write:

$$\frac{dB(\omega)}{d\omega} = \frac{2/\pi}{\sqrt{\Omega_b^2 - \omega^2}} \sum_{n=1}^{2N_e} \mu_{n-1} T_{n-1}\left(\frac{\omega}{\Omega_b}\right), \tag{4.47}$$

where the higher order coefficients: $\mu_{2N_{\mathrm{it}}+1}, \ldots, \mu_{2N_e-1}$, are set to zero. Then there holds:

$$\frac{dB(\omega_k)}{d\omega} = \frac{2/\pi}{\Omega_b \sin\left(\frac{\pi}{N_e}\left(k - \frac{1}{2}\right)\right)} \mathrm{Re}\left[\sum_{n=1}^{2N_e} \left(\mu_{n-1} e^{-\pi \mathrm{i} \frac{(n-1)}{2N_e}}\right) e^{-2\pi \mathrm{i} \frac{(n-1)(k-1)}{2N_e}}\right]. \tag{4.48}$$

Previous summations can be efficiently evaluated using fast Fourier transform, e.g. freely available FFTW library [57] provides a procedure which for input sequence

$x_1, x_2, \ldots, x_N \in \mathbb{C}$ calculates $X_1, X_2, \ldots, X_N \in \mathbb{C}$ defined as:

$$X_k = \sum_{n=1}^{N} x_n e^{-2\pi \mathrm{i} \frac{(n-1)(k-1)}{N}}. \tag{4.49}$$

Therefore, after the coefficients $\mu_0, \mu_1, \ldots, \mu_{2N_{\mathrm{it}}}$ are calculated and kernel-readjusted, one can quickly evaluate the series (4.32) on a dense Chebyshev frequency grid for plotting or numerical integration purpose.

### 4.2.4 Bounding frequency

In this subsection we would like to emphasize that the bounding frequency $\Omega_b$ has to fulfill the following condition: $\pm\Omega_i \in \langle -\Omega_b, +\Omega_b \rangle$, for all $i = 1, \ldots, N_p$. Otherwise, the diagonal elements $T_n\left(\frac{\Omega_i}{\Omega_b}\right)$ in Eq. (4.30) are simply not defined. If the sequence of functions $T_n(x)$ is calculated recursively on $\mathbb{R}$ as $T_0(x) = 1, T_1(x) = x$ and $T_n(x) = 2xT_{n-1}(x) - T_{n-2}(x)$, then the following equation holds:

$$T_n(x) = \frac{1}{2}\left(\left(x - \sqrt{x^2-1}\right)^n + \left(x + \sqrt{x^2-1}\right)^n\right), \text{ for } |x| \geq 1. \tag{4.50}$$

Therefore, if the bounding frequency $\Omega_b$ does not satisfy $\pm\Omega_i \in \langle -\Omega_b, +\Omega_b \rangle$ (i.e., if $\Omega_i/\Omega_b \geq 1$), we expect that the recursive procedure (4.36) which generates the sequence of vectors $|\alpha_n\rangle \in \mathbb{C}^{2N_p}$ will quickly diverge. In practice, we can often provide a heuristic physical estimate of the upper bound for $\max(\Omega_i)_{i=1}^{N_p}$, and thus guess the value of $\Omega_b$. During the recursive procedure (4.36), we can notice immediately if the bounding frequency is underestimated due to the divergent behaviour of the $\mu_n$ coefficients. On the other hand, a more pedantic approach is to calculate the maxium eigenfrequency $\Omega_{\max} = \max(\Omega_i)_{i=1}^{N_p}$ as an extremal eigenvalue:

$$\begin{bmatrix} \mathbf{I} & \mathbf{0} \\ \mathbf{0} & -\mathbf{I} \end{bmatrix} \begin{bmatrix} A & B \\ B^* & A^* \end{bmatrix} \begin{bmatrix} X^{\max} \\ Y^{\max} \end{bmatrix} = \Omega_{\max} \begin{bmatrix} X^{\max} \\ Y^{\max} \end{bmatrix}, \quad X^{\max}, Y^{\max} \in \mathbb{C}^{N_p}. \tag{4.51}$$

Previous equation can be solved efficiently by employing one of the many existing iterative Krylov-space methods or power methods. The bounding frequency is then defined as $\Omega_b = \Omega_{\max} + \varepsilon$ for some small value of $\varepsilon$, e.g. $\varepsilon = 0.01\Omega_{\max}$. We recommend a heuristic approach for estimating $\Omega_b$ if the solver is supervised manually, although even then one can easily detect divergent behaviour automatically and readjust $\Omega_b$ accordingly. For a large-scale calculations it is better to use the latter pedantic approach.

### 4.2.5 Method summary

The steps of the proposed method are summarized in Algorithm 1. We emphasize that the method is not memory intensive, since we do not need to store vectors $(|\alpha_n\rangle)_{n=0}^{N_{\mathrm{it}}}$ in the computer memory. Keeping track of only three vectors $|\alpha_{\mathrm{new}}\rangle, |\alpha_{\mathrm{old}}\rangle, |\alpha_{\mathrm{tmp}}\rangle \in \mathbb{C}^{N_p}$ will suffice to go through the recursion (4.36). Also, when we reach $n = N_{\mathrm{it}}$, the algorithm stops and yields coefficients $(\mu_n)_{n=0}^{2N_{\mathrm{it}}}$, but

**Algorithm 1:** QRPA Chebyshev kernel polynomial method

**Input:**

- QRPA matrix-vector mapping: $\left[\begin{smallmatrix} x \\ y \end{smallmatrix}\right] \in \mathbb{C}^{2N_p} \mapsto \left[\begin{smallmatrix} A & B \\ B^* & A^* \end{smallmatrix}\right]\left[\begin{smallmatrix} x \\ y \end{smallmatrix}\right] \in \mathbb{C}^{2N_p}$, with Hermitian positive-definite QRPA matrix.
- Vectors $F^{20}, F^{02} \in \mathbb{C}^{N_p}$.
- Bounding frequency $\Omega_b > 0$ satisfying $(\pm\Omega_i)_{i=1}^{N_p} \subset \langle -\Omega_b, +\Omega_b \rangle$.
- Number of iterations $N_{\mathrm{it}}$, i.e. the number of matrix-vector products and number of Chebyshev nodes $N_e > N_{\mathrm{it}}$ for evaluation of $\frac{dB(\omega)}{d\omega}$.
- Kernel coefficients $g_n^{(2N_{\mathrm{it}}+1)}$, $n = 0, 1, \ldots, 2N_{\mathrm{it}}$.

• Initialize $|\alpha_{\mathrm{old}}\rangle \leftarrow |\alpha_0\rangle$, $|\alpha_{\mathrm{new}}\rangle \leftarrow |\alpha_1\rangle$ according to Eq. (4.35):

$$|\alpha_{\mathrm{old}}\rangle \leftarrow \left[\begin{smallmatrix} F^{20} \\ -F^{02} \end{smallmatrix}\right] \quad \text{and} \quad |\alpha_{\mathrm{new}}\rangle \leftarrow \frac{1}{\Omega_b}\left[\begin{smallmatrix} \mathbf{I} & \mathbf{0} \\ \mathbf{0} & -\mathbf{I} \end{smallmatrix}\right]\left[\begin{smallmatrix} A & B \\ B^* & A^* \end{smallmatrix}\right]\left[\begin{smallmatrix} F^{20} \\ -F^{02} \end{smallmatrix}\right]. \tag{4.52}$$

• Initialize $\mu_0$ and $\mu_1$ according to Eq. (4.37):

$$\mu_0 \leftarrow \frac{1}{2}\left[\begin{smallmatrix} F^{20} \\ F^{02} \end{smallmatrix}\right]^\dagger |\alpha_{\mathrm{old}}\rangle \quad \text{and} \quad \mu_1 \leftarrow \left[\begin{smallmatrix} F^{20} \\ F^{02} \end{smallmatrix}\right]^\dagger |\alpha_{\mathrm{new}}\rangle. \tag{4.53}$$

**for** $n = 1, 2, \ldots, N_{it}$ **do**

*// Now there holds:* $|\alpha_{new}\rangle = |\alpha_n\rangle$ *and* $|\alpha_{old}\rangle = |\alpha_{n-1}\rangle$.

- Calculate $\mu_{2n-1}$ and $\mu_{2n}$ according to Eq. (4.39) and (4.40):
  - $\mu_{2n-1} \leftarrow 2\langle\alpha_{\mathrm{old}}|\left[\begin{smallmatrix} \mathbf{I} & \mathbf{0} \\ \mathbf{0} & -\mathbf{I} \end{smallmatrix}\right]|\alpha_{\mathrm{new}}\rangle - \mu_1$,
  - $\mu_{2n} \leftarrow 2\langle\alpha_{\mathrm{new}}|\left[\begin{smallmatrix} \mathbf{I} & \mathbf{0} \\ \mathbf{0} & -\mathbf{I} \end{smallmatrix}\right]|\alpha_{\mathrm{new}}\rangle - 2\mu_0$.
- If $\mu_{2n-1}, \mu_{2n}$ start to diverge, $\Omega_b$ is too small, restart with new $\Omega_b$!
- If $n < N_{\mathrm{it}}$, update vectors $|\alpha_{\mathrm{new}}\rangle, |\alpha_{\mathrm{old}}\rangle$ according to Eq. (4.36):
  - $|\alpha_{\mathrm{tmp}}\rangle \leftarrow |\alpha_{\mathrm{new}}\rangle$,
  - $|\alpha_{\mathrm{new}}\rangle \leftarrow \frac{2}{\Omega_b}\left[\begin{smallmatrix} \mathbf{I} & \mathbf{0} \\ \mathbf{0} & -\mathbf{I} \end{smallmatrix}\right]\left[\begin{smallmatrix} A & B \\ B^* & A^* \end{smallmatrix}\right]|\alpha_{\mathrm{new}}\rangle - |\alpha_{\mathrm{old}}\rangle$,
  - $|\alpha_{\mathrm{old}}\rangle \leftarrow |\alpha_{\mathrm{tmp}}\rangle$.

**end**

• Apply kernel transformation $\mu_n \leftarrow g_n^{(2N_{\mathrm{it}}+1)}\mu_n$, for $n = 0, 1, \ldots, 2N_{\mathrm{it}}$.
• Evaluate $\frac{dB(\omega_k)}{d\omega}$ on Chebyshev nodes $(\omega_k)_{k=1}^{N_e}$ using Eq. (4.48) via FFT.

**Output:** Truncated Chebyshev expansion of the response function $\frac{dB(\omega)}{d\omega}$ as in Eq. (4.32) evaluated on Chebyshev frequency nodes (4.46).

if the last two vectors $|\alpha_{N_{it}-2}\rangle$, $|\alpha_{N_{it}-1}\rangle$ are stored on drive, we can later continue calculating higher coefficients $\mu_n$ for $n > 2N_{\text{it}}$.

## 4.3 Numerical results

To validate our implementation of the KPM for calculating the QRPA response function, as described in Algorithm 1, we have performed several test calculations. All tests are available at the public GitHub repository:

**https://github.com/abjelcic/ChebyshevQRPA**,

in a form of MATLAB scripts, tested on the MATLAB releases R2018a and R2021a. We have also verified that scripts are running with GNU Octave 5.2.0 as a publicly available alternative which is mostly compatible with MATLAB. We notice that for some calculations Octave is considerably slower in comparison to MATLAB. To reduce the computation time, we have included the recommended values of numerical parameters to be used with Octave in the scripts that would otherwise be time consuming.

### 4.3.1 Test 1: Synthetic model

For our first test case we use synthetically generated QRPA matrices $A$, $B$ and vectors $F^{20}, F^{02}$ by employing the procedure described in B.2. The matrix dimension and the bounding frequency are set to $N_p = 1000$ and $\Omega_b = 250$ MeV, respectively. 500 random eigenfrequencies $\Omega_i$ are generated uniformly in range from 0 MeV to 200 MeV and combined with another 500 random eigenfrequencies $\Omega_i$ generated uniformly in range from 0 MeV to 50 MeV. The resulting QRPA spectrum will obviously be more dense in the low energy region. Next, we generate random sequence of values $\theta_1, \ldots, \theta_{N_p} \geq 0$ and two unitary matrices $C, D \in \mathbb{C}^{N_p \times N_p}$ as $Q$ factors in the QR decomposition of two random $N_p \times N_p$ complex matrices. The $X$ and $Y$ matrices are constructed as:

$$X = D \operatorname{diag}[\cosh \theta_i]_{i=1}^{N_p} C \quad \text{and} \quad Y = D^* \operatorname{diag}[\sinh \theta_i]_{i=1}^{N_p} C, \tag{4.54}$$

and used to generate the $A$ and $B$ matrices:

$$A = + \left[ X \Omega X^\dagger + \left( Y \Omega Y^\dagger \right)^* \right] \quad \text{and} \quad B = - \left[ X \Omega Y^\dagger + \left( X \Omega Y^\dagger \right)^T \right], \tag{4.55}$$

as explained in Remark 1.

Notice that from Eq. (4.23) the response function $\frac{dB(\omega)}{d\omega}$ can be written as:

$$\frac{dB(\omega)}{d\omega} = \sum_{i=1}^{N_p} |\langle i|\hat{F}|0\rangle|^2 \delta(\omega - \Omega_i) - \sum_{i=1}^{N_p} |\langle 0|\hat{F}|i\rangle|^2 \delta(\omega + \Omega_i), \tag{4.56}$$

where vectors $(\langle i|\hat{F}|0\rangle)_{i=1}^{N_p} \in \mathbb{C}^{N_p}$ and $(\langle i|\hat{F}|0\rangle)_{i=1}^{N_p} \in \mathbb{C}^{N_p}$ are defined as:

$$\begin{bmatrix} (\langle i|\hat{F}|0\rangle)_{i=1}^{N_p} \\ (\langle 0|\hat{F}|i\rangle)_{i=1}^{N_p} \end{bmatrix} = \begin{bmatrix} X & Y^* \\ Y & X^* \end{bmatrix}^\dagger \begin{bmatrix} F^{20} \\ F^{02} \end{bmatrix}. \tag{4.57}$$

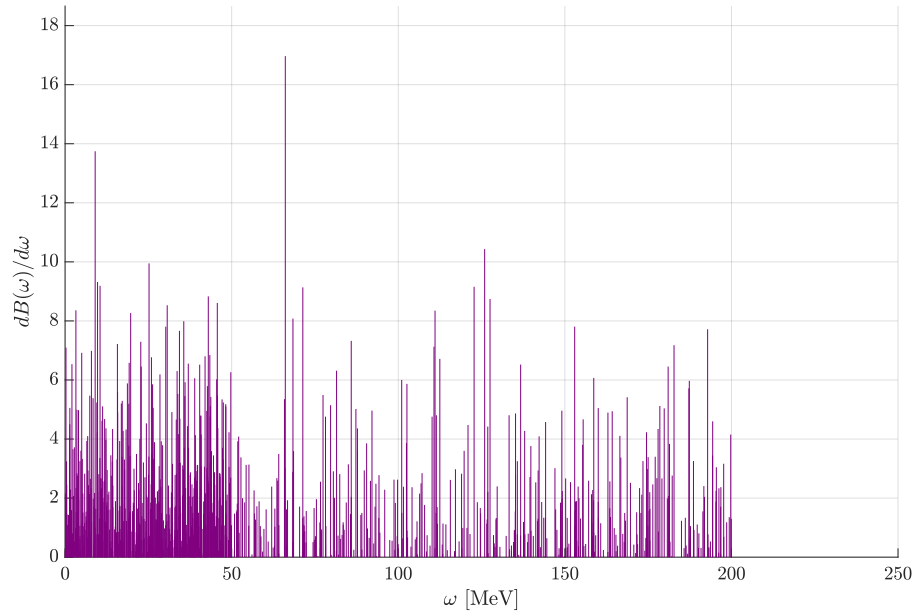


Figure 4.4: Synthetically generated response function $\frac{dB(\omega)}{d\omega}$ calculated by using Eq. (4.56). The positions of the vertical lines are given by the eigenfrequencies $\Omega_i$, while the heights are equal to $|\langle i|\hat{F}|0\rangle|^2$. Figure taken from Ref. [34].

The real and imaginary parts of the matrix elements $\langle i|\hat{F}|0\rangle$ are generated from the standard normal distribution and since we assume that the operator $\hat{F}$ is Hermitian. we set: $\langle 0|\hat{F}|i\rangle = \langle i|\hat{F}|0\rangle^*$.

Finally, we construct vectors $F^{20}, F^{02} \in \mathbb{C}^{N_p}$ so that Eq. (4.57) is satisfied:

$$\begin{bmatrix} F^{20} \\ F^{02} \end{bmatrix} = \begin{bmatrix} \mathbf{I} & \mathbf{0} \\ \mathbf{0} & -\mathbf{I} \end{bmatrix} \begin{bmatrix} X & Y^* \\ Y & X^* \end{bmatrix} \begin{bmatrix} \mathbf{I} & \mathbf{0} \\ \mathbf{0} & -\mathbf{I} \end{bmatrix} \begin{bmatrix} (\langle i|\hat{F}|0\rangle)_{i=1}^{N_p} \\ (\langle 0|\hat{F}|i\rangle)_{i=1}^{N_p} \end{bmatrix}. \tag{4.58}$$

In Fig. 4.4 we display the response function Eq. (4.56) calculated on the interval $\langle -\Omega_b, +\Omega_b\rangle$ for one such generated example. Next, we will try to reproduce this response function by employing the KPM. We select the allowed number of the QRPA matrix-vector multiplications $N_{\text{it}}$ and perform steps of Algorithm 1, using the Lorentz kernel with parameter $\lambda = 1.5$. The results are shown in Fig. 4.5 on the low-energy interval from 0 MeV to 50 MeV, where we increase $N_{\text{it}}$ from 200 up to 6400 iterations, each time doubling the value of $N_{\text{it}}$. Since the Lorentz kernel approximates delta functions in eq. (4.56) with Lorentzian distributions of width:

$$\gamma_{\text{KPM}} = \Omega_b \frac{\lambda}{2N_{\text{it}} + 1}, \tag{4.59}$$

we expect that doubling the number of iterations $N_{\text{it}}$ in Algorithm 1 will yield the sum of two times narrower Lorentzians. For comparison, we also plotted in Fig.

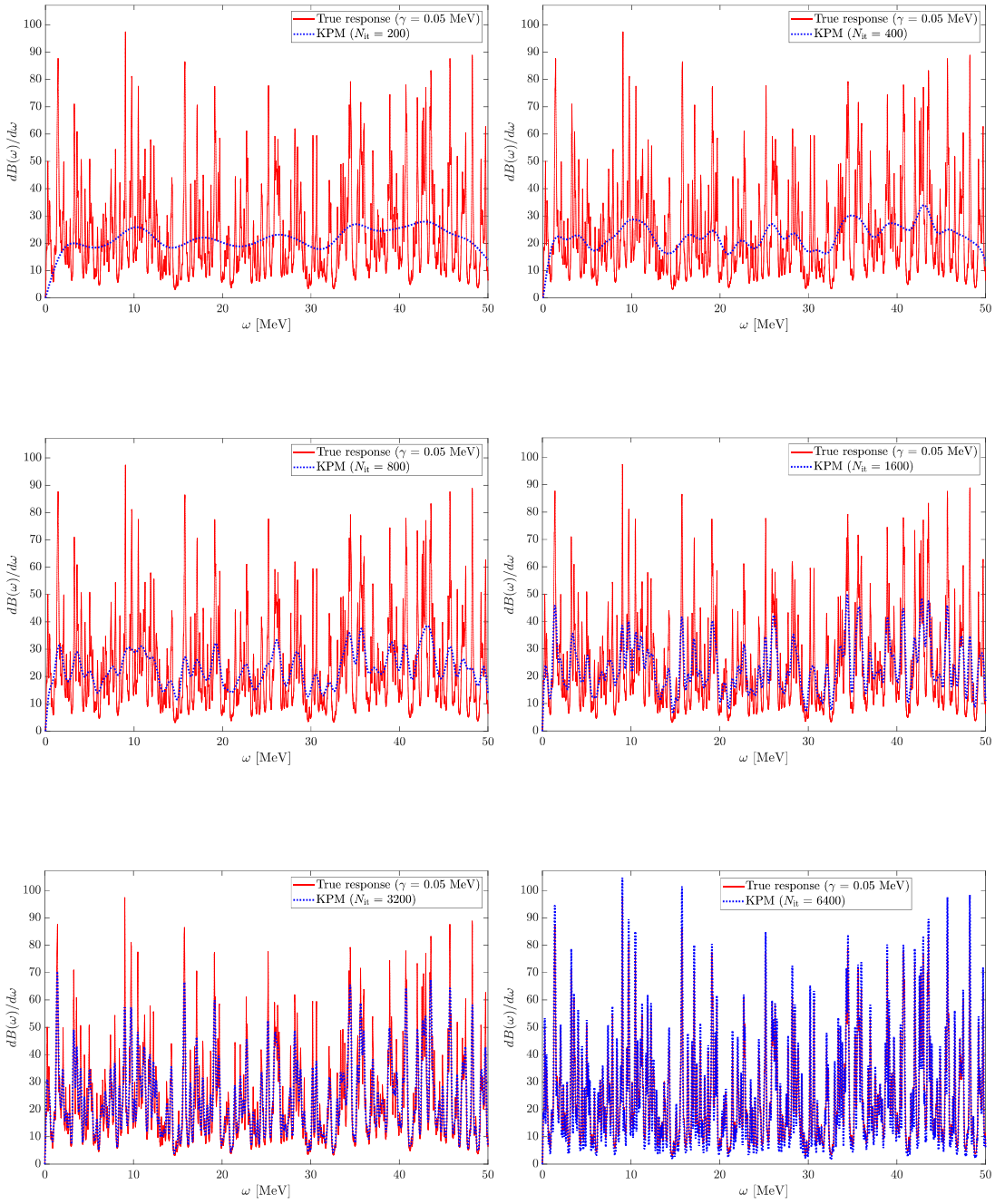


Figure 4.5: True response function (solid red curve) folded with Lorentzian of width $\gamma = 0.05$ MeV in comparison to the response function calculated by using Algorithm 1 (dot-dashed blue curve) as the number of QRPA matrix-vector multiplications $N_{\rm it}$ increases from 200 to 6400. We plot only the low-energy region from 0 MeV to 50 MeV. Figure taken from Ref. [34].

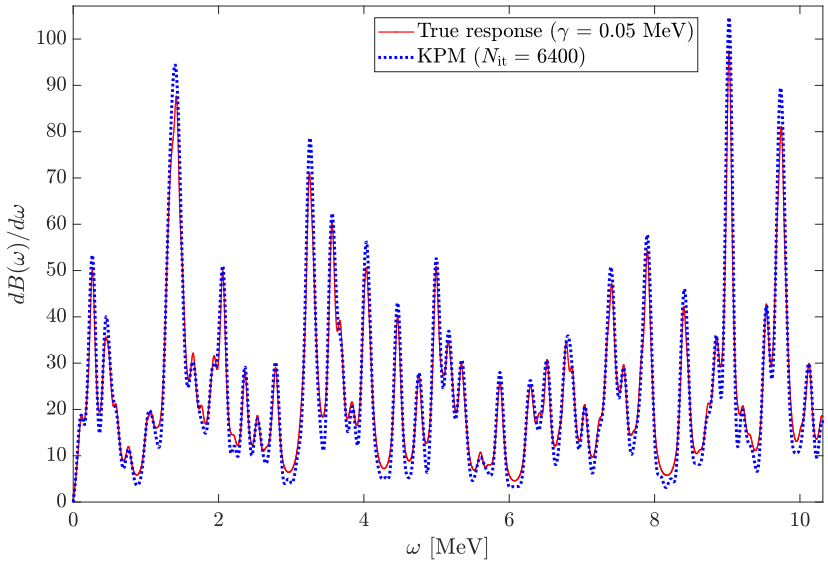


Figure 4.6: Zoom of the response function displayed in Fig. 4.5 for frequency in range from 0 MeV to 10 MeV. The number of iterations used is $N_{\rm it} = 6400$. Figure taken from Ref. [34].

4.5 a true response function folded with a Lorentzian of width $\gamma = 0.05$ MeV:

$$\frac{dB(\omega)}{d\omega}\Big|_{\gamma} = \sum_{i=1}^{N_p} |\langle i|\hat{F}|0\rangle|^2 \frac{\gamma/\pi}{(\omega-\Omega_i)^2+\gamma^2} - \sum_{i=1}^{N_p} |\langle 0|\hat{F}|i\rangle|^2 \frac{\gamma/\pi}{(\omega+\Omega_i)^2+\gamma^2}. \quad (4.60)$$

In Fig. 4.6 we show a zoom of the response function for frequency in range from 0 MeV to 10 MeV and $N_{\rm it} = 6400$. We notice that some artefacts of the Gibbs oscillations are still present and although they could be further damped by increasing the Lorentz kernel parameter $\lambda$, this would require more iterations $N_{\rm it}$ in Algorithm 1 according to Eq. (4.59) in order to obtain the same $\gamma_{\rm KPM}$. We have found that $\lambda \approx 1.5$ provides a good compromise between speed and accuracy of the KPM calculation. From Eq. (4.59) it follows that one should select the smallest possible bounding frequency $\Omega_b$ (but still larger than the largest eigenfrequency $\Omega_{\rm max}$) in order to minimize the necessary number of iterations $N_{\rm it}$ for the targeted smearing width $\gamma_{\rm KPM}$, assuming fixed $\lambda$ parameter.

We can conclude that the proposed implementation of the KPM to calculate the QRPA response function successfully reproduces the results obtained by direct diagonalization of synthetically generated QRPA matrix. We have also verified that the same results are obtained if linear response equations (4.16) are solved for a range of frequencies $\omega$ with fixed $\gamma = 0.05$ MeV.

### 4.3.2 Test 2: Matrix RPA solver

In this test, we would like to validate the KPM implementation for calculating the RPA response function when applied to a realistic RPA solver. For this purpose we have selected publicly available RPA solver `skyrme_rpa` [58]. This solver is implemented for closed shell spherical nuclei with Skyrme-type interactions. The Hartree-Fock equations are solved on a radial mesh using the box boundary condition and the RPA matrix is explicitly constructed and diagonalized for a given value of total angular momentum and parity $J^\pi$. The output of the `skyrme_rpa` solver contains calculated eigenfrequencies and transition strengths for isoscalar and isovector multipole operators $\hat{F}^{IS/IV}_{J^\pi}$. Also, the isoscalar and isovector response functions (4.60) folded with Lorentzian functions of selected width $\gamma$ are provided.

We have modified the `skyrme_rpa` code and extracted the RPA matrices $A$ and $B$ and vectors $F^{20}, F^{02}$ for the $^{120}$Sn isotope and $J^\pi = 5^-$ isovector operator. Calculation was performed by employing the SLy5 Skyrme interaction [63] in a 20 fm radius box with 0.1 fm radial step and 100 MeV cutoff energy[1]. The resulting $2N_p \times 2N_p$ RPA matrix is of order $N_p = 1310$. Based on the value of the cutoff energy $E_c$, we do not expect that the particle-hole energies will be larger than $\approx 250$ MeV, therefore we set the value of the bounding frequency to $\Omega_b = 250$ MeV. Indeed, we have verified that the largest calculated RPA eigenfrequency is $\Omega_{\rm max} = 156$ MeV. In order to damp Gibbs oscillations, Lorentzian kernel with parameter $\lambda = 1.5$ was used. Figure 4.7 displays the response function obtained by the original `skyrme_rpa` code folded with the Lorentzian function of width $\gamma = 0.05$ MeV in comparison to the results obtained using the KPM with $N_{\rm it} = 6400$ iterations. It is worth noting that the necessary number of iterations $N_{\rm it}$ could be reduced by choosing the bounding frequency $\Omega_b$ closer to the largest RPA eigenfrequency $\Omega_{\rm max}$.

In Fig. 4.8 we display a zoom of the response functions shown in Fig. 4.7 for frequency in range from 20 MeV to 30 MeV. The two response functions are virtually identical although there are still some Gibbs oscillation effects visible in the response function calculated by the KPM.

### 4.3.3 Test 3: Quasiparticle Finite Amplitude Method solver

Next, we would like to validate the KPM implementation for calculating the QRPA response function when applied in conjunction with a realistic QFAM solver. Similar to the previous test, we have selected publicly available finite amplitude method solver `DIRQFAM` [2]. The `DIRQFAM` code calculates the QRPA multipole response of even–even open-shell nuclei with axially deformed ground state using the finite amplitude method, based on the relativistic self-consistent mean-field models. The QFAM amplitudes are expanded in the basis of the eigenfunctions of the axially symmetric harmonic oscillator with simplex-y symmetry imposed. The `DIRQFAM`

[1] Cutoff energy $E_c$ denotes maximum energy of the unoccupied single-particle states included in the RPA model space. The maximum particle–hole energy is thus $E_c - \epsilon_h$, where $\epsilon_h$ is the deepest hole energy. For the chosen value $E_c = 100$ MeV, rough estimate of the maximum particle-hole energy is $\approx 150$ MeV.

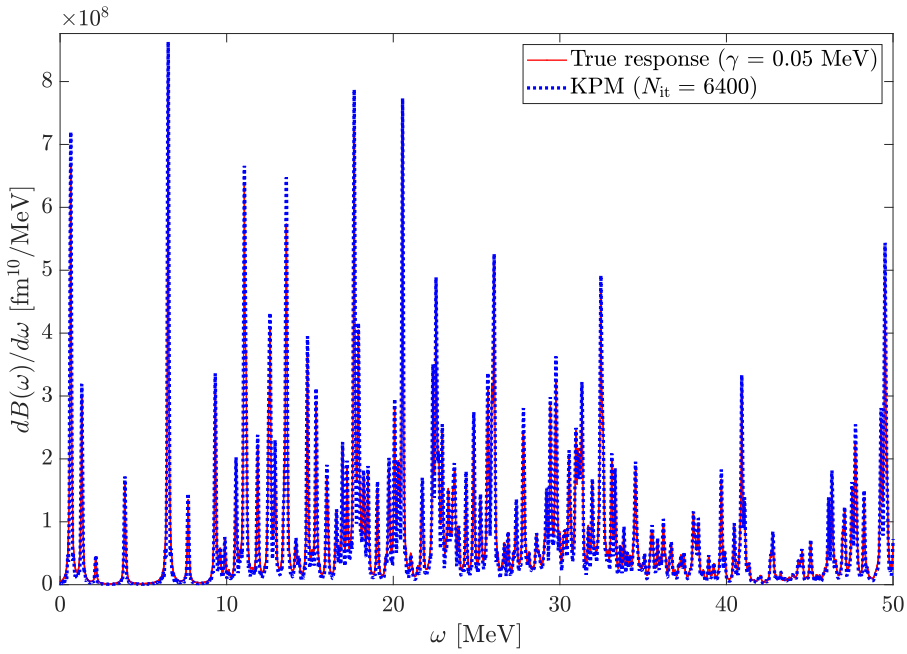


Figure 4.7: Comparison of the response functions obtained by using the original `skyrme_rpa` code (red curve) and the KPM (blue curve) for the $^{120}$Sn isotope and isovector $J^\pi = 5^-$ excitation. Figure taken from Ref. [34].

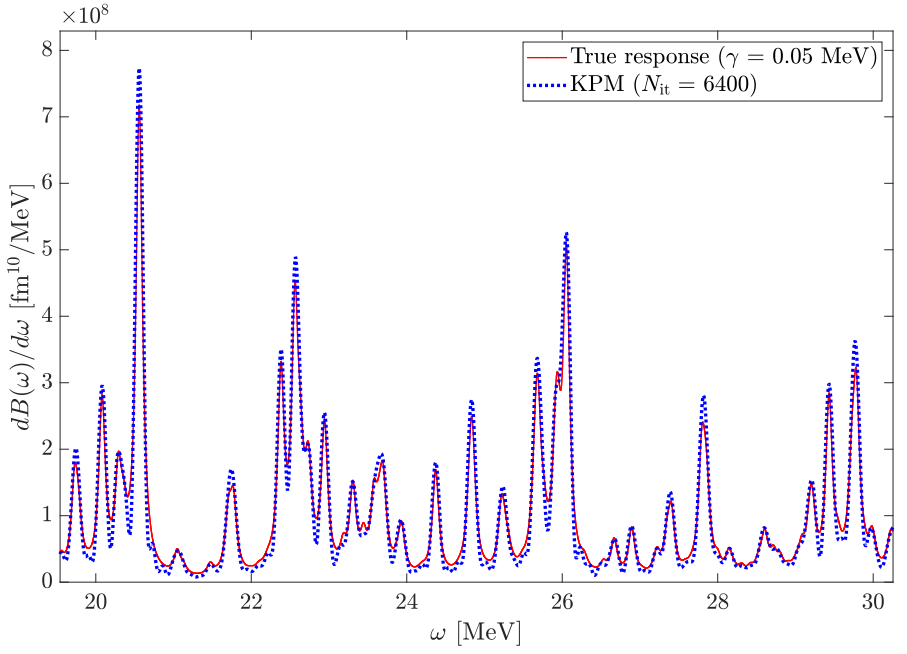


Figure 4.8: Zoom of the response function displayed in Fig. 4.7 for energy in range from 20 MeV to 30 MeV. Figure taken from Ref. [34].

code iteratively solves the QFAM equations for a given frequency $\omega_\gamma$:

$$(E_\mu + E_\nu - \omega_\gamma)X_{\mu\nu}(\omega_\gamma) + \delta H^{20}_{\mu\nu}(\omega_\gamma) = -F^{20}_{\mu\nu}, \tag{4.61}$$

$$(E_\mu + E_\nu + \omega_\gamma)Y_{\mu\nu}(\omega_\gamma) + \delta H^{02}_{\mu\nu}(\omega_\gamma) = -F^{02}_{\mu\nu}. \tag{4.62}$$

It should be emphasized that the QFAM calculations can be performed very efficiently by using the self-consistent symmetries of the ground state [2], together with the structure of the excitation operator $\hat{F}$. For initial guess of the QFAM amplitudes we usually choose:

$$X_{\mu\nu}(\omega_\gamma) = Y_{\mu\nu}(\omega_\gamma) = 0, \tag{4.63}$$

and during the iterations QFAM equations preserve the symmetry of the excitation operator. For example, if the excitation operator proportional to the spherical harmonic $Y_{JK}(\theta, \phi)$ is used, all matrices involved in the calculations turn out to have block structure and the induced densities and currents have simple $\cos(K\phi)$ or $\sin(K\phi)$ angular dependence. By utilizing these properties, the computational cost of the QFAM calculations is reduced drastically.

At the core of any QFAM solver is the implementation of the linear mapping:

$$\begin{aligned}\begin{bmatrix} X_{\mu\nu} \\ Y_{\mu\nu} \end{bmatrix} &\mapsto \begin{bmatrix} \delta H^{20}_{\mu\nu} \\ \delta H^{02}_{\mu\nu} \end{bmatrix} \\ &= \begin{bmatrix} -(E_\mu + E_\nu)X_{\mu\nu} + \sum_{\mu'<\nu'} A_{\mu\nu,\mu'\nu'}X_{\mu'\nu'} + B_{\mu\nu,\mu'\nu'}Y_{\mu'\nu'} \\ -(E_\mu + E_\nu)Y_{\mu\nu} + \sum_{\mu'<\nu'} B^*_{\mu\nu,\mu'\nu'}X_{\mu'\nu'} + A^*_{\mu\nu,\mu'\nu'}Y_{\mu'\nu'} \end{bmatrix},\end{aligned} \tag{4.64}$$

which together with the QFAM equations (4.61) and (4.62) is used to solve these equations iteratively. However, the `DIRQFAM` solver does not implement the full mapping (4.64) for arbitrary amplitudes $X_{\mu\nu}, Y_{\mu\nu}$, but rather only for those belonging to the linear subspace defined by the self-consistent symmetries of the ground state and structure of the excitation operator. Therefore, it seems that we might encounter problems implementing the KPM since the `DIRQFAM` code actually has no access to the full mapping:

$$\begin{bmatrix} x \\ y \end{bmatrix} \in \mathbb{C}^{2N_p} \mapsto \begin{bmatrix} A & B \\ B^* & A^* \end{bmatrix} \begin{bmatrix} x \\ y \end{bmatrix} \in \mathbb{C}^{2N_p}, \tag{4.65}$$

required by the Algorithm 1. However, the algorithm initializes vectors $|\alpha_{\text{old}}\rangle$, $|\alpha_{\text{new}}\rangle$ as in Eq. (4.52) which are consistent with the selection rules of the excitation operator and all selection rules are preserved throughout the recursion in Algorithm 1. This means that the KPM for calculating the QRPA response function does not require the full mapping (4.65), but only restricted mapping on vectors consistent with the selection rules of the particular excitation operator. This point is very important in practical calculations because virtually every QFAM solver assumes some form of symmetry in order to reduce the computational complexity.

For the purpose of this test, we have selected the $^{100}$Zr nucleus with deformed

[2] In the `DIRQFAM` code one assumes the axial symmetry, parity and time-reversal invariance in the ground state.

ground state ($\beta \approx 0.485$), subjected to the isovector octupole $J = 3$, $K = 3$ excitation. In the particle-hole channel we employ the DD-PC1 effective interaction, while the particle-particle channel is described by a separable finite-range force. Dirac spinors are expanded in the basis of the eigenfunctions of the axially symmetric harmonic oscillator with 14 major shells for large and 15 major shells for small components. First, for comparison purpose, we have performed the QFAM calculation sweeping through frequencies from 0 MeV to 50 MeV and using the smearing $\gamma = 0.05$ MeV. Then, we employ Algorithm 1 with Lorentz kernel with parameter $\lambda = 1.5$. In order to obtain an assessment of the bounding frequency, we need a rough approximation of the QRPA eigenfrequencies $(\Omega_i)_{i=1}^{N_p}$. As a starting point, we can ignore the residual interaction $\delta H^{20}_{\mu\nu} = \delta H^{02}_{\mu\nu} = 0$ in QFAM equations (4.61) and (4.62) (often refereed to as the free response) which yields the lowest order approximation value of the largest QRPA eigenfrequency:

$$\Omega_{\max} \approx \max_{\mu\nu} |E_\mu + E_\nu| \leq 2 \max_\mu |E_\mu|. \tag{4.66}$$

Since `DIRQFAM` solver relies on the relativistic EDFs, configuration space includes, not only the Fermi sea, but also the Dirac sea of negative energy states. In addition to the configurations built from two-quasiparticle states of positive energy, the configuration space must also contain pair-configurations formed from the fully or partially occupied states of positive energy and the empty negative-energy states from the Dirac sea. The inclusion of configurations built from occupied positive-energy states and empty negative-energy states is essential for current conservation and the decoupling of spurious states [59]. Since the energies of the states in Dirac sea reach typical values of $E_\mu \approx -2000$ MeV, the value of the maximal QRPA eigenfrequency is very large and thus we have to use a comparable value of the bounding frequency $\Omega_b$. In this particular test we use the value $\Omega_b = 4500$ MeV. Indeed, the Algorithm 1 diverges quickly if one tries to reduce the bounding frequency below 4000 MeV. This behavior suggest that the KPM in not well suited for calculations based on the relativistic EDFs, because according to the Eq. (4.59) we would have to perform a large number of iterations $N_{\text{it}}$ in order to obtain a reasonably sharp resolution $\gamma_{\text{KPM}}$ of the KPM approximation of the response function. Nevertheless, since `DIRQFAM` code is the only publicly available QFAM solver at this time, for demonstration purpose we have implemented the KPM in conjunction with this solver. In Fig. 4.9 we show the response function for the $J = 3$, $K = 3$ excitation built on top of the deformed ground state in the $^{100}$Zr. Results obtained with the `DIRQFAM` code (solid red line) are compared with those obtained by the KPM implementation (dotted blue line). A large number of iterations $N_{\text{it}} = 100000$ was used in the KPM calculation due to the effects of the Dirac sea. In Fig. 4.10 we show a zoom of the response function displayed in Fig. 4.9 for frequencies in range from 20 MeV to 40 MeV. If we estimate that one typically requires 50 QFAM iterations to find the QFAM response at any given frequency $\omega_\gamma$, in 100000 QFAM iterations we would have obtained 2000 points $\left(\omega_\gamma, \frac{dB(\omega)}{d\omega}\Big|_\gamma\right)$ which is more than enough to display a good approximation of the response function on energy interval 0-50 MeV even for a small smearing $\gamma$. In the QRPA calculations, sometimes one encounters zero-energy modes known as the Nambu-Goldstone (NG) modes. The NG modes originate from

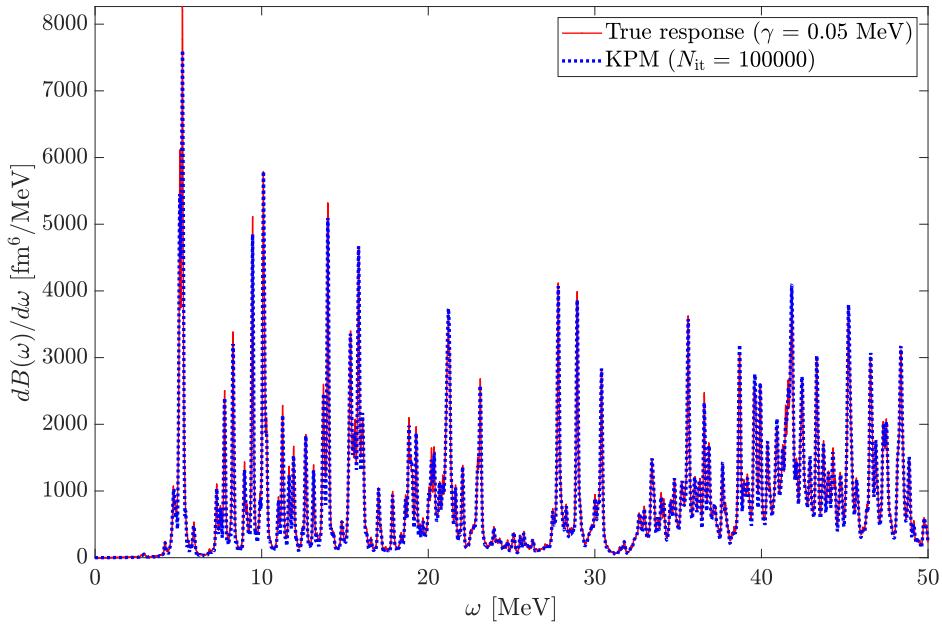


Figure 4.9: Comparison of the response functions obtained using the original DIRQFAM code and the proposed method for deformed ($\beta \approx 0.485$) isotope $^{100}$Zr subjected to isovector $J = 3, K = 3$ excitation. Figure taken from Ref. [34].

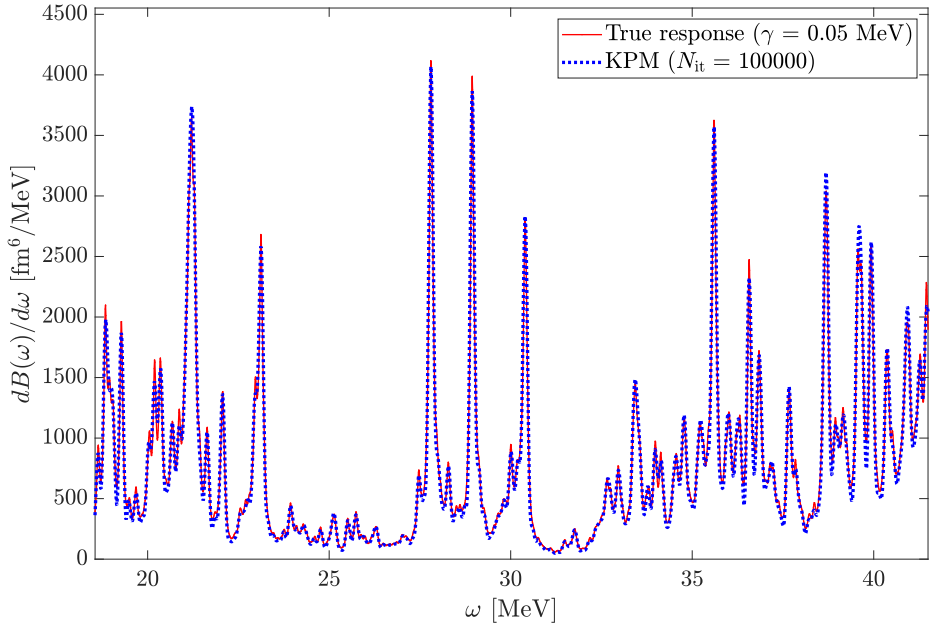


Figure 4.10: Zoom of the response function displayed in Fig. 4.9 for frequencies in range from 20 MeV to 40 MeV. Figure taken from Ref. [34].

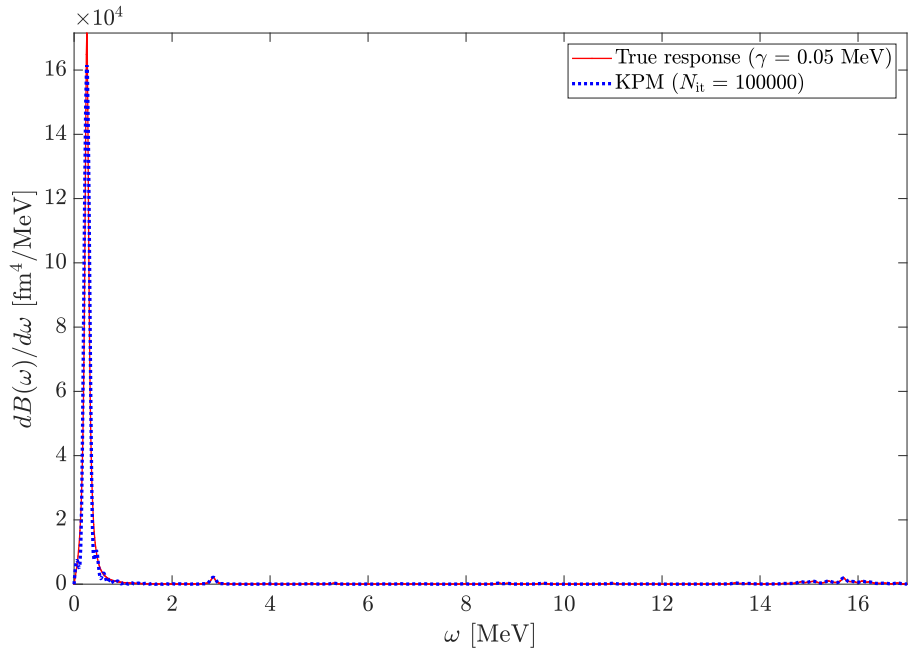


Figure 4.11: Comparison of the response functions obtained using the original DIRQFAM code and the KPM for deformed $^{100}$Zr isotope subjected to the isoscalar $J = 2$, $K = 1$ excitation. Figure taken from Ref. [34].

the broken symmetries on the mean-field level of the calculation: translational symmetry, rotational symmetry and particle-number gauge symmetry. Since the NG modes do not represent physical excitations within the intrinsic frame, they are also referred to as spurious modes. So far, we have used the $XY$ representation of the QRPA and assumed that the QRPA matrix is positive definite, yielding $\Omega_i > 0$. The $XY$ representation is not adequate to treat the zero-energy NG modes because they are not normalizable in this representation and, in principle, one should switch to the $PQ$ representation (for extensive discussion see Ref. [60] and references cited therein). However, due to the various numerical inaccuracies in practical calculations (e.g. single-particle states are expanded in the finite harmonic oscillator basis or in the coordinate lattice of a finite box), the frequency of the NG modes is small but still finite. Hence, such states can still be safely treated in the $XY$ representation. Nevertheless, one can show that KPM method works even in $PQ$ representation of QRPA. For completeness, in Appendix B.3 we include the derivation of KPM method for QRPA problem in $PQ$ representation.

To illustrate this, we analyze the $K^\pi = 1^+$ spurious mode originating from broken rotational symmetry. In Fig. 4.11 we display the response functions for the $J = 2$, $K = 1$ excitation operator built on top of the deformed ground state of the $^{100}$Zr isotope. A zoom of Fig. 4.11 is shown in Fig. 4.12 with smaller span on the vertical axis. Indeed we observe one dominant spurious mode originating from the broken rotational symmetry and again we find an excellent agreement between the DIRQFAM and KPM response. We have also verified that the KPM

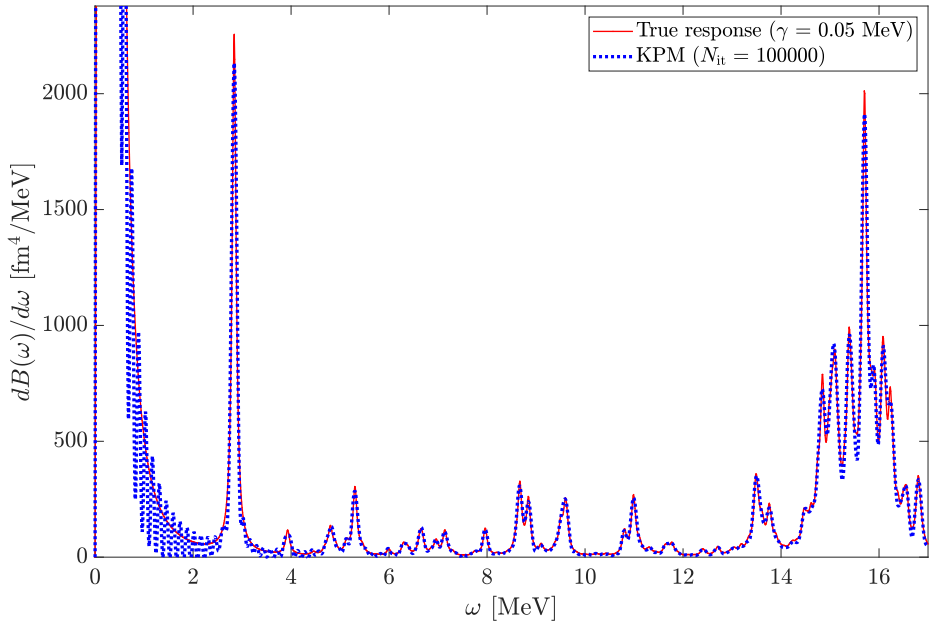


Figure 4.12: Zoom of the response function displayed in Fig. 4.11 with smaller span on the vertical axis. Figure taken from Ref. [34].

method successfully reproduces the DIRQFAM $K^\pi = 0^+$ response to the particle number operator. In this case, only the NG mode is present and the KPM is still applicable. We notice that the DIRQFAM solver separates the spurious center of mass $K^\pi = 1^-$ mode from physical modes by using a method described in Ref. [36].

Finally, we would like to emphasize that in the presence of imaginary QRPA eigenfrequency [3] the KPM calculation diverges. Essentially, the KPM deals with the Chebyshev polynomials evaluated at the eigenfrequencies: $T_n\left(\frac{\Omega_i}{\Omega_b}\right)$, as can be seen from Eq. (4.30). Since $T_n(\mathrm{i}x)$ diverges as $n$ increases for $x > 0$, one can easily see that the existence of eigenfrequency with significant imaginary part yields a fast divergence of the KPM method. On the other hand, such a fast divergence can be used as a clear indicator that one is performing calculation based on the stability matrix which is not positive definite.

In conclusion, we have demonstrated as a proof-of-concept that Algorithm 1 can be rapidly integrated into an existing QFAM solver (e.g. additional $\approx 300$ lines of code in the DIRQFAM solver). However, the method is not well suited for models based on the relativistic energy density functionals because of the contributions from the states in the Dirac sea, and it diverges if the calculated ground state does not correspond to the HFB minimum.

[3] E.g. if one tries to perform the spherical $J^\pi = 2^+$ QRPA calculation on a nucleus with deformed ground state. In this case the constrained spherical configuration on top of which the QRPA calculation is performed does not correspond to the HFB minimum and therefore the HFB stability matrix, i.e., the QRPA matrix, is not positive definite.

### 4.3.4 Test 4: Moments of the response function

It is well known that the sum rules represent a very important tool in studies of collective excitation, especially giant resonances [21]. Although sum rules provide less detailed description of the response function in comparison to the full QRPA calculation, they are still very useful for calculating the global properties of the response function. In this section we show how the Chebyshev expansion of the response function Eq. (4.32) can be used to calculate the moments defined as:

$$m_k = \sum_{i=1}^{N_p} \Omega_i^k |\langle i|\hat{F}|0\rangle|^2, \quad \text{for} \quad k \in \mathbb{Z}. \tag{4.67}$$

From Eq. (4.56) one easily sees:

$$m_k = \int_0^{+\infty} \omega^k \frac{dB(\omega)}{d\omega} d\omega. \tag{4.68}$$

We assume that the excitation operator $\hat{F}$ is Hermitian giving $\langle 0|\hat{F}|i\rangle = \langle i|\hat{F}|0\rangle^*$ and consequently $(F^{02})^* = F^{20}$. First we focus on the odd moments $k \in \mathbb{Z}$ since they can be efficiently calculated directly [61]. Recall the Lemma 1 and equation:

$$\begin{bmatrix} \mathbf{I} & \mathbf{0} \\ \mathbf{0} & -\mathbf{I} \end{bmatrix} \begin{bmatrix} A & B \\ B^* & A^* \end{bmatrix} = \begin{bmatrix} X & Y^* \\ Y & X^* \end{bmatrix} \begin{bmatrix} +\Omega & \mathbf{0} \\ \mathbf{0} & -\Omega \end{bmatrix} \begin{bmatrix} X & Y^* \\ Y & X^* \end{bmatrix}^{-1}. \tag{4.69}$$

Notice that for any $k \in \mathbb{Z}$ (even for negative) the following equation holds:

$$\left( \begin{bmatrix} \mathbf{I} & \mathbf{0} \\ \mathbf{0} & -\mathbf{I} \end{bmatrix} \begin{bmatrix} A & B \\ B^* & A^* \end{bmatrix} \right)^k = \begin{bmatrix} X & Y^* \\ Y & X^* \end{bmatrix} \begin{bmatrix} (+\Omega)^k & \mathbf{0} \\ \mathbf{0} & (-\Omega)^k \end{bmatrix} \begin{bmatrix} X & Y^* \\ Y & X^* \end{bmatrix}^{-1}. \tag{4.70}$$

By using Eqs. (4.20) and (4.58), one can easily show:

$$\begin{aligned} &\begin{bmatrix} F^{20} \\ F^{02} \end{bmatrix}^\dagger \left( \begin{bmatrix} \mathbf{I} & \mathbf{0} \\ \mathbf{0} & -\mathbf{I} \end{bmatrix} \begin{bmatrix} A & B \\ B^* & A^* \end{bmatrix} \right)^k \begin{bmatrix} \mathbf{I} & \mathbf{0} \\ \mathbf{0} & -\mathbf{I} \end{bmatrix} \begin{bmatrix} F^{20} \\ F^{02} \end{bmatrix} = \\ &= \sum_{i=1}^{N_p} (+\Omega_i)^k |\langle i|\hat{F}|0\rangle|^2 - \sum_{i=1}^{N_p} (-\Omega_i)^k |\langle 0|\hat{F}|i\rangle|^2. \end{aligned} \tag{4.71}$$

Using the fact that $k \in \mathbb{Z}$ is odd integer and $\langle 0|\hat{F}|i\rangle = \langle i|\hat{F}|0\rangle^*$ we finally obtain:

$$\begin{aligned} m_k &= \sum_{i=1}^{N_p} \Omega_i^k |\langle i|\hat{F}|0\rangle|^2 \\ &= \frac{1}{2} \begin{bmatrix} F^{20} \\ F^{02} \end{bmatrix}^\dagger \left( \begin{bmatrix} \mathbf{I} & \mathbf{0} \\ \mathbf{0} & -\mathbf{I} \end{bmatrix} \begin{bmatrix} A & B \\ B^* & A^* \end{bmatrix} \right)^k \begin{bmatrix} \mathbf{I} & \mathbf{0} \\ \mathbf{0} & -\mathbf{I} \end{bmatrix} \begin{bmatrix} F^{20} \\ F^{02} \end{bmatrix}. \end{aligned} \tag{4.72}$$

Notice that $m_k$ is indeed a real number. If $k > 0$, Eq. (4.72) can be used to evaluate $m_k$ by applying the mapping Eq. (4.65) $k$ times. On the other hand, if

$k < 0$, one has to solve the linear system $k$ times with invertible matrix:

$$\begin{bmatrix} \mathbf{I} & \mathbf{0} \\ \mathbf{0} & -\mathbf{I} \end{bmatrix} \begin{bmatrix} A & B \\ B^* & A^* \end{bmatrix}. \tag{4.73}$$

This is exactly what the QFAM solver does when finding the QFAM amplitudes $X_{\mu\nu}(\omega_\gamma), Y_{\mu\nu}(\omega_\gamma)$ for fixed frequency $\omega_\gamma$, i.e. when solving the linear equation (4.16) having only access to the mapping (4.65). In conclusion, if $k \in \mathbb{Z}$ is odd, QFAM solver can use equation (4.72) to efficiently calculate the odd moments $m_k$ directly. We have validated Eq. (4.72) on synthetically generated examples used in Sec. 4.3.1 and on realistic example used in Sec. 4.3.2.

Now we turn to a more difficult case, where $k \in \mathbb{Z}$ is an even integer. Also, we assume that $k \geq 0$. Since all the eigenfrequencies are located in an interval $\langle -\Omega_b, +\Omega_b \rangle$, when inserting the expansion (4.32) into Eq. (4.68), we obtain:

$$m_k = \int_0^{\Omega_b} \omega^k \frac{dB(\omega)}{d\omega} d\omega \approx m_k^{(\text{Chebyshev})} = \Omega_b^k \sum_{n=0}^{2N_{\text{it}}} \mu_n I_n^{(k)}, \tag{4.74}$$

with integrals $I_n^{(k)}$ defined as:

$$I_n^{(k)} = \frac{2}{\pi} \int_0^1 x^k \frac{T_n(x)}{\sqrt{1-x^2}} dx. \tag{4.75}$$

For $x \in [-1, +1]$ and even $k \in \mathbb{N}_0$, the following expression holds:

$$x^k = \frac{1}{2^{k-1}} \sum_{j=0}^{k/2} \frac{1}{1+\delta_{j,0}} \binom{k}{\frac{k}{2}-j} T_j(x). \tag{4.76}$$

Combined with the identity:

$$2T_m(x)T_n(x) = T_{m+n}(x) + T_{|m-n|}(x), \tag{4.77}$$

one can easily calculate:

$$I_n^{(k)} = \sum_{j=0}^{k/2} \frac{1}{1+\delta_{j,0}} \frac{1}{2^k} \binom{k}{\frac{k}{2}-j} \left( \operatorname{sinc}\left(\frac{\pi}{2}(n+j)\right) + \operatorname{sinc}\left(\frac{\pi}{2}|n-j|\right) \right), \tag{4.78}$$

where $\operatorname{sinc}(x) = \sin x / x$. If we precalculate and store the integrals $I_n^{(k)}$, the moment $m_k^{(\text{Chebyshev})}$ for even $k \geq 0$ is, according to Eq. (4.74), given by a simple scalar product of the $(\mu_n)_{n=0}^{2N_{\text{it}}}$ coefficients with the integrals $\left(I_n^{(k)}\right)_{n=0}^{2N_{\text{it}}}$. In the case of even but negative values of $k$, we cannot follow the same procedure of integrating term-by-term in Eq. (4.74) because for negative $k$, the integrals $I_n^{(k)}$ diverge in general. Therefore, because we have the response function evaluated on Chebyshev frequency nodes:

$$\left( \frac{dB(\omega_i)}{d\omega} \right)_{i=1}^{N_e}, \quad \left( \omega_i = \Omega_b \cos\left( \frac{\pi}{N_e} \left( i - \frac{1}{2} \right) \right) \right)_{i=1}^{N_e}, \tag{4.79}$$

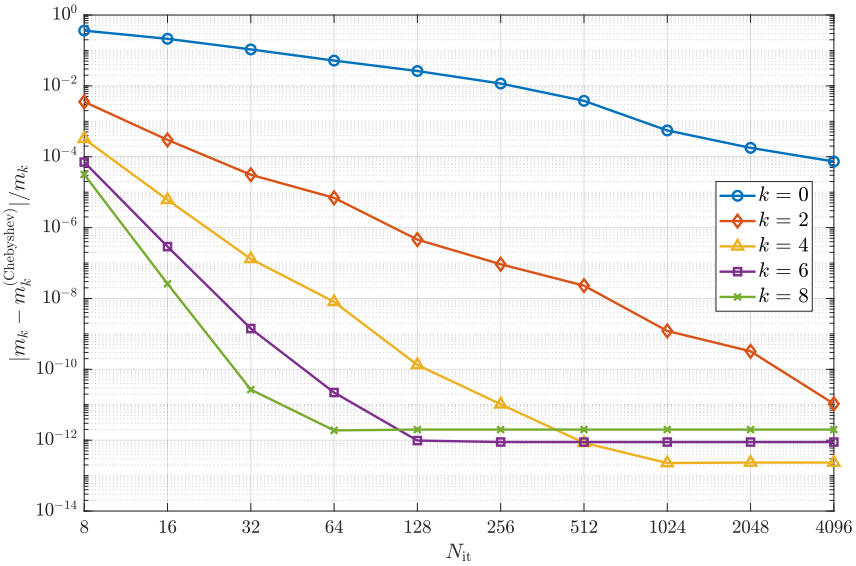


Figure 4.13: Convergence of even $k \geq 0$ moments as number of iterations $N_{\mathrm{it}}$ is increased. For $k = 0$ moment, Jackson kernel is used, while for $k > 0$ moments, Dirichlet kernel is used. Notice the logarithmic scales. Figure taken from Ref. [34].

we can try using the Gauss-Chebyshev integration formula:

$$\int_0^1 f(x)dx \approx \frac{\pi}{n} \sum_{i=\lceil \frac{n+1}{2} \rceil}^{n} f(x_i)\sqrt{1-x_i^2}, \quad x_i = \cos\left(\frac{\pi}{n}\left(i - \frac{1}{2}\right)\right), \tag{4.80}$$

and obtain an approximate value of the moment $m_k$:

$$m_k \approx \frac{\pi}{N_e} \sum_{i=\lceil \frac{N_e+1}{2} \rceil}^{N_e} \omega_i^k \frac{dB(\omega_i)}{d\omega}\sqrt{\Omega_b^2 - \omega_i^2}. \tag{4.81}$$

However, it turns out that this approximation is poor and the method is not suited for calculating the moments with $k < 0$ due to the $\omega^k$ factor that appears in the integrand of Eq. (4.68).

In order to test the method for even $k \geq 0$, we have again generated synthetic QRPA matrices $A$ and $B$ and vectors $F^{20}$ and $F^{02}$, as in Sec. 4.3.1. After experimenting with various kernels, we have found that for the $k = 0$ moment, the best results (in a sense of convergence speed with increasing $N_{\mathrm{it}}$) are obtained with Jackson kernel, while for other even $k > 0$ moments, Dirichlet kernel yields fastest convergence. In Fig. 4.13 we display the difference between the true value of the moment $m_k$, for even $k \geq 0$, and the value calculated by using the KPM as a function of the number of iterations $N_{\mathrm{it}}$. We notice that convergence rate increases with $k$ and for the $k = 0$ moment $m_0$ the convergence rate is very slow.

This behaviour can easily be explained by the structure of the response function Eq. (4.56). The delta functions $\delta(\omega \pm \Omega_i)$ are smeared when approximated by the Chebyshev series and by increasing the number of iterations $N_{\text{it}}$ they become more narrow. For instance, if Lorentz kernel is used, the smearing is given by $\gamma_{\text{KPM}}$ in Eq. (4.59). For small QRPA eigenfrequencies and insufficient number of iterations (i.e. too large smearing), approximations of delta functions are smeared outside the integration interval Eq. (4.68). This problem is less pronounced for $k > 0$ because the $\omega^k$ factor reduces the value of the integrand for small values of $\omega$. Hence, the convergence will be faster for larger $k$ values and very slow for $k = 0$, in accordance with results shown in Fig. 4.13.

We have also verified that moments are calculated correctly if realistic RPA matrices $A$ and $B$ and vectors $F^{20}, F^{02}$, generated by the `skyrme_rpa` code, are used.

In this section we have shown how to efficiently calculate the moments of the response function $m_k$ for $k \geq -1$. We notice that we could generalize our approach, e.g. to calculate the integrals that include product of the Fermi integral function $f_{FI}(E)$ and the response function, appearing in the beta-decay rates formulas:

$$\lambda = \frac{\ln 2}{\kappa} \int_0^{+\infty} f_{FI}(\omega) \frac{dB(\omega)}{d\omega} d\omega = \frac{\ln 2}{\kappa} \sum_{i=1}^{N_p} f_{FI}(\Omega_i) |\langle i|\hat{F}|0\rangle|^2. \tag{4.82}$$

The only difference is that instead of the integrals $I_n^{(k)}$ in Eq. (4.75), we would calculate:

$$\frac{2}{\pi} \int_0^1 f_{FI}\left(\Omega_b x\right) \frac{T_n(x)}{\sqrt{1-x^2}} dx. \tag{4.83}$$

Because the Fermi integral function $f_{FI}(E)$ in the low-energy region is relatively small, we expect fast convergence in the same way we obtained fast convergence for even $k > 0$ moments. Approach using the contour integration of the QFAM strength function has already been applied on beta-decay rates calculations [62] and it would be interesting to compare the efficiency of the two approaches on realistic examples.

## 4.4 Summary and outlook

In this paper we have proposed an implementation of the kernel polynomial method, already successfully employed in the solid state physics [55, 64], adapted for efficient calculation of the QRPA response function. The method is based on the expansion of the QRPA response function in an orthonormal basis of Chebyshev polynomials thus reducing the problem to the evaluation of the expansion coefficients. In practical calculations the expansion has to be truncated and because the QRPA response function is essentially a sum of weighted delta functions one encounters the problem of Gibbs oscillations. Standard procedure to damp the Gibbs oscillations and improve the precision of the Chebyshev series expansion is to convolute the response function with various damping kernels, e.g. Jackson or Lorentz kernel.

The proposed implementation of the KPM has been benchmarked and tested by comparing the QRPA response function with the one calculated by direct di-

agonalization of the QRPA matrices or by solving the QFAM equations. Our results demonstrate that the KPM can reproduce the QRPA and QFAM results to a high numerical accuracy. However, the efficiency of implementing the KPM depends significantly on the range of the eigenvalues of the QRPA matrix, i.e., broad range of eigenvalues requires a large number of iterations within the KPM implementation. In the following, we list the main advantages and drawbacks of implementing the KPM in calculating the QRPA response function.

Advantages of the KPM include:

- The KPM provides the response function on the entire frequency interval $\langle -\Omega_b, +\Omega_b \rangle$[4] compared to QFAM which calculates the response for a discrete set of frequencies.
- If one performs QFAM calculation with very small value of smearing width $\gamma$ and frequency $\omega$ close to the pole, the linear system (4.1) is ill-conditioned requiring a large number of iterations to be solved, e.g. by the Broyden method which is often used for that purpose in QFAM solvers. The proposed implementation of the KPM circumvents this problem.
- The KPM can be implemented into any available QFAM solver with minimum programming effort.
- If the bounding frequency $\Omega_b$ is small, i.e. if the eigenfrequencies $\Omega_i$ are bounded in a relatively small interval, the method can locate the QRPA poles with large transition strength much quicker in comparison to the QFAM approach which can be crucial for many applications.
- The resolution of the standard QFAM calculation is determined by the smearing $\gamma$, i.e., in order to increase the resolution of the response one has to repeat the entire calculation with smaller value of $\gamma$. On the contrary, the Chebyshev KPM approach requires only larger number of iterations $N_{\mathrm{it}}$ to obtain a response function with better resolution in terms of smearing $\gamma_{\mathrm{KPM}}$ and there is no need to repeat the entire calculation.

Drawbacks of the KPM include:

- Appearance of the Gibbs oscillations. This problem can be addressed by introducing damping kernel, e.g. Lorentz kernel. The damping is controlled by the $\lambda$ parameter in Eq. (4.44) with large values (e.g. $\lambda \approx 5$) leading to negligible effects of the Gibbs oscillations. However, according to Eq. (4.59), increasing the value of the $\lambda$ parameter requires larger number of iterations $N_{\mathrm{it}}$ in order to obtain targeted resolution $\gamma_{\mathrm{KPM}}$. Hence, one has to choose a value of the $\lambda$ parameter that presents a satisfactory compromise between sufficient damping of Gibbs oscillations and convergence speed in terms of resolution $\gamma_{\mathrm{KPM}}$.
- If the poles of the response function $\Omega_i$ are distributed across large energy region, i.e. if the bounding frequency $\Omega_b$ has to be relatively large in order to include all the poles in the interval $\langle -\Omega_b, +\Omega_b \rangle$, the KPM requires a large number of iterations $N_{\mathrm{it}}$ in order to produce a satisfactory resolution $\gamma_{\mathrm{KPM}}$.

[4] Once we calculate the coefficients in the Chebyshev expansion, we can easily evaluate the approximation of the response function for any given frequency.

- The KPM cannot be used to calculate the response function in a localized energy region of interest (e.g. low-energy region up to 20 MeV), but rather globally on the entire $\langle -\Omega_b, +\Omega_b \rangle$ interval.
- The KPM can not be parallelized since recursion (4.36) operates sequentially. On the contrary, QFAM calculation can be easily parallelized because the response for each frequency is calculated independently.
- The KPM calculation diverges in the presence of the imaginary QRPA eigenfrequency, thus it should be applied only if the ground state corresponds to the HFB minimum.

Overall, the KPM is better suited for models based on the nonrelativistic EDFs because in models based on relativistic EDFs the appearance of the Dirac sea necessitates large values of the bounding frequency. When applied to the models based on the nonrelativistic EDFs, we believe that the method can significantly speed up the process of finding the response function with high resolution in terms of smearing.

# Chapter 5

# Low-energy cluster modes in $N = Z$ nuclei

Significant transition strength in light $\alpha$-conjugate nuclei at low energy, typically below 10 MeV, has been observed in many experiments. In this Chapter, we follow Ref. [65] and explore the isoscalar low-energy response of $N = Z$ nuclei. Depending on the multipolarity of the excitation and the equilibrium deformation of a particular isotope, the low-energy QRPA strength functions display prominent peaks attributed to cluster mode structures: $\alpha + {}^{12}\mathrm{C} + \alpha$ and $\alpha + {}^{16}\mathrm{O}$ in ${}^{20}\mathrm{Ne}$, ${}^{12}\mathrm{C} + {}^{12}\mathrm{C}$ in ${}^{24}\mathrm{Mg}$. Such cluster modes are favored in light nuclei with large deformation.

## 5.1 Background

A number of experiments have observed a significant increase of the $E0$ strength at excitation energies below the giant monopole resonance in relatively light nuclei [66, 67, 68, 69, 70, 71]. Theoretical studies using, e.g., the cluster model [72, 73, 74, 75, 76, 77, 78, 79, 80], or the antisymmetrized molecular dynamics (generally combined with generator coordinate method (GCM)) [81, 82, 83, 84, 85], consistently interpret these observations as excitations of cluster structures. Cluster excitations can also occur with higher multipoles [68, 86, 87, 88, 89]. For instance, a low-energy $E1$ excitation has been associated with a reflection-asymmetric vibration of an $\alpha$ cluster against the ${}^{16}\mathrm{O}$ core in ${}^{20}\mathrm{Ne}$ [80, 83], with a strength that is enhanced in comparison to similar excitations contributing in the $E0$ and $E2$ response.

Valuable information about the structure of a nucleus can be obtained by analyzing how the system responds to an external perturbation with a given multipolarity (see, for instance, [90, 91]). A useful theoretical framework for such studies is provided by RPA and the QRPA which extends the former to superfluid systems. QRPA calculations on top of reference mean-field states computed using EDF, have demonstrated the capacity to describe excitation modes ranging from tens of keV to tens of MeV [92, 93]. The method has also been extended to charge-exchange modes [94, 95, 96].

QFAM as a method for solving QRPA problem has been implemented for Skyrme interactions and relativistic functionals [97, 98]. The Skyrme-based FAM has been applied to photoabsorption cross sections [99], higher multipole excita-

tion modes [100], giant dipole resonances in heavy nuclei [101], and $\beta$-decay studies [102]. Relativistic EDFs have successfully been used to describe both liquid and cluster-like nuclear properties [103, 104, 105], starting from nucleonic degrees of freedom. Recently the multireference implementation of the GCM based on relativistic EDFs has been employed in the analysis of spectroscopic properties (energies of excited states, elastic and inelastic form factors) of nuclei with cluster structures [106, 107]. A QFAM approach based on relativistic EDF is hence expected to provide an alternative consistent and microscopic description of cluster modes in nuclei.

Here we perform a systematic calculation of isoscalar multipole ($J = 0, 1, 2, 3$) strength in $\alpha$-conjugate nuclei from $^{12}$C to $^{32}$S, and analyze the low-energy structure of the strength functions. The calculations are based on the DD-PC1 parametrization. The first nucleus to be analyzed is $^{20}$Ne whose large equilibrium deformation favors clusterization, and hence cluster modes are expected to occur at low energy [16]. It will be shown that the lowest modes correspond to reflection-symmetric $\alpha - {}^{12}\mathrm{C} - \alpha$ and reflection-asymmetric $\alpha - {}^{16}\mathrm{O}$ configurations oscillating around the axially symmetric deformed equilibrium. The study of $^{20}$Ne is extended to other $\alpha$-conjugate nuclei, and the evolution of the strength function is analyzed when the quadrupole moment deformation $\beta$ of the mean-field reference state is varied from oblate $\beta < 0$ to prolate $\beta > 0$ deformations.

## 5.2 Isoscalar vibrations in $^{20}$Ne

### 5.2.1 Ground state and convergence

We begin our analysis with the isotope $^{20}$Ne. The left panel of Fig. 5.1 displays the prolate deformed $\beta = 0.525$ ground-state intrinsic density of $^{20}$Ne obtained obtained with the DD-PC1 parametrization. The density exhibits cluster structures at the outer ends of the symmetry axis with density peaks of 0.2 fm$^{-3}$, and an oblate deformed core, reminiscent of a quasimolecular $\alpha - {}^{12}\mathrm{C} - \alpha$ structure. The spatial localization and cluster formation in atomic nuclei can also be quantified by using the localization function $\mathcal{C}(\boldsymbol{r})$, defined in Section 3.1.6. Recall that a value of the localization measure close to 0.5 signals that nucleons are delocalized, while a value close to one corresponds to a localized $\alpha$-like structure at point $\boldsymbol{r}$ in an even-even $N = Z$ nucleus. The localization function for $^{20}$Ne is plotted in the right panel of Fig. 5.1, and consistently confirms the $\alpha$-like nature of the localized structures appearing in the density. Although the normalization of the localization function is to a certain extent arbitrary [108, 109], there are several methods that address this issue. Because of the kinetic term, the localization function usually exhibits a larger spatial extension compared to the density, especially for lighter nuclei. To enable a more direct comparison, the spatial extension of the localization function is here rescaled to that of the corresponding intrinsic density.

The isoscalar strength function of the monopole operator $\sum_{i=1}^{A} |\boldsymbol{r}_i|^2$ for $^{20}$Ne is analyzed using the `DIRQFAM` solver. The calculation has been performed in the harmonic oscillator basis with $N_{\mathrm{shells}} = 10, 12, 14, 16$ and 18 oscillator shells. In Fig. 5.2 we compare the strength functions of the isoscalar monopole operator for $^{20}$Ne, calculated with increasing $N_{\mathrm{shells}}$ from 12 to 18. The low-energy part

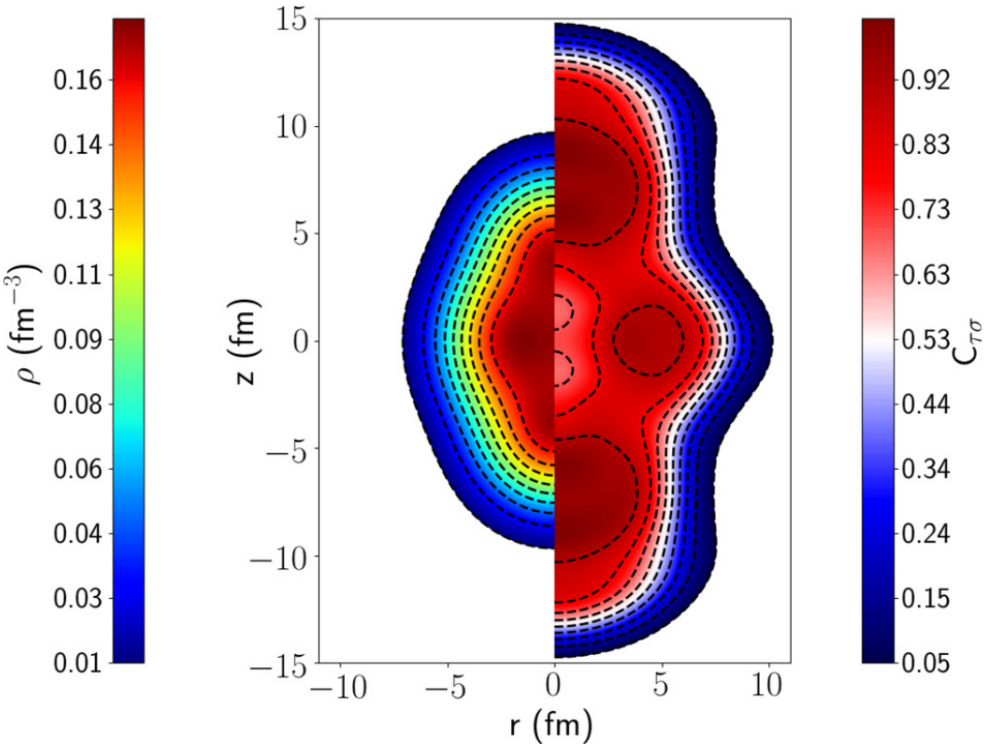


Figure 5.1: The self-consistent equilibrium density of $^{20}$Ne (left panel) and localication function $\mathcal{C}(\boldsymbol{r})$ (right panel) obtained using the RHB model with the DD-PC1 parameterization of the EDF. Figure taken from Ref. [65].

of the strength function is fully converged even for relatively small values of the $N_{\text{shells}}$. However, for higher energies, the strength function displays a pronounced dependence on the dimension of the harmonic oscillator basis, essentially because these excitations involve states in the continuum. Therefore, the high-energy part of the strength function is strongly affected by the details of single-particle configurations. We note, however, that the centroids of the strength distribution in the high energy region are much less sensitive to the basis dimension, as shown in Table 5.1. Since this study is focused on the properties of low-lying states, all subsequent calculations are performed by using $N_{\text{shells}} = 14$ oscillator shells.

Table 5.1: Centroids of the monopole strength function (see. Fig. 5.2) defined as the ratio of moments $m_1/m_0$. The moments of the strength function are $m_k = \int E^k S(E) dE$. The $\bar{E}_{\text{low}}$ and $\bar{E}_{\text{high}}$ centroids are calculated in the energy intervals 10 MeV $\leq E \leq$ 22.5 MeV and 22.5 MeV $\leq E \leq$ 35 MeV.

| $N_{\text{shells}}$ | $\bar{E}_{\text{low}}$ | $\bar{E}_{\text{high}}$ |
|---|---|---|
| 10 | 18.4 | 27.0 |
| 12 | 18.1 | 27.0 |
| 14 | 18.1 | 27.3 |
| 16 | 18.0 | 27.6 |
| 18 | 18.1 | 28.0 |

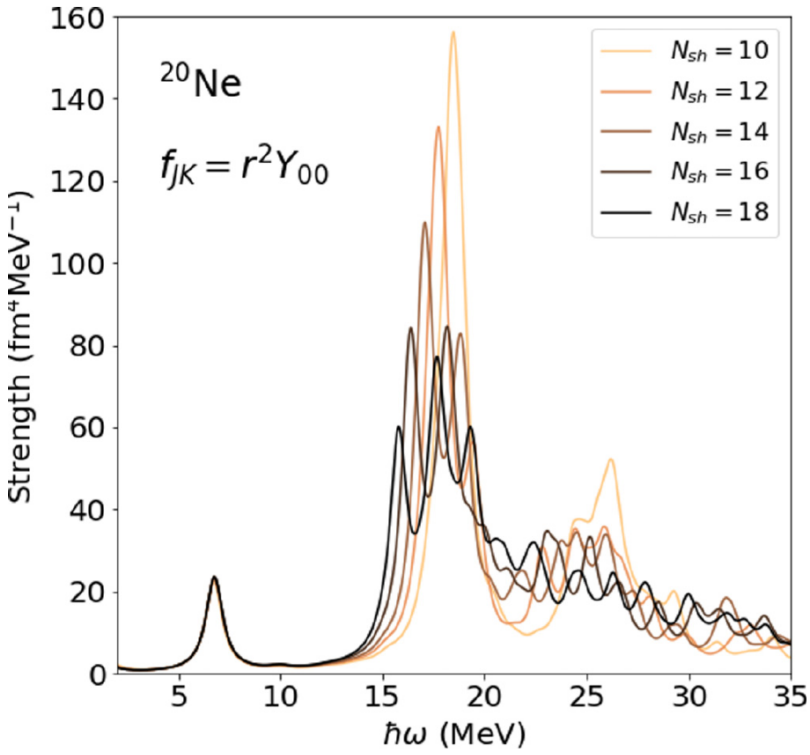


Figure 5.2: Evolution of the monopole strength function in $^{20}$Ne with the size of the harmonic oscillator basis. Figure taken from Ref. [65].

### 5.2.2 Isoscalar response and density vibrations

Figure 5.3 displays the strength functions for the QFAM response to the isoscalar monopole [panel (a)], isoscalar dipole [panel (b)], isoscalar quadrupole [panel (c)], and isoscalar octupole [panel (d)] operator. In addition to the $K = 0$ components, for the multipoles $J = 1, 2, 3$ we also plot the contributions of the higher-$K$ projections separately, as well as the total strengths. For the quadrupole $K = 1^+$ strength distribution one notices the appearance of the spurious state related to the breaking of rotational symmetry, and also the ordering of the $K = 0^+, K = 1^+, K = 2^+$ peaks in the high energy region above 15 MeV is consistent with the prolate deformed ground state of $^{20}$Ne. Although all strength distributions exhibit pronounced fragmentation in the $E \geq 10$ MeV region, a sizable portion of strength is located at $E \approx 7$ MeV. We have verified that for all multipoles these low-energy peaks are stable with respect to the number of oscillator shells used in the basis expansion.

The nature of the low-energy excitations can be analyzed by considering the corresponding transitions densities. Recall the time-dependent density (see Eq. (3.98)) reads:

$$\rho_v(\boldsymbol{r}, t) = \rho_v^0(z, r_\perp) + 2\eta \mathrm{Re}\left[e^{-\mathrm{i}\omega t}\delta\rho_v(z, r_\perp, \omega)\right] \cos K\varphi, \tag{5.1}$$

where $\rho_v^0(z, r_\perp)$ denotes the axially symmetric ground-state density and $\delta\rho_v(z, r_\perp, \omega)$ is the transition density at a given excitation energy $\omega$. Recall that $\eta$ corresponds to the small parameter used in the QFAM linearization (see Eq. (2.68)). We note that for the $K = 0$ modes, the time-dependent densities are axially symmetric

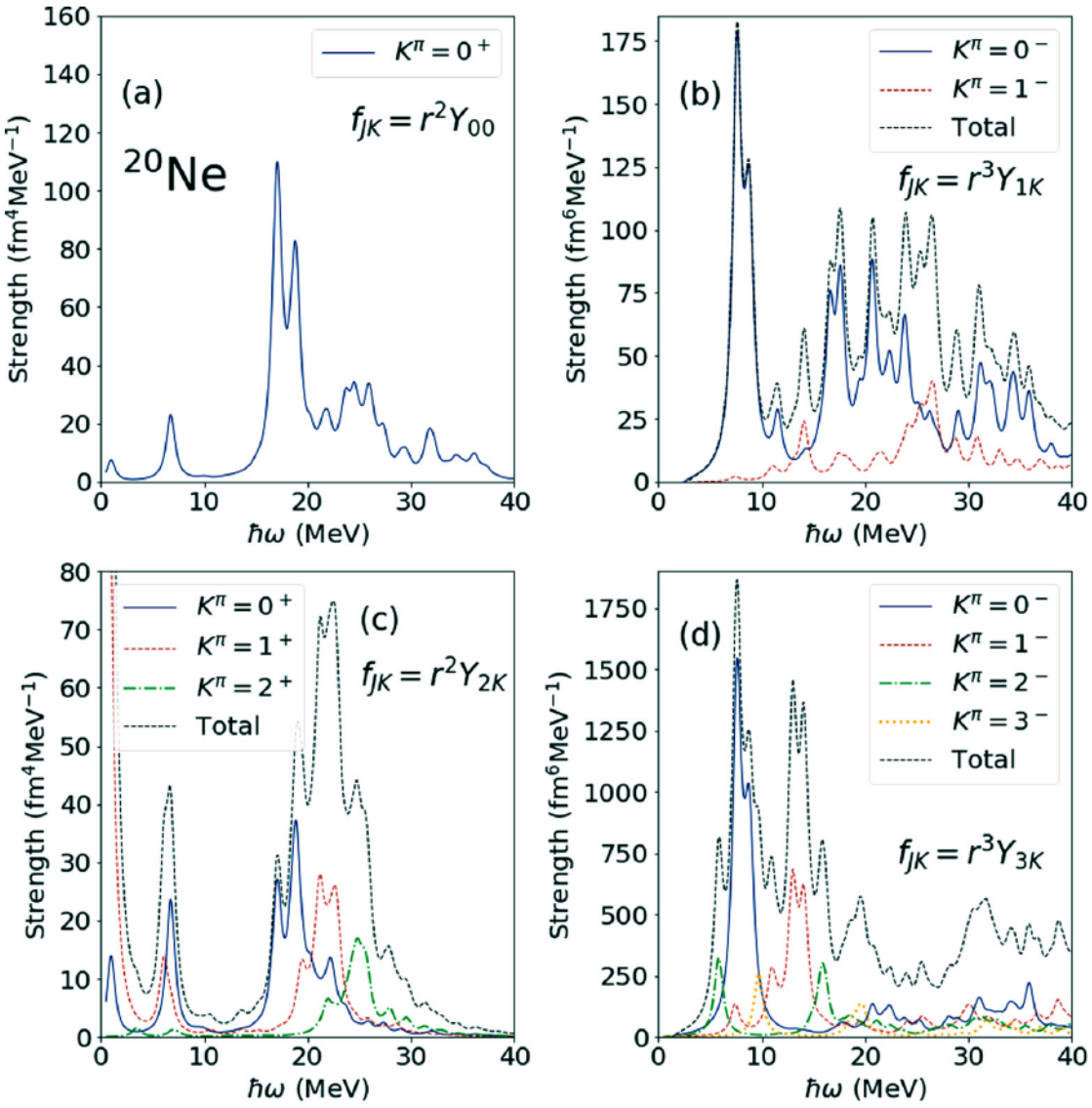


Figure 5.3: $^{20}$Ne strength distribution functions for the QFAM response to the isoscalar monopole (a), isoscalar dipole (b), isoscalar quadrupole (c), and isoscalar octupole (d) operator. For $J > 0$ multipoles, the corresponding $K = 0$ (solid blue), $K = 1$ (dashed red), $K = 2$ (dot-dashed green), and $K = 3$ (dotted orange) are potted separately. The thin dashed curves denote the total strength. Figure taken from Ref. [65].

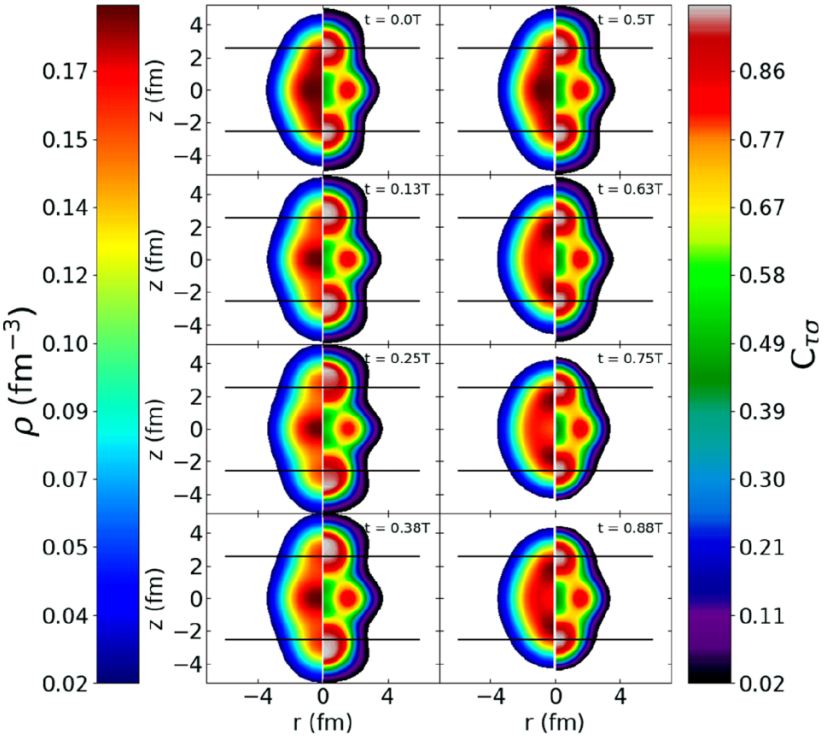


Figure 5.4: Snapshots of the $^{20}$Ne density and localization function at energy $\omega = 6.75$ MeV induced by monopole perturbation. Time increases from top to bottom. The horizontal black lines represent the position of the center of mass of the cluster in the ground state. Figure taken from Ref. [65].

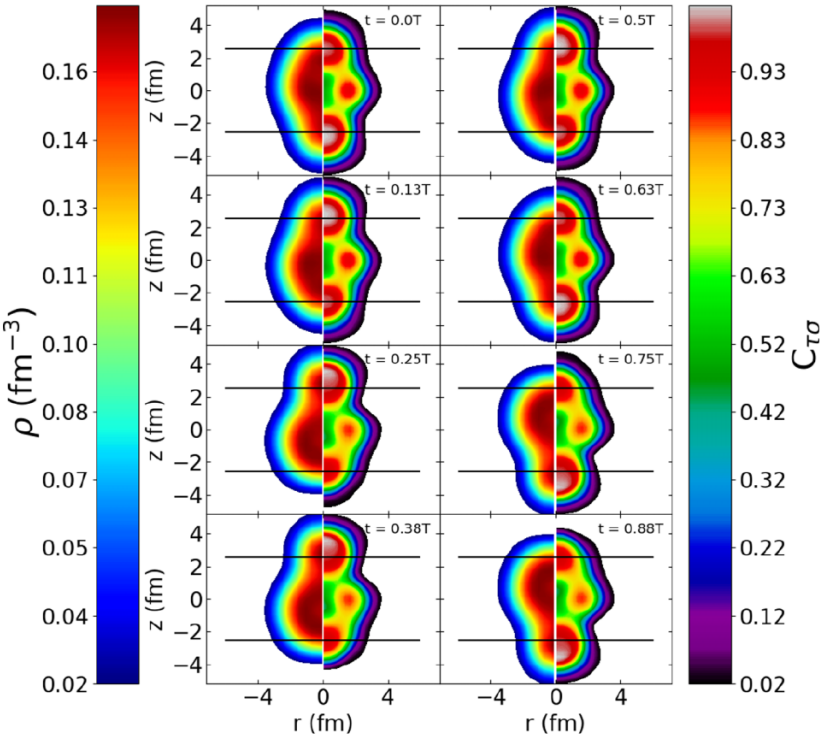


Figure 5.5: Same as Fig. 5.4 but for the octupole perturbation ($K = 0$ component) at energy $\omega = 7.65$ MeV. Figure taken from Ref. [65].

$\rho_v(\boldsymbol{r},t) = \rho_v(z,r_\perp,t)$, hence it is sufficient to study their behavior in the $xz$ plane. Figures 5.4 and 5.4 display the snapshots of the time-dependent density in the $xz$ plane for the low-energy modes induced by monopole and octupole ($K=0$) component. Time increases from the top to the bottom, with the time step $\Delta t = T/4$, where $T = 2\pi/\omega$ is the period of oscillations. For visualization purposes, the parameter $\eta$ equals 0.05 for the monopole and 0.005 for the octupole perturbation, respectively. The large value of the intrinsic equilibrium deformation of $^{20}$Ne leads to cluster formation already in its ground state, and one finds that clusters present at the initial time step move towards the center where they are diluted with respect to the core density, before being reformed as a cluster for both modes shown in Figs. 5.4 and 5.5. Furthermore, two different types of modes are observed: i) the two $\alpha$ clusters against the $^{12}$C core for the $J=0$ reflection-symmetric mode, ii) an $\alpha$ cluster oscillates against the $^{16}$O core for the $J=3$ reflection-asymmetric mode. To make these modes more explicit and emphasize the cluster aspect of the excitation, recall the time dependant localization [108] function computed using the QFAM approach (see Eq. (3.77)):

$$\mathcal{C}(\boldsymbol{r},t) = \mathcal{C}^0(z,r_\perp) + 2\eta\,\mathrm{Re}\left[e^{-\mathrm{i}\omega t}\delta\mathcal{C}(z,r_\perp,\omega)\right]\cos K\varphi + \mathcal{O}(\eta^2), \tag{5.2}$$

where $\mathcal{C}^0(z,r_\perp)$ denotes the ground state localization function shown in Fig. 5.1 for $^{20}$Ne and $\delta\mathcal{C}(z,r_\perp,\omega)$ the transition localization. The snapshots of the localization are plotted on the right hand-side of each panel of Figs. 5.4 and 5.5. For the monopole excitation illustrated in Fig. 5.4, the two $\alpha$-like structures, characterized by a value of the localization close to one, are clearly concentrated at the poles, and one follows their oscillations against the core. In the case of octupole vibrations shown in Fig. 5.5, only one $\alpha$-like cluster [white area with $\mathcal{C}(\boldsymbol{r},t) \approx 1$] can be traced during the oscillation period. In general, however, this excitation will also contain isoscalar dipole admixtures.

The two-dimensional intrinsic transition densities $\delta\rho(z,r_\perp,\omega)$ can be projected onto good angular momentum to yield the transition densities in the laboratory frame of reference. For a particular value of the angular momentum $J \geq K$, the two-dimensional projected transition density can be approximated using its radial part by:

$$\delta\rho^J_{\mathrm{tr}}(\boldsymbol{r}) = \delta\rho^J_{\mathrm{tr}}(r)Y_{J,K}(\Omega), \tag{5.3}$$

with the radial part defined as:

$$\delta\rho^J_{\mathrm{tr}}(r) = \int d\Omega\delta\rho(z,r_\perp,\omega)Y^*_{J,K}(\Omega). \tag{5.4}$$

Figure 5.6 compares the radial parts of the angular-momentum-projected transition densities $\delta\rho^{J=0}_{\mathrm{tr}}(r)$, $\delta\rho^{J=2}_{\mathrm{tr}}(r)$ and $\delta\rho^{J=4}_{\mathrm{tr}}(r)$ that correspond the the low-energy peak of the isoscalar monopole response in $^{20}$Ne. The real and imaginary parts of the transition density are displayed in the left and right panels, respectively. For the real parts we note the characteristic node of the transition density close to the position of the rms radius. The radial parts of the angular-momentum-projected transition densities $\delta\rho^{J=1}_{\mathrm{tr}}(r)$, $\delta\rho^{J=3}_{\mathrm{tr}}(r)$ and $\delta\rho^{J=5}_{\mathrm{tr}}(r)$ that correspond the the low-energy peak of the isoscalar octupole response are shown in Fig. 5.7. In contrast to the volume monopole mode, the isoscalar octupole transition densities exhibit the predominantly surface nature of the octupole mode.

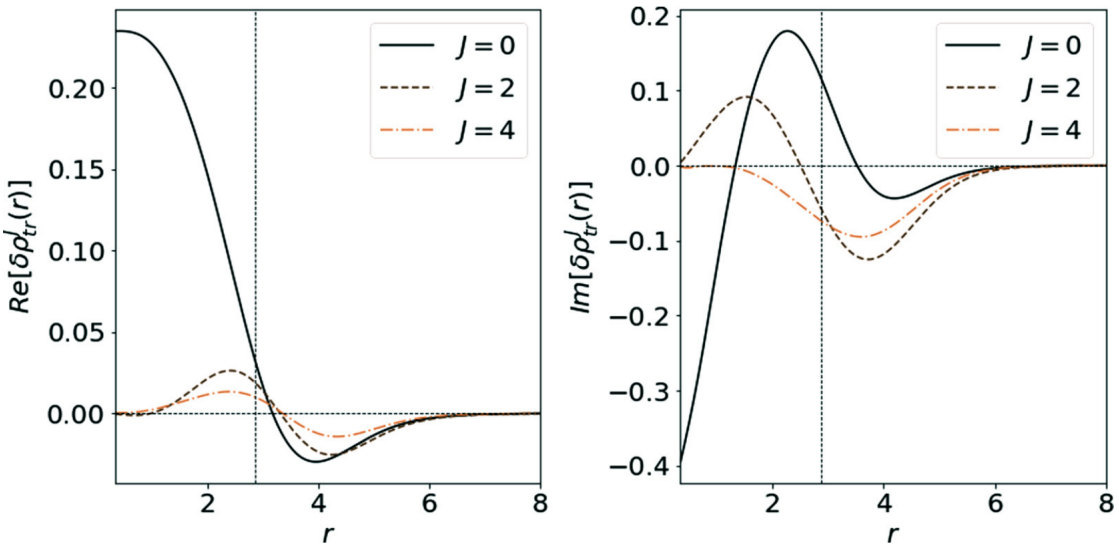


Figure 5.6: Radial parts of the angular-momentum projected transition densities that correspond to the low-energy peak of the isoscalar monopole response of $^{20}$Ne. The real and imaginary parts of the transition density are shown in the left and right panels, respectively. The ground state rms radius is indicated by the vertical dashed line. Figure taken from Ref. [65].

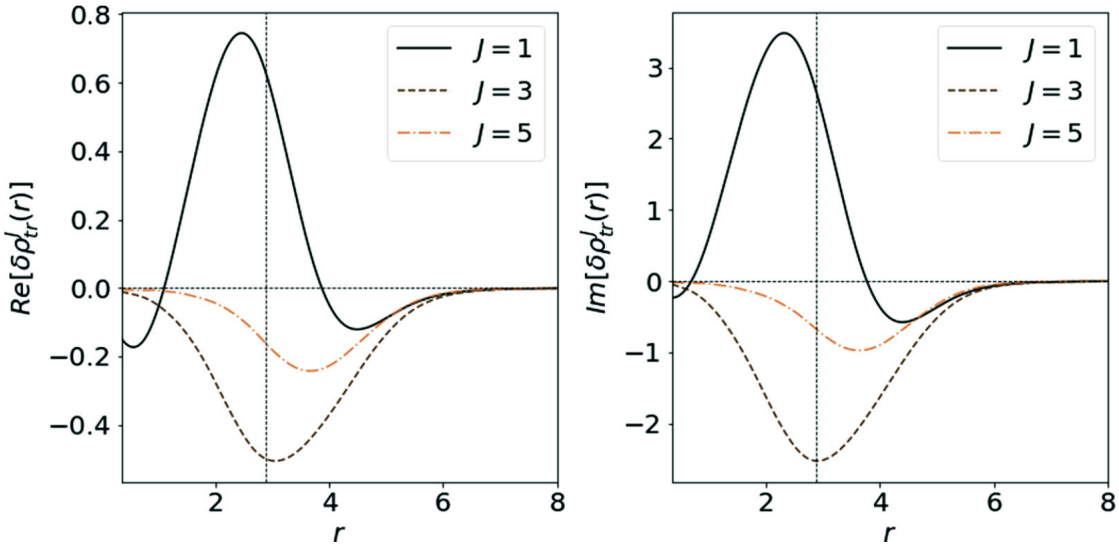


Figure 5.7: Same as Fig. 5.6 but for the isoscalar octupole response ($K = 0$ component). Figure taken from Ref. [65].

### 5.2.3 Two-quasiparticle contributions

It is instructive to decompose the excitation modes in terms of two-quasiparticle (2-*qp*) contributions [110]. This can be achieved by using the contour integration procedure introduced in Section 3.1.7. Recall that the individual QRPA eigenamplitudes $X^i_{\mu\nu}$ and $Y^i_{\mu\nu}$ corresponding to the excitation mode with QRPA eigenfrequency $\Omega_i$ are calculated as:

$$X^i_{\mu\nu} = e^{-\mathrm{i}\theta_i}|\langle i|\hat{F}|0\rangle|^{-1}\frac{1}{2\pi\mathrm{i}}\oint_{C_i} X_{\mu\nu}(\omega_\gamma)d\omega_\gamma, \tag{5.5}$$

$$Y^i_{\mu\nu} = e^{-\mathrm{i}\theta_i}|\langle i|\hat{F}|0\rangle|^{-1}\frac{1}{2\pi\mathrm{i}}\oint_{C_i} Y_{\mu\nu}(\omega_\gamma)d\omega_\gamma, \tag{5.6}$$

where $C_i$ is the contour in the complex energy plane that encloses the first-order pole on the real axis at $\omega_\gamma = \Omega_i$. We note that the common phase $e^{\mathrm{i}\theta_i}$ remains arbitrary. The individual 2-*qp* contributions to some particular excitation mode $i$ can be quantified by the following quantity:

$$\xi^i_{2qp} = |X^i_{2qp}|^2 - |Y^i_{2qp}|^2. \tag{5.7}$$

The difference in previous norm originates from QRPA natural metrics given by matrix $\begin{bmatrix} I & 0 \\ 0 & -I \end{bmatrix}$.

Figure 5.8 displays in a schematic way the most important neutron 2-*qp* contributions to the isoscalar monopole excitation at energy $\omega = 6.7$ MeV. The single-particle levels correspond to the diagonal matrix elements of the single-particle Hamiltonian in the canonical basis, and the occupation numbers are the eigenvalues of the density matrix. We have obtained almost identical results for the proton contributions. Obviously this excitation is only very weakly collective with just a few relevant 2-*qp* contributions. Among them, by far the most significant is the transition from the almost fully occupied $1/2^+$ state that originates from the spherical $1d_{5/2}$ shell, to the unoccupied $1/2^+$ state based on the spherical $2s_{1/2}$ shell. Such a 2-*qp* excitation can be considered in the context of spontaneous breaking of rotational symmetry which captures in an economic way nontrivial correlations as the source of collective behavior of the nucleus. This spontaneous breaking of rotational symmetry leads to the appearance of new excitation modes commonly referred to as a density wave [111]. Density waves are related to the variation of the modulus of the order parameter of the broken symmetry.

### 5.2.4 Deformation effects

Large deformations favor the formation of clusters [112, 113] and the previous discussion also suggests that there is a close link between cluster modes and nuclear deformation. The evolution of the low-energy cluster modes with deformation can be studied in more detail by performing a deformation-constrained calculation. In Fig. 5.9 we display the isoscalar monopole strength in $^{20}$Ne for several values of the axial quadrupole constraint, from $\beta = 0.275$ to $\beta = 0.625$. The dashed curve ($\beta = 0.525$) corresponds to the strength distribution built on top of the mean-field equilibrium deformation. Significant strength in the region $\omega \approx 5 - 7$ MeV begins

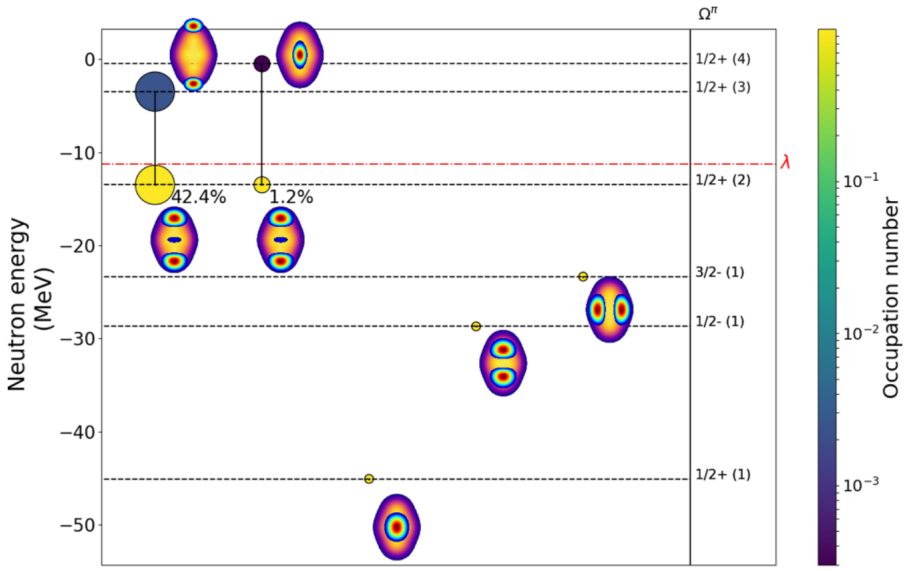


Figure 5.8: Schematic illustration of the most important neutron 2-$qp$ contributions to the isoscalar monopole excitation at energy $\omega = 6.7$ MeV in $^{20}$Ne. The area and the number below represent the fraction of the total $\xi^i_{2qp}$ (see Eq. (5.7)) for this particular excitation. The $\Omega^\pi$ quantum numbers are listed on the right of the figure. The associated partial densities are also plotted for each of the configurations as well as the total density in the background. The Fermi level is shown as a red dash-dotted line. Occupation number of each state is color coded, notice the logarithmic scale. Figure taken from Ref. [65].

to appear at $\beta \approx 0.2$ and, with increasing deformation, the fragmented strength evolves towards a single peak at slightly higher energy.

The appearance of cluster modes can be related to the structure of single-nucleon levels in the canonical basis. In the upper panel of Fig. 5.10 we display the two largest neutron 2-$qp$ contributions to the low-lying cluster mode at the energy corresponding to a given constrained deformation (see also caption to Fig. 5.8). The lower panels show the evolution of the single-particle energies and occupation probabilities in the canonical basis. As the deformation increases the $1d_{5/2}$ spherical shell splits into three levels: $1/2^+$ , $3/2^+$ , and $5/2^+$. In particular, the occupation probability for the $1/2^+$ level increases with deformation thus enabling hole-particle excitations to the $1/2^+$ states originating from the spherical $2s_{1/2}$ and $1d_{3/2}$ shells. We note that the occupation of the $1/2^+$ level based on the $1d_{5/2}$ spherical shell is, of course, also responsible for the formation of clusters in the ground state of $^{20}$Ne. As shown in Fig. 5.10, the lowest deformation for which the low-energy monopole excitation is obtained is $\beta \approx 0.2$, which coincides with the intersection of the $1/2^+[400]$ level and the Fermi level. A further increase of deformation between $\beta = 0.4$ and $\beta = 0.5$ leads to a rearrangement of the contribution of the levels $1/2^+[110]$ and $1/2^+[301]$ to the QFAM transition strength. The contribution of these levels to the total strength increases from 25% to more than 40%.

The very low-energy excitation at $\omega \approx 2$ MeV (see Fig. 5.3) can also be understood from the $1d_{5/2}$ splitting. It turns out that this excitation can be attributed to a pure pairing effect due to the partial filling of the $1/2^+[400]$ and

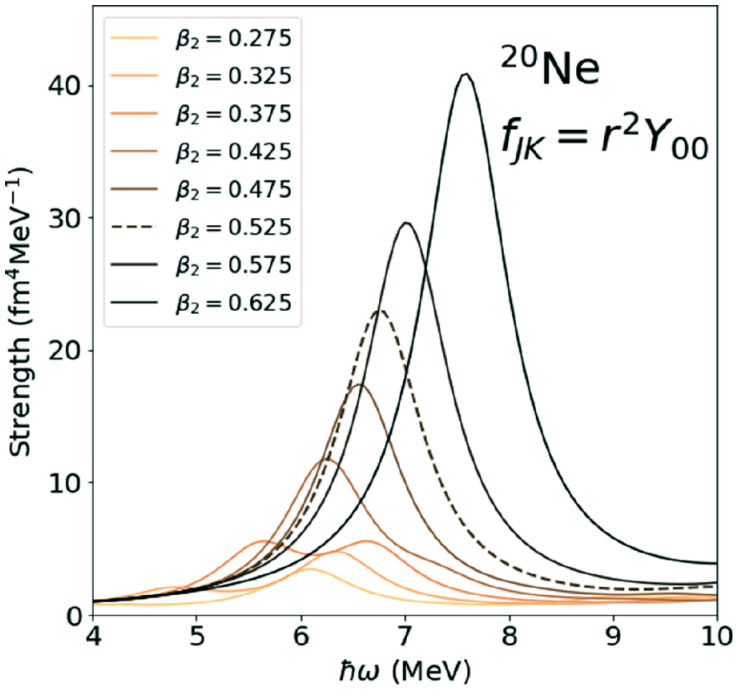


Figure 5.9: The low-energy isoscalar monopole strength distribution in $^{20}$Ne isotope. The QFAM response is calculated for several constrained values of the axial quadrupole deformation $\beta$, and the dashed curve corresponds to the equilibrium deformation $\beta = 0.525$. Figure taken from Ref. [65].

$3/2^+[301]$ levels. They are competing between $\beta = 0$ and $\beta = 0.5$, at which deformation the $1/2^+[400]$ becomes fully occupied. Between these deformations, and because these levels are very close to the Fermi energy, pairing excitations can occur, depending on the pairing gap as well as the quasiparticle energies.

## 5.3 Monopole response of $^{24}$Mg, $^{28}$Si and $^{32}$S

In this section we extend the analysis of low-lying isoscalar monopole QFAM response to $^{24}$Mg, $^{28}$Si and $^{32}$S. Figure 5.11 displays the corresponding isoscalar monopole strength functions for several values of the axial quadrupole constraint $\beta$. One notices the appearance of the low-energy and large prolate deformation peak of the strength distribution for all isotopes shown in Fig. 5.11, similar to the results obtained for $^{20}$Ne in the previous section. We have also performed corresponding calculations for other light and medium-heavy $N = Z$ nuclei, from $^{12}$C to $^{56}$Ni. The appearance of low-energy strength is much less pronounced for isotopes in the vicinity of doubly closed shells.

The structure of the strength distributions can be analyzed by considering the principal 2-*qp* contributions, displayed in Fig. 5.12. We have selected several low-energy peaks in $^{24}$Mg, $^{28}$Si, and $^{32}$S, and the results again indicate that these low-energy excitations are primarily determined by a single 2-*qp* excitation. In $^{24}$Mg we obtain two peaks, one at $\approx$ 7 MeV and a second one at $\approx$ 10 MeV, that have already been observed in experiment [114]. Similar to the case of $^{20}$Ne, the lower state in $^{24}$Mg (first column of Fig. 5.12) is mainly determined by the

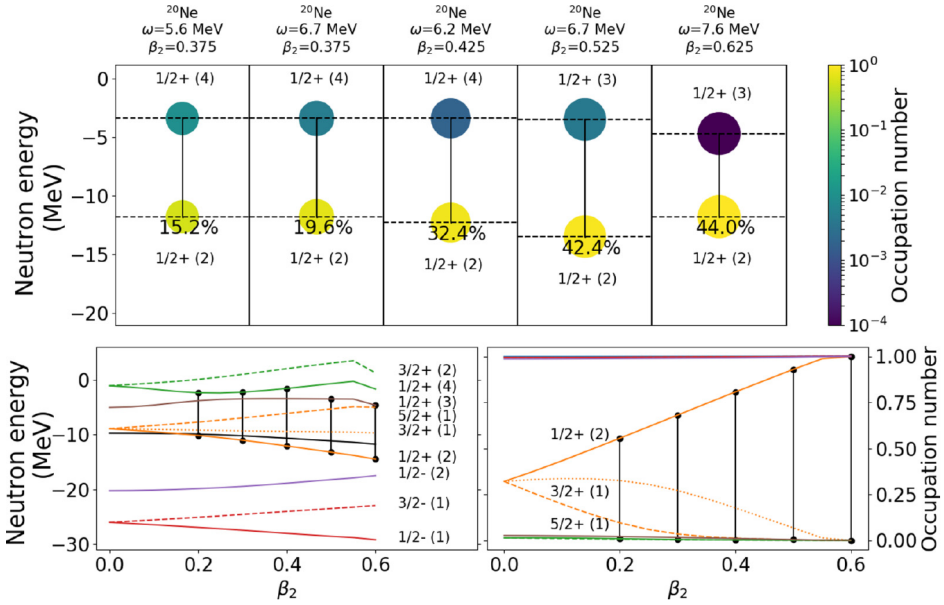


Figure 5.10: Evolution of the leading neutron 2-*qp* contributions to the low-energy monopole mode with constrained deformation (upper panel). The lower panel shows the evolution of the single-particle energies (left) and occupation number (right) in the canonical basis with deformation. The vertical black lines denote the transitions that correspond to the prinicipal 2-*qp* contribution shown in the upper panel. The thick black curve denotes the Fermi level. Figure taken from Ref. [65].

transition between the $1/2^+$ states originating from the $1d_{5/2}$ spherical shell (hole-like) and $2s_{1/2}$ spherical shell (particle-like). The addition of two neutron and two protons leads to the appearance of the second mode at excitation energy $\omega = 10.03$ MeV (second column of Fig. 5.12). This excitation, involving two large clusters ($^{12}$C + $^{12}$C), is determined by the transition between the $3/2^+$ states originating from the $1d_{5/2}$ spherical shell (hole-like) and $1d_{3/2}$ spherical shell (particle-like). While for $^{20}$Ne the $3/2^+[301]$ state was not occupied, two more particles in $^{24}$Mg start filling the $3/2^+[301]$ state with the occupation probability approaching 1 for $\beta \approx 0.7$. Hence, the mechanism that drives the low-energy excitations in $^{24}$Mg isotope is generally the same as for $^{20}$Ne. The splitting of the spherical $1d_{5/2}$ and $1d_{3/2}$ levels with deformation allows now for two transitions, one between $\Omega^\pi = 1/2^+$ states, and another between $\Omega^\pi = 3/2^+$ states. Similar arguments apply to other low-energy excitations shown in Fig. 5.12.

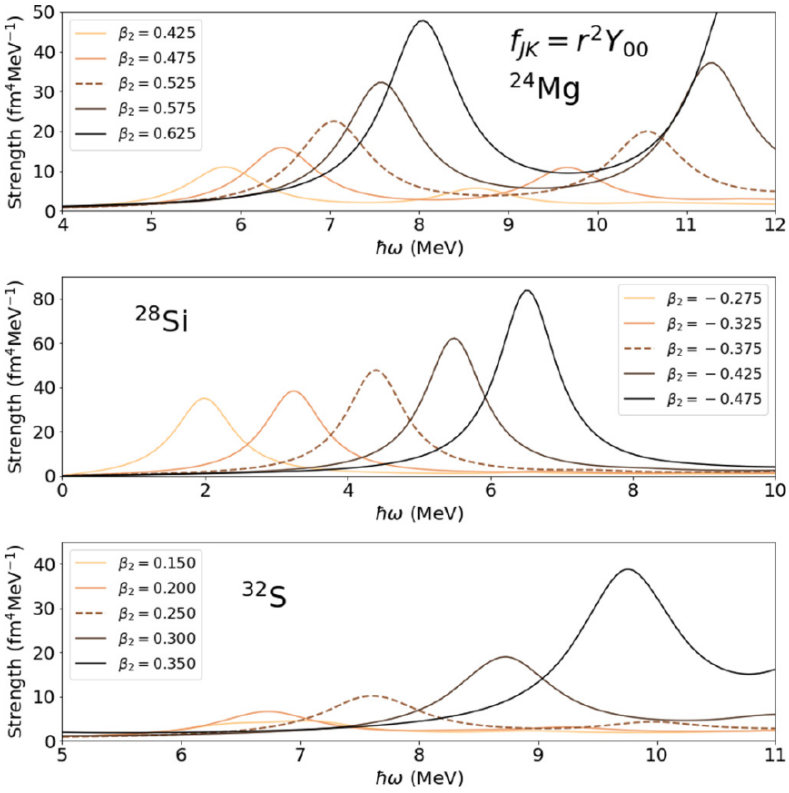


Figure 5.11: Low-energy isoscalar monopole strength distribution in $N = Z$ nuclei: $^{24}$Mg, $^{28}$Si and $^{32}$S. The QFAM response is calculated for several values of constrained axial quadrupole deformation $\beta$, and the dashed curves correspond to the equilibrium deformation for each nucleus. Figure taken from Ref. [65].

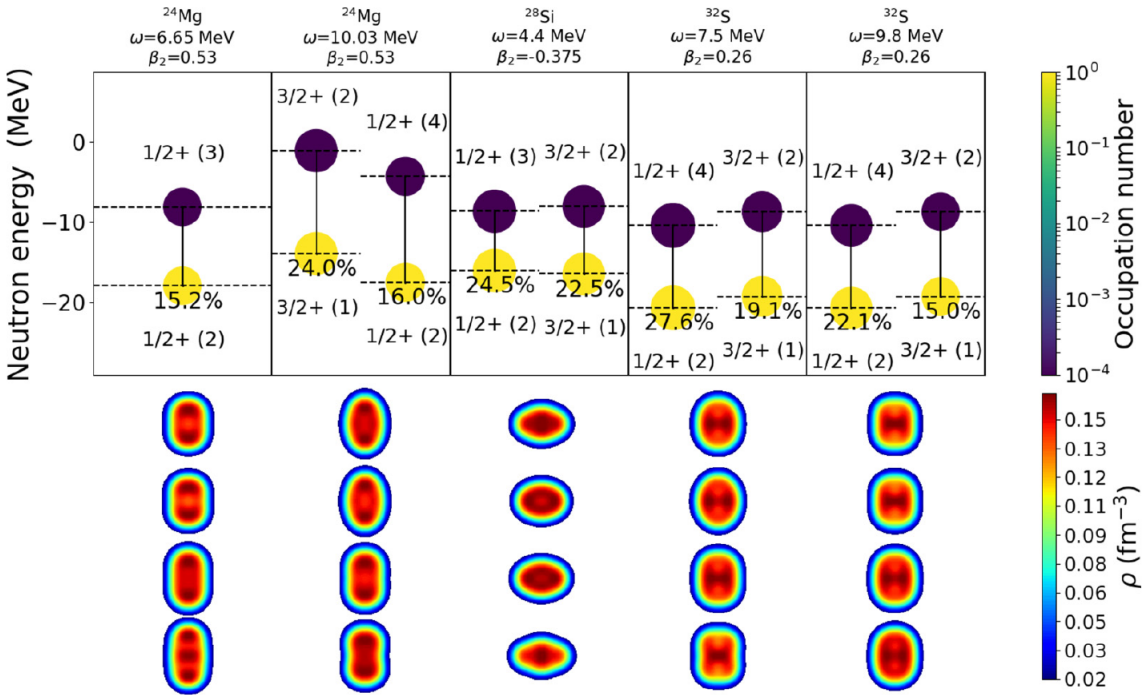


Figure 5.12: Upper panel: leading neutron 2-$qp$ contributions to the low-energy monopole modes in $^{24}$Mg, $^{28}$Si and $^{32}$S isotopes. Lower panel: snapshots of the corresponding density. Figure taken from Ref. [65].

# Chapter 6

# Quasiparticle-vibration coupling in deformed nuclei

Starting from a general many-body fermionic Hamiltonian, the resulting equation of motion of the Dyson type can be formulated for nucleonic propagators in a superfluid systems via the basis of Bogoliubov's quasiparticles. As the leading contributions to the dynamical kernel of this equation of motion in strongly-coupled regimes contain phonon degrees of freedom in various channels, an efficient method for calculating phonon's characteristics is required to successfully model these kernels. The traditional quasiparticle random phase approximation solvers are typically used for this purpose in nuclear structure calculations, however, they become very prohibitive in nonspherical geometries.

By linking the notion of the quasiparticle-vibration coupling (qPVC) vertex to the variation of the Bogoliubov's Hamiltonian, we show that the `DIRQFAM` solver can be efficiently employed to compute the vertices within the QFAM approach. The workflow for calculating the qPVC contribution is depicted in Fig. 6.1. In the first step the deformed ground-state calculation is performed within the RHB framework using axially symmetric `DIRHB` solver [1]. On top of that deformed ground-state, in the second step the `DIRQFAM` solver [2] is used to find the QRPA response function of phonons with various multipolarity $J$ and $0 \leq K \leq J$. The most significant phonon spectrum is localized and the qPVC vertices are extracted. In the final third step, the Dyson equation is constructed using the data obtained in the first two steps. Solution of the Dyson equation yields the fragmentation of quasiparticle spectra and spectroscopic factors.

qPVC calculation was performed in collaboration with nuclear physics group from Michigan. We provided the first two parts (RHB+QRPA) of the workflow, while the Michigan group dealed with the third step and interpretation of the final results. In this chapter, we briefly summarize the qPVC formalism and present the results from Ref. [115]. To illustrate the validity of qPVC method, calculations based on the relativistic density-dependent point-coupling DD-PC1 Lagrangian are performed for the single-nucleon states in heavy and medium-heavy nuclei with axial deformations. Here the case of $^{38}$Si is presented and discussed. Details regarding the formalism for the fermionic quasiparticle propagator in a superfluid fermionic system can be found in Ref. [116].

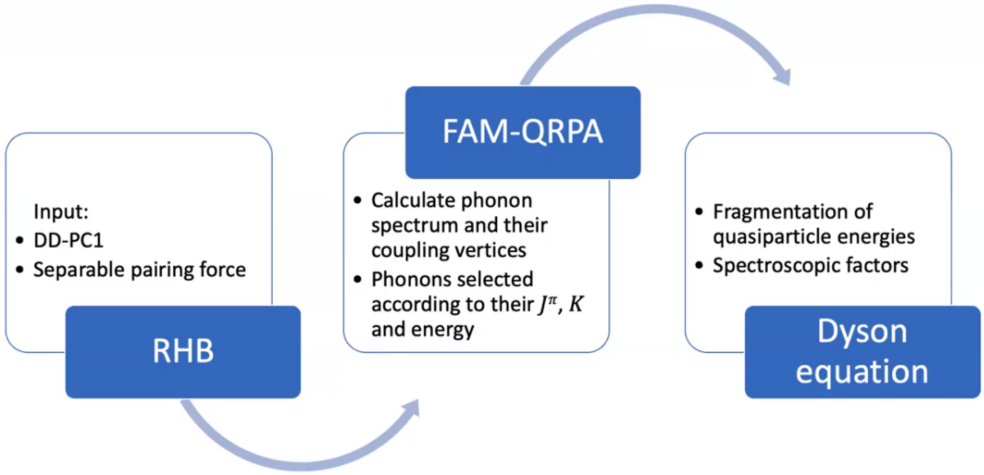


Figure 6.1: Workflow for calculating the qPVC. First the deformed ground state calculation is performed within the RHB framework. On top of that RHB ground state, QFAM is used to find the QRPA response function of phonons with various multipolarity $J, K$. Most significant phonon spectrum is localized and the coupling vertices are extracted. Finally, the Dyson equation is constructed and solved which yields the spectra and spectroscopic factors.

## 6.1 Introduction

Theoretical description of nuclear shell structure and response remain challenging aspects of nuclear physics for decades. The nuclear shell model pioneered by M. Goeppert-Mayer [117] and J.H.D. Jensen [118] and later promoted by them to the inclusion of nuclear pairing has provided the essential building blocks for understanding the fermionic motion in medium-mass and heavy nuclei. The paradigm of the mean-field dominating higher-rank fermionic correlations was developed throughout further decades into the sophisticated microscopic self-consistent mean-fields linked to the density functional theory [119, 120], which are capable of reproducing the experimentally established nuclear shells, both spherical and deformed, reasonably well.

With the advent of the radioactive beam facilities, the concept of firm nuclear shells and well-defined magic numbers associated with the enhanced stability of closed-shell nuclei started to change. It turned out, in particular, that the unstable systems with exotic neutron-to-proton ratios may exhibit the magic numbers, which are different from those in stable nuclei. This phenomenon is studied extensively, both experimentally and theoretically, and there are indications that it can be associated with the enhanced role of beyond-mean-field correlations in exotic nuclear systems. Although the criteria of magicity are not unambiguously defined and can be associated with the shell gaps, the peculiarities in the systematic behavior of the lowest quadrupole states or charge radii, the idea of violation of magic numbers in nuclei with extreme neutron-to-proton ratios is widely accepted [121].

As the most successful density functionals are based on a considerably reduced effective nucleon mass, as compared to its bare values, they typically underestimate the fermionic level densities and overestimate the respective occupation probabilities. The inclusion of correlations beyond the mean-field helps resolving

these deficiencies and can be done by taking into account the dynamical part of the nucleonic self-energy, which arises from the model-independent equations of motion for the in-medium fermionic propagator [122] and which is neglected in the DFT. This leads to the fragmentation of the mean-field states and the densifying of the single-particle spectra [123, 124, 125, 126, 127, 128].

The important ingredients for the dynamical selfenergy in the leading approximation are the particle-vibration coupling (PVC) vertices and the frequencies of the vibrational modes (phonons). In the EDF-based self-consistent approaches they can be calculated within the QRPA approach. This strategy based on the traditional QRPA diagonalization solvers works reasonably well for spherically-symmetric nuclear systems, however, it becomes very prohibitive for calculations in non-spherical geometries. This fact limited the existing applications of the EDF-PVC method to only spherical nuclei.

Here we present the first results of the approach designed to overcome this limitation. We employ the QFAM method to solve the relativistic QRPA equations in the deformed Dirac-Hartree-Bogoliubov basis for the variations of the fermionic density and extract the qPVC vertices by linking these solutions to the fermionic dynamical self-energy.

## 6.2 Formalism

To accurately account for the superfluid pairing correlations, we start from generating the equation of motion for the single-quasiparticle in-medium propagator. After proceeding for the anomalous fermionic Green functions analogously to that for the normal ones as in Ref. [122], we obtain the Dyson equation in the quasiparticle basis:

$$G^{(\eta)}_{\mu\nu}(\varepsilon) = \tilde{G}^{(\eta)}_{\mu\nu}(\eta)(\varepsilon) + \sum_{\mu'\nu'} \tilde{G}^{(\eta)}_{\mu\mu'}(\varepsilon)\Sigma^{e(\eta)}_{\mu'\nu'}(\varepsilon)G^{(\eta)}_{\nu'\nu}(\varepsilon), \tag{6.1}$$

where the basis states $|\mu\rangle$ and $|\nu\rangle$ are the eigenstates of the Dirac-Hartree-Bogoliubov Hamiltonian and the upper index $\eta = \pm 1$ stands for the upper and lower components in the Nambu space. The uncorrelated $\tilde{G}^{(\eta)}$ and the correlated $G^{(\eta)}$ quasiparticle propagators in Eq. (6.1) are, respectively:

$$\tilde{G}^{(\eta)}_{\mu\nu}(\varepsilon) = \frac{\delta_{\mu\nu}}{\varepsilon - \eta(E_\mu - i\gamma)}, \tag{6.2}$$

$$G^{(\eta)}_{\mu\nu}(\varepsilon) = \sum_n \frac{S^{(\eta)n}_{\mu\nu}}{\varepsilon - \eta(E_n - i\gamma)}, \tag{6.3}$$

where $E_\mu$ are the quasiparticle energies and $E_n$ are the energies of the final correlated quasiparticle states $|n\rangle$. As the solutions of Eq. (6.1) for $\eta = \pm 1$ lead to the same $E_n$ and $S^{(+)n}_{\mu\nu} = S^{(-)n}_{\mu\nu}$, solving one of the two equations (6.1) is sufficient. Focusing on the component $\eta = +1$, we need to specify the dynamical self-energy

$\Sigma^{e(+)}$ which, in the leading approximation for the strong coupling regime, reads:

$$\Sigma^{e(+)}_{\mu\nu}(\varepsilon) = \sum_{\mu',i} \left[ \frac{\Gamma^{(11)i}_{\mu\mu'} \left(\Gamma^{(11)i}_{\nu\mu'}\right)^*}{\varepsilon - E_{\mu'} - \Omega_i + i\gamma} + \frac{\left(\Gamma^{(02)i}_{\mu\mu'}\right)^* \Gamma^{(02)i}_{\nu\mu'}}{\varepsilon + E_{\mu'} + \Omega_i - i\gamma} \right], \tag{6.4}$$

where the vertices $\Gamma^{(11)}, \Gamma^{(02)}$ are related to the components of the variation of the single-quasiparticle Hamiltonian in the external field as:

$$\Gamma^{(11)i}_{\mu\nu} = \lim_{\gamma\to 0} \sqrt{\frac{\gamma}{\pi S(\Omega_i + i\gamma)}}\, \mathrm{Im}\left[\delta H^{(11)}_{\mu\nu}(\Omega_i + i\gamma)\right], \tag{6.5}$$

$$\Gamma^{(02)i}_{\mu\nu} = \lim_{\gamma\to 0} \sqrt{\frac{\gamma}{\pi S(\Omega_i + i\gamma)}}\, \mathrm{Im}\left[\delta H^{(02)}_{\mu\nu}(\Omega_i + i\gamma)\right]. \tag{6.6}$$

Variation of the induced Hamiltonian, defined within QFAM in Eq. (2.73), is taken at the QRPA eigenfrequencies $\Omega_i$. Further details are provided in Ref. [116].

## 6.3 Calculation details

The numerical implementation of the approach described above is based on the QFAM solver `DIRQFAM`, which is employed to generate the quasiparticle-phonon model space in axial geometry. The RHB equations for the stationary fermionic basis states resulting from the relativistic point-coupling Lagrangian were solved by expanding the Dirac spinors in terms of eigenfunctions of an axially symmetric harmonic oscillator potential. Ten major oscillator shells were used in the calculations. The density-dependent point-coupling interaction DD-PC1 and the finite-range pairing force with D1S parametrization in the separable form were employed in the calculations. The imaginary part $\gamma = 0.1$ MeV of the frequency argument $\omega$ was employed to eliminate the divergencies of the subsequently computed strength distribution $S(\omega+i\gamma)$ at the QRPA eigenfrequencies $\Omega_i$. This value of $\gamma$ is sufficiently small for the extraction of the qPVC vertices by Eqs. (6.5) and (6.6) with a reasonable accuracy. Both normal and pairing phonon modes with $J^\pi = 2^+, 3^-, 4^+, 5^-$ and $0 \le K \le J$ were included in the quasiparticle dynamical self-energy (6.4). Although it is technically difficult to extend the calculations beyond $J = 5$ at this point, we have found gradually decreasing contributions from large-$J$ phonons, similarly to the spherical case. Contributions from the $J^\pi = 0^+$ and $J^\pi = 1^-$ were found negligible. The dynamical self-energy (6.4) was treated in the diagonal approximation $|\mu\rangle = |\nu\rangle$, which was found quite accurate in the calculations for spherical nuclei. It is expected to be a good approximation also for deformed systems because of destructive interference between the non-diagonal terms. The phonon frequency cutoff $\Omega_{\max} = 15$ MeV was adopted for. The phonon modes within each $\{J^\pi, K\}$ family were selected by their reduced transition probabilities of the electric multipole transitions. The phonons with the reduced transition probabilities equal or exceeding 10% of the maximal one were kept in the model space. The quasiparticle intermediate states $|\mu'\rangle$ with the energy differences $|E_\mu - E_{\mu'}| \le 60$ MeV were included in the summation of Eq. (6.4), that ensured its convergence. This calculation scheme allowed us to include the leading contributions to Eq. (6.4) and it is justified by the preceding qPVC

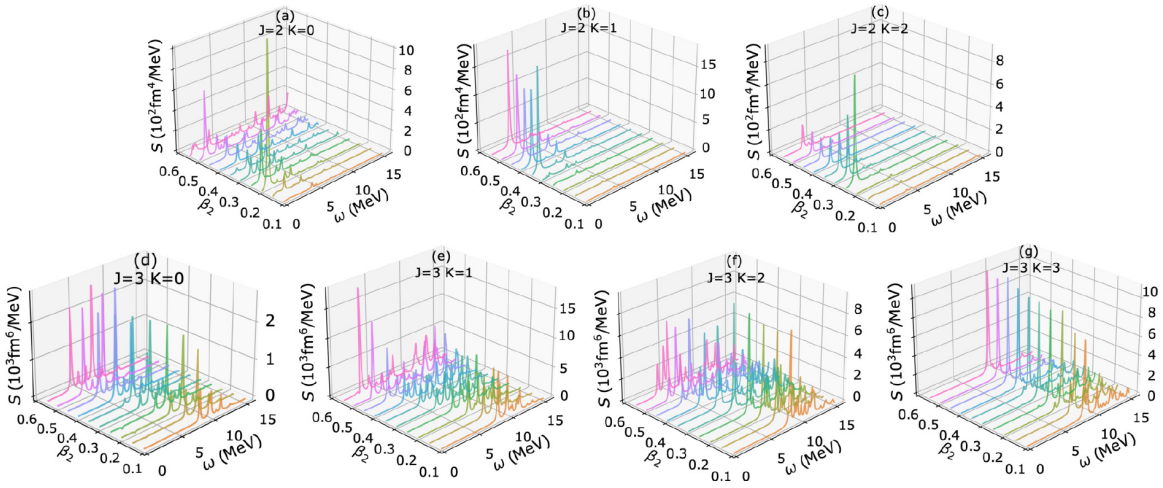


Figure 6.2: The $J^\pi = 2^+$ and $J^\pi = 3^-$ low-energy isoscalar strength functions for varying quadrupole deformation in $^{38}$Si computed with DIRQFAM solver. The smearing parameter $\gamma = 0.1$ MeV was used in the calculations. Figure taken from Ref. [115].

calculations for medium-heavy spherical nuclei [126, 127, 128].

Figure 6.2 displays the QFAM response to isoscalar $J^\pi = 2^+$ and $J^\pi = 3^-$ in $^{38}$Si, illustrating their evolution with quadrupole deformation parameter $\beta$. In the approaches based on effective nucleon-nucleon interactions, QRPA provides a reasonable description of both low-energy and high-energy collective states. Although the observed response indicates that correlations of higher complexity than those of QRPA are needed to describe the excitation spectra [129, 130], QRPA phonons are sufficient to capture the leading qPVC effects in both the one-fermion and two-fermion self-energies. This point was investigated and confirmed explicitly in Ref. [131] in beyond-QRPA calculations based on the Skyrme EDF. In *ab initio* frameworks based on the bare nucleon-nucleon interaction QRPA, however, produces too unrealistic results for the nuclear response and, thus, for the phonon modes, so that higher-complexity approaches beyond QRPA should be employed [132, 133, 134]. Fully *ab initio* solutions for fermionic equation of motion, remain tasks for future research.

After obtaining the spectra of quasiparticles and phonons, the matrix elements $\delta H^{(11)}$ and $\delta H^{(02)}$ were retrieved at the energies corresponding to the QRPA eigenfrequencies. Subsequently, the qPVC vertices were extracted with the aid of Eqs. (6.5) and (6.6) for the selected phonon modes. This information was then used for constructing the dynamical self-energy of Eq. (6.4). With this input, the Dyson equation (6.1) was solved by the ordinary diagonalization procedure. In this work we focused on the quasiparticle states located within ±10 MeV energy window around the Fermi energy, and Eq. (6.1) was solved separately for each of these states. The spectroscopic factors were determined via the derivatives of the dynamical self-energy at the poles of the resulting quasiparticle propagator:

$$S^{(\eta)n}_{\mu\nu} = \left[ \delta_{\mu\nu} - \frac{d\Sigma^{e(\eta)}_{\mu\nu}(\varepsilon)}{d\varepsilon}\Big|_{\varepsilon=\eta E_n} \right]^{-1} . \tag{6.7}$$

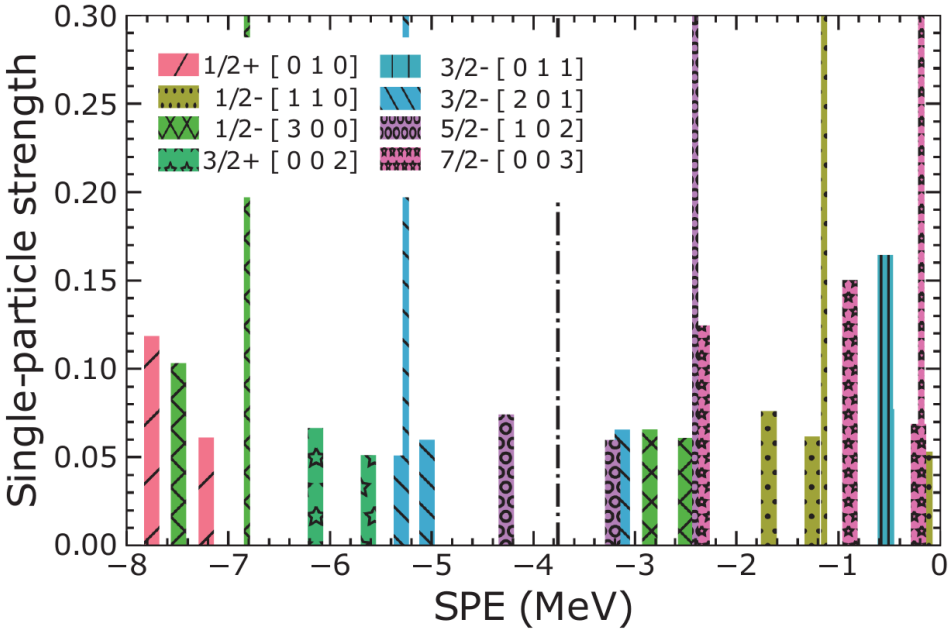


Figure 6.3: Single-particle energies (SPE) and strength of the neutron states in the axially deformed $^{38}$Si obtained in the RHB+qPVC calculations (thick bars) in comparison with the RHB reference states (thin bars). The vertical dash-dotted line denotes the RHB Fermi energy. Figure taken from Ref. [115].

## 6.4 Results

Figure 6.3 displays the correlated neutron quasiparticle states obtained in the RHB-qPVC calculations for the neutron-rich nucleus $^{38}$Si with the self-consistent prolate deformation $\beta = 0.31$. The thick bars represent the fragments of the final quasiparticle states located at $\lambda \pm E_n$, i.e., above (below) the RHB Fermi energy $\lambda$ if their RHB occupancies are smaller (greater) than 0.5. Their heights correspond to the spectroscopic factors of these states in the canonical basis. The RHB reference states at energies $\lambda \pm E_\mu$ are given by the thin bars with the unity hight. The comparison between the thin and thick bars reveals the effects of the qPVC in the nucleonic dynamical self-energy on the quasiparticles. One can see that a remarkable fragmentation occurs already at the Fermi surface indicated by the dash-dotted line. The analytic structure of the dynamical self-energy $\Sigma^{e(\eta)}_{\mu\mu'}(\varepsilon)$ implies that each RHB basis state $|\mu\rangle$ splits into a large number of fragments corresponding to the number of terms in Eq. (6.4). The first, forward-going, term is responsible for the main qPVC effect and the second, backward going one, is the counter term famously associated with the ground state correlations, which reduce the qPVC. As a result, the major part of the obtained correlated quasiparticle states are represented by a few competing fragments as, for instance, the states $1/2^+[010], 1/2^-[110], 3/2^+[002]$ and $3/2^-[201]$. These states are characterized by the presence of two or three fragment with comparable spectroscopic factors $S^{(\pm)n}_{\mu\mu}$ of the order of 0.1-0.2 units. This is a new feature as compared to the previously studied spherical nuclei, where typically a dominant fragment with large spectroscopic factor can be extracted for the states at the Fermi energy, with the most pronounced dominance in closed-shell systems. The axial deformation, together with the superfluid pairing correlations in deformed open-shell nuclei,

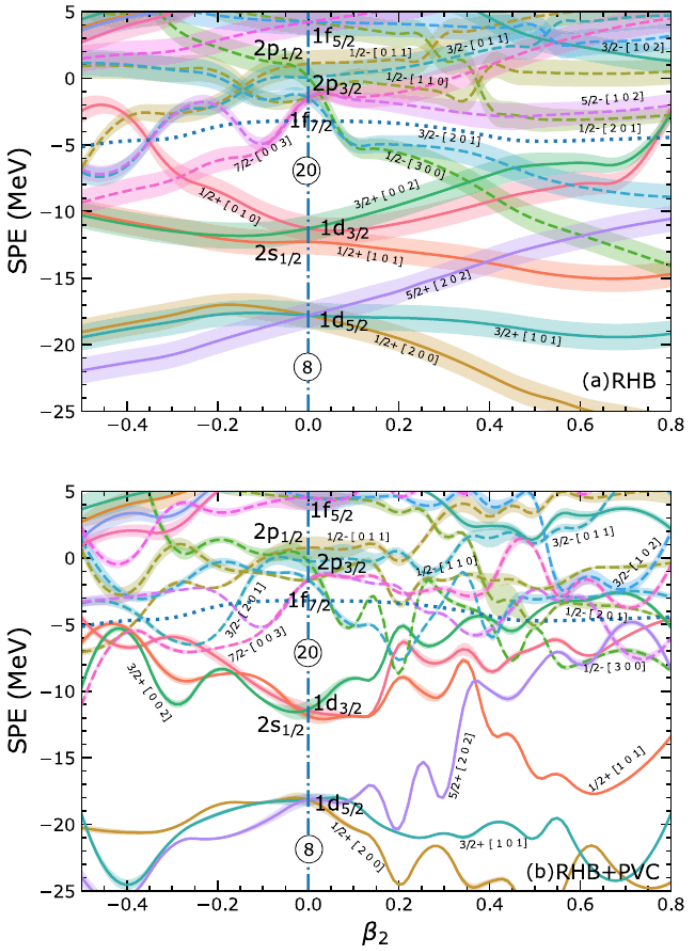


Figure 6.4: The Nilsson diagram for $^{38}$Si extracted from the RHB calculations (top) and from the RHB-qPVC calculations (bottom). Figure taken from Ref. [115].

induce a considerably stronger fragmentation, which can be linked to the fact that these two effects stipulate the formation of the collective phonon modes at lower energies. The overall trend is, however, similar to that found for spherical nuclei: the center of gravity of the major fragments is moving toward the Fermi energy, with respect to the reference RHB quasiparticle states.

In order to illuminate the effect of deformation, we performed similar calculations with different values of the deformation parameter $-0.5 \leq \beta \leq 0.8$, spanning a wide range from prolate to oblate deformations with the step of $\Delta\beta = 0.05$. The results for the dominant fragments, i.e., the fragments with the largest spectroscopic factors and with the energies $E_n$ of the correlated neutron quasiparticle states are displayed in the bottom panel of Fig. 6.4. Their energies are plotted as functions of the deformation parameter $\beta$ and compared to the RHB Nilsson diagram shown in the top panel. The finite width of each color band is proportional to the value of $v_\mu^2 S_{\mu\mu}^{(\eta)n}$ and $(1 - v_\mu^2) S_{\mu\mu}^{(\eta)n}$, with $v_\mu^2$ being the RHB occupancies, for the states below and above the Fermi energy, respectively, as these products represent the resulting single-particle spectroscopic factors. The noticeably thinner bands in the case of the RHB-qPVC states indicate the considerable reduction of the occupancies with respect to the pure RHB calculations, if only one dominant

fragment is taken into account.

One can see in Fig. 6.4 that both the energies and the occupancies of the dominant fragments show notable variations with the deformation parameter. First of all, we emphasize that for the vanishing deformation parameter the calculations in the axial symmetry yield the correct limit, which is verified by the degeneracy of the quasiparticle states at $\beta = 0$ reproduced with good accuracy. The occupancies of the dominant fragments are maximized at the spherical shape. The next observation is the additional oscillations of the positions of the dominant fragments on the energy scale with respect to the relatively smooth evolution of the RHB states with the deformation. Such oscillations are attributed to the evolution of the low-energy collective phonon modes, which play the major role in the qPVC, with deformations. The corresponding isoscalar strength functions for $J^\pi = 2^+$ and $J^\pi = 3^-$ in $^{38}$Si shown in Fig 6.2 illustrate this evolution. We observe, for instance, the disappearance of the $J = 2$ low-lying states with $K = 0$ and the simultaneous appearance of the $J = 2$ and $J = 3$ low-energy modes with $K = 1$ as well as the $J = 2, K = 2$ one in the interval $0.3 \leq \beta \leq 0.6$, while the $J = 2, K = 0$ mode reappears again at $\beta = 5.5$. Similar irregularities are observed in $J = 4$ and $J = 5$ channels. The non-smooth behavior of quite a few dominant quasiparticle states in this interval is a direct consequence of these irregularities in the phonon spectra. Remarkably, this effect gives rise to the formation of the new shell closure with the neutron number $N = 12$ at $\beta \geq 0.5$.

# Chapter 7

# Summary and future work

In the presented work the Quasiparticle Random Phase Approximation built on top of the basis of a relativistic Hartree-Bogoliubov model has been formulated. The RHB model provides a unified description of mean field and pairing correlations, making it an ideal tool for the study of nuclei over the entire nuclear chart. The RHB+QRPA model employed in this work is fully self-consistent. For the interaction in the particle-hole channel two different energy density functionals were used, the RMF functional DD-ME2 with density-dependent meson-nucleon coupling constants and the RMF functional DD-PC1 with density dependent point couplings. Pairing correlations are described by a force separable in momentum space.

Described RHB+QRPA solver has been implemented in a form of `DIRQFAM` software package which calculates the multipole response of even–even axially symmetric deformed nuclei by using the Quasiparticle Finite Amplitude Method built on top of the self-consistent mean-field ground state with constrained quadrupole deformation. The presented `DIRQFAM` solver solves the QFAM equations by expanding the QFAM amplitudes in a basis of eigenstates of axially symmetric harmonic oscillator and the simplex-y operator. The exceptional performance of the solver allows systematic studies of collective model even in medium-heavy and heavy deformed nuclei. Applicability of the developed `DIRQFAM` solver has been demonstrated in this work on two case studies.

First is the systematic analysis of low-lying multipole response in deformed $N = Z$ nuclei. It has been shown that the low-energy modes correspond to cluster modes for all considered isoscalar multipole operators. In particular, in $^{20}$Ne the monopole and quadrupole operators induce two $\alpha$-cluster modes around the $^{12}$C core, while the dipole and octupole operators induce an $\alpha$-cluster mode with respect to the $^{16}$O core. The appearance of cluster modes is closely related to the structure of single-nucleon levels in the canonical basis and, in particular, to the splitting of the $1d_{5/2}$ spherical shell. The monopole response is governed predominantly by the transition from the $1/2^+$ state originating from the spherical $1d_{5/2}$ shell to the $1/2^+$ state that corresponds to the spherical $2s_{1/2}$ shell.

In second application, we approximated the superfluid phonons by the relativistic QRPA, that provides efficient computation of the phonon frequencies and the quasiparticle-vibration coupling vertices, which are incorporated into the Dyson equation for the nucleonic propagator. The approach is formulated in the basis of Dirac-Hartree-Bogoliubov quasiparticles and implemented for open-shell

nuclei with axial deformations. The analysis of the solution obtained for the medium-light neutron-rich nucleus $^{38}$Si reveals a significant fragmentation of the quasiparticle states around the Fermi level and an increase of the level densities in both neutron and proton subsystems. This improves considerably the agreement with experimental data for axially-deformed nuclei as compared to the mean-field approximation.

In addition to QFAM implementation and its applications we presented a new KPM method to calculate the QRPA response by expanding the response function in Chebyshev series. The coefficient for the Chebyshev series can be evaluated efficiently by utilizing the same module used in any QFAM solver. To avoid the Gibbs oscillation phenomenon when truncating the Chebyshev series, the coefficients of the series are adjusted by multiplying with the kernel coefficient. The bounding frequency is one of the input parameters of the KPM method, and all the QRPA eigenfrequencies have to be below the bounding frequency. The bounding frequency has to be larger for the relativistic EDFs than for the non-relativistic EDFs because the QRPA includes the excitation from the Dirac sea. It was demonstrated that KPM method can significantly reduce the computational cost for finding the QRPA response function especially for the non-relativistic EDFs.

Lessons learned regarding the QFAM implementation for axially symmetric nuclei presented in this work will provide valuable insight for future efforts. For example, microscopic description of spontaneous fission is one of the most challenging subjects in nuclear physics. It is necessary to evaluate the collective potential and the collective inertia along a fission path for a description of quantum tunneling in spontaneous or low-energy fission. In past studies of the fission dynamics based on nuclear EDF theory, the collective inertia has been evaluated with the cranking approximation, which neglects dynamical residual effects. The QRPA is used to evaluate the collective inertia along a fission path obtained by the deformation constrained Hartree-Bogoliubov method with dynamical residual effects taken into account. The QFAM method with a contour integration techniques enables us to efficiently compute the collective inertia in a large model space. In a recent study [135] the QFAM-QRPA collective inertia has been evaluated along a symmetric fission path in $^{240}$Pu and $^{256}$Fm. The QFAM-QRPA inertia is significantly larger than the one of the cranking approximation and shows pronounced peaks around the ground state and the fission isomer. This is due to dynamical residual effects. Ref. [135] is a starting point for a systematic study of fission dynamics in heavy and superheavy nuclei with microscopical descrption of nuclear large-amplitude collective motions. Future efforts accompanying this work would ideally follow that same pattern, i.e. an implementation of triaxially deformed extension of `DIRQFAM` solver would be the first relativistic solver to calculate the collective inertia parameters.

# Bibliography


[1] T. Nikšić, N. Paar, D. Vretenar, P. Ring, Comp. Phys. Comm. **185**, 1808 (2014).

[2] A. Bjelčić, T. Nikšić, Comp. Phys. Comm. **253**, 107184 (2020).

[3] M. Bender, P.-H. Heenen, P.-G. Reinhard, Rev. Modern Phys. **75**, 121 (2003).

[4] D. Vretenar, A.V. Afanasjev, G.A. Lalazissis, P. Ring, Phys. Rep. **409**, 101 (2005).

[5] J.R. Stone, P.-G. Reinhard, Prog. Part. Nucl. Phys. **58**, 101 (2005).

[6] T. Nikšić, D. Vretenar, P. Ring, Prog. Part. Nucl. Phys. **58**, 587 (2007).

[7] P. Ring, Prog. Part. Nucl. Phys. **37**, 193 (1996).

[8] W. Panert, P. Ring, J. Boguta, Phys. Rev. Lett. **59**, 2420 (1987).

[9] R. Brockmann, H. Toki, Phys. Rev. Lett. **68**, 3408 (1992).

[10] S. Typel, H.H. Wolter, Nucl. Phys. A **656**, 331 (1999).

[11] F. Hofmann, C.M. Keil, H. Lenske, Phys. Rev. C **64**, 034314 (2001).

[12] T. Nikšić, D. Vretenar, P. Finelli, P. Ring, Phys. Rev. C **66**, 024306 (2002).

[13] G.A. Lalazissis, T. Nikšić, D. Vretenar, P. Ring, Phys. Rev. C **71**, 024312 (2005).

[14] F. de Jong, H. Lenske, Phys. Rev. C **57**, 3099 (1998).

[15] P. Manakos, T. Mannel, Z. Phys. A **330**, 223 (1989).

[16] J.J. Rusnak, R.J. Furnstahl, Nuclear Physics A **627**, 495 (1997).

[17] T. Burvenich, D.G. Madland, J.A. Maruhn, P.G. Reinhard, Phys. Rev. C **65**, 044308 (2002).

[18] T. Nikšić, D. Vretenar, P. Ring, Phys. Rev. C **78**, 034318 (2008).

[19] P.W. Zhao, Z.P. Li, J.M. Yao, J. Meng, Phys. Rev. C **82**, 054319 (2010).

[20] H. Kucharek, P. Ring, Z. Phys. A **339**, 23 (1991).

[21] P. Ring, P. Schuck, *The Nuclear Many-Body Problem*, Springer-Verlag, Berlin (1980).

[22] M. Serra, P. Ring, Phys. Rev. C **65**, 064324 (2002).

[23] Y. Tian, Z.Y. Ma, P. Ring, Phys. Lett. B **676**, 44 (2009).

[24] Y. Tian, Z.Y. Ma, P. Ring, Phys. Rev. C **79**, 064301 (2009).

[25] Y. Tian, Z.Y. Ma, P. Ring, Phys. Rev. C **80**, 024313 (2009).

[26] J.F. Berger, M. Girod, D. Gogny, Comp. Phys. Comm. **61**, 365 (1991).

[27] D. Vautherin, Phys. Rev. C **7**, 296 (1973).

[28] A. Staszack, M. Stoitsov, A. Baran, W. Nazarewicz, Eur. Phys. J. A **46**, 85 (2010).

[29] A. Baran, A. Bulgac, M.M. Forbes, G. Hagen, W. Nazarewicz, N. Schunck, M.V. Stoitsov, Phys. Rev. C **78**, 014318 (2008).

[30] J.G. Valatin, Phys. Rev. **122**, 1012 (1961).

[31] Y. Saad, *Iterative Methods for Sparse Linear Systems*, 2nd edition, SIAM (2003).

[32] P.-G. Reinhard, J.A. Maruhn, A.S. Umar, V.E. Oberacker, Phys. Rev. C **83**, 034312 (2011).

[33] N. Hinohara, M. Kortelainen, W. Nazarewicz, Phys. Rev. C **87**, 064309 (2013).

[34] A Bjelčić, T Nikšić, Z Drmač, Comp. Phys. Comm. **280**, 108477 (2022).

[35] N. Paar, D. Vretenar, E. Khan, G. Colo, Rep. Prog. Phys. 70, 691 (2007).

[36] T. Nakatsukasa, T. Inakura, K. Yabana, Phys. Rev. C **76**, 024318 (2007).

[37] https://netlib.org/blas/.

[38] https://netlib.org/lapack/.

[39] D. Pena Arteaga, P. Ring, Phys. Rev. C **77**, 034317 (2008).

[40] D. Pena Arteaga, E. Khan, P. Ring, Phys. Rev. C **79**, 034311 (2009).

[41] D. P. Arteaga, *Relativistic Quasiparticle Random Phase Approximation in Deformed Nuclei*, Ph.D. dissertation (2007).

[42] J. Toivanen, B.G. Carlsson, J. Dobaczewski, K. Mizuyama, R.R. Rodríguez-Guzmán, P. Toivanen, P. Veselý, Phys. Rev. C **81**, 034312 (2010).

[43] S. Péru, H. Goutte, Phys. Rev. C **77**, 044313 (2008).

[44] T. Inakura, T. Nakatsukasa, and K. Yabana, Phys. Rev. C **80**, 044301 (2009).

[45] T. Inakura, T. Nakatsukasa, K. Yabana, Phys. Rev. C **84**, 021302 (2011).

[46] P. Avogadro, T. Nakatsukasa, Phys. Rev. C **84**, 014314 (2011).

[47] M. Stoitsov, M. Kortelainen, T. Nakatsukasa, C. Losa, and W. Nazarewicz, Phys. Rev. C **84**, 041305(R) (2011).

[48] N. Hinohara, M. Kortelainen, and W. Nazarewicz, Phys. Rev. C **87**, 064309 (2013).

[49] H. Liang, T. Nakatsukasa, Z. Niu, J. Meng, Phys. Rev. C **87**, 054310 (2013).

[50] T. Nikšić, N. Kralj, T. Tutiš, D. Vretenar, and P. Ring, Phys. Rev. C **88**, 044327 (2013).

[51] M. Kortelainen, N. Hinohara, and W. Nazarewicz, Phys. Rev. C **92**, 051302 (2015).

[52] N. Hinohara, M. Kortelainen, W. Nazarewicz, E. Olse, Phys. Rev. C **91**, 044323 (2015).

[53] X. Sun, and D. Lu, Phys. Rev. C **96**, 024614 (2017).

[54] J.-P. Blaizot, G. Ripka, *Quantum Theory of Finite Systems*, MIT, Cambridge, MA (1986).

[55] A. Weisse, G. Wellein, A. Alvermann, and H. Fehske, Rev. Mod. Phys. **78**, 275 (2006).

[56] C. W. Clenshaw, Math. Comp. **9**, 118-120 (1955).

[57] FFTW Fast Fourier Transform Library, http://www.fftw.org/.

[58] G. Colò, L. Cao, N. Van Giai, L. Capelli, Comp. Phys. Commun. **184**, 142-161 (2013).

[59] F. Dawson, R.J. Furnstahl, Phys. Rev. C **42**, 2009 (1990).

[60] N. Hinohara, Phys. Rev. C **92**, 034321 (2015).

[61] L. Capelli, G. Colò, J. Li, Phys. Rev. C **79**, 054329 (2009).

[62] M. T. Mustonen, T. Shafer, Z. Zenginerler, J. Engel, Phys. Rev. C **90**, 024308 (2014).

[63] E. Chabanat, P. Bonche, P. Hanesel, J. Meyer, R. Schaeffer, Nucl. Phys. A **627**, 710 (1997).

[64] L. Covaci, F. M. Peeters, M. Berciu, Phys. Rev. Lett. **105**, 167006 (2010).

[65] F. Mercier, A. Bjelčić, T. Nikšić, J.-P. Ebran, E. Khan, D. Vretenar, Phys. Rev. C **103**, 024303 (2021).

[66] D. H. Youngblood, Y.-W. Lui, and H. L. Clark, Phys. Rev. C **55**, 2811 (1997).

[67] D. H. Youngblood, Y.-W. Lui, and H. L. Clark, Phys. Rev. C **57**, 2748 (1998).

[68] Y.-W. Lui, H. L. Clark, and D. H. Youngblood, Phys. Rev. C **64**, 064308 (2001).

[69] D. H. Youngblood, Y.-W. Lui, and H. L. Clark, Phys. Rev. C **65**, 034302 (2002).

[70] S. Yildiz, M. Freer, N. Soic, S. Ahmed, N. I. Ashwood, N. M. Clarke, N. Curtis, B. R. Fulton, C. J. Metelko, B. Novatski, N. A. Orr, R. Pitkin, S. Sakuta, V. A. Ziman, Phys. Rev. C **73**, 034601 (2006).

[71] Y. K. Gupta et al., Phys. Lett. B **748**, 343 (2015).

[72] T. Tomoda and A. Arima, Nucl. Phys. A **303**, 217 (1978).

[73] E. Uegaki, Y. Abe, S. Okabe, and H. Tanaka, Prog. Theor. Phys. **62**, 1621 (1979).

[74] M. Kamimura, Nucl. Phys. A **351**, 456 (1981).

[75] P. Descouvemont and D. Baye, Phys. Rev. C **36**, 54 (1987).

[76] Y. Suzuki and S. Hara, Phys. Rev. C **39**, 658 (1989).

[77] M. Chernykh, H. Feldmeier, T. Neff, P. von Neumann-Cosel, A. Richter, Phys. Rev. Lett. **98**, 032501 (2007).

[78] M. Ito, Phys. Rev. C **83**, 044319 (2011).

[79] D. S. Delion, R. J. Liotta, P. Schuck, A. Astier, and M.-G. Porquet, Phys. Rev. C **85**, 064306 (2012).

[80] Y. Kanada-En'yo and Y. Shikata, Phys. Rev. C **100**, 014301 (2019).

[81] M. Kimura, Phys. Rev. C **69**, 044319 (2004).

[82] Y. Chiba and M. Kimura, Phys. Rev. C **91**, 061302 (2015).

[83] Y. Chiba, M. Kimura, and Y. Taniguchi, Phys. Rev. C **93**, 034319 (2016).

[84] Y. Kanada-En'yo, Phys. Rev. C **93**, 054307 (2016).

[85] Y. Kanada-En'yo and K. Ogata, Phys. Rev. C **101**, 014317 (2020).

[86] D. H. Youngblood, Y.-W. Lui, and H. L. Clark, Phys. Rev. C **60**, 014304 (1999).

[87] D. H. Youngblood, Y.-W. Lui, X. F. Chen, and H. L. Clark, Phys. Rev. C **80**, 064318 (2009).

[88] X. Chen, Y.-W. Lui, H. L. Clark, Y. Tokimoto, and D. H. Youngblood, Phys. Rev. C **80**, 014312 (2009).

[89] M. Itoh, H. Akimune, M. Fujiwara, U. Garg, N. Hashimoto, T. Kawabata, K. Kawase, S. Kishi, T. Murakami, K. Nakanishi, Y. Nakatsugawa, B. K. Nayak, S. Okumura, H. Sakaguchi, H. Takeda, S. Terashima, M. Uchida, Y. Yasuda, M. Yosoi, and J. Zenihiro, Phys. Rev. C **84**, 054308 (2011).

[90] T. Nakatsukasa and N. Schunk, *Energy Density Functional Methods for Atomic Nuclei* (6-1 to 6-55), IOP Publishing, Bristol (2019).

[91] S. Péru and M. Martini, Eur. Phys. J. A **50**, 88 (2014).

[92] E. Khan, N. Paar, and D. Vretenar, Phys. Rev. C **84**, 051301 (2011).

[93] S. Péru, H. Goutte, and J. F. Berger, Nuc. Phys. A **788**, 44 (2007).

[94] S. Fracasso and G. Colo, Phys. Rev. C **72**, 064310 (2005).

[95] M. Martini, S. Péru, and S. Goriely, Phys. Rev. C **89**, 044306 (2014).

[96] H. Liang, P. Zhao, and J. Meng, Phys. Rev. C **85**, 064302 (2012).

[97] H. Liang, T. Nakatsukasa, Z. Niu, and J. Meng, Phys. Rev. C **87**, 054310 (2013).

[98] T. Nikšić, N. Kralj, T. Tutiš, D. Vretenar, P. Ring, Phy. Rev. C **88**, 044327 (2013).

[99] T. Inakura, T. Nakatsukasa, and K. Yabana, Phys. Rev. C **80**, 044301 (2009).

[100] M. Kortelainen, N. Hinohara, and W. Nazarewicz, Phys. Rev. C **92**, 051302(R) (2015).

[101] T. Oishi, M. Kortelainen, and N. Hinohara, Phys. Rev. C **93**, 034329 (2016).

[102] M. T. Mustonen and J. Engel, Phys. Rev. C **93**, 014304 (2016).

[103] J. P. Ebran, E. Khan, T. Nikšić, and D. Vretenar, Nature **487**, 341 (2012).

[104] J.P. Ebran, E. Khan, T. Nikšić, and D. Vretenar, Phys. Rev. C **90**, 054329 (2014).

[105] J.-P. Ebran, E. Khan, R.-D. Lasseri, and D. Vretenar, Phys. Rev. C 97, 061301(R) (2018).

[106] P. Marević, J.-P. Ebran, E. Khan, T. Nikšić, and D. Vretenar, Phys. Rev. C **97**, 024334 (2018).

[107] P. Marević, J.-P. Ebran, E. Khan, T. Nikšić, and D. Vretenar, Phys. Rev. C **99**, 034317 (2019).

[108] B. Schuetrumpf and C. L. Zhang, Eur. Phys. Web **163**, 00050 (2017).

[109] T. Li, M. Z. Chen, C. L. Zhang, W. Nazarewicz, and M. Kortelainen, Phys. Rev. C **102**, 044305 (2020).

[110] I. Deloncle, S. Péru, and M. Martini, Eur. Phys. J. A **53**, 170 (2017).

[111] Y. Kanada-En'yo and Y. Hidaka, Phys. Rev. C **84**, 014313 (2011).

[112] T. Ichikawa, J. A. Maruhn, N. Itagaki, and S. Ohkubo, Phys. Rev. Lett. **107**, 112501 (2011).

[113] J. M. Yao, N. Itagaki, and J. Meng, Phys. Rev. C **90**, 054307 (2014).

[114] Y. K. Gupta et al., Phys. Rev. C **93**, 044324 (2016).

[115] Y. Zhang, A. Bjelčić, T. Nikšić, E. Litvinova, P. Ring, P. Schuck, Phys. Rev. C **105**, 044326 (2022).

[116] E. Litvinova and Y. Zhang, Phys. Rev. C **104**, 044303 (2021).

[117] M. Goeppert-Mayer, Physical Review **75**, 1969 (1949).

[118] O. Haxel, J. H. D. Jensen, and H. E. Suess, Physical Review C **75**, 1766 (1949).

[119] M. Bender, P.-H. Heenen, and P.-G. Reinhard, Reviews of Modern Physics **75**, 121 (2003).

[120] D. Vretenar, A. V. Afanasjev, G. A. Lalazissis, and P. Ring, Physics Reports **409**, 101 (2005).

[121] T. Otsuka, A. Gade, O. Sorlin, T. Suzuki, and Y. Utsuno, Rev. Mod. Phys. **92**, 015002 (2020).

[122] E. Litvinova and P. Schuck, Physical Review C **100**, 064320 (2019).

[123] P. Ring and E. Werner, Nuclear Physics A **211**, 198 (1973).

[124] E. Litvinova and P. Ring, Physical Review C **73**, 044328 (2006).

[125] E. Litvinova and A. V. Afanasjev, Physical Review C **84**, 014305 (2011).

[126] A. V. Afanasjev and E. Litvinova, Physical Review C **92**, 044317 (2015).

[127] E. Litvinova, Physical Review C **85**, 021303 (2012).

[128] E. Litvinova, Physics Letters B **755**, 138 (2016).

[129] E. Litvinova, P. Ring, and V. Tselyaev, Phys. Rev. C **78**, 014312 (2008).

[130] E. Litvinova, P. Ring, and V. Tselyaev, Phys. Rev. Lett. **105**, 022502 (2010).

[131] V. Tselyaev, N. Lyutorovich, J. Speth, and P. G. Reinhard, Phys. Rev. C **97**, 044308 (2018).

[132] P. Papakonstantinou and R. Roth, Phys. Lett. B **671**, 356 (2009).

[133] D. Bianco, F. Knapp, N. Lo Iudice, F. Andreozzi, and A. Porrino, Phys. Rev. C **85**, 014313 (2012).

[134] G. De Gregorio, F. Knapp, N. Lo Iudice, and P. Vesely, Phys. Rev. C **93**, 044314 (2016).

[135] K. Washiyama, N. Hinohara, T. Nakatsukasa, Phys. Rev. C **103**, 014306 (2021).

# List of Figures

# List of Tables

# Appendix A

# QFAM Appendix

## A.1 Transformation to simplex-y basis

The following transformation between the quasiparticle spinors in HO basis (used for solving the RHB model in ground state) and simplex-y HO basis (used to solve the QFAM equations) hold:

$$\begin{aligned}
f^{(u_\mu)}_{\left(n_z,n_r,+\Omega-\frac{1}{2}\right)} &= +1 \times f^{(U_\mu)}_{\left(n_z,n_r,\Omega-\frac{1}{2},m_s=+\frac{1}{2}\right)} \\
f^{(u_\mu)}_{\left(n_z,n_r,-\Omega-\frac{1}{2}\right)} &= +i \times f^{(U_\mu)}_{\left(n_z,n_r,\Omega+\frac{1}{2},m_s=-\frac{1}{2}\right)} \\
g^{(u_\mu)}_{\left(n_z,n_r,+\Omega-\frac{1}{2}\right)} &= +i \times g^{(U_\mu)}_{\left(n_z,n_r,\Omega-\frac{1}{2},m_s=+\frac{1}{2}\right)} \\
g^{(u_\mu)}_{\left(n_z,n_r,-\Omega-\frac{1}{2}\right)} &= +1 \times g^{(U_\mu)}_{\left(n_z,n_r,\Omega+\frac{1}{2},m_s=-\frac{1}{2}\right)}
\end{aligned}, \tag{A.1}$$

$$\begin{aligned}
f^{(v_\mu)}_{\left(n_z,n_r,+\Omega-\frac{1}{2}\right)} &= -1 \times f^{(V_\mu)}_{\left(n_z,n_r,\Omega-\frac{1}{2},m_s=+\frac{1}{2}\right)} \\
f^{(v_\mu)}_{\left(n_z,n_r,-\Omega-\frac{1}{2}\right)} &= -i \times f^{(V_\mu)}_{\left(n_z,n_r,\Omega+\frac{1}{2},m_s=-\frac{1}{2}\right)} \\
g^{(v_\mu)}_{\left(n_z,n_r,+\Omega-\frac{1}{2}\right)} &= -i \times g^{(V_\mu)}_{\left(n_z,n_r,\Omega-\frac{1}{2},m_s=+\frac{1}{2}\right)} \\
g^{(v_\mu)}_{\left(n_z,n_r,-\Omega-\frac{1}{2}\right)} &= -1 \times g^{(V_\mu)}_{\left(n_z,n_r,\Omega+\frac{1}{2},m_s=-\frac{1}{2}\right)}
\end{aligned}. \tag{A.2}$$

The wave functions on the left-hand side of eqs. (A.1) and (A.2) are expanded in the basis defined in Eqs. (3.13-3.14), while those on the right-hand side are expanded in the HO basis. Therefore, one can easily construct the $U$ and $V$ matrices in the HO simplex-y basis from the ground-state solution represented in HO basis. We emphasise that the large and small components of the Dirac spinors in particular simplex block are expanded in the simplex-y eigenfunctions of opposite eigenvalues.

## A.2 Klein-Gordon equation in cylindrical coordinates

The Klein-Gordon equation for the scalar field and the time-like components of the vector fields reads:

$$\left[-\triangle + m_\phi^2\right] \delta\Phi_0(\boldsymbol{r},\omega) = \delta S_0(\boldsymbol{r},\omega), \tag{A.3}$$

where $\delta\Phi_0(\boldsymbol{r},\omega)$ and $\delta S_0(\boldsymbol{r},\omega)$ denote the induced field and the source term, respectively (see Eqs. (3.31-3.33)). The angular dependence of each source terms originates from the angular dependence of the induced vector or scalar density[1] which corresponds to the $\cos K\varphi$ function, i.e.,

$$\delta S_0(\boldsymbol{r},\omega) = \delta S_0(z, r_\perp, \omega)\cos K\varphi. \tag{A.4}$$

One can show that the induced fields inherit the same angular dependence:

$$\delta\Phi_0(\boldsymbol{r},\omega) = \delta\Phi_0(z, r_\perp, \omega)\cos K\varphi. \tag{A.5}$$

The remaining part of the solution $\Phi_0(z, r_\perp, \omega)$ is calculated by solving the equation:

$$\left[-\triangle_{z,r_\perp,K} + m_\phi^2\right] \delta\Phi_0(z, r_\perp, \omega) = \delta S_0(z, r_\perp, \omega). \tag{A.6}$$

For the space-like components (see Eqs. (3.34-3.35)) of the vector fields, the Klein-Gordon equation reads:

$$\left[-\triangle + m_\phi^2\right] \delta\boldsymbol{\Phi}(\boldsymbol{r},\omega) = \delta\boldsymbol{S}(\boldsymbol{r},\omega). \tag{A.7}$$

The angular dependence of the space-like components of the source term includes both the $\cos K\varphi$ and the $\sin K\varphi$ functions:

$$\begin{aligned}\delta\boldsymbol{S}(\boldsymbol{r},\omega) = {} & \delta S_z(z, r_\perp, \omega)\cos K\varphi\, \boldsymbol{e}_z + \delta S_\perp(z, r_\perp, \omega)\cos K\varphi\, \boldsymbol{e}_\perp \\ & + \delta S_\varphi(z, r_\perp, \omega)\sin K\varphi\, \boldsymbol{e}_\varphi.\end{aligned} \tag{A.8}$$

We express the $\boldsymbol{e}_\perp$ and $\boldsymbol{e}_\varphi$ unit vectors in terms of the Cartesian unit vectors $\boldsymbol{e}_x$ and $\boldsymbol{e}_y$:

$$\boldsymbol{e}_\perp = \cos\varphi\, \boldsymbol{e}_x + \sin\varphi\, \boldsymbol{e}_y, \quad \boldsymbol{e}_\varphi = -\sin\varphi\, \boldsymbol{e}_x + \cos\varphi\, \boldsymbol{e}_y, \tag{A.9}$$

thus obtaining:

$$\begin{aligned}\delta\boldsymbol{S}(\boldsymbol{r},\omega) = {} & \frac{1}{\sqrt{2}}\left[+\delta S_1(z, r_\perp, \omega)\cos(K-1)\varphi + \delta S_2(z, r_\perp, \omega)\cos(K+1)\varphi\right]\boldsymbol{e}_x \\ & + \frac{1}{\sqrt{2}}\left[-\delta S_1(z, r_\perp, \omega)\sin(K-1)\varphi + \delta S_2(z, r_\perp, \omega)\sin(K+1)\varphi\right]\boldsymbol{e}_y \\ & + \delta S_3(z, r_\perp, \omega)\cos K\varphi \boldsymbol{e}_z,\end{aligned} \tag{A.10}$$

[1] Notice that the ground state densities are axially symmetric.

where we have defined the following quantities:

$$\delta S_1(z,r_\perp,\omega) = \frac{1}{\sqrt{2}}\left[+\delta S_\perp(z,r_\perp,\omega) - \delta S_\varphi(z,r_\perp,\omega)\right], \tag{A.11}$$

$$\delta S_2(z,r_\perp,\omega) = \frac{1}{\sqrt{2}}\left[+\delta S_\perp(z,r_\perp,\omega) + \delta S_\varphi(z,r_\perp,\omega)\right], \tag{A.12}$$

$$\delta S_3(z,r_\perp,\omega) = S_z(z,r_\perp,\omega). \tag{A.13}$$

The angular dependence of the induced fields $\delta\boldsymbol{\Phi}(\boldsymbol{r},\omega)$ is inherited from the source terms $\delta\boldsymbol{S}(\boldsymbol{r},\omega)$:

$$\begin{aligned}\delta\boldsymbol{\Phi}(\boldsymbol{r},\omega) = {}& \delta\Phi_z(z,r_\perp,\omega)\cos K\varphi\ \boldsymbol{e}_z + \delta\Phi_\perp(z,r_\perp,\omega)\cos K\varphi\ \boldsymbol{e}_\perp \\ & + \delta\Phi_\varphi(z,r_\perp,\omega)\sin K\varphi\ \boldsymbol{e}_\varphi,\end{aligned} \tag{A.14}$$

and can be decomposed in an analogous way:

$$\begin{aligned}\delta\boldsymbol{\Phi}(\boldsymbol{r},\omega) = {}& \frac{1}{\sqrt{2}}\left[+\delta\Phi_1(z,r_\perp,\omega)\cos(K-1)\varphi + \delta\Phi_2(z,r_\perp,\omega)\cos(K+1)\varphi\right]\boldsymbol{e}_x \\ & + \frac{1}{\sqrt{2}}\left[-\delta\Phi_1(z,r_\perp,\omega)\sin(K-1)\varphi + \delta\Phi_2(z,r_\perp,\omega)\sin(K+1)\varphi\right]\boldsymbol{e}_y \\ & + \delta\Phi_3(z,r_\perp,\omega)\cos K\varphi\boldsymbol{e}_z.\end{aligned} \tag{A.15}$$

We insert Eqs. (A.15) and (A.10) in the Klein-Gordon equation (A.7), equate the terms with $\cos K\varphi$ and $\sin K\varphi$ angular dependence and obtain the equations for the components of the induced fields:

$$\left[-\triangle_{z,r_\perp,|K-1|} + m_\phi^2\right]\delta\Phi_1(z,r_\perp,\omega) = \delta S_1(z,r_\perp,\omega), \tag{A.16}$$

$$\left[-\triangle_{z,r_\perp,|K+1|} + m_\phi^2\right]\delta\Phi_2(z,r_\perp,\omega) = \delta S_2(z,r_\perp,\omega), \tag{A.17}$$

$$\left[-\triangle_{z,r_\perp,|K|} + m_\phi^2\right]\delta\Phi_3(z,r_\perp,\omega) = \delta S_3(z,r_\perp,\omega). \tag{A.18}$$

By employing the solutions of Eqs. (A.16-A.18), we can reconstruct the components of the meson fields in the cylindrical coordinate system:

$$\delta\Phi_\perp(z,r_\perp,\omega) = \frac{1}{\sqrt{2}}\left[+\delta\Phi_1(z,r_\perp,\omega) + \delta\Phi_2(z,r_\perp,\omega)\right], \tag{A.19}$$

$$\delta\Phi_\varphi(z,r_\perp,\omega) = \frac{1}{\sqrt{2}}\left[-\delta\Phi_1(z,r_\perp,\omega) + \delta\Phi_2(z,r_\perp,\omega)\right], \tag{A.20}$$

$$\delta\Phi_z(z,r_\perp,\omega) = \delta\Phi_3(z,r_\perp,\omega). \tag{A.21}$$

We expand the solutions of the Klein-Gordon equations (A.6,A.16-A.18) in terms of the eigenfunctions of the axially symmetric harmonic oscillator potential. Detailed description of the HO basis can be found in Section 3.1.1, but here we use smaller oscillator length $\tilde{b}_0 = b_0/\sqrt{2}$. This particular choice is a consequence of the fact that the induced densities and currents, i.e. the source terms of Klein-Gordon equations, are a linear combinations of products of HO basis functions. Following the expressions for induced densities and currents given in Appendix

A.9, the source terms can be written as:

$$\delta S_0(z,r_\perp,\omega) = \sum_{n_z,n_r} (\delta S_0)_{(n_z,n_r)} \phi_{n_z}(z,\tilde{b}_z)\phi_{n_r}^{|K|}(r_\perp,\tilde{b}_\perp), \tag{A.22}$$

$$\delta S_1(z,r_\perp,\omega) = \sum_{n_z,n_r} (\delta S_1)_{(n_z,n_r)} \phi_{n_z}(z,\tilde{b}_z)\phi_{n_r}^{|K-1|}(r_\perp,\tilde{b}_\perp), \tag{A.23}$$

$$\delta S_2(z,r_\perp,\omega) = \sum_{n_z,n_r} (\delta S_2)_{(n_z,n_r)} \phi_{n_z}(z,\tilde{b}_z)\phi_{n_r}^{|K+1|}(r_\perp,\tilde{b}_\perp), \tag{A.24}$$

$$\delta S_3(z,r_\perp,\omega) = \sum_{n_z,n_r} (\delta S_3)_{(n_z,n_r)} \phi_{n_z}(z,\tilde{b}_z)\phi_{n_r}^{|K|}(r_\perp,\tilde{b}_\perp). \tag{A.25}$$

Fields $\delta\Phi_i(z,r_\perp,\omega)$ are approximated by the same truncated expansion via coefficients $(\delta\Phi_i)_{(n_z,n_r)}$ for $i=0,1,2,3$.

Inserting each of the expansions (A.22-A.25) into their respective Klein-Gordon equations, we obtain a set of linear equations:

$$\sum_{n_z' n_r'} \boldsymbol{\mathcal{H}}^{\Lambda_i}_{(n_z,n_r)(n_z',n_r')} (\delta\Phi_i)_{(n_z',n_r')} = (\delta S_i)_{(n_z,n_r)}, \tag{A.26}$$

with

$$\Lambda_i = \begin{cases} |K| & \text{for } i=0,3, \\ |K-1| & \text{for } i=1, \\ |K+1| & \text{for } i=2. \end{cases} \tag{A.27}$$

The $\boldsymbol{\mathcal{H}}^K_{(n_z,n_r)(n_z',n_r')}$ matrix elements can be calculated analytically:

$$\begin{aligned} \boldsymbol{\mathcal{H}}^K_{(n_z,n_r)(n_z',n_r')} = & \left[ \frac{n_z+\frac{1}{2}}{\tilde{b}_z^2} + \frac{2n_r+K+1}{\tilde{b}_\perp^2} + m_\phi^2 \right] \delta_{n_r n_r'} \delta_{n_z n_z'} \\ & - \frac{\delta_{n_r n_r'}}{2\tilde{b}_z^2} \left[ \sqrt{(n_z+1)(n_z+2)}\delta_{n_z' n_z+2} + \sqrt{(n_z'+1)(n_z'+2)}\delta_{n_z n_z'+2} \right] \\ & + \frac{\delta_{n_z n_z'}}{\tilde{b}_\perp^2} \left[ \sqrt{n_r(n_r+K)}\delta_{n_r n_r'+1} + \sqrt{n_r'(n_r'+K)}\delta_{n_r' n_r+1} \right], \end{aligned} \tag{A.28}$$

while the matrix elements of the source terms are calculated numerically by employing Gauss-Hermite and Gauss-Laguerre quadrature formulas:

$$(\delta S_i)_{(n_z,n_r)} = \int_{-\infty}^{+\infty} dz \int_0^{+\infty} r_\perp dr_\perp \phi_{n_z}(z,\tilde{b}_z)\phi_{n_r}^{|\Lambda_i|}(r_\perp,\tilde{b}_\perp)\delta S_i(z,r_\perp,\omega). \tag{A.29}$$

By inverting the set of equations (A.26), we obtain the coefficients $(\delta\Phi_i)_{(n_z,n_r)}$ that are used to calculate the induced fields $\delta\Phi_i(z,r_\perp,\omega)$ $(i=0,1,2,3)$.

In the `DIRQFAM` code, all fields $\delta S_i(z,r_\perp,\omega)$ in coordinate space are represented by their values on Gauss-Hermite and Gauss-Laguerre quadrature nodes $\delta S_i(z^{i_{GH}},r_\perp^{i_{GL}},\omega)$. By defining the matrix:

$$\boldsymbol{\Phi}^K_{(n_z,n_r)(i_{GH},i_{GL})} = \phi_{n_z}(z^{i_{GH}},\tilde{b}_z)\phi_{n_r}^{|K|}(r_\perp^{i_{GL}},\tilde{b}_\perp), \tag{A.30}$$

the numerical integration in Eq. (A.29) can be written as a matrix-vector multi-

plication:

$$(\delta S_i)_{(n_z,n_r)} = \sum_{i_{GH},i_{GL}} \mathbf{\Phi}^{\Lambda_i}_{(n_z,n_r)(i_{GH},i_{GL})} w_{b_z}^{i_{GH}} w_{b_\perp}^{i_{GL}} \delta S_i(z^{i_{GH}}, r_\perp^{i_{GL}}, \omega). \tag{A.31}$$

$w_{b_z}^{i_{GH}}$ and $w_{b_\perp}^{i_{GL}}$ denote the Gaussian quadrature weights. Inverting Eq. (A.26) yields:

$$\left[(\delta\Phi_i)_{(n_z,n_r)}\right]_{(n_z,n_r)} = \left(\boldsymbol{\mathcal{H}}^{\Lambda_i}\right)^{-1} \mathbf{\Phi}^{\Lambda_i} \left[w_{b_z}^{i_{GH}} w_{b_\perp}^{i_{GL}} \delta S_i(z^{i_{GH}}, r_\perp^{i_{GL}}, \omega)\right]_{(i_{GH},i_{GL})}. \tag{A.32}$$

Because in practical calculations we need $\delta\Phi_i(z, r_\perp, \omega)$ evaluated on the Gaussian quadrature grid, the Eqs. (A.22-A.25) analogous for the induced meson fields $\delta\Phi_i(z, r_\perp, \omega)$ can be written as:

$$\begin{aligned}\left[\delta\Phi_i(z^{i_{GH}}, r_\perp^{i_{GL}}, \omega)\right]_{(i_{GH},i_{GL})} &= \left(\mathbf{\Phi}^{\Lambda_i}\right)^T \left(\boldsymbol{\mathcal{H}}^{\Lambda_i}\right)^{-1} \mathbf{\Phi}^{\Lambda_i} \times \\ &\times \left[w_{b_z}^{i_{GH}} w_{b_\perp}^{i_{GL}} \delta S_i(z^{i_{GH}}, r_\perp^{i_{GL}}, \omega)\right]_{(i_{GH},i_{GL})}.\end{aligned} \tag{A.33}$$

$\boldsymbol{\mathcal{H}}^K$ is a matrix representation of the linear operator $-\triangle_{z,r_\perp,K} + m_\phi^2$ in the truncated HO basis, and since $-\triangle_{z,r_\perp,K}$ is positive operator, the real matrix $\boldsymbol{\mathcal{H}}^K$ is positive definite. Thus, we can find its Cholesky factorization $\boldsymbol{\mathcal{H}}^K = \boldsymbol{\mathcal{L}}^K \left(\boldsymbol{\mathcal{L}}^K\right)^T$, for regular lower-triangular matrix $\boldsymbol{\mathcal{L}}^K$. By defining the matrix $\boldsymbol{\mathcal{P}}^K = \left(\boldsymbol{\mathcal{L}}^K\right)^{-1} \mathbf{\Phi}^K$, we can write:

$$\begin{aligned}\left[\delta\Phi_i(z^{i_{GH}}, r_\perp^{i_{GL}}, \omega)\right]_{(i_{GH},i_{GL})} &= \left(\boldsymbol{\mathcal{P}}^{\Lambda_i}\right)^T \boldsymbol{\mathcal{P}}^{\Lambda_i} \times \\ &\times \left[w_{b_z}^{i_{GH}} w_{b_\perp}^{i_{GL}} \delta S_i(z^{i_{GH}}, r_\perp^{i_{GL}}, \omega)\right]_{(i_{GH},i_{GL})}.\end{aligned} \tag{A.34}$$

To summarize, if the source terms $\delta S_i(z, r_\perp, \omega)$ are given on the Gaussian quadrature grid, Eq. (A.34) provides a transformation for calculating the fields $\delta\Phi_i(z, r_\perp, \omega)$ on the same quadrature grid. We notice that the total computational cost consists of only two matrix-vector multiplications with a precomputed matrix $\boldsymbol{\mathcal{P}}^{\Lambda_i}$.

## A.3 Induced Coulomb potential

The induced potential for protons includes the direct Coulomb field:

$$\delta V_C(\boldsymbol{r}, \omega) = e^2 \int d\boldsymbol{r}' \frac{\delta\rho_v^p(\boldsymbol{r}', \omega)}{|\boldsymbol{r} - \boldsymbol{r}'|}, \tag{A.35}$$

where $\delta\rho_v^p(\boldsymbol{r}, \omega)$ denotes the induced proton vector density. The logarithmic singularity in the integrand at the point $\boldsymbol{r} = \boldsymbol{r}'$ can be eliminated by using the identity:

$$\triangle_{\boldsymbol{r}'} |\boldsymbol{r} - \boldsymbol{r}'| = \frac{2}{|\boldsymbol{r} - \boldsymbol{r}'|}, \tag{A.36}$$

that together with an integration by parts, gives:

$$\delta V_C(\boldsymbol{r}, \omega) = \frac{e^2}{2} \int d^3r' |\boldsymbol{r} - \boldsymbol{r}'| \triangle_{\boldsymbol{r}'} \delta\rho_v^p(\boldsymbol{r}', \omega). \tag{A.37}$$

Since the induced proton density can be written as $\delta\rho_v^p(\boldsymbol{r},\omega) = \delta\rho_v^p(z, r_\perp, \omega)\cos K\phi$, this angular dependence also holds for the Laplacian:

$$\triangle_{\boldsymbol{r}}\delta\rho_v^p(\boldsymbol{r},\omega) = \left[\frac{1}{r_\perp}\partial_{r_\perp}\left(r_\perp\partial_{r_\perp}\right) - \frac{K^2}{r_\perp^2} + \partial_z^2\right]\delta\rho_v^p(z, r_\perp, \omega)\cos K\phi, \tag{A.38}$$

and the angular part of the integral (A.37) can be solved analytically. We insert the following relation into Eq. (A.37):

$$|\boldsymbol{r} - \boldsymbol{r}'| = \sqrt{(r_\perp + r'_\perp)^2 + (z - z')^2}\sqrt{1 - a\cos^2\frac{\phi - \phi'}{2}}, \tag{A.39}$$

with:

$$a = \frac{4r_\perp r'_\perp}{(r_\perp + r'_\perp)^2 + (z - z')^2}. \tag{A.40}$$

Next, we substitute $\phi - \phi' = 2x$ and use the symmetry properties of the integrand to reduce the integration interval. Finally, we obtain the following integral:

$$I_K(a) = \int_0^{\pi/2}\sqrt{1 - a\cos^2 x}\cos\left(2Kx\right)dx. \tag{A.41}$$

We notice that $K \geq 0$ and $a \in [0, 1]$. For the $K = 0$ value Eq. (A.41) is reduced to the definition of the complete elliptic integral of the second kind:

$$I_0(a) = E(a) = \int_0^{\pi/2}\sqrt{1 - a\cos^2 x}dx, \tag{A.42}$$

while for the $K = 1$ value it can be written as:

$$I_1(a) = \left(\frac{2 - 2a}{3a}\right)K(a) - \left(\frac{2 - a}{3a}\right)E(a), \tag{A.43}$$

where $K(a)$ denotes the complete elliptic integral of the first kind:

$$K(a) = \int_0^{\pi/2}\frac{dx}{\sqrt{1 - a\cos^2 x}}. \tag{A.44}$$

Finally, for $K \geq 2$ the following recursive relation can be used to calculate $I_K(a)$:

$$I_K(a) = \left(\frac{(4K - 4)(2 - a)}{(2K + 1)a}\right)I_{K-1}(a) - \left(\frac{2K - 5}{2K + 1}\right)I_{K-2}(a). \tag{A.45}$$

The entire problem of calculating the $I_K$ is reduced to computation of the complete elliptic integrals $E(a)$ and $K(a)$ and this can be accomplished easily by using a polynomial approximation or any other well established numerical method. The induced Coulomb field also inherits the $\cos K\phi$ angular dependence:

$$\delta V_C(\boldsymbol{r},\omega) = \delta V_C(z, r_\perp, \omega)\cos K\phi, \tag{A.46}$$

with:

$$\delta V_C(z, r_\perp, \omega) = \int_{-\infty}^{+\infty} dz' \int_0^{+\infty} dr'_\perp r'_\perp G(z', r'_\perp, z, r_\perp) \triangle_{z', r'_\perp} \delta\rho_v^p(z', r'_\perp, \omega). \quad \text{(A.47)}$$

$\triangle_{z,r_\perp}$ denotes the $z$ and $r_\perp$ components of the Laplacian operator (A.38) and the Green's function $G(z', r'_\perp, z, r_\perp)$ reads:

$$G(z', r'_\perp, z, r_\perp) = 2e^2 \sqrt{(r_\perp + r'_\perp)^2 + (z - z')^2} I_K \left( \frac{4 r_\perp r'_\perp}{(r_\perp + r'_\perp)^2 + (z - z')^2} \right). \quad \text{(A.48)}$$

## A.4 Poisson equation in cylindrical coordinates

The procedure of solving the Poisson equation for the time-like component of the Coulomb field is described in details in Appendix A.3 and in this section we focus on the space-like components, i.e. we solve the following equation:

$$-\triangle \delta \boldsymbol{V}_C(\boldsymbol{r}, \omega) = e^2 \delta \boldsymbol{j}_p(\boldsymbol{r}, \omega), \quad \text{(A.49)}$$

where $\delta \boldsymbol{j}_p(\boldsymbol{r}, \omega)$ denotes the induced proton current. The induced potential $\delta \boldsymbol{V}_C(\boldsymbol{r}, \omega)$ reads:

$$\delta \boldsymbol{V}_C(\boldsymbol{r}, \omega) = e^2 \int d\boldsymbol{r}' \frac{\delta \boldsymbol{j}_p(\boldsymbol{r}', \omega)}{|\boldsymbol{r} - \boldsymbol{r}'|}. \quad \text{(A.50)}$$

By using the identity:

$$\triangle_{\boldsymbol{r}'} |\boldsymbol{r} - \boldsymbol{r}'| = \frac{2}{|\boldsymbol{r} - \boldsymbol{r}'|}, \quad \text{(A.51)}$$

similar as in Appendix A.3, the induced potential can be written in the following form:

$$\delta \boldsymbol{V}_C(\boldsymbol{r}, \omega) = \frac{e^2}{2} \int d\boldsymbol{r}' |\boldsymbol{r} - \boldsymbol{r}'| \triangle_{\boldsymbol{r}'} \delta \boldsymbol{j}_p(\boldsymbol{r}', \omega). \quad \text{(A.52)}$$

The angular dependence of the induced currents includes both the $\cos K\varphi$ and $\sin K\varphi$ functions (see Appendix A.9):

$$\begin{aligned} \delta \boldsymbol{j}_p(\boldsymbol{r}, \omega) = {} & \delta j_{p,z}(z, r_\perp, \omega) \cos K\varphi \, \boldsymbol{e}_z + \delta j_{p,\perp}(z, r_\perp, \omega) \cos K\varphi \, \boldsymbol{e}_\perp \\ & + \delta j_{p,\varphi}(z, r_\perp, \omega) \sin K\varphi \, \boldsymbol{e}_\varphi. \end{aligned} \quad \text{(A.53)}$$

We decompose the induced proton current into Cartesian components:

$$\begin{aligned} \delta \boldsymbol{j}_p(\boldsymbol{r}, \omega) = {} & \frac{1}{\sqrt{2}} \left[ +\delta j_{p,1}(z, r_\perp, \omega) \cos(K-1)\varphi + \delta j_{p,2}(z, r_\perp, \omega) \cos(K+1)\varphi \right] \boldsymbol{e}_x \\ & + \frac{1}{\sqrt{2}} \left[ -\delta j_{p,1}(z, r_\perp, \omega) \sin(K-1)\varphi + \delta j_{p,2}(z, r_\perp, \omega) \sin(K+1)\varphi \right] \boldsymbol{e}_y \\ & + \delta j_{p,3}(z, r_\perp, \omega) \cos K\varphi \boldsymbol{e}_z, \end{aligned} \quad \text{(A.54)}$$

where we have defined:

$$\delta j_{p,1}(z, r_\perp, \omega) = \frac{1}{\sqrt{2}} \left[\delta j_{p,\perp}(z, r_\perp, \omega) - \delta j_{p,\varphi}(z, r_\perp, \omega)\right], \tag{A.55}$$

$$\delta j_{p,2}(z, r_\perp, \omega) = \frac{1}{\sqrt{2}} \left[\delta j_{p,\perp}(z, r_\perp, \omega) + \delta j_{p,\varphi}(z, r_\perp, \omega)\right], \tag{A.56}$$

$$\delta j_{p,3}(z, r_\perp, \omega) = \delta j_{p,z}(z, r_\perp, \omega). \tag{A.57}$$

One can show that the induced Coulomb potential inherits the angular dependence from the induced proton current:

$$\begin{aligned}\delta \boldsymbol{V}_C(\boldsymbol{r}, \omega) = {} & \delta V_{C,z}(z, r_\perp, \omega) \cos K\varphi \; \boldsymbol{e}_z + \delta V_{C,\perp}(z, r_\perp, \omega) \cos K\varphi \; \boldsymbol{e}_\perp \\ & + \delta V_{C,\varphi}(z, r_\perp, \omega) \sin K\varphi \; \boldsymbol{e}_\varphi,\end{aligned} \tag{A.58}$$

and can be decomposed in an analogous way:

$$\begin{aligned}\delta \boldsymbol{V}_C(\boldsymbol{r}, \omega) = {} & \frac{1}{\sqrt{2}} \left[\delta V_{C,1}(z, r_\perp, \omega) \cos{(K-1)\varphi} + \delta V_{C,2}(z, r_\perp, \omega) \cos{(K+1)\varphi}\right] \boldsymbol{e}_x \\ & + \frac{1}{\sqrt{2}} \left[\delta V_{C,1}(z, r_\perp, \omega) \sin{(K-1)\varphi} - \delta V_{C,2}(z, r_\perp, \omega) \sin{(K+1)\varphi}\right] \boldsymbol{e}_y \\ & + \delta V_{C,3}(z, r_\perp, \omega) \cos K\varphi \boldsymbol{e}_z.\end{aligned} \tag{A.59}$$

Inserting Eqs. (A.54) and (A.59) into Eq. (A.52), and equating the terms with identical angular dependence leads to the following expressions:

$$\delta V_{C,1}(z, r_\perp, \omega) = \frac{e^2}{2} \int d\boldsymbol{r}' |\boldsymbol{r} - \boldsymbol{r}'| \triangle_{z', r'_\perp, |K-1|} \delta j_{p,1}(z', r'_\perp, \omega), \tag{A.60}$$

$$\delta V_{C,2}(z, r_\perp, \omega) = \frac{e^2}{2} \int d\boldsymbol{r}' |\boldsymbol{r} - \boldsymbol{r}'| \triangle_{z', r'_\perp, |K+1|} \delta j_{p,2}(z', r'_\perp, \omega), \tag{A.61}$$

$$\delta V_{C,3}(z, r_\perp, \omega) = \frac{e^2}{2} \int d\boldsymbol{r}' |\boldsymbol{r} - \boldsymbol{r}'| \triangle_{z', r'_\perp, |K|} \delta j_{p,3}(z', r'_\perp, \omega). \tag{A.62}$$

The detailed description of the procedure for solving integrals in Eqs. (A.60-A.62) by employing the Green's function can be found in Appendix A.3. Finally, the solutions of the integrals (A.60-A.62) are used to reconstruct the components of the induced Coulomb potential in the cylindrical coordinates:

$$\delta V_{C,\perp}(z, r_\perp, \omega) = \frac{1}{\sqrt{2}} \left[+\delta V_{C,1}(z, r_\perp, \omega) + \delta V_{C,2}(z, r_\perp, \omega)\right], \tag{A.63}$$

$$\delta V_{C,\varphi}(z, r_\perp, \omega) = \frac{1}{\sqrt{2}} \left[-\delta V_{C,1}(z, r_\perp, \omega) + \delta V_{C,2}(z, r_\perp, \omega)\right], \tag{A.64}$$

$$\delta V_{C,z}(z, r_\perp, \omega) = \delta V_{C,3}(z, r_\perp, \omega). \tag{A.65}$$

## A.5 Induced single particle Hamiltonian

The induced single-particle Hamiltonian reads:

$$\delta\hat{h} = \begin{bmatrix} \delta V + \delta S & -\boldsymbol{\sigma}\cdot\delta\boldsymbol{\Sigma} \\ -\boldsymbol{\sigma}\cdot\delta\boldsymbol{\Sigma} & \delta V - \delta S \end{bmatrix}, \tag{A.66}$$

with:

$$\delta V(\boldsymbol{r},\omega) = \delta V(z, r_\perp, \omega)\cos K\varphi, \tag{A.67}$$
$$\delta S(\boldsymbol{r},\omega) = \delta S(z, r_\perp, \omega)\cos K\varphi, \tag{A.68}$$
$$\begin{aligned}\delta\boldsymbol{\Sigma}(\boldsymbol{r},\omega) = {} & \delta\Sigma_z(z, r_\perp, \omega)\cos K\varphi\, \boldsymbol{e}_z + \delta\Sigma_\perp(z, r_\perp, \omega)\cos K\varphi\, \boldsymbol{e}_\perp \\ & + \delta\Sigma_\varphi(z, r_\perp, \omega)\sin K\varphi\, \boldsymbol{e}_\varphi.\end{aligned} \tag{A.69}$$

One can show that the induced single-particle Hamiltonian is block diagonal in the simplex-y HO basis:

$$\delta h(\omega) = \begin{bmatrix} \delta h_1(\omega) & 0 \\ 0 & \delta h_2(\omega) \end{bmatrix}. \tag{A.70}$$

Next, we describe the calculation of the matrix elements of the $\delta h_1(\omega)_{\alpha_1,\alpha_2}$ block. We use the same notation $\alpha = (d, n_z, n_r, \Lambda)$ as in Section 3.1.1, where $d = f, g$ denotes the large or small Dirac spinor component. First introduce the auxiliary potentials:

$$\delta\Sigma_1(z, r_\perp, \omega) = \frac{1}{\sqrt{2}}\left[\delta\Sigma_\perp(z, r_\perp, \omega) - \delta\Sigma_\varphi(z, r_\perp, \omega)\right], \tag{A.71}$$
$$\delta\Sigma_2(z, r_\perp, \omega) = \frac{1}{\sqrt{2}}\left[\delta\Sigma_\perp(z, r_\perp, \omega) + \delta\Sigma_\varphi(z, r_\perp, \omega)\right], \tag{A.72}$$
$$\delta\Sigma_3(z, r_\perp, \omega) = \delta\Sigma_z(z, r_\perp, \omega). \tag{A.73}$$

For convenience, we omit the $\omega$ and $z, r_\perp$ variables in the following expressions. If $d_1 = d_2 = f$ and $|\Lambda_1 - \Lambda_2| = K$, the matrix element $\delta h_1(\omega)_{\alpha_1,\alpha_2}$ reads:

$$\delta h_1(\omega)_{\alpha_1,\alpha_2} = \frac{1+\delta_{K,0}}{2}\int_{-\infty}^{+\infty} dz \int_0^{+\infty} r_\perp dr_\perp (\delta V + \delta S)\phi_{n_{z_1}}\phi_{n_{z_2}}\phi^{|\Lambda_1|}_{n_{r_1}}\phi^{|\Lambda_2|}_{n_{r_2}}. \tag{A.74}$$

If $d_1 = d_2 = g$ and $|\Lambda_1 - \Lambda_2| = K$, the matrix element $\delta h_1(\omega)_{\alpha_1,\alpha_2}$ reads:

$$\delta h_1(\omega)_{\alpha_1,\alpha_2} = \frac{1+\delta_{K,0}}{2}\int_{-\infty}^{+\infty} dz \int_0^{+\infty} r_\perp dr_\perp (\delta V - \delta S)\phi_{n_{z_1}}\phi_{n_{z_2}}\phi^{|\Lambda_1|}_{n_{r_1}}\phi^{|\Lambda_2|}_{n_{r_2}}. \tag{A.75}$$

If $d_1 \neq d_2$ and $\Lambda_1 + \Lambda_2 + 1 = +K$, the matrix element $\delta h_1(\omega)_{\alpha_1,\alpha_2}$ reads:

$$\delta h_1(\omega)_{\alpha_1,\alpha_2} = -\frac{1+\delta_{K,0}}{2}\sqrt{2}\mathrm{i}A^{\Sigma}_{\alpha_1,\alpha_2}\int_{-\infty}^{+\infty} dz \int_0^{+\infty} r_\perp dr_\perp \delta\Sigma_1\phi_{n_{z_1}}\phi_{n_{z_2}}\phi^{|\Lambda_1|}_{n_{r_1}}\phi^{|\Lambda_2|}_{n_{r_2}}. \tag{A.76}$$

If $d_1 \neq d_2$ and $\Lambda_1 + \Lambda_2 + 1 = -K$, the matrix element $\delta h_1(\omega)_{\alpha_1,\alpha_2}$ reads:

$$\delta h_1(\omega)_{\alpha_1,\alpha_2} = -\frac{1+\delta_{K,0}}{2}\sqrt{2}\mathfrak{i}A^{\Sigma}_{\alpha_1,\alpha_2}\int_{-\infty}^{+\infty}dz\int_0^{+\infty}r_\perp dr_\perp \delta\Sigma_2\phi_{n_{z_1}}\phi_{n_{z_2}}\phi^{|\Lambda_1|}_{n_{r_1}}\phi^{|\Lambda_2|}_{n_{r_2}}. \tag{A.77}$$

If $d_1 \neq d_2$ and $|\Lambda_1 - \Lambda_2| = K$, the matrix element $\delta h_1(\omega)_{\alpha_1,\alpha_2}$ reads:

$$\delta h_1(\omega)_{\alpha_1,\alpha_2} = -\frac{1+\delta_{K,0}}{2}\int_{-\infty}^{+\infty}dz\int_0^{+\infty}r_\perp dr_\perp \delta\Sigma_3\phi_{n_{z_1}}\phi_{n_{z_2}}\phi^{|\Lambda_1|}_{n_{r_1}}\phi^{|\Lambda_2|}_{n_{r_2}}. \tag{A.78}$$

The factor $A^{\Sigma}_{\alpha_1,\alpha_2}$ is equal to $-1$ if $d_1 = g$ and $d_2 = f$, otherwise it is equal to $+1$. All other matrix elements $\delta h_1(\omega)_{\alpha_1,\alpha_2}$ not listed above vanish. Notice that it is sufficient to calculate only the upper triangle of the matrix $\delta h_1(\omega)$, because there holds: $\delta h_1(\omega)_{\alpha_1,\alpha_2} = \delta h_1(\omega)_{\alpha_2,\alpha_1}$ for all $(\alpha_1,\alpha_2)$, except for those pairs $(\alpha_1,\alpha_2)$ satisfying $d_1 \neq d_2$ and $|\Lambda_1 + \Lambda_2 + 1| = K$, in which case there holds: $\delta h_1(\omega)_{\alpha_1,\alpha_2} = -\delta h_1(\omega)_{\alpha_2,\alpha_1}$.

The second block $\delta h_2(\omega)$ can be calculated directly from the first block $\delta h_1(\omega)$ because one can show that there holds: $\delta h_2(\omega)_{\alpha_1,\alpha_2} = \delta h_1(\omega)_{\alpha_1,\alpha_2}$ for all $(\alpha_1,\alpha_2)$, except for those pairs $(\alpha_1,\alpha_2)$ satisfying $d_1 \neq d_2$ and $|\Lambda_1 - \Lambda_2| = K$, in which case there holds: $\delta h_2(\omega)_{\alpha_1,\alpha_2} = -\delta h_1(\omega)_{\alpha_1,\alpha_2}$.

Integrals in Eqs. (A.74-A.78) are numerically calculated using the values of the induced potentials $\delta V(z^{iGH}, r_\perp^{iGL}, \omega)$, $\delta S(z^{iGH}, r_\perp^{iGL}, \omega)$ and $\delta\mathbf{\Sigma}(z^{iGH}, r_\perp^{iGL}, \omega)$ on the Gaussian quadrature grid. However, the domain of integration can be further reduced because functions $\phi_{n_z}(z)$ have a well defined parity: $\phi_{n_z}(-z) = (-1)^{n_z}\phi_{n_z}(z)$. For illustration, suppose we have a function $f(z, r_\perp)$ and want to calculate the integral:

$$I_{\alpha_1,\alpha_2} = \int_{-\infty}^{+\infty}dz\int_0^{+\infty}r_\perp dr_\perp f(z,r_\perp)\phi_{n_{z_1}}\phi_{n_{z_2}}\phi^{|\Lambda_1|}_{n_{r_1}}\phi^{|\Lambda_2|}_{n_{r_2}}. \tag{A.79}$$

Integral $I_{\alpha_1,\alpha_2}$ can be written as:

$$I_{\alpha_1,\alpha_2} = \int_0^{+\infty}dz\int_0^{+\infty}r_\perp dr_\perp \left(f(z,r_\perp) + (-1)^{n_{z_1}+n_{z_2}}f(-z,r_\perp)\right)\phi_{n_{z_1}}\phi_{n_{z_2}}\phi^{|\Lambda_1|}_{n_{r_1}}\phi^{|\Lambda_2|}_{n_{r_2}}. \tag{A.80}$$

Thus, if we have the values $f(z^{iGH}, r_\perp^{iGL})$ on Gaussian quadrature grid, we can calculate:

$$f_0(z^{iGH}, r_\perp^{iGL}) = f(+z^{iGH}, r_\perp^{iGL}) + f(-z^{iGH}, r_\perp^{iGL}), \tag{A.81}$$

$$f_1(z^{iGH}, r_\perp^{iGL}) = f(+z^{iGH}, r_\perp^{iGL}) - f(-z^{iGH}, r_\perp^{iGL}), \tag{A.82}$$

only for $z^{iGH} > 0$, and then depending on the parity of $n_{z_1} + n_{z_2}$ use $f_0$ or $f_1$ for calculating $I_{\alpha_1,\alpha_2}$, but now integrating only for $z^{iGH} > 0$, thus reducing the number of operations by half.

## A.6 Induced pairing field

In the following sections, for a given set $A \subseteq \mathbb{R}$, we use $\mathbf{1}_A(\cdot)$ to denote the characteristic function of the set $A$, and $\mathrm{sgn}(\cdot)$ to denote the signum function.

The induced pairing field in the HO simplex-y basis takes the following form:

$$\delta\Delta^{(\pm)}(\omega) = \begin{pmatrix} 0 & \delta\Delta_1^{(\pm)}(\omega) \\ -\left[\delta\Delta_1^{(\pm)}(\omega)\right]^T & 0 \end{pmatrix}. \tag{A.83}$$

In this section, we give an efficient formula for calculating $\delta\Delta_1^{(\pm)}(\omega)$ obtained from formula (2.89). Suppose we have $N_z, N_r, n_{z1}, n_{z2}, n_{r1}, n_{r2} \in \mathbb{N}_0$ and $\Lambda_1, \Lambda_2 \in \mathbb{Z}$. We will use the shorthand $k = (n_z, n_r, \Lambda)$ for triples of large component expansion of the Dirac spinor just as we did in Section 3.1.1. First we define:

$$\begin{aligned} W^{N_z,N_r}_{(n_{z1},n_{r1},\Lambda_1),(n_{z2},n_{r2},\Lambda_2)} =& \mathbf{1}_{\mathbb{N}_0\cap[0,n_{z1}+n_{z2}]}(N_z) \times \delta_{\mathrm{mod}(n_{z1}+n_{z2},2),\mathrm{mod}(N_z,2)} \times \\ & \mathbf{1}_{\mathbb{N}_0\cap\left[0,n_{r1}+n_{r2}+\frac{|\Lambda_1|+|\Lambda_2|-|\Lambda_1-\Lambda_2|}{2}\right]}(N_r) \times \\ & M^{n_{z1},n_{z2}}_{N_z,n_z} \times M^{n_{r1},\Lambda_1,n_{r2},-\Lambda_2}_{N_r,\Lambda_1-\Lambda_2,n_r,0} \times \\ & \frac{b_\perp\sqrt{b_z}}{(2\pi)^{3/4}} \times \frac{\sqrt{n_z!}}{2^{\frac{n_z}{2}}\left(\frac{n_z}{2}\right)!} \times \frac{\left(a^2-b_z^2\right)^{\frac{n_z}{2}}}{\left(a^2+b_z^2\right)^{\frac{n_z+1}{2}}} \times \frac{\left(b_\perp^2-a^2\right)^{n_r}}{\left(b_\perp^2+a^2\right)^{n_r+1}}, \end{aligned} \tag{A.84}$$

where we used the shorthand: $n_z = n_{z1} + n_{z2} - N_z$ and $n_r = n_{r1} + n_{r2} - N_r + \frac{|\Lambda_1|+|\Lambda_2|-|\Lambda_1-\Lambda_2|}{2}$. Coefficients $M^{n_{z1},n_{z2}}_{N_z,n_z}$ and $M^{n_{r1},\Lambda_1,n_{r2},\Lambda_2}_{N_r,\Lambda,n_r,\lambda}$ are Talmi-Moshinsky brackets, and are given in Appendix A.7. Notice that $W^{N_z,N_r}_{k,l}$ enjoy symmetry property: $W^{N_z,N_r}_{l,k} = W^{N_z,N_r}_{k,l}$.

Next, for any $N_z, N_r \in \mathbb{N}_0$, we define:

$$P^{(\pm)}_{N_z,N_r}(\omega) = \sum_{\substack{\mathrm{Shell}(k')\le N_{max} \\ \mathrm{Shell}(l')\le N_{max}}} W^{N_z,N_r}_{k',l'} \left(\delta\kappa_1^{(\pm)}(\omega)\right)_{k'l'}. \tag{A.85}$$

Similar to the selection rules governed in $\delta\rho_1(\omega)$ and $\delta\rho_2(\omega)$ from A.9, one can show that the following selection rule is fulfilled in the induced pairng tensor: $\left(\delta\kappa_1^{(\pm)}(\omega)\right)_{kl} + \left(\delta\kappa_1^{(\pm)}(\omega)\right)_{lk} \propto \delta_{|\Lambda_k-\Lambda_l|,K}$. Therefore, if we rewrite (A.85) as:

$$P^{(\pm)}_{N_z,N_r}(\omega) = \sum_{\substack{\mathrm{Shell}(k')\le N_{max} \\ \mathrm{Shell}(l')\le N_{max}}} W^{N_z,N_r}_{k',l'} \frac{1}{2}\left[\left(\delta\kappa_1^{(\pm)}(\omega)\right)_{k'l'} + \left(\delta\kappa_1^{(\pm)}(\omega)\right)_{l'k'}\right], \tag{A.86}$$

we see that the sum in (A.85) can be constrained by the additional selection rule: $|\Lambda_{k'}-\Lambda_{l'}| = K$. Finally, for any $k_1 = (n_{z1}, n_{r1}, \Lambda_1), k_2 = (n_{z2}, n_{r2}, \Lambda_2)$, the following formula holds:

$$\left(\delta\Delta_1^{(\pm)}(\omega)\right)_{k_1k_2} = -G \times \frac{1+\delta_{K,0}}{2} \times \delta_{|\Lambda_1-\Lambda_2|,K} \times \sum_{N_z'} \sum_{N_r'} W^{N_z',N_r'}_{k_1,k_2} P^{(\pm)}_{N_z',N_r'}(\omega), \tag{A.87}$$

where the first summation is over all $0 \le N_z' \le n_{z1} + n_{z2}$, satisfying $\mathrm{mod}(N_z', 2) = \mathrm{mod}(n_{z1} + n_{z2}, 2)$, and the second summation is over all $0 \le N_r' \le n_{r1} + n_{r2} + \frac{|\Lambda_1|+|\Lambda_2|-|\Lambda_1-\Lambda_2|}{2}$. We see that the tedious summation over all quantum numbers

has been separated in two independent parts: $\{k', l'\}$ and $\{N_z, N_r\}$ by means of coefficients $W$ which can be easily pre-calculated.

## A.7 Talmi-Moshinsky brackets

### A.7.1 One dimensional Talmi-Moshinsky brackets

For a given scale parameter $b_0 \geq 0$, and for any $n_z \in \mathbb{N}_0$, we introduce a sequence of functions:

$$\phi_{n_z}(z) = \frac{1}{\sqrt{b_0}} \frac{1}{\sqrt{\sqrt{\pi} 2^{n_z} n_z!}} H_{n_z}\left(\frac{z}{b_0}\right) \exp\left\{\left(-\frac{1}{2}\left(\frac{z}{b_0}\right)^2\right)\right\}, \quad \forall z \in \mathbb{R}, \tag{A.88}$$

where $H_n(\cdot)$ denotes $n^{\text{th}}$-degree Hermite polynomial. For any non-negative integers: $n_{z1}, n_{z1}, N_z, n_z \in \mathbb{N}_0$, we define one dimensional Talmy-Moshinsky bracket $M^{n_{z1},n_{z2}}_{N_z,n_z}$ as follows:

$$\begin{aligned} M^{n_{z1},n_{z2}}_{N_z,n_z} =& \mathbf{1}_{\mathbb{N}_0 \cap [0, n_{z1}+n_{z2}]}(N_z) \times \delta_{n_{z1}+n_{z2}, N_z+n_z} \\ & \times \frac{1}{\sqrt{2^{n_{z1}+n_{z2}}}} \times \sqrt{\frac{n_{z1}!\, n_{z2}!}{N_z!\, n_z!}} \\ & \times \sum_{p=\max\{0, n_{z1}-N_z\}}^{\min\{n_z, n_{z1}\}} (-1)^p \binom{n_z}{p} \binom{N_z}{n_{z1}-p}. \end{aligned} \tag{A.89}$$

Then, for any fixed $n_{z1}, n_{z2} \in \mathbb{N}_0$, and $z_1, z_2 \in \mathbb{R}$, it holds that:

$$\phi_{n_{z1}}(z_1)\phi_{n_{z2}}(z_2) = \sum_{N_z=0}^{+\infty} \sum_{n_z=0}^{+\infty} M^{n_{z1},n_{z2}}_{N_z,n_z} \phi_{N_z}\left(\frac{z_1+z_2}{\sqrt{2}}\right) \phi_{n_z}\left(\frac{z_2-z_1}{\sqrt{2}}\right). \tag{A.90}$$

Previous equations have been numerically verified for variuous combinations of $n_{z1}, n_{z2} \in \mathbb{N}_0, z_1, z_2 \in \mathbb{R}$. Notice that due to the constraints on $N_z$ and $n_z$ in (A.89), infinite series in (A.90) reduces to finite sum. Also notice that from equation (A.90), one can easily see the following symmetry:

$$M^{n_{z2},n_{z1}}_{N_z,n_z} = (-1)^{n_z} M^{n_{z1},n_{z2}}_{N_z,n_z}. \tag{A.91}$$

### A.7.2 Two dimensional Talmi-Moshinsky brackets

Let us assume that $b_0 > 0$ is a scale parameter, and for any $n_r \in \mathbb{N}_0, m \in \mathbb{Z}$, we define a sequence of functions:

$$\phi_{n_r,m}(\boldsymbol{\rho}) = \frac{1}{b_0}\sqrt{\frac{2n_r!}{(n_r+|m|)!}} \left(\frac{|\boldsymbol{\rho}|}{b_0}\right)^{|m|} L^{|m|}_{n_r}\left(\frac{|\boldsymbol{\rho}|^2}{b_0^2}\right) \exp\left(-\frac{1}{2}\frac{|\boldsymbol{\rho}|^2}{b_0^2}\right) \frac{e^{im\varphi}}{\sqrt{2\pi}}. \tag{A.92}$$

$\boldsymbol{\rho} = (|\boldsymbol{\rho}|\cos\varphi, |\boldsymbol{\rho}|\sin\varphi) \in \mathbb{R}^2$, where $L^{\alpha}_n(\cdot)$ denotes associated Laguerre polynomial. For any $n_{r1}, n_{r2}, N_r, n_r \in \mathbb{N}_0$ and $m_1, m_2, M, m \in \mathbb{Z}$, we define two dimensional Talmy-Moshinky bracket $M^{n_{r1},m_1,n_{r2},m_2}_{N_r,M,n_r,m}$ as follows:

$$
\begin{aligned}
M_{N_r,M,n_r,m}^{n_{r1},m_1,n_{r2},m_2} =& \mathbf{1}_{\mathbb{N}_0\cap\left[0,n_{r1}+n_{r2}+\frac{|m_1|+|m_2|-|M|-|m|}{2}\right]}(N_r)\times \\
& \mathbf{1}_{\mathbb{Z}\cap\left[-\frac{2n_{r1}+|m_1|+2n_{r2}+|m_2|}{2},+\frac{2n_{r1}+|m_1|+2n_{r2}+|m_2|}{2}\right]}\left(M-\frac{m_1+m_2}{2}\right)\times \\
& \delta_{m_1+m_2,M+m}\times\delta_{2n_{r1}+|m_1|+2n_{r2}+|m_2|,2N_r+|M|+2n_r+|m|}\times \\
& \frac{(-1)^{N_r+n_r+n_{r1}+n_{r2}}}{\sqrt{2^{2N_r+|M|+2n_r+|m|}}}\times\sqrt{\frac{n_{r1}!\,(n_{r1}+|m_1|)!\,n_{r2}!\,(n_{r2}+|m_2|)!}{N_r!\,(N_r+|M|)!\,n_r!\,(n_r+|m|)!}}\times \\
& \sum_{\substack{0\le p,q,r,s\le n_r\\ 0\le P,Q,R,S\le N_r\\ 0\le t\le|m|\\ 0\le T\le|M|\\ \text{(C1),(C2),(C3),(C4)}}}(-1)^{t+r+s}\binom{n_r}{p\;\;q\;\;r\;\;s}\binom{N_r}{P\;\;Q\;\;R\;\;S}\binom{|M|}{T}\binom{|m|}{t},
\end{aligned}
\tag{A.93}
$$

where the summation over $p,q,r,s,P,Q,R,S,t,T\in\mathbb{N}_0$, is performed with four additional constraints:

$$(\text{C1}) \;:\; p+q+r+s=n_r$$

$$(\text{C2}) \;:\; P+Q+R+S=N_r$$

$$(\text{C3}) \;:\; (2n_{r1}+|m_1|)-(2n_{r2}+|m_2|)+|m|+|M|=2(p+P)-2(q+Q)+2(t+T)$$

$$(\text{C4}) \;:\; m_1=(r+R)-(s+S)+\operatorname{sgn}(m)t+\operatorname{sgn}(M)T.$$

In (A.93), we use standard notation for the multinomial coefficients. Then, for any $n_{r1},n_{r2}\in\mathbb{N}_0$ and $m_1,m_2\in\mathbb{Z}$, there holds:

$$
\begin{aligned}
\phi_{n_{r1},m_1}(\boldsymbol{\rho}_1)\phi_{n_{r2},m_2}(\boldsymbol{\rho}_2) =& \sum_{M=-\infty}^{+\infty}\sum_{N_r=0}^{+\infty}\sum_{m=-\infty}^{+\infty}\sum_{n_r=0}^{+\infty}M_{N_r,M,n_r,m}^{n_{r1},m_1,n_{r2},m_2}\times \\
& \phi_{N_r,M}\left(\frac{\boldsymbol{\rho}_1+\boldsymbol{\rho}_2}{\sqrt{2}}\right)\phi_{n_r,m}\left(\frac{\boldsymbol{\rho}_2-\boldsymbol{\rho}_1}{\sqrt{2}}\right),
\end{aligned}
\tag{A.94}
$$

for all $\boldsymbol{\rho}_1,\boldsymbol{\rho}_2\in\mathbb{R}^2$. Previous equation has also been proven correct and numerically verified. Again, constraints on $N_r,n_r\in\mathbb{N}_0$ and $M,m\in\mathbb{Z}$ in (A.93) result in truncating the series in (A.94) to finite sum. Notice that from (A.94), one can easily confirm the following symmetry properties:

$$M_{N_r,M,n_r,m}^{n_{r2},m_2,n_{r1},m_1}=(-1)^m M_{N_r,M,n_r,m}^{n_{r1},m_1,n_{r2},m_2}, \tag{A.95}$$

$$M_{N_r,-M,n_r,-m}^{n_{r1},-m_1,n_{r2},-m_2}=M_{N_r,M,n_r,m}^{n_{r1},m_1,n_{r2},m_2}. \tag{A.96}$$

## A.8 QFAM equations in simplex-y basis

The matrix element of the multipole operator $f_{JK} = |\boldsymbol{r}|^J Y_{JK}(\theta,\phi)$ calculated in the HO basis reads:

$$\langle n_z n_r \Lambda m_s | |\boldsymbol{r}|^J Y_{JK}(\theta,\phi) | n'_z n'_r \Lambda' m'_s \rangle = \delta_{m_s,m'_s}\delta_{\Lambda-\Lambda',K}\times \\ \times \sqrt{\frac{2J+1}{4\pi}\frac{(J-K)!}{(J+K)!}}\langle n_z n_r|\Lambda|||\boldsymbol{r}|^J P_{JK}(\cos\theta)|n'_z n'_r|\Lambda'|\rangle, \tag{A.97}$$

where $P_{JK}(\cos\theta)$ denotes the associated Legendre polynomial. Due to the selection rule $m_s = m'_s$ in the previous expression, the $f_{JK}$ operator is block diagonal in the simplex-y basis:

$$\langle n_z n_r \Lambda; s=\pm i | |\boldsymbol{r}|^J Y_{JK}(\theta,\phi) | n'_z n'_r \Lambda'; s=\pm i\rangle = (\delta_{\Lambda'-\Lambda,K} + \delta_{\Lambda-\Lambda',K})\times \\ \times \sqrt{\frac{2J+1}{4\pi}\frac{(J-K)!}{(J+K)!}}\langle n_z n_r|\Lambda|||\boldsymbol{r}|^J P_{JK}(\cos\theta)|n'_z n'_r|\Lambda'|\rangle. \tag{A.98}$$

For $K \geq 0$ we have:

$$\langle n_z n_r \Lambda; s=\pm i | f^{(+)}_{JK} | n'_z n'_r \Lambda'; s=\pm i\rangle = \sqrt{\frac{1+\delta_{K,0}}{2}}\delta_{|\Lambda'-\Lambda|,K}\times \\ \times \sqrt{\frac{2J+1}{4\pi}\frac{(J-K)!}{(J+K)!}}\langle n_z n_r|\Lambda|||\boldsymbol{r}|^J P_{JK}(\cos\theta)|n'_z n'_r|\Lambda|'\rangle, \tag{A.99}$$

$$f^{(+)}_{JK} = \begin{pmatrix} f_1 & 0 \\ 0 & f_2 \end{pmatrix}. \tag{A.100}$$

For this particular operator the following relation holds: $f_1 = f_2$, where $f_1$ (and $f_2$) are real and symmetric matrices. The single-quasiparticle states are ordered so that we first list states with $s = +i$, and then states with $s = -i$. The corresponding $U$ and $V$ matrices read:

$$U = \begin{pmatrix} u & 0 \\ 0 & u^* \end{pmatrix}, \quad V = \begin{pmatrix} 0 & -v^* \\ v & 0 \end{pmatrix}, \tag{A.101}$$

while the $F^{20}$ and $F^{02}$ matrices for the external operator $f$ read:

$$F^{20} = \begin{pmatrix} 0 & f^{20} \\ -[f^{20}]^T & \end{pmatrix}, \quad F^{02} = \begin{pmatrix} 0 & f^{02} \\ -[f^{02}]^T & \end{pmatrix}, \tag{A.102}$$

with $f^{20} = -\left(u^\dagger f_1 v + \left(u^\dagger f_2^* v\right)^\dagger\right)$ and $f^{02} = -\left(v^\dagger f_1 u + \left(v^\dagger f_2^* u\right)^\dagger\right)^T$. In the initial step of the QFAM iteration, we set the matrix elements of the induced Hamiltonian to zero, i.e. $\delta H^{20}_{\mu\nu}(\omega) = \delta H^{02}_{\mu\nu}(\omega) = 0$, and the initial QFAM matrices $X(\omega)$ and $Y(\omega)$ inherit the structure of the $F^{20}$ and $F^{02}$ matrices (see Eq. (A.102)). This structure is retained in all subsequent QFAM iterations:

$$X(\omega) = \begin{pmatrix} 0 & x(\omega) \\ -x^T(\omega) & 0 \end{pmatrix}, \quad Y(\omega) = \begin{pmatrix} 0 & y(\omega) \\ -y^T(\omega) & 0 \end{pmatrix}. \tag{A.103}$$

The induced density matrix is block diagonal:

$$\delta\rho(\omega) = UX(\omega)V^T + V^*Y^T(\omega)U^\dagger = \begin{pmatrix} \delta\rho_1(\omega) & 0 \\ 0 & \delta\rho_2(\omega) \end{pmatrix}, \tag{A.104}$$

with $\delta\rho_1(\omega) = -\left(ux(\omega)v^\dagger + vy^T(\omega)u^\dagger\right)$ and $\delta\rho_2(\omega) = -\left(vx(\omega)u^\dagger + uy^T(\omega)v^\dagger\right)^T$. Consequently, the induced single-particle Hamiltonian is also block diagonal:

$$\delta h(\omega) = \begin{pmatrix} \delta h_1(\omega) & 0 \\ 0 & \delta h_2(\omega) \end{pmatrix}. \tag{A.105}$$

The pairing tensors $\delta\kappa^{(+)}(\omega)$ and $\delta\kappa^{(-)}(\omega)$ are skew symmetric:

$$\delta\kappa^{(+)}(\omega) = UX(\omega)U^T + V^*Y^T(\omega)V^\dagger = \begin{pmatrix} 0 & \delta{\kappa_1}^{(+)}(\omega) \\ -\left[\delta{\kappa_1}^{(+)}(\omega)\right]^T & 0 \end{pmatrix}, \tag{A.106}$$

$$\delta\kappa^{(-)}(\omega) = V^*X^\dagger(\omega)V^\dagger + UY^*(\omega)U^T = \begin{pmatrix} 0 & \delta{\kappa_1}^{(-)}(\omega) \\ -\left[\delta{\kappa_1}^{(-)}(\omega)\right]^T & 0 \end{pmatrix}, \tag{A.107}$$

with $\delta{\kappa_1}^{(+)}(\omega) = ux(\omega)u^\dagger - vy^T(\omega)v^\dagger$ and $\delta{\kappa_1}^{(-)}(\omega) = -vx^\dagger(\omega)v^\dagger + uy^*(\omega)u^\dagger$. The pairing field acquires analogous form:

$$\delta\Delta^{(\pm)}(\omega) = \begin{pmatrix} 0 & \delta\Delta_1^{(\pm)}(\omega) \\ -\left[\delta\Delta_1^{(\pm)}(\omega)\right]^T & 0 \end{pmatrix}. \tag{A.108}$$

Finally, the induced Hamiltonian elements $\delta H^{20}(\omega)$ and $\delta H^{02}(\omega)$ read:

$$\delta H^{20}(\omega) = \begin{pmatrix} 0 & \delta h^{20}(\omega) \\ -\left[\delta h^{20}(\omega)\right]^T & 0 \end{pmatrix}, \quad \delta H^{02}(\omega) = \begin{pmatrix} 0 & \delta h^{02}(\omega) \\ -\left[\delta h^{02}(\omega)\right]^T & 0 \end{pmatrix}, \tag{A.109}$$

with:

$$\delta h^{20}(\omega) = -\left(u^\dagger\delta h_1(\omega)v + v^\dagger\delta h_2^T(\omega)u - u^\dagger\delta\Delta_1^{(+)}(\omega)u + v^\dagger\left[\delta\Delta_1^{(-)}(\omega)\right]^\dagger v\right), \tag{A.110}$$

$$\delta h^{02}(\omega) = -\left(v^\dagger\delta h_1(\omega)u + u^\dagger\delta h_2^T(\omega)v + v^\dagger\delta\Delta_1^{(+)}(\omega)v - u^\dagger\left[\delta\Delta_1^{(-)}(\omega)\right]^\dagger u\right)^T. \tag{A.111}$$

QFAM Eqs. (2.74) and (2.75) in simplex-y basis are reduced to the following form:

$$(E_\mu + E_\nu - \omega)x_{\mu\nu}(\omega) + \delta h^{20}_{\mu\nu}(\omega) + f^{20}_{\mu\nu} = 0, \tag{A.112}$$

$$(E_\mu + E_\nu + \omega)y_{\mu\nu}(\omega) + \delta h^{02}_{\mu\nu}(\omega) + f^{02}_{\mu\nu} = 0. \tag{A.113}$$

We notice that the quasiparticle-vibration coupling (qPVC) calculation necessitates also the $H^{11}$ part of the induced Hamiltonian and not just the $H^{20}$ and $H^{02}$ parts, even though the induced $H^{11}$ part doens't contribute to QFAM. Here we provide the details on calculating the induced $H^{11}$ part. Let us recall that the

induced Hamiltonian in quasiparticle basis is:

$$\begin{bmatrix} \delta H^{11}(\omega) & \delta H^{20}(\omega) \\ -\delta H^{02}(\omega) & -\left(\delta H^{11}(\omega)\right)^T \end{bmatrix} = \begin{bmatrix} U & V^* \\ V & U^* \end{bmatrix}^\dagger \begin{bmatrix} \delta h(\omega) & \delta\Delta^{(+)}(\omega) \\ -\left(\delta\Delta^{(-)}(\omega)\right)^* & -\delta h^T(\omega) \end{bmatrix} \begin{bmatrix} U & V^* \\ V & U^* \end{bmatrix}. \tag{A.114}$$

$\delta H^{11}(\omega)$ is thus given by:

$$\delta H^{11}(\omega) = U^\dagger \delta h(\omega) U - V^\dagger \delta h^T(\omega) V + U^\dagger \delta\Delta^{(+)}(\omega) V - V^\dagger \left(\delta\Delta^{(-)}(\omega)\right)^* U. \tag{A.115}$$

$\delta H^{11}(\omega)$ in the simplex-y HO basis is given by:

$$\delta H^{11}(\omega) = \begin{bmatrix} \delta h_1^{11}(\omega) & 0 \\ 0 & \delta h_2^{11}(\omega) \end{bmatrix}, \tag{A.116}$$

where $\delta h_1^{11}(\omega)$ and $\delta h_2^{11}(\omega)$ are given by:

$$\delta h_1^{11}(\omega) = u^\dagger \delta h_1(\omega) u - v^\dagger \delta h_2^T(\omega) v + u^\dagger \delta\Delta_1^{(+)}(\omega) v + v^\dagger \left(\delta\Delta_1^{(-)}(\omega)\right)^\dagger u, \tag{A.117}$$

$$\delta h_2^{11}(\omega) = -\left(v^\dagger \delta h_1(\omega) v - u^\dagger \delta h_2^T(\omega) u - v^\dagger \delta\Delta_1^{(+)}(\omega) u - u^\dagger \left(\delta\Delta_1^{(-)}(\omega)\right)^\dagger v\right)^T. \tag{A.118}$$

## A.9 Induced densities and currents

For completeness, in this section we provide detailed expressions for induced densities and currents. Again, we use set of indices $\alpha = (d, n_z, n_r, \Lambda)$ denoting an element of basis within a given simplex block, where $d = f$ denotes large, and $d = g$ small component of the Dirac spinor, respectively.

The selection rules for the induced density matrix $\delta\rho(\omega)$ is as follows. For $(\alpha_1, \alpha_2)$ such that $d_1 = d_2$, the matrix elements of $(\delta\rho_1(\omega) + \delta\rho_2(\omega))_{\alpha_1,\alpha_2}$ are zero if $|\Lambda_1 - \Lambda_2| \neq K$, while for $d_1 \neq d_2$ they are zero if $|\Lambda_1 + \Lambda_2 + 1| \neq K$. On the other hand, for $(\alpha_1, \alpha_2)$ such that $d_1 \neq d_2$ the matrix elements of $(\delta\rho_1(\omega) - \delta\rho_2(\omega))_{\alpha_1,\alpha_2}$ are zero if $|\Lambda_1 - \Lambda_2| \neq K$. For simplicity, in the following discussion we omit the frequency $\omega$ in $\delta\rho_1(\omega), \delta\rho_2(\omega)$, and the cylindrical coordinates $z, r_\perp$ in the HO eigenfunctions $\phi_{n_z}(z)$ and $\phi_{n_r}^{|\Lambda|}(r_\perp)$. Below we list the expressions for the induced densities and currents:

$$\delta\rho_v(\boldsymbol{r}, \omega) = \frac{\cos K\varphi}{2\pi} \sum_{\substack{\alpha_1,\alpha_2 \\ |\Lambda_1 - \Lambda_2| = K}} \left(\delta\rho_1 + \delta\rho_2\right)_{\alpha_1,\alpha_2} A^{\rho_v}_{\alpha_1,\alpha_2} \phi_{n_{z_1}} \phi_{n_{z_2}} \phi^{|\Lambda_1|}_{n_{r_1}} \phi^{|\Lambda_2|}_{n_{r_2}}, \tag{A.119}$$

$$A^{\rho_v}_{\alpha_1,\alpha_2} = \begin{cases} +1 & \text{for} \quad d_1 = d_2, \\ 0 & \text{for} \quad d_1 \neq d_2, \end{cases} \tag{A.120}$$

$$\delta\rho_s(\boldsymbol{r}, \omega) = \frac{\cos K\varphi}{2\pi} \sum_{\substack{\alpha_1,\alpha_2 \\ |\Lambda_1 - \Lambda_2| = K}} \left(\delta\rho_1 + \delta\rho_2\right)_{\alpha_1,\alpha_2} A^{\rho_s}_{\alpha_1,\alpha_2} \phi_{n_{z_1}} \phi_{n_{z_2}} \phi^{|\Lambda_1|}_{n_{r_1}} \phi^{|\Lambda_2|}_{n_{r_2}}, \tag{A.121}$$

$$A^{\rho_s}_{\alpha_1,\alpha_2} = \begin{cases} +1 & \text{for} \quad d_1 = d_2 = f, \\ -1 & \text{for} \quad d_1 = d_2 = g, \\ 0 & \text{for} \quad d_1 \neq d_2, \end{cases} \tag{A.122}$$

$$\delta j_z(\boldsymbol{r},\omega) = \frac{\cos K\varphi}{2\pi} \sum_{\substack{\alpha_1,\alpha_2 \\ |\Lambda_1-\Lambda_2|=K}} (\delta\rho_1 - \delta\rho_2)_{\alpha_1,\alpha_2} A^{j_z}_{\alpha_1,\alpha_2} \phi_{n_{z_1}} \phi_{n_{z_2}} \phi^{|\Lambda_1|}_{n_{r_1}} \phi^{|\Lambda_2|}_{n_{r_2}}, \tag{A.123}$$

$$A^{j_z}_{\alpha_1,\alpha_2} = \begin{cases} 0 & \text{for} \quad d_1 = d_2, \\ +1 & \text{for} \quad d_1 \neq d_2 = f, \end{cases} \tag{A.124}$$

$$\delta j_\perp(\boldsymbol{r},\omega) = \frac{\cos K\varphi}{2\pi\mathrm{i}} \sum_{\substack{\alpha_1,\alpha_2 \\ |\Lambda_1+\Lambda_2+1|=K}} (\delta\rho_1 + \delta\rho_2)_{\alpha_1,\alpha_2} A^{j_\perp}_{\alpha_1,\alpha_2} \phi_{n_{z_1}} \phi_{n_{z_2}} \phi^{|\Lambda_1|}_{n_{r_1}} \phi^{|\Lambda_2|}_{n_{r_2}}, \tag{A.125}$$

$$A^{j_\perp}_{\alpha_1,\alpha_2} = \begin{cases} 0 & \text{for} \quad d_1 = d_2, \\ +1 & \text{for} \quad d_1 = f \text{ and } d_2 = g, \\ -1 & \text{for} \quad d_1 = g \text{ and } d_2 = f, \end{cases} \tag{A.126}$$

$$\delta j_\varphi(\boldsymbol{r},\omega) = \frac{\sin K\varphi}{-2\pi\mathrm{i}} \sum_{\substack{\alpha_1,\alpha_2 \\ |\Lambda_1+\Lambda_2+1|=K}} (\delta\rho_1 + \delta\rho_2)_{\alpha_1,\alpha_2} A^{j_\varphi}_{\alpha_1,\alpha_2} \phi_{n_{z_1}} \phi_{n_{z_2}} \phi^{|\Lambda_1|}_{n_{r_1}} \phi^{|\Lambda_2|}_{n_{r_2}}, \tag{A.127}$$

$$A^{j_\varphi}_{\alpha_1,\alpha_2} = \mathrm{sgn}(\Lambda_1 + \Lambda_2 + 1) A^{j_\perp}_{\alpha_1,\alpha_2}. \tag{A.128}$$

In order to solve the Klein-Gordon equation for the space-like components of the currents, it is convenient to define: $\delta j_1 = (\delta j_\perp - \delta j_\varphi)/\sqrt{2}$ and $\delta j_2 = (\delta j_\perp + \delta j_\varphi)/\sqrt{2}$. Explicit expressions for $\delta j_1$ and $\delta j_2$ are given below:

$$\delta j_1(z, r_\perp, \omega) = \frac{\sqrt{2}}{1+\delta_{K,0}} \frac{1}{2\pi\mathrm{i}} \sum_{\substack{\alpha_1,\alpha_2 \\ \Lambda_1+\Lambda_2+1=+K}} (\delta\rho_1 + \delta\rho_2)_{\alpha_1,\alpha_2} A^{j_\perp}_{\alpha_1,\alpha_2} \phi_{n_{z_1}} \phi_{n_{z_2}} \phi^{|\Lambda_1|}_{n_{r_1}} \phi^{|\Lambda_2|}_{n_{r_2}}, \tag{A.129}$$

$$\delta j_2(z, r_\perp, \omega) = \frac{\sqrt{2}}{1+\delta_{K,0}} \frac{1}{2\pi\mathrm{i}} \sum_{\substack{\alpha_1,\alpha_2 \\ \Lambda_1+\Lambda_2+1=-K}} (\delta\rho_1 + \delta\rho_2)_{\alpha_1,\alpha_2} A^{j_\perp}_{\alpha_1,\alpha_2} \phi_{n_{z_1}} \phi_{n_{z_2}} \phi^{|\Lambda_1|}_{n_{r_1}} \phi^{|\Lambda_2|}_{n_{r_2}}. \tag{A.130}$$

Next we show how to calculate the Laplacians of the induced densities and currents. Using Talmi-Moshinsky brackets, one can show that the induced densities $\delta\rho_v(z, r_\perp, \omega)$, $\delta\rho_s(z, r_\perp, \omega)$ and current $\delta j_z(z, r_\perp, \omega)$ can be written as linear combinations of the basis functions:

$$\left\{ \phi_{N_z}(z, \tilde{b}_z) \phi^{|K|}_{N_r}(r_\perp, \tilde{b}_\perp) \right\},$$

with reduced oscillator length $\tilde{b}_0 = b_0/\sqrt{2}$. On the other hand, induced current $\delta j_1(z, r_\perp, \omega)$ is a linear combination of the basis functions:

$$\left\{ \phi_{N_z}(z, \tilde{b}_z) \phi^{|K-1|}_{N_r}(r_\perp, \tilde{b}_\perp) \right\},$$

while the induced current $\delta j_2(z, r_\perp, \omega)$ is a linear combination of basis functions:

$$\left\{ \phi_{N_z}(z, \tilde{b}_z) \phi^{|K+1|}_{N_r}(r_\perp, \tilde{b}_\perp) \right\}.$$

Finally, we can easily obtain expressions for the Laplacians of various densities and current components. For example, let us focus on $\delta\rho_v(z, r_\perp, \omega)$. As we have stated, $\delta\rho_v(z, r_\perp, \omega)$ can be written as:

$$\delta\rho_v(z, r_\perp, \omega) = \sum_{N_z, N_r} c_{N_z,N_r} \phi_{N_z}(z, \tilde{b}_z) \phi^{|K|}_{N_r}(r_\perp, \tilde{b}_\perp). \tag{A.131}$$

Essentially, we are interested in induced densities and currents evaluated only on a Gaussian quadrature grid points $(z^{i_{GH}}, r^{i_{GL}}_\perp)$ given by Gauss-Hermite and Gauss-Laguerre quadrature nodes. Once we have calculated the values of $\delta\rho_v(z^{i_{GH}}, r^{i_{GL}}_\perp, \omega)$, we can extract the coefficients $c_{N_z,N_r}$ by numerical integration:

$$c_{N_z,N_r} = \int_{-\infty}^{+\infty} dz \int_0^{+\infty} r_\perp dr_\perp \delta\rho_v(z, r_\perp, \omega) \phi_{N_z}(z, \tilde{b}_z) \phi^{|K|}_{N_r}(r_\perp, \tilde{b}_\perp). \tag{A.132}$$

If we apply the Laplacian operator on the basis function, we obtain the following expression:

$$\begin{aligned} \triangle_{z,r_\perp,K} \phi_{N_z}(z, \tilde{b}_z) \phi^{|K|}_{N_r}(r_\perp, \tilde{b}_\perp) = \left( \frac{z^2}{\tilde{b}_z^4} + \frac{r_\perp^2}{\tilde{b}_\perp^4} - \frac{2N_z + 1}{\tilde{b}_z^2} - \frac{2(2N_r + K + 1)}{\tilde{b}_\perp^2} \right) \times \\ \times \phi_{N_z}(z, \tilde{b}_z) \phi^{|K|}_{N_r}(r_\perp, \tilde{b}_\perp), \end{aligned} \tag{A.133}$$

where the cylindrical Laplace operator for a given value of $K$ is defined as:

$$\triangle_{z,r_\perp,K} = \frac{1}{r_\perp} \partial_{r_\perp} (r_\perp \partial_{r_\perp}) - \frac{K^2}{r_\perp^2} + \partial_z^2. \tag{A.134}$$

Now we can easily evaluate the Laplacian of the induced density $\delta\rho_v(z, r_\perp, \omega)$ on the Gaussian quadrature grid:

$$\triangle_{z,r_\perp,K} \delta\rho_v(z^{i_{GH}}, r^{i_{GL}}_\perp, \omega) = \sum_{N_z N_r} c_{N_z,N_r} \left( \triangle_{z,r_\perp,K} \phi_{N_z}(z^{i_{GH}}, \tilde{b}_z) \phi^{|K|}_{N_r}(r^{i_{GL}}_\perp, \tilde{b}_\perp) \right), \tag{A.135}$$

using Eq. (A.133) and calculated coefficients $c_{N_z,N_r}$ via Eq. (A.132).

## A.10 Performance and convergence of GMRES method

As an illustration, we have calculated the matrix $\mathbb{T}(\omega_\gamma)$ (defined in Eq. (3.58)) explicitly for deformed isotope $^{100}$Zr and $J = 1$, $K = 0$ isovector excitation operator. The ground state deformation is $\beta \approx 0.47$ and we have used the DD-ME2 effective interaction. However, we use only $N_{\text{shells}} = 6$ shells, otherwise it would be difficult to fit the matrix $\mathbb{T}(\omega_\gamma)$ into the computer memory. In Fig. A.1 we show the spectrum $\sigma(\mathbb{I} - \mathbb{T}(\omega_\gamma))$ for excitation frequency $\omega_\gamma = 30 + 0.05\mathrm{i}$ MeV. As we have anticipated, only a small fraction of eigenvalues are scattered away from 1. Motivated by the illustrative example shown in Section 3.1.5, this situation is well suited for the GMRES method, and thus in the `DIRQFAM` code we have substituted the previously used modified Broyden's method [29] with GMRES method.

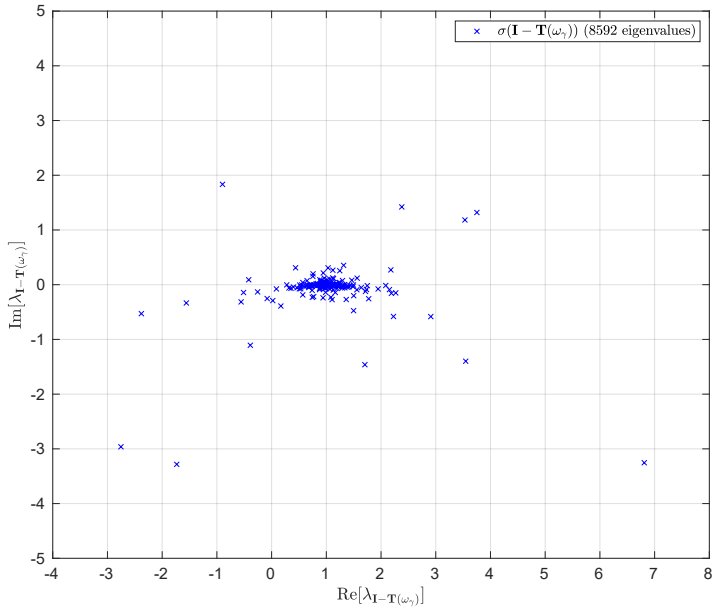


Figure A.1: Example of spectrum of matrix $\sigma(\mathbb{I}-\mathbb{T}(\omega_\gamma))$ for isovector $J=1,\ K=0$ excitation of $^{100}$Zr at $\omega_\gamma = 30+0.05\mathrm{i}$ MeV. We notice a large cluster of eigenvalues localized around 1, while only a small fraction of eigenvalues are scattered away from 1.

To demonstrate the superiority of the GMRES method in terms of convergence speed, we perform a calculation of the isovector $J=3,\ K=1$ response of heavy deformed $^{240}$Pu isotope with deformed ground state $\beta \approx 0.28$, where we use $N_{\mathrm{shells}} = 20$ oscillator shells and smearing width $\gamma = 0.05$ MeV. Again, DD-ME2 interaction and separable pairing are used. We sweep across frequencies in range from 0 MeV to 50 MeV with an increment of 0.02 MeV. The response function is shown in Fig. A.2 and it looks rather involved with many significant peaks. We compare the number of QFAM iterations performed by the modified Broyden's method where 70 vectors are retained in Broyden's history with the GMRES method using a maximum of 70 Arnoldi vectors. The same self-consistency tolerance is used in both methods. Modified Broyden's method took a total of 364527 QFAM iterations, i.e. on the average 146 QFAM iterations per frequency, while GMRES took a total of 107596 QFAM iterations[2], i.e. on the average 44 QFAM iterations per frequency. Thus, for this example, GMRES method required 3.4 times less QFAM iterations to find the response function compared to previously used Broyden's method. Maximum number of QFAM iterations for GMRES method was obtained at $\omega = 38.76$ MeV, where GMRES took 61 QFAM iterations, while Broyden's method took a maximum of 924 iterations at $\omega = 39.480$ MeV.

In Figure A.3 we show the number of QFAM iterations for a given frequency for GMRES and Broyden's method. We can see that Broyden's method tends

[2]We have taken into the account additional two QFAM iterations needed in GMRES, one for finding $b$, and another for finding the final solution $x_n$. We use $x_0 = 0$ as initial guess and thus the initial Arnoldi vector is $q_1 = r_0/\|r_0\| = b/\|b\|$, i.e. $q_1$ is given by $b$.

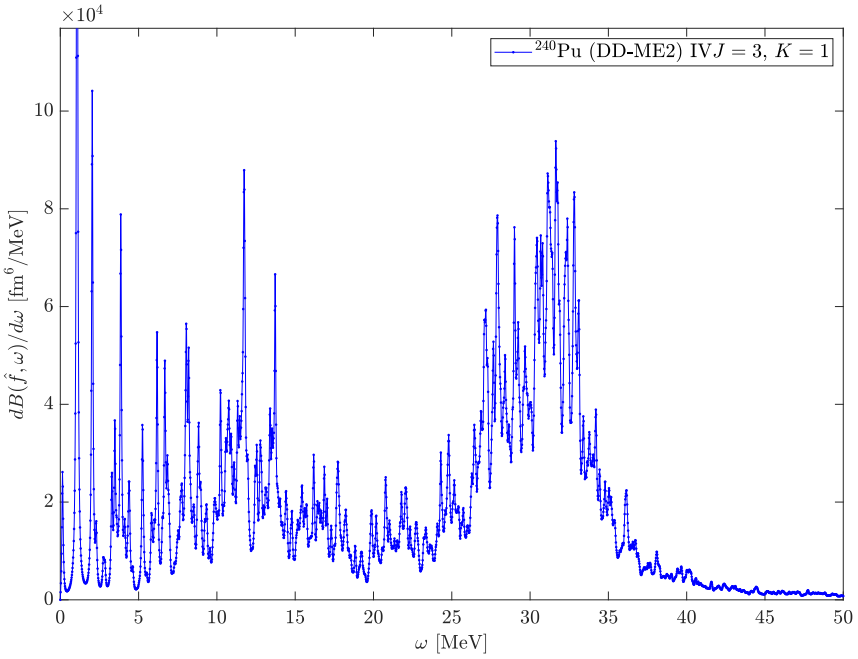


Figure A.2: Isovector octupole $J = 3$, $K = 1$ response of ground state $^{240}$Pu using DD-ME2 effective interaction and separable pairing. $\gamma = 0.05$ MeV is used as the complex part of the frequency $\omega_\gamma$ and $N_{\text{shells}} = 20(21)$ oscillator shells are used in the expansion of large (small) component of the spinor wave-function.

to have rather oscillating number of iterations while GMRES is approximatelly uniform regardless of the frequency $\omega$.

For lighter nuclei with a simpler profile of the response function and for a larger smearing $\gamma$, (e.g. $\gamma \sim 0.5$ MeV) performance superiority of GMRES compared to Broyden's method is less pronounced. After experimenting with various nuclei and smearing width value $\gamma$, the GMRES method has always proved superior to the modified Broyden's method. Firstly, the number of QFAM iterations is reduced at least by a factor of two, which is a significant improvement. Secondly, the number of iterations performed with the GMRES method does not depend significantly on the excitation energy, contrary to the Broyden's method. Obviously, this is a great advantage when distributing the calculations on separate computing nodes.

### Self-consistency tolerance and the number of Arnoldi vectors

Relative residual error $\frac{\|b-Ax_n\|}{\|b\|}$ of GMRES method applied on the QFAM problem is:

$$\frac{\|\boldsymbol{x}_{\text{free}}(\omega_\gamma) - (\mathbb{I} - \mathbb{T}(\omega_\gamma))\boldsymbol{x}_n(\omega_\gamma)\|}{\|\boldsymbol{x}_{\text{free}}(\omega_\gamma)\|} = \frac{\left\| \overbrace{\mathbb{T}(\omega_\gamma)\boldsymbol{x}_n(\omega_\gamma) + \boldsymbol{x}_{\text{free}}(\omega_\gamma)}^{\boldsymbol{x}_{n+1}(\omega_\gamma)} - \boldsymbol{x}_n(\omega_\gamma) \right\|}{\|\boldsymbol{x}_{\text{free}}(\omega_\gamma)\|}, \tag{A.136}$$

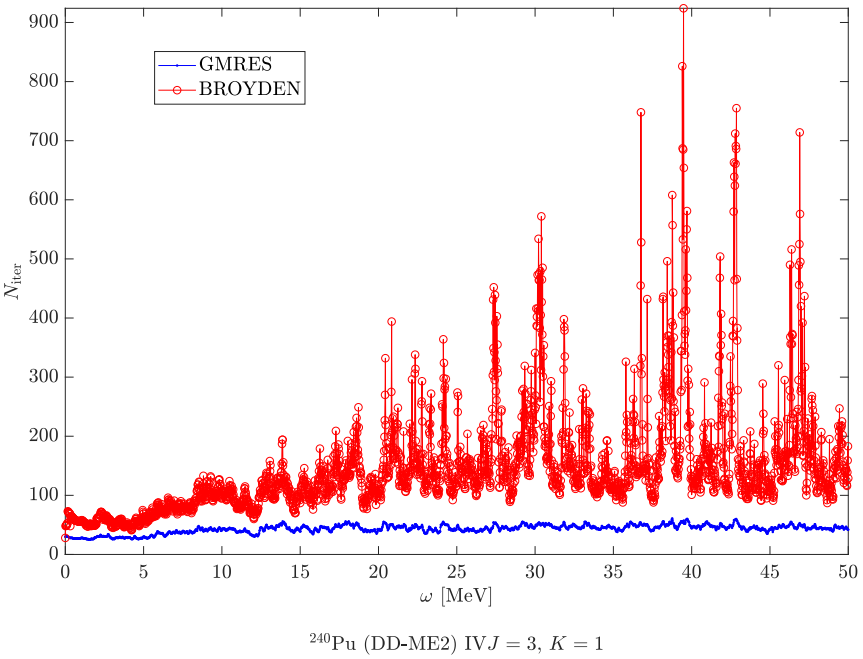


Figure A.3: Number of iterations needed for both GMRES and Broyden's method at particular frequency for obtaining the response shown in Figure A.2.

which means that the GMRES method terminates when the norm of the difference between two vectors: $\boldsymbol{x}_{n+1}(\omega_\gamma)$ and $\boldsymbol{x}_n(\omega_\gamma)$ in two consecutive GMRES iterations (relative to the norm of the free response) is below a certain threshold tolerance $\varepsilon$:

$$\frac{\|\boldsymbol{x}_{n+1}(\omega_\gamma) - \boldsymbol{x}_n(\omega_\gamma)\|}{\|\boldsymbol{x}_{\text{free}}(\omega_\gamma)\|} < \varepsilon. \tag{A.137}$$

Experience has shown that for reasonable values of smearing $\gamma \approx 0.01-1$ MeV, if $\varepsilon$ is set to $\varepsilon = 10^{-d}$, one obtains a strength function with at least $d-1$ correct most significant digits. Thus we recommend using $\varepsilon = 10^{-6}$, however, we have included this parameter in a set of input parameters and the user can select the specific value depending on the desired accuracy. During an extensive testing, even in the most extreme cases, GMRES method converged with tolerance of $\varepsilon = 10^{-6}$ within approximatelly $50-60$ iterations, i.e. retaining $50-60$ Arnoldi vectors are enough, however we have also included the number of retained Arnoldi vectors in computer memory as an input parameter. We recommend using a value of 70 vectors. This means that if GMRES fails to satisfy the relative residual error tolerance $\varepsilon$ within 70 iterations, the currently available GMRES solution after 70 iterations will be selected, and the corresponding strength function will be printed, where the final relative residual error will also be printed (with a message that the tolerance hasn't been satisfied). Thus, if the user insists on having a very small tolerance $\varepsilon$, which is not obtainable within 70 GMRES iterations, the user can easily increase the maximun allowed number of GMRES iterations via input parameter. Keep in mind that this increases the memory consumption of the program.

## A.11 Nucleon localization function

Here we derive the expression for the induced nucleon localization function given in Eq. (3.73). First we calculate the terms appearing in Eq. (3.71). Following the notation given in Section 3.1.1, first we calculate the following matrix elements:

$$\begin{aligned}
&\langle n_{z1}, n_{r_1}, \Lambda_1; \pm\mathbf{i}| \overleftarrow{\nabla}\overrightarrow{\nabla} |n_{z_2}, n_{r_2}, \Lambda_2; \pm\mathbf{i}\rangle = \\
&+ \partial_z\phi_{n_{z_1}}(z)\partial_z\phi_{n_{z_2}}(z)\phi^{|\Lambda_1|}_{n_{r_1}}(r_\perp)\phi^{|\Lambda_2|}_{n_{r_2}}(r_\perp)\frac{\cos((\Lambda_1-\Lambda_2)\varphi)}{2\pi} \\
&+ \phi_{n_{z_1}}(z)\phi_{n_{z_2}}(z)\partial_{r_\perp}\phi^{|\Lambda_1|}_{n_{r_1}}(r_\perp)\partial_{r_\perp}\phi^{|\Lambda_2|}_{n_{r_2}}(r_\perp)\frac{\cos((\Lambda_1-\Lambda_2)\varphi)}{2\pi} \\
&+ \phi_{n_{z_1}}(z)\phi_{n_{z_2}}(z)\phi^{|\Lambda_1|}_{n_{r_1}}(r_\perp)\phi^{|\Lambda_2|}_{n_{r_2}}(r_\perp)\frac{\Lambda_1\Lambda_2}{r_\perp^2}\frac{\cos((\Lambda_1-\Lambda_2)\varphi)}{2\pi},
\end{aligned} \tag{A.138}$$

$$\begin{aligned}
&\langle n_{z1}, n_{r_1}, \Lambda_1; \pm\mathbf{i}| \overrightarrow{\nabla} |n_{z_2}, n_{r_2}, \Lambda_2; \pm\mathbf{i}\rangle = \\
&+ \left(\phi_{n_{z_1}}(z)\partial_z\phi_{n_{z_2}}(z)\phi^{|\Lambda_1|}_{n_{r_1}}(r_\perp)\phi^{|\Lambda_2|}_{n_{r_2}}(r_\perp)\frac{\cos((\Lambda_1-\Lambda_2)\varphi)}{2\pi}\right)\boldsymbol{e}_z \\
&+ \left(\phi_{n_{z_1}}(z)\phi_{n_{z_2}}(z)\phi^{|\Lambda_1|}_{n_{r_1}}(r_\perp)\partial_{r_\perp}\phi^{|\Lambda_2|}_{n_{r_2}}(r_\perp)\frac{\cos((\Lambda_1-\Lambda_2)\varphi)}{2\pi}\right)\boldsymbol{e}_\perp \\
&+ \left(\phi_{n_{z_1}}(z)\phi_{n_{z_2}}(z)\phi^{|\Lambda_1|}_{n_{r_1}}(r_\perp)\phi^{|\Lambda_2|}_{n_{r_2}}(r_\perp)\frac{\Lambda_2}{r_\perp}\frac{\sin((\Lambda_1-\Lambda_2)\varphi)}{2\pi}\right)\boldsymbol{e}_\varphi.
\end{aligned} \tag{A.139}$$

Notice that the previous matrix elements are all real. We will drop the frequency $\omega$ and coordinate $(z, r_\perp, \varphi)$ variables for brevity and focus our attention on the second term in Eq. (3.71). Again we use the notation $\alpha = (d, n_z, n_r, \Lambda)$ for index of basis vector within the given simplex block. For each simplex $s = \pm\mathbf{i}$ block there holds:

$$\begin{aligned}
&\mathrm{Re}\left[\sum_{\alpha_1,\alpha_2}\left(\rho_0^{\cdot/T} + \eta e^{-\mathrm{i}\omega t}\delta\rho_{1/2} + \eta e^{+\mathrm{i}\omega t}\delta\rho^\dagger_{1/2}\right)_{\alpha_1,\alpha_2}\langle\alpha_2; \pm i|\overrightarrow{\nabla}|\alpha_1; \pm i\rangle\right] = \\
&\sum_{\substack{\alpha_1,\alpha_2\\ d_1=d_2}}\mathrm{Re}\left[\rho_0^{\cdot/T}\right]_{\alpha_1,\alpha_2}\frac{\langle\alpha_2; \pm\mathbf{i}|\overrightarrow{\nabla}|\alpha_1; \pm\mathbf{i}\rangle + \langle\alpha_1; \pm\mathbf{i}|\overrightarrow{\nabla}|\alpha_2; \pm\mathbf{i}\rangle}{2} \\
&+ \sum_{\substack{\alpha_1,\alpha_2\\ d_1=d_2}} 2\eta\,\mathrm{Re}\left[e^{-\mathrm{i}\omega t}\delta\rho_{1/2}\right]_{\alpha_1,\alpha_2}\frac{\langle\alpha_2; \pm\mathbf{i}|\overrightarrow{\nabla}|\alpha_1; \pm\mathbf{i}\rangle + \langle\alpha_1; \pm\mathbf{i}|\overrightarrow{\nabla}|\alpha_2; \pm\mathbf{i}\rangle}{2}.
\end{aligned} \tag{A.140}$$

Since we are averaging over the simplex number $s = \pm\mathbf{i}$, instead of $\rho_0^{\cdot/T}$ and $\delta\rho_{1/2}$, we use $\frac{1}{2}\left(\rho_0 + \rho_0^T\right)$ and $\frac{1}{2}\left(\delta\rho_1 + \delta\rho_2\right)$. For $(\alpha_1, \alpha_2)$ such that $d_1 = d_2$, matrix $(\rho_0)_{\alpha_1,\alpha_2}$ has selection rule $|\Lambda_1 - \Lambda_2| = 0$, while matrix $\frac{1}{2}\left(\delta\rho_1 + \delta\rho_2\right)_{\alpha_1,\alpha_2}$ has $|\Lambda_1 - \Lambda_2| = K$. Thus, if we define:

$$f_z^0 = \sum_{\substack{\alpha_1,\alpha_2\\ d_1=d_2\\ |\Lambda_1-\Lambda_2|=0}}\mathrm{Re}[\rho_0]_{\alpha_1,\alpha_2}\frac{\partial_z\phi_{n_{z_1}}\phi_{n_{z_2}} + \phi_{n_{z_1}}\partial_z\phi_{n_{z_2}}}{2}\phi^{|\Lambda_1|}_{n_{r_1}}\phi^{|\Lambda_2|}_{n_{r_2}}\frac{1}{2\pi}, \tag{A.141}$$

$$f_\perp^0 = \sum_{\substack{\alpha_1,\alpha_2 \\ d_1=d_2 \\ |\Lambda_1-\Lambda_2|=0}} \mathrm{Re}[\rho_0]_{\alpha_1,\alpha_2}\phi_{n_{z_1}}\phi_{n_{z_2}}\frac{\partial_{r_\perp}\phi_{n_{r_1}}^{|\Lambda_1|}\phi_{n_{r_2}}^{|\Lambda_2|}+\phi_{n_{r_1}}^{|\Lambda_1|}\partial_{r_\perp}\phi_{n_{r_2}}^{|\Lambda_2|}}{2}\frac{1}{2\pi}, \tag{A.142}$$

$$\delta f_z = \sum_{\substack{\alpha_1,\alpha_2 \\ d_1=d_2 \\ |\Lambda_1-\Lambda_2|=K}} \left(\frac{\delta\rho_1+\delta\rho_2}{2}\right)_{\alpha_1,\alpha_2}\frac{\partial_z\phi_{n_{z_1}}\phi_{n_{z_2}}+\phi_{n_{z_1}}\partial_z\phi_{n_{z_2}}}{2}\phi_{n_{r_1}}^{|\Lambda_1|}\phi_{n_{r_2}}^{|\Lambda_2|},\frac{\cos K\varphi}{2\pi}, \tag{A.143}$$

$$\delta f_\perp = \sum_{\substack{\alpha_1,\alpha_2 \\ d_1=d_2 \\ |\Lambda_1-\Lambda_2|=K}} \left(\frac{\delta\rho_1+\delta\rho_2}{2}\right)_{\alpha_1,\alpha_2}\phi_{n_{z_1}}\phi_{n_{z_2}}\frac{\partial_{r_\perp}\phi_{n_{r_1}}^{|\Lambda_1|}\phi_{n_{r_2}}^{|\Lambda_2|}+\phi_{n_{r_1}}^{|\Lambda_1|}\partial_{r_\perp}\phi_{n_{r_2}}^{|\Lambda_2|}}{2}\frac{\cos K\varphi}{2\pi}, \tag{A.144}$$

we have:

$$\begin{aligned}\mathrm{Re}\left[\left\langle\sum_{\alpha_1,\alpha_2}\rho_{\alpha_1,\alpha_2}\langle\alpha_2;s|\overrightarrow{\nabla}|\alpha_1;s\rangle\right\rangle_{s=\pm\mathrm{i}}\right] &= \left(f_z^0+2\eta\,\mathrm{Re}\left[e^{-\mathrm{i}\omega t}\delta f_z\right]+\mathcal{O}(\eta^2)\right)\boldsymbol{e}_z \\ &+\left(f_\perp^0+2\eta\,\mathrm{Re}\left[e^{-\mathrm{i}\omega t}\delta f_\perp\right]+\mathcal{O}(\eta^2)\right)\boldsymbol{e}_\perp \\ &+\mathcal{O}(\eta)\boldsymbol{e}_\varphi.\end{aligned} \tag{A.145}$$

Following analogous steps, but now for imaginary part, it is easy to see that the ground state part vanishes and we have:

$$\mathrm{Im}\left[\left\langle\sum_{\alpha_1,\alpha_2}\rho_{\alpha_1,\alpha_2}\langle\alpha_2;s|\overrightarrow{\nabla}|\alpha_1;s\rangle\right\rangle_{s=\pm\mathrm{i}}\right] = \mathcal{O}(\eta)\boldsymbol{e}_z+\mathcal{O}(\eta)\boldsymbol{e}_\perp+\mathcal{O}(\eta)\boldsymbol{e}_\varphi. \tag{A.146}$$

In total, when real and imaginary parts are combined, the second term in Eq. (3.71) is given by:

$$\begin{aligned}\left|\left\langle\sum_{\alpha_1,\alpha_2}\rho_{\alpha_1,\alpha_2}\langle\alpha_2;s|\overrightarrow{\nabla}|\alpha_1;s\rangle\right\rangle_{s=\pm\mathrm{i}}\right|^2 &= \left(f_z^0\right)^2+\left(f_\perp^0\right)^2 \\ &+4\eta\,\mathrm{Re}\left[e^{-\mathrm{i}\omega t}\left(f_z^0\delta f_z+f_\perp^0\delta f_\perp\right)\right]+\mathcal{O}(\eta^2).\end{aligned} \tag{A.147}$$

Following the same steps, if we define:

$$g^0 = \sum_{\substack{\alpha_1,\alpha_2 \\ d_1=d_2 \\ |\Lambda_1-\Lambda_2|=0}} \mathrm{Re}[\rho_0]_{\alpha_1,\alpha_2}\phi_{n_{z_1}}\phi_{n_{z_2}}\phi_{n_{r_1}}^{|\Lambda_1|}\phi_{n_{r_2}}^{|\Lambda_2|}\frac{1}{2\pi}, \tag{A.148}$$

$$h^0 = \sum_{\substack{\alpha_1,\alpha_2 \\ d_1=d_2 \\ |\Lambda_1-\Lambda_2|=0}} \mathrm{Re}[\rho_0]_{\alpha_1,\alpha_2} \Big( \partial_z \phi_{n_{z_1}} \partial_z \phi_{n_{z_2}} \phi_{n_{r_1}}^{|\Lambda_1|} \phi_{n_{r_2}}^{|\Lambda_2|} + \phi_{n_{z_1}} \phi_{n_{z_2}} \partial_{r_\perp} \phi_{n_{r_1}}^{|\Lambda_1|} \partial_{r_\perp} \phi_{n_{r_2}}^{|\Lambda_2|} + \phi_{n_{z_1}} \phi_{n_{z_2}} \phi_{n_{r_1}}^{|\Lambda_1|} \phi_{n_{r_2}}^{|\Lambda_2|} \frac{\Lambda_1 \Lambda_2}{r_\perp^2} \Big) \frac{1}{2\pi}, \tag{A.149}$$

$$\delta g = \sum_{\substack{\alpha_1,\alpha_2 \\ d_1=d_2 \\ |\Lambda_1-\Lambda_2|=K}} \left( \frac{\delta\rho_1 + \delta\rho_2}{2} \right)_{\alpha_1,\alpha_2} \phi_{n_{z_1}} \phi_{n_{z_2}} \phi_{n_{r_1}}^{|\Lambda_1|} \phi_{n_{r_2}}^{|\Lambda_2|} \frac{\cos K\varphi}{2\pi}, \tag{A.150}$$

$$\delta h = \sum_{\substack{\alpha_1,\alpha_2 \\ d_1=d_2 \\ |\Lambda_1-\Lambda_2|=K}} \left( \frac{\delta\rho_1 + \delta\rho_2}{2} \right)_{\alpha_1,\alpha_2} \Big( \partial_z \phi_{n_{z_1}} \partial_z \phi_{n_{z_2}} \phi_{n_{r_1}}^{|\Lambda_1|} \phi_{n_{r_2}}^{|\Lambda_2|} + \phi_{n_{z_1}} \phi_{n_{z_2}} \partial_{r_\perp} \phi_{n_{r_1}}^{|\Lambda_1|} \partial_{r_\perp} \phi_{n_{r_2}}^{|\Lambda_2|} + \phi_{n_{z_1}} \phi_{n_{z_2}} \phi_{n_{r_1}}^{|\Lambda_1|} \phi_{n_{r_2}}^{|\Lambda_2|} \frac{\Lambda_1 \Lambda_2}{r_\perp^2} \Big) \frac{\cos K\varphi}{2\pi}, \tag{A.151}$$

the remaining parts needed to calculate $D$ in Eq. (3.71) are given by:

$$\left\langle \sum_{\alpha_1,\alpha_2} \rho_{\alpha_1,\alpha_2} \langle \alpha_2; s | \alpha_1; s \rangle \right\rangle_{s=\pm\mathrm{i}} = g^0 + 2\eta \,\mathrm{Re}\left[ e^{-\mathrm{i}\omega t} \delta g \right] + \mathcal{O}(\eta^2), \tag{A.152}$$

$$\left\langle \sum_{\alpha_1,\alpha_2} \rho_{\alpha_1,\alpha_2} \langle \alpha_2; s | \overleftarrow{\nabla}\overrightarrow{\nabla} | \alpha_1; s \rangle \right\rangle_{s=\pm\mathrm{i}} = h^0 + 2\eta \,\mathrm{Re}\left[ e^{-\mathrm{i}\omega t} \delta h \right] + \mathcal{O}(\eta^2). \tag{A.153}$$

Next, we plug those parts into Eq. (3.71) and again keeping only the terms up to linear order in $\eta$ parameter, we get:

$$D(\boldsymbol{x}, t) = D^0(\boldsymbol{x}) + 2\eta \,\mathrm{Re}\left[ e^{-\mathrm{i}\omega t} \delta D(\boldsymbol{x}, \omega) \right] + \mathcal{O}(\eta^2), \tag{A.154}$$

where:

$$D^0(\boldsymbol{x}) = h^0(\boldsymbol{x}) - \frac{\left(f_z^0(\boldsymbol{x})\right)^2 + \left(f_\perp^0(\boldsymbol{x})\right)^2}{g^0(\boldsymbol{x})}, \tag{A.155}$$

$$\delta D(\boldsymbol{x}, \omega) = \delta h(\boldsymbol{x}, \omega) + \delta g(\boldsymbol{x}, \omega) \frac{\left(f_z^0(\boldsymbol{x})\right)^2 + \left(f_\perp^0(\boldsymbol{x})\right)^2}{\left(g^0(\boldsymbol{x})\right)^2} - 2 \frac{f_z^0(\boldsymbol{x}) \delta f_z(\boldsymbol{x}, \omega) + f_\perp^0(\boldsymbol{x}) \delta f_\perp(\boldsymbol{x}, \omega)}{g^0(\boldsymbol{x})}. \tag{A.156}$$

Next, the scaled $D(\boldsymbol{x},t)$ with Thomas-Fermi density is:

$$\frac{D(\boldsymbol{x},t)}{\tau_{\mathrm{TF}}(\boldsymbol{x})} = \underbrace{\frac{D^0(\boldsymbol{x},t)}{\tau^0_{\mathrm{TF}}(\boldsymbol{x})}}_{F^0(\boldsymbol{x})} + 2\eta\,\mathrm{Re}\left[e^{-\mathrm{i}\omega t}\underbrace{\left(\frac{\delta D(\boldsymbol{x},\omega)}{\tau^0_{\mathrm{TF}}(\boldsymbol{x})} - \frac{5}{3}\frac{D^0(\boldsymbol{x})}{\tau^0_{\mathrm{TF}}(\boldsymbol{x})}\frac{\delta g(\boldsymbol{x},\omega)}{g^0(\boldsymbol{x})}\right)}_{\delta F(\boldsymbol{x},\omega)}\right] + \mathcal{O}(\eta^2), \tag{A.157}$$

and finally, the nucleon localization function $\mathcal{C}(\boldsymbol{x},t)$ is:

$$\mathcal{C}(\boldsymbol{x},t) = \underbrace{\frac{1}{1+\left(F^0(\boldsymbol{x})\right)^2}}_{\mathcal{C}^0(\boldsymbol{x})} + 2\eta\,\mathrm{Re}\left[e^{-\mathrm{i}\omega t}\underbrace{\left(\frac{-2F^0(\boldsymbol{x})\delta F(\boldsymbol{x},\omega)}{\left(1+\left(F^0(\boldsymbol{x})\right)^2\right)^2}\right)}_{\delta\mathcal{C}(\boldsymbol{x},\omega)}\right] + \mathcal{O}(\eta^2). \tag{A.158}$$

## A.12 Spurious translational mode removal

Following the discussion in Section 3.1.8, we now focus on the specific operators in the simplex-y HO basis used within the `DIRQFAM` solver. The excitation operator is given by:

$$\hat{f}^{(+)}_{JK} = \frac{\hat{f}_{J,K} + (-1)^K \hat{f}_{J,-K}}{\sqrt{2+2\delta_{K,0}}}, \tag{A.159}$$

where:

$$\hat{f}_{J,K} = \sum_{p=1}^{Z} |\boldsymbol{r}^{(p)}|^J Y_{J,K}(\theta^{(p)},\varphi^{(p)}) \pm \sum_{n=1}^{N} |\boldsymbol{r}^{(n)}|^J Y_{J,K}(\theta^{(n)},\varphi^{(n)}). \tag{A.160}$$

The center of mass operator $\hat{R}^K_{\mathrm{CM}}$ is given by:

$$\hat{R}^K_{\mathrm{CM}} = \frac{1}{A}\sum_{i=1}^{A} \boldsymbol{r}^{(i)}_{1,K}, \tag{A.161}$$

with:

$$\boldsymbol{r}_{1,+1} = \frac{+1}{\sqrt{2}} r_\perp e^{-\mathrm{i}\varphi}, \quad \boldsymbol{r}_{1,0} = z, \quad \boldsymbol{r}_{1,-1} = \frac{-1}{\sqrt{2}} r_\perp e^{+\mathrm{i}\varphi}. \tag{A.162}$$

However, because the operator $\hat{f}^{(+)}_{J,K}$ excites both $+K$ and $-K$ modes, we have to make an analogous adjustment as in Eq. (A.159). For $K=0$ the operator $\hat{R}^{K=0}_{\mathrm{CM}}$ remains unmodified:

$$\hat{R}^{K=0}_{\mathrm{CM}} = \frac{1}{A}\sum_{i=1}^{A} z^{(i)}, \tag{A.163}$$

while for $K=1$ we define the operator:

$$\hat{R}^{K=1}_{\mathrm{CM}} = \frac{1}{A}\sum_{i=1}^{A} r^{(i)}_\perp \cos\varphi^{(i)} = \frac{1}{A}\sum_{i=1}^{A} x^{(i)}. \tag{A.164}$$

The corresponding total momentum operators are given by:

$$\hat{P}^{K=0}_{\rm CM} = -\mathrm{i}\sum_{i=1}^{A}\partial_{z^{(i)}}, \tag{A.165}$$

$$\hat{P}^{K=1}_{\rm CM} = -\mathrm{i}\sum_{i=1}^{A}\partial_{x^{(i)}} = -\mathrm{i}\sum_{i=1}^{A}\cos\varphi^{(i)}\partial_{r_\perp^{(i)}} - \frac{\sin\varphi^{(i)}}{r_\perp^{(i)}}\partial_{\varphi^{(i)}}. \tag{A.166}$$

Next we calculate the matrix representations of operators $\hat{R}^{K}_{\rm CM}$ and $\hat{P}^{K}_{\rm CM}$ One can easily prove the following relations:

$$\langle\alpha_1,s_1|\hat{R}^{K=0}_{\rm CM}|\alpha_2,s_2\rangle = \frac{1}{A}\delta_{s_1,s_2}\delta_{d_1,d_2}\delta_{n_{r_1},n_{r_2}}\delta_{|\Lambda_1-\Lambda_2|,0}\int_{-\infty}^{+\infty} z\phi_{n_{z_1}}\phi_{n_{z_2}}dz, \tag{A.167}$$

$$\begin{aligned}\langle\alpha_1,s_1|\hat{P}^{K=0}_{\rm CM}|\alpha_2,s_2\rangle = {}& \frac{-\mathrm{i}}{2}\delta_{s_1,s_2}\delta_{d_1,d_2}\delta_{n_{r_1},n_{r_2}}\delta_{|\Lambda_1-\Lambda_2|,0}\times\\ &\times\int_{-\infty}^{+\infty}\left(\phi_{n_{z_1}}\partial_z\phi_{n_{z_2}} - \phi_{n_{z_2}}\partial_z\phi_{n_{z_1}}\right)dz,\end{aligned} \tag{A.168}$$

$$\langle\alpha_1,s_1|\hat{R}^{K=1}_{\rm CM}|\alpha_2,s_2\rangle = \frac{1}{2A}\delta_{s_1,s_2}\delta_{d_1,d_2}\delta_{n_{z_1},n_{z_2}}\delta_{|\Lambda_1-\Lambda_2|,1}\int_{0}^{+\infty} r_\perp\phi^{|\Lambda_1|}_{n_{r_1}}\phi^{|\Lambda_2|}_{n_{r_2}}r_\perp dr_\perp, \tag{A.169}$$

$$\begin{aligned}&\langle\alpha_1,s_1|\hat{P}^{K=1}_{\rm CM}|\alpha_2,s_2\rangle = \frac{-\mathrm{i}}{4}\delta_{s_1,s_2}\delta_{d_1,d_2}\delta_{n_{z_1},n_{z_2}}\delta_{|\Lambda_1-\Lambda_2|,1}\times\\ &\times\int_{0}^{+\infty}\left[\left(\phi^{|\Lambda_1|}_{n_{r_1}}\partial_{r_\perp}\phi^{|\Lambda_2|}_{n_{r_2}} - \phi^{|\Lambda_2|}_{n_{r_2}}\partial_{r_\perp}\phi^{|\Lambda_1|}_{n_{r_1}}\right) + \frac{\Lambda_2^2-\Lambda_1^2}{r_\perp}\phi^{|\Lambda_1|}_{n_{r_1}}\phi^{|\Lambda_2|}_{n_{r_2}}\right]r_\perp dr_\perp.\end{aligned} \tag{A.170}$$

Previous equations show that the matrices $R_{CM}$ and $P_{CM}$ are block diagonal in the simplex-y HO basis:

$$R_{\rm CM} = \begin{bmatrix} r_{\rm CM} & 0\\ 0 & r_{\rm CM}\end{bmatrix} \quad\text{and}\quad P_{\rm CM} = \begin{bmatrix} p_{\rm CM} & 0\\ 0 & p_{\rm CM}\end{bmatrix}, \tag{A.171}$$

where Hermitian matrix $r_{\rm CM}$ satisfies $r_{\rm CM} = r^*_{\rm CM} = r^T_{\rm CM}$ and Hermitian matrix $p_{\rm CM}$ satisfies $p_{\rm CM} = -p^*_{\rm CM} = -p^T_{\rm CM}$. Matrices $r_{\rm CM}$ and $p_{\rm CM}$ can easily be calculated by using Eqs. (A.167-A.170) thus yielding the matrices $R^{20}$ and $P^{20}$:

$$R^{20} = \begin{bmatrix} 0 & r^{20}\\ -\left(r^{20}\right)^T & 0\end{bmatrix} \quad\text{and}\quad P^{20} = \begin{bmatrix} 0 & p^{20}\\ -\left(p^{20}\right)^T & 0\end{bmatrix}. \tag{A.172}$$

Matrices $r^{20}$ and $p^{20}$ read[3]:

$$r^{20} = -\left(u^\dagger r_{\rm CM}v + v^\dagger r^T_{\rm CM}u\right) \quad\text{and}\quad p^{20} = -\left(u^\dagger p_{\rm CM}v + v^\dagger p^T_{\rm CM}u\right). \tag{A.173}$$

[3]See Eq. (B.6) in Ref. [2]

The general expression for the expectation value $\langle\Phi|\left[\hat{R},\hat{P}\right]|\Phi\rangle$ in Eq. (3.94) can be written as:

$$\langle\Phi|\left[\hat{R},\hat{P}\right]|\Phi\rangle = 2\,\mathrm{Tr}\left[\left(r^{20}\right)^{\dagger}p^{20}\right]. \tag{A.174}$$

Using the block simplex form of the $X$ and $Y$ matrices:

$$X=\begin{bmatrix}0 & x\\ -x^{T} & 0\end{bmatrix} \quad \text{and} \quad Y=\begin{bmatrix}0 & y\\ -y^{T} & 0\end{bmatrix}, \tag{A.175}$$

we obtain the following expressions for the expectation values $\langle\Phi|\left[\hat{O}^{\dagger}_{(\mathrm{calc})},\hat{R}\right]|\Phi\rangle$ and $\langle\Phi|\left[\hat{O}^{\dagger}_{(\mathrm{calc})},\hat{P}\right]|\Phi\rangle$ in Eqs. (3.92) and (3.93):

$$\langle\Phi|\left[\hat{O}^{\dagger}_{(\mathrm{calc})},\hat{R}\right]|\Phi\rangle = -\,\mathrm{Tr}\left[\left(r^{20}\right)^{\dagger}\left(+x+y^{T}\right)\right], \tag{A.176}$$

$$\langle\Phi|\left[\hat{O}^{\dagger}_{(\mathrm{calc})},\hat{P}\right]|\Phi\rangle = +\,\mathrm{Tr}\left[\left(p^{20}\right)^{\dagger}\left(-x+y^{T}\right)\right]. \tag{A.177}$$

Equations (3.95) and (3.96), providing the spurious free values for the QFAM amplitudes, read:

$$x^{(\mathrm{phys})}_{\mu\nu} = x^{(\mathrm{calc})}_{\mu\nu} - \lambda_R r^{20}_{\mu\nu} - \lambda_P p^{20}_{\mu\nu}, \tag{A.178}$$

$$y^{(\mathrm{phys})}_{\mu\nu} = y^{(\mathrm{calc})}_{\mu\nu} + \lambda_R \left(r^{20}_{\mu\nu}\right)^{*} + \lambda_P \left(p^{20}_{\mu\nu}\right)^{*}. \tag{A.179}$$

To summarize, if the excitation operator has an odd value of $J$ and $K$ is equal to 0 or 1, the response is contaminated by the spurious $K^{\pi}=0^{-}$ or $K^{\pi}=1^{-}$ contributions. Once the self-consistent solution $x^{(\mathrm{calc})}(\omega), y^{(\mathrm{calc})}(\omega)$ is found, we first calculate the scalar coefficients:

$$\lambda_R = \frac{\mathrm{Tr}\left[\left(p^{20}\right)^{\dagger}\left(-x^{(\mathrm{calc})}(\omega)+y^{(\mathrm{calc})}(\omega)^{T}\right)\right]}{\langle\Phi|\left[\hat{R},\hat{P}\right]|\Phi\rangle}, \tag{A.180}$$

$$\lambda_P = \frac{\mathrm{Tr}\left[\left(r^{20}\right)^{\dagger}\left(+x^{(\mathrm{calc})}(\omega)+y^{(\mathrm{calc})}(\omega)^{T}\right)\right]}{\langle\Phi|\left[\hat{R},\hat{P}\right]|\Phi\rangle}. \tag{A.181}$$

Notice that both expressions in the numerator and denominator have to be summed over both the proton and the neutron contribution. Next, we calculate the corrected values of the QFAM amplitudes $x^{(\mathrm{phys})}(\omega)$ and $y^{(\mathrm{phys})}(\omega)$ according to Eqs. (A.178) and (A.179). Finally, these corrected values are used to calculate the spurious mode free response function. We have verified that for the isoscalar $J=1$ and $K=0,1$ excitation operator Eq. (A.159), the calculated response after correction is precisely zero.

# Appendix B

# KPM Appendix

## B.1 Existence of the QRPA eigenproblem solution

In this Appendix, we rigorously prove that in the case of positive-definite QRPA matrix, there exist positive eigenfrequencies $\Omega_i > 0$ and QRPA amplitudes $X^i, Y^i$, which are the generalized eigenpair of the QRPA matrix (4.7) satisfying the generalized normalization and closure relations (4.8). We start with two lemmas which describe the structure of eigenvectors of the QRPA and HFB matrices followed by a proposition covering the result. Much more detailed treatment of general QRPA eigenproblem can be found in Refs. [21, 54], however for convenience we provide here an easy to follow proof.

**Lemma 4.** *Let $A, B \in \mathbb{C}^{n\times n}$ such that $A^\dagger = A$ and $B^T = B$. Then there exist $Q \in \mathbb{C}^{n\times 2n}$ and diagonal $\mathrm{diag}[D_i]_{i=1}^{2n} \in \mathbb{R}^{2n\times 2n}$ such that $\begin{bmatrix} Q \\ Q^* \end{bmatrix} \in \mathbb{C}^{2n\times 2n}$ is unitary and:*

$$\begin{bmatrix} A & B \\ B^* & A^* \end{bmatrix} = \begin{bmatrix} Q \\ Q^* \end{bmatrix} \mathrm{diag}[D_i]_{i=1}^{2n} \begin{bmatrix} Q \\ Q^* \end{bmatrix}^\dagger . \tag{B.1}$$

*Proof.* Let us denote a Hermitian matrix $\mathcal{S} := \left[\begin{smallmatrix} A & B \\ B^* & A^* \end{smallmatrix}\right] \in \mathbb{C}^{2n\times 2n}$. Notice that for an eigenvalue $D \in \mathbb{R}$, if $\left[\begin{smallmatrix} x \\ y \end{smallmatrix}\right] \in \mathrm{Ker}\,(\mathcal{S} - D\mathbf{I}_{2n\times 2n})$, then also $\left[\begin{smallmatrix} y^* \\ x^* \end{smallmatrix}\right] \in \mathrm{Ker}\,(\mathcal{S} - D\mathbf{I}_{2n\times 2n})$. Let us fix an eigenvalue $D \in \sigma(\mathcal{S}) \subset \mathbb{R}$ with eigenspace $V_D := \mathrm{Ker}\,(\mathcal{S} - D\mathbf{I}_{2n\times 2n})$, and suppose $\dim V_D = p \in \mathbb{N}$. We will show that there exist orthonormal set of vectors: $\left[\begin{smallmatrix} x_1 \\ x_1^* \end{smallmatrix}\right], \ldots, \left[\begin{smallmatrix} x_p \\ x_p^* \end{smallmatrix}\right] \in \mathbb{C}^{2n}$, such that: $\mathrm{span}\left\{\left[\begin{smallmatrix} x_1 \\ x_1^* \end{smallmatrix}\right], \ldots, \left[\begin{smallmatrix} x_p \\ x_p^* \end{smallmatrix}\right]\right\} = V_D$. Suppose we have $0 \leq l < p$ orthonormal vectors: $\left[\begin{smallmatrix} x_1 \\ x_1^* \end{smallmatrix}\right], \ldots, \left[\begin{smallmatrix} x_l \\ x_l^* \end{smallmatrix}\right] \in V_D$. We will show how to construct a normalized vector $\left[\begin{smallmatrix} x_{l+1} \\ x_{l+1}^* \end{smallmatrix}\right] \in V_D$, which is orthogonal to previous vectors: $\left[\begin{smallmatrix} x_{l+1} \\ x_{l+1}^* \end{smallmatrix}\right] \perp \left[\begin{smallmatrix} x_1 \\ x_1^* \end{smallmatrix}\right], \ldots, \left[\begin{smallmatrix} x_l \\ x_l^* \end{smallmatrix}\right]$. Since $l < p$, there exists $\left[\begin{smallmatrix} x \\ y \end{smallmatrix}\right] \in V_D$ such that $\left[\begin{smallmatrix} x \\ y \end{smallmatrix}\right] \notin \mathrm{span}\left\{\left[\begin{smallmatrix} x_1 \\ x_1^* \end{smallmatrix}\right], \ldots, \left[\begin{smallmatrix} x_l \\ x_l^* \end{smallmatrix}\right]\right\}$. We can easily orthogonalize $\left[\begin{smallmatrix} x \\ y \end{smallmatrix}\right]$ against other vectors $\left\{\left[\begin{smallmatrix} x_1 \\ x_1^* \end{smallmatrix}\right], \ldots, \left[\begin{smallmatrix} x_l \\ x_l^* \end{smallmatrix}\right]\right\}$, i.e. there exists a normalized vector $\left[\begin{smallmatrix} x \\ y \end{smallmatrix}\right] \in V_D$, such that $\left[\begin{smallmatrix} x \\ y \end{smallmatrix}\right] \perp \left[\begin{smallmatrix} x_1 \\ x_1^* \end{smallmatrix}\right], \ldots, \left[\begin{smallmatrix} x_l \\ x_l^* \end{smallmatrix}\right]$. This gives a normalized vector $\left[\begin{smallmatrix} y^* \\ x^* \end{smallmatrix}\right] \in V_D$, such that:

$$\left\langle \left[\begin{smallmatrix} y^* \\ x^* \end{smallmatrix}\right], \left[\begin{smallmatrix} x_i \\ x_i^* \end{smallmatrix}\right] \right\rangle = \left\langle \left[\begin{smallmatrix} x \\ y \end{smallmatrix}\right], \left[\begin{smallmatrix} x_i \\ x_i^* \end{smallmatrix}\right] \right\rangle^* = 0, \ \forall i = 1, \ldots, l. \tag{B.2}$$

Thus, there exist two normalized vectors $\left[\begin{smallmatrix} x \\ y \end{smallmatrix}\right], \left[\begin{smallmatrix} y^* \\ x^* \end{smallmatrix}\right] \in V_D$, orthogonal to previous vectors: $\left[\begin{smallmatrix} x \\ y \end{smallmatrix}\right], \left[\begin{smallmatrix} y^* \\ x^* \end{smallmatrix}\right] \perp \left[\begin{smallmatrix} x_1 \\ x_1^* \end{smallmatrix}\right], \ldots, \left[\begin{smallmatrix} x_l \\ x_l^* \end{smallmatrix}\right]$. We differentiate two cases:

1. Assume that $y = -x^*$. Define $z := \mathfrak{i}x \in \mathbb{C}^n$. Then $\left[\begin{smallmatrix} z \\ z^* \end{smallmatrix}\right] = \mathfrak{i}\left[\begin{smallmatrix} x \\ y \end{smallmatrix}\right]$, and thus we constructed a normalized vector $\left[\begin{smallmatrix} z \\ z^* \end{smallmatrix}\right] \in V_D$, orthogonal to previous vectors: $\left[\begin{smallmatrix} z \\ z^* \end{smallmatrix}\right] \perp \left[\begin{smallmatrix} x_1 \\ x_1^* \end{smallmatrix}\right], \ldots, \left[\begin{smallmatrix} x_l \\ x_l^* \end{smallmatrix}\right]$.
2. Assume that $y \neq -x^*$, i.e. $x + y^* \neq \mathbf{0}_n$. Define $z := \frac{1}{\sqrt{2}||x+y^*||}(x + y^*) \in \mathbb{C}^n$. Then $\left[\begin{smallmatrix} z \\ z^* \end{smallmatrix}\right] = \frac{1}{\sqrt{2}||x+y^*||}\left(\left[\begin{smallmatrix} x \\ y \end{smallmatrix}\right] + \left[\begin{smallmatrix} y^* \\ x^* \end{smallmatrix}\right]\right) \in V_D$ is a normalized vector orthogonal to previous vectors: $\left[\begin{smallmatrix} z \\ z^* \end{smallmatrix}\right] \perp \left[\begin{smallmatrix} x_1 \\ x_1^* \end{smallmatrix}\right], \ldots, \left[\begin{smallmatrix} x_l \\ x_l^* \end{smallmatrix}\right]$.

Thus, we constructed a normalized vector $\left[\begin{smallmatrix} x_{l+1} \\ x_{l+1}^* \end{smallmatrix}\right] \in V_D$ orthogonal to previous vectors $\left[\begin{smallmatrix} x_{l+1} \\ x_{l+1}^* \end{smallmatrix}\right] \perp \left[\begin{smallmatrix} x_1 \\ x_1^* \end{smallmatrix}\right], \ldots, \left[\begin{smallmatrix} x_l \\ x_l^* \end{smallmatrix}\right]$. Repeating this procedure $p = \dim V_D$ times, we obtain an orthonormal basis for the eigenspace $V_D = \operatorname{span}\left\{\left[\begin{smallmatrix} x_1 \\ x_1^* \end{smallmatrix}\right], \ldots, \left[\begin{smallmatrix} x_p \\ x_p^* \end{smallmatrix}\right]\right\}$. Therefore, there exists $\boldsymbol{x}_D \in \mathbb{C}^{n \times \dim V_D}$ such that the matrix $\left[\begin{smallmatrix} \boldsymbol{x}_D \\ \boldsymbol{x}_D^* \end{smallmatrix}\right] \in \mathbb{C}^{2n \times \dim V_D}$ has orthonormal column vectors and $\mathcal{S}\left[\begin{smallmatrix} \boldsymbol{x}_D \\ \boldsymbol{x}_D^* \end{smallmatrix}\right] = D\left[\begin{smallmatrix} \boldsymbol{x}_D \\ \boldsymbol{x}_D^* \end{smallmatrix}\right]$. Repeating this argument for each eigenvalue $D \in \sigma(\mathcal{S})$ having degeneracy $\dim V_D$, and using the fact that two eigenvectors of Hermitian matrix that correspond to two different eigenvalues are orthogonal, we obtain a matrix $Q \in \mathbb{C}^{n \times 2n}$ such that $\left[\begin{smallmatrix} Q \\ Q^* \end{smallmatrix}\right] \in \mathbb{C}^{2n \times 2n}$ is unitary and $\mathcal{S}\left[\begin{smallmatrix} Q \\ Q^* \end{smallmatrix}\right] = \left[\begin{smallmatrix} Q \\ Q^* \end{smallmatrix}\right] \operatorname{diag}[D]_{D \in \sigma(\mathcal{S})}$. □

**Lemma 5.** *Let $h, \Delta \in \mathbb{C}^{n \times n}$ such that $h^\dagger = h$ and $\Delta^T = -\Delta$ with $\begin{bmatrix} h & \Delta \\ -\Delta^* & -h^* \end{bmatrix} \in \mathbb{C}^{2n \times 2n}$ invertible. Then there exist $U, V \in \mathbb{C}^{n \times n}$ and diagonal $E \in \mathbb{R}^{n \times n}$ with positive diagonal elements such that $\begin{bmatrix} U & V^* \\ V & U^* \end{bmatrix} \in \mathbb{C}^{2n \times 2n}$ is unitary and:*

$$\begin{bmatrix} h & \Delta \\ -\Delta^* & -h^* \end{bmatrix} = \begin{bmatrix} U & V^* \\ V & U^* \end{bmatrix} \begin{bmatrix} +E & \mathbf{0} \\ \mathbf{0} & -E \end{bmatrix} \begin{bmatrix} U & V^* \\ V & U^* \end{bmatrix}^\dagger. \tag{B.3}$$

*Proof.* The proof can be found in Ref. [54]. □

**Proposition 1.** *Let $A, B \in \mathbb{C}^{n \times n}$ such that $A^\dagger = A$, $B^T = B$ and $\begin{bmatrix} A & B \\ B^* & A^* \end{bmatrix} \in \mathbb{C}^{2n \times 2n}$ is positive-definite. Then there exist $X, Y \in \mathbb{C}^{n \times n}$ and diagonal $\Omega \in \mathbb{R}^{n \times n}$ with positive diagonal elements such that there holds:*

$$\begin{bmatrix} A & B \\ B^* & A^* \end{bmatrix} \begin{bmatrix} X & Y^* \\ Y & X^* \end{bmatrix} = \begin{bmatrix} \mathbf{I} & \mathbf{0} \\ \mathbf{0} & -\mathbf{I} \end{bmatrix} \begin{bmatrix} X & Y^* \\ Y & X^* \end{bmatrix} \begin{bmatrix} +\Omega & \mathbf{0} \\ \mathbf{0} & -\Omega \end{bmatrix}, \tag{B.4}$$

*and:*

$$\begin{bmatrix} X & Y^* \\ Y & X^* \end{bmatrix} \begin{bmatrix} \mathbf{I} & \mathbf{0} \\ \mathbf{0} & -\mathbf{I} \end{bmatrix} \begin{bmatrix} X & Y^* \\ Y & X^* \end{bmatrix}^\dagger = \begin{bmatrix} \mathbf{I} & \mathbf{0} \\ \mathbf{0} & -\mathbf{I} \end{bmatrix}. \tag{B.5}$$

*Proof.* Due to the Lemma 4 and positive-definitness of $\begin{bmatrix} A & B \\ B^* & A^* \end{bmatrix}$, there exist unitary $\begin{bmatrix} q_1 & q_2 \\ q_1^* & q_2^* \end{bmatrix} \in \mathbb{C}^{2n \times 2n}$ for $q_1, q_2 \in \mathbb{C}^{n \times n}$ and diagonal $d_1, d_2 \in \mathbb{R}^{n \times n}$ with positive diagonal elements such that:

$$\begin{bmatrix} A & B \\ B^* & A^* \end{bmatrix} = \begin{bmatrix} q_1 & q_2 \\ q_1^* & q_2^* \end{bmatrix} \begin{bmatrix} d_1 & \mathbf{0} \\ \mathbf{0} & d_2 \end{bmatrix} \begin{bmatrix} q_1 & q_2 \\ q_1^* & q_2^* \end{bmatrix}^\dagger. \tag{B.6}$$

Then, a square root matrix $\begin{bmatrix} A & B \\ B^* & A^* \end{bmatrix}^{1/2}$ is well defined as:

$$\begin{bmatrix} A & B \\ B^* & A^* \end{bmatrix}^{1/2} := \begin{bmatrix} q_1 & q_2 \\ q_1^* & q_2^* \end{bmatrix} \begin{bmatrix} \sqrt{d_1} & \mathbf{0} \\ \mathbf{0} & \sqrt{d_2} \end{bmatrix} \begin{bmatrix} q_1 & q_2 \\ q_1^* & q_2^* \end{bmatrix}^\dagger . \tag{B.7}$$

Trivial calculation shows that the invertible matrix:

$$\begin{bmatrix} A & B \\ B^* & A^* \end{bmatrix}^{1/2} \begin{bmatrix} \mathbf{I} & \mathbf{0} \\ \mathbf{0} & -\mathbf{I} \end{bmatrix} \begin{bmatrix} A & B \\ B^* & A^* \end{bmatrix}^{1/2} , \tag{B.8}$$

has the same structure as the HFB matrix in Lemma 5. Therefore, according to Lemma 5, there exist unitary $\begin{bmatrix} x & y^* \\ y & x^* \end{bmatrix} \in \mathbb{C}^{2n\times 2n}$ and diagonal $\Omega \in \mathbb{R}^{n\times n}$ with positive diagonal elements, such that:

$$\begin{bmatrix} A & B \\ B^* & A^* \end{bmatrix}^{1/2} \begin{bmatrix} \mathbf{I} & \mathbf{0} \\ \mathbf{0} & -\mathbf{I} \end{bmatrix} \begin{bmatrix} A & B \\ B^* & A^* \end{bmatrix}^{1/2} = \begin{bmatrix} x & y^* \\ y & x^* \end{bmatrix} \begin{bmatrix} +\Omega & \mathbf{0} \\ \mathbf{0} & -\Omega \end{bmatrix} \begin{bmatrix} x & y^* \\ y & x^* \end{bmatrix}^\dagger . \tag{B.9}$$

Let us define matrices $X, Y \in \mathbb{C}^{n\times n}$ as:

$$\begin{bmatrix} X & Y^* \\ Y & X^* \end{bmatrix} := \begin{bmatrix} \mathbf{I} & \mathbf{0} \\ \mathbf{0} & -\mathbf{I} \end{bmatrix} \begin{bmatrix} A & B \\ B^* & A^* \end{bmatrix}^{1/2} \begin{bmatrix} x & y^* \\ y & x^* \end{bmatrix} \begin{bmatrix} +\Omega^{-1/2} & \mathbf{0} \\ \mathbf{0} & -\Omega^{-1/2} \end{bmatrix} . \tag{B.10}$$

Notice that the matrix on the right-hand side in Eq. (B.10) indeed has the structure as the one on the left-hand side, i.e. matrices $X$ and $Y$ are well defined. Straightforward calculation then gives:

$$\begin{bmatrix} A & B \\ B^* & A^* \end{bmatrix} \begin{bmatrix} X & Y^* \\ Y & X^* \end{bmatrix} = \begin{bmatrix} \mathbf{I} & \mathbf{0} \\ \mathbf{0} & -\mathbf{I} \end{bmatrix} \begin{bmatrix} X & Y^* \\ Y & X^* \end{bmatrix} \begin{bmatrix} +\Omega & \mathbf{0} \\ \mathbf{0} & -\Omega \end{bmatrix} , \tag{B.11}$$

and:

$$\begin{bmatrix} X & Y^* \\ Y & X^* \end{bmatrix}^\dagger \begin{bmatrix} \mathbf{I} & \mathbf{0} \\ \mathbf{0} & -\mathbf{I} \end{bmatrix} \begin{bmatrix} X & Y^* \\ Y & X^* \end{bmatrix} = \begin{bmatrix} \mathbf{I} & \mathbf{0} \\ \mathbf{0} & -\mathbf{I} \end{bmatrix} . \tag{B.12}$$

Previous equation shows that:

$$\begin{bmatrix} X & Y^* \\ Y & X^* \end{bmatrix}^{-1} = \begin{bmatrix} \mathbf{I} & \mathbf{0} \\ \mathbf{0} & -\mathbf{I} \end{bmatrix} \begin{bmatrix} X & Y^* \\ Y & X^* \end{bmatrix}^\dagger \begin{bmatrix} \mathbf{I} & \mathbf{0} \\ \mathbf{0} & -\mathbf{I} \end{bmatrix} , \tag{B.13}$$

which finally gives:

$$\begin{bmatrix} X & Y^* \\ Y & X^* \end{bmatrix} \begin{bmatrix} \mathbf{I} & \mathbf{0} \\ \mathbf{0} & -\mathbf{I} \end{bmatrix} \begin{bmatrix} X & Y^* \\ Y & X^* \end{bmatrix}^\dagger = \begin{bmatrix} \mathbf{I} & \mathbf{0} \\ \mathbf{0} & -\mathbf{I} \end{bmatrix} . \tag{B.14}$$

□

## B.2 Synthetic generation of the QRPA matrices

In this Appendix we present some mathematical results that can be useful for synthetic generation of matrices involved in the QRPA equation. Such synthetic matrices can be used for numerical experiments and various tests. First, we prove the Bloch-Messiah theorem for bosons stated in Appendix E of Ref. [21], and then give a Remark explaining a procedure for generating QRPA matrix. In the literature, we could not find a detailed and easy to follow proof of the Bloch-Messiah theorem for bosons, and for completeness we provide a detailed proof here.

**Theorem 1.** *Let $X, Y \in \mathbb{C}^{n\times n}$ such that they satisfy:*

$$\begin{bmatrix} X & Y^* \\ Y & X^* \end{bmatrix} \begin{bmatrix} \mathbf{I} & \mathbf{0} \\ \mathbf{0} & -\mathbf{I} \end{bmatrix} \begin{bmatrix} X & Y^* \\ Y & X^* \end{bmatrix}^\dagger = \begin{bmatrix} \mathbf{I} & \mathbf{0} \\ \mathbf{0} & -\mathbf{I} \end{bmatrix}. \tag{B.15}$$

*Then there exist unitary $C, D \in \mathbb{C}^{n\times n}$ and $\theta_1, \theta_2, \ldots, \theta_n \geq 0$ such that:*

$$X = D \operatorname{diag}\left[\cosh\theta_i\right]_{i=1}^n C \quad \textit{and} \quad Y = D^* \operatorname{diag}\left[\sinh\theta_i\right]_{i=1}^n C. \tag{B.16}$$

*Proof.* The proof is similar to the proof of the Bloch-Messiah decomposition where in this case the role of the Youla decomposition of skew-symmetric matrix plays the Autonne-Takagi factorization of symmetric complex matrix. From equation:

$$\begin{bmatrix} X & Y^* \\ Y & X^* \end{bmatrix} \begin{bmatrix} \mathbf{I} & \mathbf{0} \\ \mathbf{0} & -\mathbf{I} \end{bmatrix} \begin{bmatrix} X & Y^* \\ Y & X^* \end{bmatrix}^\dagger = \begin{bmatrix} \mathbf{I} & \mathbf{0} \\ \mathbf{0} & -\mathbf{I} \end{bmatrix}, \tag{B.17}$$

one obtains: $\begin{bmatrix} X & Y^* \\ Y & X^* \end{bmatrix}^{-1} = \begin{bmatrix} \mathbf{I} & \mathbf{0} \\ \mathbf{0} & -\mathbf{I} \end{bmatrix} \begin{bmatrix} X & Y^* \\ Y & X^* \end{bmatrix}^\dagger \begin{bmatrix} \mathbf{I} & \mathbf{0} \\ \mathbf{0} & -\mathbf{I} \end{bmatrix}$, which gives:

$$\begin{bmatrix} X & Y^* \\ Y & X^* \end{bmatrix}^\dagger \begin{bmatrix} \mathbf{I} & \mathbf{0} \\ \mathbf{0} & -\mathbf{I} \end{bmatrix} \begin{bmatrix} X & Y^* \\ Y & X^* \end{bmatrix} = \begin{bmatrix} \mathbf{I} & \mathbf{0} \\ \mathbf{0} & -\mathbf{I} \end{bmatrix}. \tag{B.18}$$

Thus, the assumption of the Theorem gives $X, Y \in \mathbb{C}^{n\times n}$ which according to (B.17) and (B.18) satisfy:

$$XX^\dagger - Y^*Y^T = \mathbf{I}, \tag{B.19}$$

$$YX^\dagger = X^*Y^T, \tag{B.20}$$

$$X^\dagger X - Y^\dagger Y = \mathbf{I}, \tag{B.21}$$

$$Y^T X = X^T Y. \tag{B.22}$$

Let $X = U_x^\dagger \Sigma_x V_x$ be singular value decomposition of $X$, where $U_x, V_x \in \mathbb{C}^{n\times n}$ are unitary and $\Sigma_x = \operatorname{diag}[x_i]_{i=1}^n$ is diagonal matrix containing singular values: $(x_i)_{i=1}^n \subset [0, +\infty\rangle$. We will first show that all $(x_i)_{i=1}^n$ are positive. From (B.21) there holds: $Y^\dagger Y = V_x^\dagger(\Sigma_x^2 - \mathbf{I})V_x$, which gives $\sigma(Y^\dagger Y) = \{x_i^2 - 1 : i = 1, \ldots, n\}$. Since $Y^\dagger Y$ is Hermitian and positive-semidefinite, there holds $\sigma(Y^\dagger Y) \subset [0, +\infty\rangle$, which yields $x_i^2 - 1 \geq 0$, and thus $x_i \geq 1 > 0$, for all $i = 1, \ldots, n$. Define $\widetilde{X} := U_x X V_x^\dagger = \Sigma_x$ and $\widetilde{Y} := U_x^* Y V_x^\dagger$. One can easily show that $\widetilde{X}, \widetilde{Y} \in \mathbb{C}^{n\times n}$ also satisfy relations (B.19)-(B.22). Let us assume that the Theorem is true in the case if $X \in \mathbb{C}^{n\times n}$ is Hermitian and positive-definite. In that case, applying the

Theorem on $\widetilde{X},\widetilde{Y}\in\mathbb{C}^{n\times n}$, there exist $\widetilde{D},\widetilde{C}\in\mathbb{C}^{n\times n}$ unitary and $\theta_1,\ldots,\theta_n\geq 0$, such that $\widetilde{X}=\widetilde{D}\,\mathrm{diag}[\cosh\theta_i]_{i=1}^n\widetilde{C}$ and $\widetilde{Y}=\widetilde{D}^*\,\mathrm{diag}[\sinh\theta_i]_{i=1}^n\widetilde{C}$, yielding finally: $X=D\,\mathrm{diag}[\cosh\theta_i]_{i=1}^n C$ and $Y=D^*\,\mathrm{diag}[\sinh\theta_i]_{i=1}^n C$, where $D=U_x^\dagger\widetilde{D}$ and $C=\widetilde{C}V_x$ are unitary matrices. Therefore, if we prove the Theorem with additional assumption that $X\in\mathbb{C}^{n\times n}$ is Hermitian and positive definite, the proof will be completed and thus assume that $X,Y\in\mathbb{C}^{n\times n}$ satisfy (B.19)-(B.22), where $X\in\mathbb{C}^{n\times n}$ is Hermitian and positive-definite matrix. Since $X$ is Hermitian and positive-definite, its spectral decomposition is:

$$X=Z\left[\bigoplus_{i=1}^{p}x_i\mathbf{I}_{n_i\times n_i}\right]Z^\dagger, \tag{B.23}$$

where $Z\in\mathbb{C}^{n\times n}$ is unitary and $x_1^{[n_1]},\ldots,x_p^{[n_p]}>0$, are its eigenvalues having degeneracies: $n_1,\ldots,n_p\in\mathbb{N}$, with $n_1+\cdots+n_p=n$. Define $\rho:=XX^\dagger\in\mathbb{C}^{n\times n}$ and $\kappa:=YX^\dagger\in\mathbb{C}^{n\times n}$. According to Eq. (B.20), $\kappa\in\mathbb{C}^{n\times n}$ satisfies: $\kappa=YX^\dagger=X^*Y^T$, thus giving: $\kappa^T=\kappa$. Multiplying Eq. (B.22) by $X^\dagger$ from the right and by $X^*$ from the left yields:

$$\kappa\rho=\rho^*\kappa. \tag{B.24}$$

We have $\rho=XX^\dagger=Z\left[\bigoplus_{i=1}^n x_i^2\mathbf{I}_{n_i\times n_i}\right]Z^\dagger$, which combined with (B.24) gives:

$$(Z^T\kappa Z)\left[\bigoplus_{i=1}^{n}x_i^2\mathbf{I}_{n_i\times n_i}\right]=\left[\bigoplus_{i=1}^{n}x_i^2\mathbf{I}_{n_i\times n_i}\right](Z^T\kappa Z). \tag{B.25}$$

Previous equation gives the equality for blocks in matrix $Z^T\kappa Z$:

$$(x_i^2-x_j^2)(Z^T\kappa Z)_{[i,j]}=\mathbf{0}_{n_i\times n_j},\ i,j=1,\ldots,p, \tag{B.26}$$

which because $x_1,\ldots,x_p>0$ are positive gives:

$$(Z^T\kappa Z)_{[i,j]}=\mathbf{0}_{n_i\times n_j},\ i\neq j=1,\ldots,p, \tag{B.27}$$

i.e. $Z^T\kappa Z$ is block diagonal matrix:

$$Z^T\kappa Z=\bigoplus_{i=1}^{p}\widetilde{\kappa}_i, \tag{B.28}$$

having diagonal blocks $\widetilde{\kappa}_i\in\mathbb{C}^{n_i\times n_i}$, which are symmetric: $\widetilde{\kappa}_i^T=\widetilde{\kappa}_i$, because $Z^T\kappa Z$ is symmetric. Every complex symmetric matrix $\widetilde{\kappa}_i\in\mathbb{C}^{n_i\times n_i}$ has Autonne-Takagi factorization:

$$\widetilde{\kappa}_i=u_i^*\,\mathrm{diag}[\sigma_j^{(i)}]_{j=1}^{n_i}u_i^\dagger,\ i=1,\ldots,p, \tag{B.29}$$

where $u_i\in\mathbb{C}^{n_i\times n_i}$ are unitary and $\sigma_1^{(i)},\ldots,\sigma_{n_i}^{(i)}\geq 0$. Using these decompositions, from Eq. (B.28) we obtain:

$$(ZU)^T\kappa(ZU)=\bigoplus_{i=1}^{p}\mathrm{diag}[\sigma_j^{(i)}]_{j=1}^{n_i}, \tag{B.30}$$

where $U:=\bigoplus_{i=1}^p u_i\in\mathbb{C}^{n\times n}$ is unitary block diagonal matrix. On the other hand,

from (B.23), writing $\mathbf{I}_{n_i\times n_i} = u_i u_i^\dagger$, there holds:

$$X = Z\left[\bigoplus_{i=1}^{p} x_i u_i u_i^\dagger\right] Z^\dagger = (ZU)\left[\bigoplus_{i=1}^{p} \mathrm{diag}[x_i]_{j=1}^{n_i}\right](ZU)^\dagger. \tag{B.31}$$

Writing $\kappa = YX^\dagger$, Eq. (B.30) gives:

$$\bigoplus_{i=1}^{p} \mathrm{diag}[\sigma_j^{(i)}]_{j=1}^{n_i} = (ZU)^T Y X^\dagger (ZU) = (ZU)^T Y (ZU)\cdot\left((ZU)^\dagger X (ZU)\right)^\dagger, \tag{B.32}$$

which after using Eq. (B.31) and positivity of $x_1,\ldots,x_p > 0$ yields:

$$(ZU)^T Y (ZU) = \bigoplus_{i=1}^{p} \mathrm{diag}[\sigma_j^{(i)}/x_i]_{j=1}^{n_i}. \tag{B.33}$$

Let us define a unitary matrix $Q := ZU \in \mathbb{C}^{n\times n}$, and real non-negative numbers: $(y_j^{(i)})_{j=1}^{n_i} := (\sigma_j^{(i)}/x_i)_{j=1}^{n_i} \subset [0,+\infty\rangle$, for $i = 1,\ldots,p$. Then (B.31) and (B.33) finally give:

$$X = Q\left[\bigoplus_{i=1}^{p} \mathrm{diag}[x_i]_{j=1}^{n_i}\right] Q^\dagger \quad \text{and} \quad Y = Q^*\left[\bigoplus_{i=1}^{p} \mathrm{diag}[y_j^{(i)}]_{j=1}^{n_i}\right] Q^\dagger. \tag{B.34}$$

Inserting (B.34) into (B.21) we obtain:

$$x_i^2 - \left(y_j^{(i)}\right)^2 = 1,\ j = 1,\ldots,n_i,\ i = 1,\ldots,p, \tag{B.35}$$

which shows that there exist $\theta_1,\ldots,\theta_n \geq 0$, and $Q \in \mathbb{C}^{n\times n}$ unitary such that:

$$X = Q\,\mathrm{diag}[\cosh\theta_i]_{i=1}^{n} Q^\dagger \quad \text{and} \quad Y = Q^*\,\mathrm{diag}[\sinh\theta_i]_{i=1}^{n} Q^\dagger, \tag{B.36}$$

which completes the proof in a special case where $X \in \mathbb{C}^{n\times n}$ is Hermitian and positive-definite.

□

**Remark 1.** Suppose we want to generate a positive-definite QRPA matrix $\begin{bmatrix} A & B \\ B^* & A^* \end{bmatrix} \in \mathbb{C}^{2n\times 2n}$ having preselected positive eigenfrequencies $(\Omega_i)_{i=1}^n$. First, guided by the Theorem 1, we generate unitary matrices $C, D \in \mathbb{C}^{n\times n}$ together with $\theta_1,\theta_2,\ldots,\theta_n \geq 0$, and define:

$$X = D\,\mathrm{diag}\left[\cosh\theta_i\right]_{i=1}^{n} C, \quad Y = D^*\,\mathrm{diag}\left[\sinh\theta_i\right]_{i=1}^{n} C. \tag{B.37}$$

Second, we define matrices:

$$A = +\left[X\Omega X^\dagger + \left(Y\Omega Y^\dagger\right)^*\right], \quad B = -\left[X\Omega Y^\dagger + \left(X\Omega Y^\dagger\right)^T\right], \tag{B.38}$$

which satisfy $A^\dagger = A$ and $B^T = B$, where $\Omega = \mathrm{diag}[\Omega_i]_{i=1}^n \in \mathbb{R}^{n\times n}$. Then, one can

easily see that (B.4) and (B.5) are satisfied. Also, (B.4) and (B.5) imply:

$$\begin{bmatrix} A & B \\ B^* & A^* \end{bmatrix} = \begin{bmatrix} \mathbf{I} & \mathbf{0} \\ \mathbf{0} & -\mathbf{I} \end{bmatrix} \begin{bmatrix} X & Y^* \\ Y & X^* \end{bmatrix} \begin{bmatrix} +\Omega & \mathbf{0} \\ \mathbf{0} & +\Omega \end{bmatrix} \begin{bmatrix} X & Y^* \\ Y & X^* \end{bmatrix}^\dagger \begin{bmatrix} \mathbf{I} & \mathbf{0} \\ \mathbf{0} & -\mathbf{I} \end{bmatrix}, \tag{B.39}$$

which evidently shows that the generated QRPA matrix $\begin{bmatrix} A & B \\ B^* & A^* \end{bmatrix}$ is positive-definite.

## B.3 KPM method in $PQ$ representation of QRPA

### B.3.1 Definition of $PQ$ representation

We follow the notation for $PQ$ representation of QRPA introduced in Ref. [60]. Assume that we have two vectors $F^{20}, F^{02} \in \mathbb{C}^n$ and a Hermitian positive semidefinite QRPA matrix $\begin{bmatrix} A & B \\ B^* & A^* \end{bmatrix} \in \mathbb{C}^{2n\times 2n}$, where $A \in \mathbb{C}^{n\times n}$ is Hermitian $A^\dagger = A$ and $B \in \mathbb{C}^{n\times n}$ is symmetric $B^T = B$. Assume that there exist $P, Q \in \mathbb{C}^{n\times n}$, positive numbers $(M_i)_{i=1}^n \subseteq \langle 0, +\infty\rangle$ and non-negative numbers $(\Omega_i)_{i=1}^n \subseteq [0, +\infty\rangle$, such that there holds:

$$\begin{bmatrix} A & B \\ B^* & A^* \end{bmatrix} \begin{bmatrix} P & Q \\ -P^* & -Q^* \end{bmatrix} = \begin{bmatrix} \mathbf{I} & \mathbf{0} \\ \mathbf{0} & -\mathbf{I} \end{bmatrix} \begin{bmatrix} P & Q \\ -P^* & -Q^* \end{bmatrix} \begin{bmatrix} \mathbf{0} & -\mathrm{i}M^{-1} \\ \mathrm{i}M\Omega^2 & \mathbf{0} \end{bmatrix}, \tag{B.40}$$

$$\begin{bmatrix} P & Q \\ -P^* & -Q^* \end{bmatrix} \begin{bmatrix} \mathbf{0} & -\mathrm{i}\mathbf{I} \\ \mathrm{i}\mathbf{I} & \mathbf{0} \end{bmatrix} \begin{bmatrix} P & Q \\ -P^* & -Q^* \end{bmatrix}^\dagger = \begin{bmatrix} \mathbf{I} & \mathbf{0} \\ \mathbf{0} & -\mathbf{I} \end{bmatrix}, \tag{B.41}$$

$$\begin{bmatrix} P & Q \\ -P^* & -Q^* \end{bmatrix}^\dagger \begin{bmatrix} \mathbf{I} & \mathbf{0} \\ \mathbf{0} & -\mathbf{I} \end{bmatrix} \begin{bmatrix} P & Q \\ -P^* & -Q^* \end{bmatrix} = \begin{bmatrix} \mathbf{0} & -\mathrm{i}\mathbf{I} \\ \mathrm{i}\mathbf{I} & \mathbf{0} \end{bmatrix}, \tag{B.42}$$

where $M = \mathrm{diag}[M_i]_{i=1}^n$ and $\Omega = \mathrm{diag}[\Omega_i]_{i=1}^n$. Notice that Eq. (B.41) and Eq. (B.42) are equivalent. Let $\Omega_b > 0$ be the bounding frequency such that there holds: $(\pm\Omega_i)_{i=1}^n \subseteq \langle -\Omega_b, +\Omega_b\rangle$. Notice that for complex frequency $\omega_\gamma = \omega + \mathrm{i}\gamma$, with $\gamma > 0$, the matrix:

$$\begin{bmatrix} A & B \\ B^* & A^* \end{bmatrix} - \omega_\gamma \begin{bmatrix} \mathbf{I} & \mathbf{0} \\ \mathbf{0} & -\mathbf{I} \end{bmatrix} \tag{B.43}$$

is invertible, and thus there exists:

$$\begin{bmatrix} X(\omega_\gamma) \\ Y(\omega_\gamma) \end{bmatrix} = \left( \begin{bmatrix} A & B \\ B^* & A^* \end{bmatrix} - \omega_\gamma \begin{bmatrix} \mathbf{I} & \mathbf{0} \\ \mathbf{0} & -\mathbf{I} \end{bmatrix} \right)^{-1} \begin{bmatrix} F^{20} \\ F^{02} \end{bmatrix}. \tag{B.44}$$

Define the strength function as:

$$S(\omega_\gamma) = \begin{bmatrix} F^{20} \\ F^{02} \end{bmatrix}^\dagger \begin{bmatrix} X(\omega_\gamma) \\ Y(\omega_\gamma) \end{bmatrix}. \tag{B.45}$$

We seek the response function:

$$\frac{dB(\omega)}{d\omega} = \lim_{\gamma\to 0^+} \frac{-1}{\pi} \mathrm{Im}\, S(\omega_\gamma). \tag{B.46}$$

### B.3.2 Derivation of the response function

Notice that Eq. (B.41) gives:

$$\begin{bmatrix} P & Q \\ -P^* & -Q^* \end{bmatrix}^{-1} = \begin{bmatrix} \mathbf{0} & -\mathrm{i}\mathbf{I} \\ \mathrm{i}\mathbf{I} & \mathbf{0} \end{bmatrix} \begin{bmatrix} P & Q \\ -P^* & -Q^* \end{bmatrix}^{\dagger} \begin{bmatrix} \mathbf{I} & \mathbf{0} \\ \mathbf{0} & -\mathbf{I} \end{bmatrix}. \tag{B.47}$$

For any $\gamma > 0$ we have:

$$\begin{bmatrix} A & B \\ B^* & A^* \end{bmatrix} - \omega_\gamma \begin{bmatrix} \mathbf{I} & \mathbf{0} \\ \mathbf{0} & -\mathbf{I} \end{bmatrix} = \begin{bmatrix} \mathbf{I} & \mathbf{0} \\ \mathbf{0} & -\mathbf{I} \end{bmatrix} \begin{bmatrix} P & Q \\ -P^* & -Q^* \end{bmatrix} \begin{bmatrix} -\omega_\gamma \mathbf{I} & -\mathrm{i}M^{-1} \\ \mathrm{i}M\Omega^2 & -\omega_\gamma \mathbf{I} \end{bmatrix} \begin{bmatrix} P & Q \\ -P^* & -Q^* \end{bmatrix}^{-1}, \tag{B.48}$$

which using Eq. (B.47) yields:

$$\left( \begin{bmatrix} A & B \\ B^* & A^* \end{bmatrix} - \omega_\gamma \begin{bmatrix} \mathbf{I} & \mathbf{0} \\ \mathbf{0} & -\mathbf{I} \end{bmatrix} \right)^{-1} = \begin{bmatrix} P & Q \\ -P^* & -Q^* \end{bmatrix} \begin{bmatrix} M\Omega^2 & \mathrm{i}\omega_\gamma \mathbf{I} \\ -\mathrm{i}\omega_\gamma \mathbf{I} & M^{-1} \end{bmatrix}^{-1} \begin{bmatrix} P & Q \\ -P^* & -Q^* \end{bmatrix}^{\dagger} \tag{B.49}$$

If we define two column vectors $(\langle P_i|\hat{F}|0\rangle)_{i=1}^n, (\langle Q_i|\hat{F}|0\rangle)_{i=1}^n \in \mathbb{C}^n$ as follows:

$$\begin{bmatrix} (\langle P_i|\hat{F}|0\rangle)_{i=1}^n \\ (\langle Q_i|\hat{F}|0\rangle)_{i=1}^n \end{bmatrix} = \begin{bmatrix} P & Q \\ -P^* & -Q^* \end{bmatrix}^{\dagger} \begin{bmatrix} F^{20} \\ F^{02} \end{bmatrix}, \tag{B.50}$$

then there holds:

$$S(\omega_\gamma) = -\begin{bmatrix} (\langle P_i|\hat{F}|0\rangle)_{i=1}^n \\ (\langle Q_i|\hat{F}|0\rangle)_{i=1}^n \end{bmatrix}^{\dagger} \begin{bmatrix} \mathrm{diag}\left[\frac{M_i^{-1}}{\omega_\gamma^2 - \Omega_i^2}\right]_{i=1}^n & \mathrm{diag}\left[\frac{-\mathrm{i}\omega_\gamma}{\omega_\gamma^2 - \Omega_i^2}\right]_{i=1}^n \\ \mathrm{diag}\left[\frac{+\mathrm{i}\omega_\gamma}{\omega_\gamma^2 - \Omega_i^2}\right]_{i=1}^n & \mathrm{diag}\left[\frac{M_i\Omega_i^2}{\omega_\gamma^2 - \Omega_i^2}\right]_{i=1}^n \end{bmatrix} \begin{bmatrix} (\langle P_i|\hat{F}|0\rangle)_{i=1}^n \\ (\langle Q_i|\hat{F}|0\rangle)_{i=1}^n \end{bmatrix}, \tag{B.51}$$

which gives the response function (weak-* limit distribution to be more pedantic):

$$\begin{aligned} \frac{dB(\omega)}{d\omega} = \sum_{i=1}^{n} \Big\{ & M_i^{-1} |\langle P_i|\hat{F}|0\rangle|^2 \mathcal{D}_i(\omega) + M_i \Omega_i^2 |\langle Q_i|\hat{F}|0\rangle|^2 \mathcal{D}_i(\omega) + \\ & 2\,\mathrm{Im}\left[\langle P_i|\hat{F}|0\rangle^* \langle Q_i|\hat{F}|0\rangle\right] \mathcal{S}_i(\omega) \Big\}, \end{aligned} \tag{B.52}$$

where distributions $\mathcal{D}_i(\omega)$ and $\mathcal{S}_i(\omega)$ are defined as:

$$\mathcal{D}_i(\omega) = \lim_{\gamma \to 0^+} \mathcal{D}_i^\gamma(\omega) = \lim_{\gamma \to 0^+} \frac{-1}{\pi} \mathrm{Im}\left[\frac{1}{\omega_\gamma^2 - \Omega_i^2}\right], \tag{B.53}$$

$$\mathcal{S}_i(\omega) = \lim_{\gamma \to 0^+} \mathcal{S}_i^\gamma(\omega) = \lim_{\gamma \to 0^+} \frac{-1}{\pi} \mathrm{Im}\left[\frac{\omega_\gamma}{\omega_\gamma^2 - \Omega_i^2}\right]. \tag{B.54}$$

One can easily show that:

$$\mathcal{S}_i(\omega) = \lim_{\gamma \to 0^+} \frac{1}{2} \left( \frac{\gamma/\pi}{(\omega - \Omega_i)^2 + \gamma^2} + \frac{\gamma/\pi}{(\omega + \Omega_i)^2 + \gamma^2} \right) = \frac{\delta(\omega - \Omega_i) + \delta(\omega + \Omega_i)}{2}. \tag{B.55}$$

On the other hand, if $\Omega_i > 0$, one can easily see as well that there holds:

$$\mathcal{D}_i(\omega) = \lim_{\gamma\to 0^+} \frac{1}{2\Omega_i}\left(\frac{\gamma/\pi}{(\omega-\Omega_i)^2+\gamma^2} - \frac{\gamma/\pi}{(\omega-\Omega_i)^2+\gamma^2}\right) = \frac{\delta(\omega-\Omega_i)-\delta(\omega+\Omega_i)}{2\Omega_i}. \tag{B.56}$$

However, if one has $\Omega_i = 0$, then calculating the $\mathcal{D}_i(\omega)$ is a bit different but can be show to be equal to:

$$\mathcal{D}_i(\omega) = -\delta'(\omega), \tag{B.57}$$

which can be formally understood as a limiting case $\Omega_i \to 0^+$ from Eq. (B.56) as a negative central difference. One can easily now see that $\frac{dB(\omega)}{d\omega}$ can be rewritten as:

$$\begin{aligned}\frac{dB(\omega)}{d\omega} &= \\ &- \begin{bmatrix}(\langle P_i|\hat{F}|0\rangle)_{i=1}^n \\ (\langle Q_i|\hat{F}|0\rangle)_{i=1}^n\end{bmatrix}^\dagger \begin{bmatrix}\mathrm{diag}\left[M_i^{-1}\mathcal{D}_i(\omega)\right]_{i=1}^n & \mathrm{diag}\left[-\mathrm{i}\mathcal{S}_i(\omega)\right]_{i=1}^n \\ \mathrm{diag}\left[+\mathrm{i}\mathcal{S}_i(\omega)\right]_{i=1}^n & \mathrm{diag}\left[M_i\Omega_i^2\mathcal{D}_i(\omega)\right]_{i=1}^n\end{bmatrix} \begin{bmatrix}(\langle P_i|\hat{F}|0\rangle)_{i=1}^n \\ (\langle Q_i|\hat{F}|0\rangle)_{i=1}^n\end{bmatrix},\end{aligned} \tag{B.58}$$

which after reinserting (B.47) and (B.50) becomes:

$$\begin{aligned}&\frac{dB(\omega)}{d\omega} \\ &= \begin{bmatrix}F^{20} \\ F^{02}\end{bmatrix}^\dagger \begin{bmatrix}P & Q \\ -P^* & -Q^*\end{bmatrix} \begin{bmatrix}\mathrm{diag}[\mathcal{S}_i(\omega)]_{i=1}^n & \mathrm{diag}[-\mathrm{i}M_i^{-1}\mathcal{D}_i(\omega)]_{i=1}^n \\ \mathrm{diag}[\mathrm{i}M_i\Omega_i^2\mathcal{D}_i(\omega)]_{i=1}^n & \mathrm{diag}[\mathcal{S}_i(\omega)]_{i=1}^n\end{bmatrix} \begin{bmatrix}P & Q \\ -P^* & -Q^*\end{bmatrix}^{-1} \begin{bmatrix}F^{20} \\ -F^{02}\end{bmatrix}\end{aligned} \tag{B.59}$$

**Analytic function of $2\times 2$ matrix**

Here we recall some elementary facts. Let $f:\mathbb{C}\to\mathbb{C}$ be analytic and let $A\in\mathbb{C}^{2\times 2}$ be $2\times 2$ matrix. Suppose that $\left(\frac{1}{2}\operatorname{Tr} A\right)^2 - \det A \neq 0$, then there holds:

$$f(A) = \frac{f(\lambda_+)+f(\lambda_-)}{2}\mathbf{I} + \frac{f(\lambda_+)-f(\lambda_-)}{2\sqrt{\left(\frac{1}{2}\operatorname{Tr} A\right)^2 - \det A}}\left(A - \frac{\operatorname{Tr} A}{2}\mathbf{I}\right), \tag{B.60}$$

where $\lambda_\pm$ are the eigenvalues of $A$:

$$\lambda_\pm = \frac{\operatorname{Tr} A}{2} \pm \sqrt{\left(\frac{1}{2}\operatorname{Tr} A\right)^2 - \det A}. \tag{B.61}$$

On the other hand, if $A$ is such that $\left(\frac{1}{2}\operatorname{Tr} A\right)^2 - \det A = 0$, then there holds:

$$f(A) = f(\lambda)\mathbf{I} + f'(\lambda)\left(A - \frac{\operatorname{Tr} A}{2}\mathbf{I}\right), \tag{B.62}$$

for degenerated eigenvalue:

$$\lambda = \frac{\operatorname{Tr} A}{2}. \tag{B.63}$$

Now, using the previous equations, for $\Omega_i > 0$ there holds:

$$f\left(\begin{bmatrix} 0 & -\mathfrak{i}M_i^{-1} \\ \mathfrak{i}M_i\Omega_i^2 & 0 \end{bmatrix}\right) = \begin{bmatrix} \left(\frac{f(+\Omega_i)+f(-\Omega_i)}{2}\right) & -\mathfrak{i}M_i^{-1}\left(\frac{f(+\Omega_i)-f(-\Omega_i)}{2\Omega_i}\right) \\ \mathfrak{i}M_i\Omega_i^2\left(\frac{f(+\Omega_i)-f(-\Omega_i)}{2\Omega_i}\right) & \left(\frac{f(+\Omega_i)+f(-\Omega_i)}{2}\right) \end{bmatrix}, \tag{B.64}$$

while on the other hand, for $\Omega_i = 0$ there holds:

$$f\left(\begin{bmatrix} 0 & -\mathfrak{i}M_i^{-1} \\ \mathfrak{i}M_i\Omega_i^2 & 0 \end{bmatrix}\right) = \begin{bmatrix} f(0) & -\mathfrak{i}M_i^{-1}f'(0) \\ \mathfrak{i}M_i\Omega_i^2 f'(0) & f(0) \end{bmatrix}. \tag{B.65}$$

Notice that one can write for any $\Omega_i \geq 0$:

$$f\left(\begin{bmatrix} 0 & -\mathfrak{i}M_i^{-1} \\ \mathfrak{i}M_i\Omega_i^2 & 0 \end{bmatrix}\right) = \int_{-\Omega_b}^{+\Omega_b} f(\omega)\begin{bmatrix} \mathcal{S}_i(\omega) & -\mathfrak{i}M_i^{-1}\mathcal{D}_i(\omega) \\ \mathfrak{i}M_i\Omega_i^2\mathcal{D}_i(\omega) & \mathcal{S}_i(\omega) \end{bmatrix} d\omega, \tag{B.66}$$

and thus, for any analytic function $f : \mathbb{C} \to \mathbb{C}$, there finally holds:

$$f\left(\begin{bmatrix} 0 & -\mathfrak{i}M^{-1} \\ \mathfrak{i}M\Omega^2 & 0 \end{bmatrix}\right) = \int_{-\Omega_b}^{+\Omega_b} f(\omega)\begin{bmatrix} \mathrm{diag}\left[\mathcal{S}_i(\omega)\right]_{i=1}^n & \mathrm{diag}\left[-\mathfrak{i}M_i^{-1}\mathcal{D}_i(\omega)\right]_{i=1}^n \\ \mathrm{diag}\left[\mathfrak{i}M_i\Omega_i^2\mathcal{D}_i(\omega)\right]_{i=1}^n & \mathrm{diag}\left[\mathcal{S}_i(\omega)\right]_{i=1}^n \end{bmatrix} d\omega. \tag{B.67}$$

### B.3.3 KPM algorithm

Continuing on Eq. (B.59) using Eq. (B.67) we have for any analytic function $f : \mathbb{C} \to \mathbb{C}$:

$$\int_{-\Omega_b}^{+\Omega_b} \frac{dB(\omega)}{d\omega} f(\omega)d\omega = \begin{bmatrix} F^{20} \\ F^{02} \end{bmatrix}^\dagger \begin{bmatrix} P & Q \\ -P^* & -Q^* \end{bmatrix} f\left(\begin{bmatrix} 0 & -\mathfrak{i}M^{-1} \\ \mathfrak{i}M\Omega^2 & 0 \end{bmatrix}\right) \begin{bmatrix} P & Q \\ -P^* & -Q^* \end{bmatrix}^{-1} \begin{bmatrix} F^{20} \\ -F^{02} \end{bmatrix}, \tag{B.68}$$

which is equal to:

$$\int_{-\Omega_b}^{+\Omega_b} \frac{dB(\omega)}{d\omega} f(\omega)d\omega = \begin{bmatrix} F^{20} \\ F^{02} \end{bmatrix}^\dagger f\left(\begin{bmatrix} P & Q \\ -P^* & -Q^* \end{bmatrix} \begin{bmatrix} 0 & -\mathfrak{i}M^{-1} \\ \mathfrak{i}M\Omega^2 & 0 \end{bmatrix} \begin{bmatrix} P & Q \\ -P^* & -Q^* \end{bmatrix}^{-1}\right) \begin{bmatrix} F^{20} \\ -F^{02} \end{bmatrix}, \tag{B.69}$$

which using the QRPA eigenvalue equation (B.40) finally reduces to:

$$\int_{-\Omega_b}^{+\Omega_b} \frac{dB(\omega)}{d\omega} f(\omega)d\omega = \begin{bmatrix} F^{20} \\ F^{02} \end{bmatrix}^\dagger f\left(\begin{bmatrix} \mathbf{I} & \mathbf{0} \\ \mathbf{0} & -\mathbf{I} \end{bmatrix} \begin{bmatrix} A & B \\ B^* & A^* \end{bmatrix}\right) \begin{bmatrix} \mathbf{I} & \mathbf{0} \\ \mathbf{0} & -\mathbf{I} \end{bmatrix} \begin{bmatrix} F^{20} \\ F^{02} \end{bmatrix}. \tag{B.70}$$

If we expand the response function in Chebyshev series as follows:

$$\frac{dB(\omega)}{d\omega} = \frac{2/\pi}{\sqrt{\Omega_b^2 - \omega^2}} \sum_{n=0}^{+\infty} \mu_n T_n\left(\frac{\omega}{\Omega_b}\right), \tag{B.71}$$

the expansion coefficients are given by:

$$\mu_n = \frac{1}{1+\delta_{n,0}} \int_{-\Omega_b}^{+\Omega_b} \frac{dB(\omega)}{d\omega} T_n\left(\frac{\omega}{\Omega_b}\right) d\omega, \tag{B.72}$$

which are according to (B.70) given by:

$$\mu_n = \frac{1}{1+\delta_{n,0}} \begin{bmatrix} F^{20} \\ F^{02} \end{bmatrix}^\dagger T_n \left( \frac{1}{\Omega_b} \begin{bmatrix} \mathbf{I} & \mathbf{0} \\ \mathbf{0} & -\mathbf{I} \end{bmatrix} \begin{bmatrix} A & B \\ B^* & A^* \end{bmatrix} \right) \begin{bmatrix} \mathbf{I} & \mathbf{0} \\ \mathbf{0} & -\mathbf{I} \end{bmatrix} \begin{bmatrix} F^{20} \\ F^{02} \end{bmatrix}. \tag{B.73}$$

We obtain the same relation for the expansion coefficients as derived in Chapter 4 for $XY$ representation of QRPA, which shows that one can use the same KPM algorithm even if $\Omega_i = 0$ eigenfrequencies are present.

#### Imaginary eigenfrequencies

From Eq. (B.40) and Eq. (B.47) one can easily see:

$$\begin{bmatrix} A & B \\ B^* & A^* \end{bmatrix} = \begin{bmatrix} \mathbf{I} & \mathbf{0} \\ \mathbf{0} & -\mathbf{I} \end{bmatrix} \begin{bmatrix} P & Q \\ -P^* & -Q^* \end{bmatrix} \begin{bmatrix} M^{-1} & \mathbf{0} \\ \mathbf{0} & M\Omega^2 \end{bmatrix} \begin{bmatrix} P & Q \\ -P^* & -Q^* \end{bmatrix}^\dagger \begin{bmatrix} \mathbf{I} & \mathbf{0} \\ \mathbf{0} & -\mathbf{I} \end{bmatrix}, \tag{B.74}$$

and thus because the QRPA matrix is Hermitian, we have $\Omega_i^2 \in \mathbb{R}$. Therefore, the eigenfrequencies are either real or pure imaginary. If the QRPA matrix is positive semidefinite, we see that ideed there holds $\Omega_i \geq 0$. However, if the QRPA matrix fails to be positive semidefinite, one may encounter pure imaginary eigenfrequency. In that case, KPM method fails because when going trough the Chebyshev recursion one effectively calculates the values $T_n(\mathrm{i}x)$, for some $x > 0$, and one can see that $T_n(\mathrm{i}x)$ diverges as $n$ is increased. Thus, the calculated KPM coefficients $\mu_n$ will start to diverge if the QRPA matrix doens't correspond to the HFB energy minimum. This is one of the drawbacks of the KPM method. However, one may argue that QRPA as a study of small oscillations only makes sense to be performed around HFB minima. Thus, if we have chosen a large enough value of bounding frequency $\Omega_b$, and the KPM method still diverges in term of $\mu_n$ coefficients, we can conclude that we have at least one imaginary eigenfrequency.

### B.3.4 Test of KPM method in $PQ$ representation

#### QRPA characterization

Before we generate synthetic QRPA matrices, first we give a characterization of every QRPA matrix which will be our guide when generating such matrices.

**Theorem 2.** *Let $P, Q \in \mathbb{C}^{n\times n}$ such that they satisfy:*

$$\begin{bmatrix} P & Q \\ -P^* & -Q^* \end{bmatrix} \begin{bmatrix} \mathbf{0} & -\mathrm{i}\mathbf{I} \\ \mathrm{i}\mathbf{I} & \mathbf{0} \end{bmatrix} \begin{bmatrix} P & Q \\ -P^* & -Q^* \end{bmatrix}^\dagger = \begin{bmatrix} \mathbf{I} & \mathbf{0} \\ \mathbf{0} & -\mathbf{I} \end{bmatrix}. \tag{B.75}$$

*Then there exist $D, C \in \mathbb{C}^{n\times n}$ unitary and $\theta_1, \ldots, \theta_n \geq 0$ such that:*

$$P = \frac{\mathrm{i}}{\sqrt{2}} \left( D \operatorname{diag}[\cosh\theta_i]_{i=1}^n C + D \operatorname{diag}[\sinh\theta_i]_{i=1}^n C^* \right), \tag{B.76}$$

$$Q = \frac{1}{\sqrt{2}} \left( D \operatorname{diag}[\cosh\theta_i]_{i=1}^n C - D \operatorname{diag}[\sinh\theta_i]_{i=1}^n C^* \right). \tag{B.77}$$

*Proof.* Let us define two matrices:

$$X := \frac{-\mathrm{i}}{\sqrt{2}}P + \frac{1}{\sqrt{2}}Q, \quad Y := \frac{\mathrm{i}}{\sqrt{2}}P^* - \frac{1}{\sqrt{2}}Q^*, \tag{B.78}$$

then there holds:

$$\begin{bmatrix} X & Y^* \\ Y & X^* \end{bmatrix} = \begin{bmatrix} P & Q \\ -P^* & -Q^* \end{bmatrix} \begin{bmatrix} \frac{-\mathrm{i}}{\sqrt{2}}\mathbf{I} & \frac{-\mathrm{i}}{\sqrt{2}}\mathbf{I} \\ \frac{1}{\sqrt{2}}\mathbf{I} & \frac{-1}{\sqrt{2}}\mathbf{I} \end{bmatrix}. \tag{B.79}$$

One can straightforwardly show using Eq. (B.75) that there holds:

$$\begin{bmatrix} X & Y^* \\ Y & X^* \end{bmatrix} \begin{bmatrix} \mathbf{I} & \mathbf{0} \\ \mathbf{0} & -\mathbf{I} \end{bmatrix} \begin{bmatrix} X & Y^* \\ Y & X^* \end{bmatrix}^\dagger = \begin{bmatrix} \mathbf{I} & \mathbf{0} \\ \mathbf{0} & -\mathbf{I} \end{bmatrix}, \tag{B.80}$$

and thus Theorem 1 gives the existence of $D, C \in \mathbb{C}^{n\times n}$ unitary and $\theta_1, \ldots, \theta_n \geq 0$ such that there holds:

$$X = D\,\mathrm{diag}[\cosh\theta_i]_{i=1}^n C, \quad Y = D^*\,\mathrm{diag}[\sinh\theta_i]_{i=1}^n C. \tag{B.81}$$

Plugging (B.81) into the inverse relations of (B.78):

$$P := \frac{\mathrm{i}}{\sqrt{2}}X + \frac{\mathrm{i}}{\sqrt{2}}Y^*, \quad Q := \frac{1}{\sqrt{2}}X - \frac{1}{\sqrt{2}}Y^*, \tag{B.82}$$

yields (B.76) and (B.77). □

Suppose now that we have $P, Q \in \mathbb{C}^{n\times n}$ satisfying Eq. (B.75). Then Eq. (B.40) is equivalent to Eq. (B.74), which is equivalent to:

$$A = PM^{-1}P^\dagger + QM\Omega^2Q^\dagger, \quad B = PM^{-1}P^T + QM\Omega^2Q^T. \tag{B.83}$$

Thus, if we generate unitary matrices $D, C \in \mathbb{C}^{n\times n}$ and numbers $\theta_1, \ldots, \theta_n \geq 0$, we can generate according to (B.76) and (B.77) matrices $P, Q \in \mathbb{C}^{n\times n}$ satisfying Eq. (B.75). Then, if we generate positive numbers $(M_i)_{i=1}^n$ and non-negative numbers $(\Omega_i)_{i=1}^n$, we can generate according to Eq. (B.83) matrices $A, B \in \mathbb{C}^{n\times n}$ which satisfy the QRPA equation (B.40). Thus, we have generated a general positive semidefinite QRPA matrix, and we have seen that every positive semidefinite QRPA matrix can be generated in this way.

### Synthetic test example

Here we show results obtained by synthetically generating a QRPA matrix and performing the KPM method.

First we generate 500 eigenfrequencies from uniform distribution in range $0 < \Omega_i < 50$ MeV and add another 500 eigenfrequencies generated from uniform distribution in a larger range $0 < \Omega_i < 200$ MeV. Then we add 5 more spurious eigenfrequencies $\Omega_i = 0$ MeV, and we obtain a set of $n = 1005$ eigenfrequencies $(\Omega_i)_{i=1}^n$. We have done the same procedure when generating the eigenfrequencies $(\Omega_i)_{i=1}^n$ as in Section 4.3.1, with only difference that now we have explicitly generated 5 degenerated spurious eigenfrequencies. Bounding frequency used is

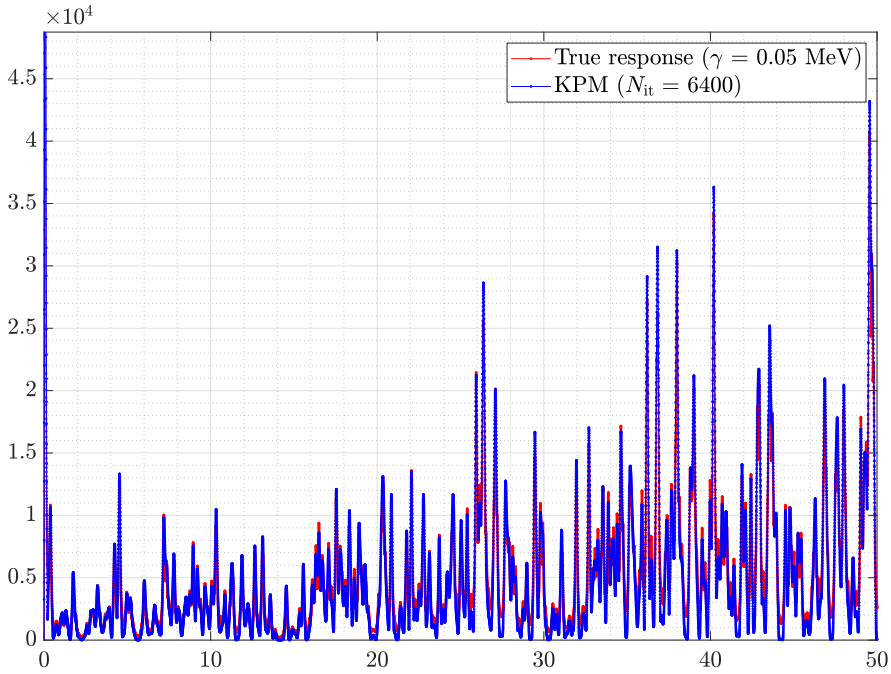


Figure B.1: Low-energy region of the smeared response function and the KPM response with Jackson kernel.

$\Omega_b = 250$ MeV. Then, we generate random values $(M_i)_{i=1}^n$ from uniform distribution in range $0 < M_i < 1$. We also generate random complex values of vectors $F^{20}, F^{02} \in \mathbb{C}^n$ drawn from standard normal distribution. Then we generate two unitary matrices $D, C \in \mathbb{C}^{n\times n}$ as Q parts in QR factorization of two random complex $n \times n$ matrices, followed by generating values $(\theta_i)_{i=1}^n$ from uniformly in range $0 < \theta_i < 3$. Then we generate $P, Q \in \mathbb{C}^{n\times n}$ as in Eqs. (B.76) and (B.77), and generate $A, B \in \mathbb{C}^{n\times n}$ as in Eq. (B.83). We also calculate the vectors $(\langle P_i|\hat{F}|0\rangle)_{i=1}^n$ and $(\langle Q_i|\hat{F}|0\rangle)_{i=1}^n$ using Eq. (B.50). Then we perform the KPM method as explained in Algorithm 1, however here we decide to use the Jackson kernel instead of the Lorentz kernel. For comparison with the KPM method, we calculate the smeared response function $dB^\gamma(\omega)/d\omega$, given by Eq. (B.52), where instead of using the distributions $\mathcal{D}_i(\omega), \mathcal{S}_i(\omega)$, we use the smeared versions $\mathcal{D}_i^\gamma(\omega), \mathcal{S}_i^\gamma(\omega)$ given in (B.53) and (B.54). We use the smearing value of $\gamma = 0.05$ MeV.

In Figure B.1 we show the low-energy region of the smeared response function $dB^\gamma(\omega)/d\omega$ compared to the KPM response when $N_{\text{it}} = 6400$ iterations in the KPM algorithm are performed. In Figure B.2 we show a detailed look of the spurious part of the smeared response function. Notice that the apparent "peak" isn't actually a QRPA pole because it depends on the smearing $\gamma$ and is closer to zero the smaller the smearing. One can easily see that from the shape of the spurious contribution to the smeared response analyzed in Section IV. of Ref. [60].

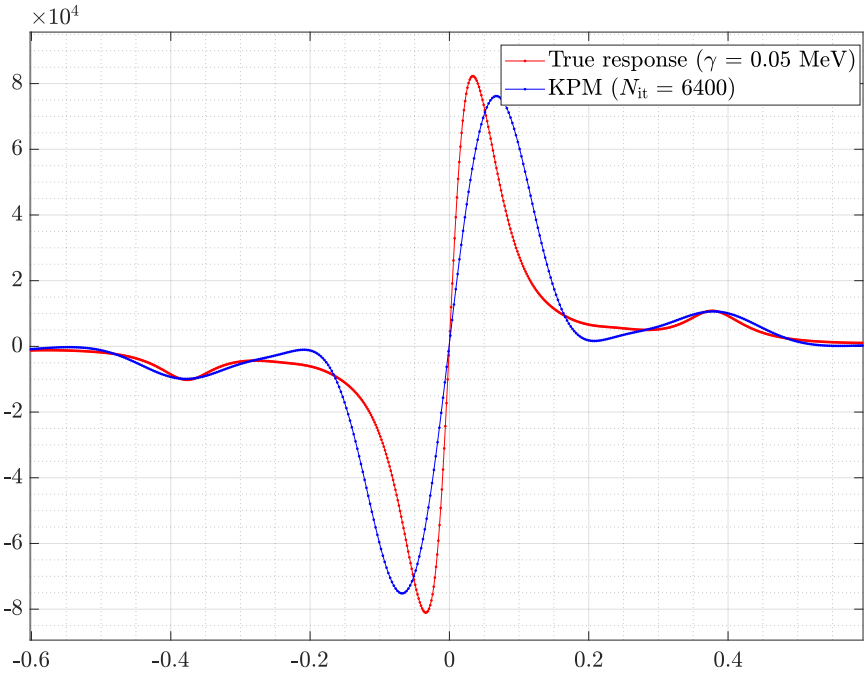


Figure B.2: Closer look of the spurious part of the smeared response function displayed in Figure B.1.

# Prošireni sažetak

Moderna teorija kvantne kromodinamike, fizikalna teorija koja opisuje djelovanje jake nuklearne sile unutar složenih subatomskih čestica interakcijom između kvarkova i gluona s pomoću triju svojstava nazvanih naboji boje: crveno, plavo i zeleno, u stanju je uspješno teorijski opisati i eksperimentalno validirati fundamentalne principe na kojima je izgrađena. Iz toga bi se naivno moglo zaključiti da je nuklearnu fiziku moguće promatrati kao samo jednu od podgrana kvantne kromodinamike, iz razloga što su međunukleonske interakcije zapravo dominantno posljedica kvark-gluon međudjelovanja, uz neke dodatne efekte koji proizlaze iz slabe interakcije. Međutim, takvi proračuni koji polaze od najfundamentalnijih principa (*ab-initio*) su daleko od izvedivih u praksi. Čak i najjednostavniji sustavi vezanih nukleona predstavljaju velik izazov u smislu numeričkog simuliranja ogromnog broja stupnjeva slobode koji proizlaze iz iznimne složenosti međunukleonske interakcije. Danas se srednje-teški i teški sustavi nukleona mogu proučavati gotovo isključivo u okviru efektivnih modela koji koriste fundamentalne principe kao mikroskopsku vodilju pri konstrukciji efektivnih modela nuklearne interakcije.

Najuspješniji pristup u tom smjeru je dobro afirmirana teorija energijskog funkcionala gustoće (eng. Energy Density Functional - EDF) korištena u brojnim drugim granama fizike gdje se pojavljuje kvantni problem više tijela. EDF teorija pruža precizan opis osnovnog stanja i kolektivnih pobuđenja atomskih jezgara od relativno lakih sustava sve do superteških nuklida. Jedan od najizazovnijih problema moderne teorijske nuklearne fizike je konstrukcija i parametrizacija efektivnog energijskog funkcionala gustoće koji bi, jednom kada mu se ugode parametri, reproducirao poznate eksperimentalne podatke s visokim stupnjem preciznosti duž cijele mape nuklida. Takav univerzalni funkcional gustoće bi se tada mogao vjerodostojno koristiti u raznim istraživanjima i primjenama gdje eksperimentalni podaci nisu dostupni, kao npr. u nuklearnoj astrofizici kod problema sinteze elemenata u zvijezdama ili kod teorijskih predviđanja egzotičnih modova pobuđenja koja bi upućivala eksperimente prema njihovoj eksperimentalnoj validaciji.

Odziv atomske jezgre na vanjsku pobudu može razotkriti vrijedne informacije o njenoj internoj strukturi. Jednom kada je funkcional gustoće konstruiran i definiran, teorijski bi trebalo biti moguće predvidjeti odziv na danu pobudu. Za takva teorijska proučavanja kolektivnih pobuđenja u atomskim jezgrama često se koristi aproksimacija slučajnih faza (eng. Random Phase Approximation - RPA) izgrađena na Hartree-Bogoliubov modelu. Glavni cilj ove disertacije je prezentirati implementaciju jednog takvog RPA rješavača te pokazati rezultate dobivene na konkretnim primjena.

Pristup rješavanju nuklearnog mnogočestičnog problema energijskim funkcionalom gustoće analogan je Kohn-Sham teoriji funkcionala gustoće u kojoj je samo-konzistentno mean-field modelom efektivno preslikan mnogočestični problem u jednočestični, a egzaktni funkcional gustoće je aproksimiran modelom koji je jednostavan funkcional potencija i gradijenata nukleonskih gustoća i struja. Jedna od klasa samo-konzistentnih mean-field modela predstavljaju relativistički (kovarijantni) funkcionali gustoće. Jezgra je opisana kao sustav Diracovih čestica vezanih izmjenom mezona kroz efektivni Lagrangian. Izoskalarni-skalarni $\sigma$ mezon, izoskalarni-vektorski $\omega$ mezon

i izovektorski-vektorski $\rho$ mezon čine minimalan skupe mezonskih polja nužnih za opis globalnih i jednočestičnih svojstava jezgre.

Već je u najranijim primjenama uočeno da ovakav jednostavan model baziran na izmjeni mezona koji u Lagrangianu interakcije sadrži samo linearne članove u mezonskim poljima nije adekvatan za kvantitativan opis složenih nuklearnih sustava. Stoga je predložen model u kojoj se zadržavamo na interakciji linearnim u ovisnosti o mezonskim poljima, ali se pretpostavlja da konstante vezanja nisu doslovno realne konstante, već funkcije gustoće (eng. density-dependent coupling). U praksi se predlažu razni fenomenološki pristupi (*ansatz*) koji modeliraju konstante vezanja ovisne o gustoći te njihovi parametri predstavljaju parametre samog funkcionala gustoće koji se ugađaju na eksperimentalne podatke. Jedan takav konkretan Lagrangian korišten u ovom radu je DD-ME2 (density-dependent meson-exchange) parametrizacija koja se kroz zadnja dva desetljeća korištenja pokazala uspješnom. Na istom tragu, alternativnu formulaciju relativističkih samokonzistentnih mean-field Lagrangiana čine modeli kontaktnog međudjelovanja koji umjesto modeliranja interakcije mezonima konačnog dosega modeliraju interakciju npr. kontaktnim dvo-fermionskim interakcijama i gradijentnim članovima dobivenim razvojem mezonskih propagatora uslijed velike mase mezona u odnosu na skalu nuklearnih interakcija. I u ovim kontaktnim modelima se za konstante vezanja pretpostavlja ovisnost o gustoći zadane tipično *ansatzom*. Jedan takav konkretan Lagrangian baziran na kontaktnoj interakciji s konstantama vezanja ovisnima o gustoći je DD-PC1 (density-dependent point-coupling) parametrizacija.

Relativistički funkcionali gustoće uspješno su korišteni u studijama osnovnih i pobuđenih stanja sfernih i deformiranih jezgara. Međutim, za kvantitativnu analizu jezgara s otvorenim ljuskama nužno je uzeti u obzir interakcije sparivanja. Sparivanje se često uzima u obzir u okviru Bardeen-Cooper-Schrieffer modela (BCS), no u mnogim slučajevima ova aproksimacija nije zadovoljavajuća. Za opise slabo vezanih sustava nužan je objedinjeni opis samokonzistentnog mean-field međudjelovanja i korelacija sparivanja. Hartree-Fock-Bogoliubov (HFB) model nudi ujedinjeni opis čestica-šupljina i čestica-čestica korelacija na mean-field razini. Relativistička ekstenzija HFB modela vodi na relativistički Hartree-Bogoliubov (RHB) model u kojem je osnovno stanje jezgre prikazano kao generalizirana Slaterova determinanta koja predstavlja vakuum s obzirom na neovisne kvazičestice čiji su operatori stvaranja i poništenja dobiveni unitarnom Bogoliubovljevom transformacijom. Varijacijski princip RHB energijskog funkcionala gustoće vodi na RHB problem svojstvenih vrijednosti s generaliziranim Hamiltonijanom čije rješenje daje osnovno stanje jezgre. Interakcija sparivanja također je modelirana. U ovom radu koristimo interakciju sparivanja konačnog dosega separabilnu u impulsnom prostoru. Posebnim tehnikama moguće je fiksirati deformaciju jezgre u RHB modelu. Ovaj rad fokusiran je na aksijalno simetrične parno-parne jezgre s mogućom kvadrupolnom deformacijom. Opisani RHB model u praksi je implementiran kao `DIRHB` rješavač koji se uspješno koristi zadnja dva desetljeća. U ovom doktorskom radu, `DIRHB` rješavač koji proračunava osnovno stanje jezgre korišten je kao temelj na kojem se proračunavaju svojstva odziva jezgre na vanjsku pobudu.

Aproksimacija slučajnih faza (eng. Random Phase Approximation - RPA) i njena kvazičestična ekstenzija QRPA (Quasiparticle RPA - QRPA) bazirane na nuk-

learnim energijskim funkcionalima gustoće predstavljaju jedan od najčešće korištenih teorijskih okvira za proučavanje kolektivnih pobuđenja u deformiranim atomskim jezgrama. Standardna formulacija QRPA modela svodi se na linearizaciju vremenski ovisne HFB teorije s obzirom na slabu vanjsku perturbaciju fiksne energije. Razvojem kvazičestičnih operatora ovisnih o vremenu i zadržavanjem samo linearnih članova QRPA problem se svodi na linearan sustav jednadžbi, gdje je desna strana linearnog sustava reprezentirana vanjskom pobudom u kvazičestičnom prostoru, matrica linearnog ustava (QRPA matrica) je matrica stabilnosti generaliziranog RHB Hamiltonijana, a rješenje linearnog sustava daje koeficijente ekspanzije kvazičestičnih operatora.

QRPA jednadžba tipično se za sferne jezgre rješava metodom dijagonalizacije koja kao rješenja daje elementarne modove pobuđenja i QRPA svojstvene frekvencije. Međutim, u praksi se valna funkcija razvija u određenoj konačnoj bazi (koja je aproksimacija potpune baze) poznatoj kao konfiguracijski prostor. Dimenzija QRPA matrice raste kvadratno s dimenzijom konfiguracijskog prostora te je stoga QRPA matrica u praksi ekstremno velika za deformirane sustave u odnosu na sferne jezgre gdje sferna simetrija drastično reducira dimenzionalnost problema. Sama eksplicitna konstrukcija QRPA matrice je gotovo nemoguće izvesti u praksi, time štoviše i njena dijagonalizacija. U svrhu rješavanja QRPA sustava nedavno je predložena metoda konačnih amplituda (eng. Finite Amplitude Method - FAM) i njena kvazičestična ekstenzija (Quasiparticle FAM - QFAM). QFAM metoda bazirana je na tvrdnji da je moguće iterativno riješiti QFAM jednadžbu (ekvivalentu QRPA jednadžbi) tako da se kod iterativnog postupka niti u jednom koraku eksplicitno ne konstruiraju matrice koje odgovaraju dvočestičnom operatoru već se zadržavamo na jednočestičnim operatorima. Mana QFAM metode je ta što se energija vanjske pobude mora fiksirati, te stoga QFAM jednadžbu treba rješavati za skup energija (frekvencija) gdje za svako rješenje dane energije kao rezultat dobivamo odzivnu funkciju na danoj energiji (frekvenciji). Ponavljanjem postupka za gust skup frekvencija u konačnici dobivamo odzivnu funkciju koju je na ovaj način moguće izračunati u razumnom vremenu čak i za velike sustave koji odgovaraju teškim deformiranim jezgrama.

U okviru ovog doktorskog rada razvijena je nadogradnja `DIRHB` rješavača u obliku `DIRQFAM` rješavača koji implementira QFAM metodu za slučaj parno-parnih nuklida s aksijalno simetričnim osnovnim stanjem i kvadrupolnom deformacijom. `DIRQFAM` rješavač kao bazu konfiguracijskog prostora koristi simplex-y bazu kvantnog harmoničkog oscilatora. Za operatore koji opisuju vanjsku pobudu implementirani su izoskalarni i izovektorski sferni harmonici. U disertaciji dani su tehnički detalji `DIRQFAM` rješavača: detaljno je opisana korištena baza, QFAM iterativni postupak, eksplicitna linearizacija jednočestičnog potencijal, metoda niskog ranga za računanje induciranih struja i gustoća u koordinatnom prostoru, primjena GMRES metode za traženje samo-konzistentnog rješenja, nukleonska lokalizacijska funkcija, tehnika konturne integracije, eliminacija spurioznog moda, tehnika rješavanja mezonskih Klein-Gordon jednadžbi, tehnika integriranja Coulombovog doprinosa te proračun potencijala sparivanja korištenjem Talmi-Moshinsky zagrada. Na ilustrativnim primjerima demonstrirana je iznimna performansa i fleksibilnost `DIRQFAM` rješavača

Kao nadogradnju postojeće QFAM metode, u ovom disertaciji predložena je nova Kernel Polynomial Method (KPM) metoda za računanje QRPA odzivne funkcije. Ideja je zaobići glavnu manu QFAM metode, a to je činjenica da se QFAM jednadžbe moraju samo-konzistentno rješavati za svaku frekvenciju pobude zasebno. Cilj se može postići tako da se QRPA odzivna funkcija razvije u red Chebyshevljevih polinoma. Pokazano je da se koeficijenti razvoja Chebyshevljevog reda mogu izračunati korištenjem postojećeg QFAM rješavača. Jer je QRPA odzivna funkcija esencijalno težinska suma delta funkcija centriranih na QRPA svojstvenim frekvencijama, javlja se fenomen Gibbsovih oscilacija jer pokušavamo razviti delta funkciju u red polinoma. Gibbsov fenomen oscilacija rješava se već poznatom KPM metodom uvođenjem dodatnih težinskih koeficijenata u Chebyshevljev red. Dan je pregled odabira KPM težinskih koeficijenata, tehnički detalji oko implementacije te KPM metoda u $PQ$ reprezentaciji QRPA problema. KPM metoda je demonstrirana na sintetski generiranom primjeru, primjeru gdje je korišten `sykrme_rpa` rješavač, primjeru gdje je korišten `DIRQFAM` rješavač, te na primjeru efikasnog računanja momenata. Jedan od ključnih ulaznih parametara KPM metode je granična frekvencija koja mora biti veća od svih QRPA svojstvenih frekvencija, u protivnom se lako pokaže da KPM metoda divergira. Zbog pojave Diracovog mora antičestičnih energija kod relativističkih funkcionala gustoće, koje su tipično za red veličine iznad čestičnih energija, odgovarajuća najveća QRPA svojstvena frekvencija je za red veličine veća nego kod tipičnih nerelativističkih funkcionala. Zbog toga što je razlučivost Chebyshevljeve aprosksimacije direktno proporcionalna graničnoj frekvenciji, a kod relativističkih modela granična frekvnecija mora biti značajno veća od nerelativističkih modela, KPM metoda je barem za red veličine inferiornija u smislu efikasnosti kada se koriste relativistički modeli. S druge strane, za nerelativističke modele, pokazano je da KPM metoda može izračunati odzivnu funkciju u bitno kraćem vremenu od konvencionalne QFAM metode.

Nakon što su prezentirane tehnike rješavanja QRPA problema, dani su rezultati primjene `DIRQFAM` rješavača.

U prvoj primjeni napravljena je sistematična analiza multipolnog odziva deformiranih $N = Z$ jezgara. Pokazano je da dominantni modovi uočeni na niskim energijama odgovaraju oscilacijama grozdova (eng. clusters) za sve proučene izoskalarne multipolne operatore pobuđenja. Na primjer, za laku deformiranu jezgru $^{20}$Ne (koja pokazuje podstrukturu grozdova čak i u osnovnom stanju) monopolni i kvadrupolni operator pobuđenja induciraju dva $\alpha$-grozda koji osciliraju oko $^{12}$C sredice, dok dipolni i oktupolni operator pobuđenja induciraju $\alpha$-grozd koji oscilira u odnosu na sredicu $^{16}$O. Računanjem QRPA odzivne funkcije u ovisnosti o parametru deformacije jezgre proučena je ovisnost deformacije na formiranje i oscilacije grozdova na slučaju monopolnog pobuđenja. Pojava opisanih dominantnih modova usko je vezana uz strukturu jedno-nukleonskih energijskih nivoa u kanonskoj bazi. Specifično za $^{20}$Ne, cijepanje sferne $1d_{5/2}$ ljuske je ključno jer je pokazano da su monopolna pobuđenja dominantno određena prijelazom iz $1/2^+$ stanja koje potječe od sferne $1d_{5/2}$ ljuske u $1/2^+$ stanje koje potječe od sferne $2s_{1/2}$ ljuske. Studija je provedena i na srednje teškim $N = Z$ jezgrama od $^{12}$C do $^{56}$Ni. Pokazano je da su niskoenergetski modovi za monopolnu pobudu izraženiji u smislu vjerojatnosti prijelaza za deformirane izotope daleko od zatvorene ljuske.

Rezultat je ilustriran na tri izotopa: $^{24}$Mg, $^{28}$Si i $^{32}$Si koji pokazuju vidljivu podstrukturu grozdova čak i u osnovnom stanju. Slično kao i kod $^{20}$Ne primjera, u pobuđenju dominantnu ulogu ima samo jedna dvočestična konfiguracija.

U drugoj primjeni korišten je `DIRQFAM` rješavač za efikasan proračun fononskih frekvencija i kvazičestica-fonon vrhova vezanja pomoću kojih je izgrađena aproksimirana Dysonova jednadžba za nukleonski propagator. Fononi su aproksimirani u prvom redu korištenjem QRPA teorije. Pristup kvazičestica-fonon vezanja formuliran je za RHB kvazičestice i proučen prvi puta za deformirane jezgre s otvorenim ljuskama. Dosadašnje studije kvazičestica-fonon vezanja bile su moguće samo korištenjem sfernih jezgara. Analizom rješenja za srednje-tešku jezgru bogatu neutronima $^{38}$Si uočena je značajna fragmentacija koreliranih kvazičestičnih energija blizu Fermijevog nivoa te povećanje gustoće stanja protona i neutrona. Ta pojava značajno poboljšava slaganje s eksperimentalnim podacima za aksijalno simetrične deformirane jezgre u odnosu na RHB aproksimaciju.

Naučene lekcije vezane uz QFAM implementaciju za aksijalno simetričan slučaj daju vrijedan uvid za daljnja istraživanja gdje je poželjno dodatno oslabiti pretpostavku aksijalne simetrije. Na primjer, mikroskopski opis spontane fisije je jedan ona najvećih izazova u nuklearnoj fizici. Pri simulacijama fisije nužna je evaluacija kolektivnih potencijala i kolektivnih parametara tromosti duž fisijske linije u prostoru parametara deformacije za opis kvantnog tuneliranja u spontanoj ili niskoenergijskoj fisiji. Do nedavno, u studijama dinamike fisije u okviru teorije energijskog funkcionala gustoće, kolektivni parametri tromosti evaluirani su koristeći tzv. *cranking* aproksimaciju, koja je ekvivalentna QRPA problemu ako zanemarimo rezidualnu interakciju. Ako se za svaki parametar u deformacijskom prostoru RHB modela riješi QRPA problem, moguće je evaluirati parametre tromosti gdje su efekti rezidualne interakcije uzeti u obzir. Pokazuje se da QFAM metoda kombinirana sa tehnikama konturne integracije omogućuje efikasno računanje kolektivnih parametara tromosti čak i u slučaju teških deformiranih jezgara. Kolektivni parametri tromosti evaluirani su u recentnoj studiji [135] za simetrični fisijski put u $^{240}$Pu i $^{256}$Fm jezgri. Tamo je pokazano da je QFAM-QRPA parametar tromosti značajno veći od one dobivene *cranking* aproksimacijom s netrivijalnom ovisnošću o deformaciji fisijskog izomera što je direktna posljedica rezidualnih efekata. Ta studija je početna točka za sistematične studije fisijske dinamike teških i superteških jezgara gdje su parametri tromosti po prvi puta evaluirani bez *cranking* aproksimacije. Budući razvoj `DIRQFAM` rješavača bi idealno išao u istom smijeru.

# Information on the supervisor

Tamara Nikšić is an full-time professor at the Department of Physics, Faculty of Science, University of Zagreb, where she has been employed from 2000. She received her Ph.D. degree from the University of Zagreb in 2004 (*Relativistic description of nuclear structure: models with density-dependent meson-nucleon couplings*, supervised by professor Dario Vretenar). She was an Alexander von Humboldt fellow at the Technical University Munich (2005-2006) in the group of professor Peter Ring. Her research interests span both theoretical nuclear physics and computational physics. Most of her work has been on developing the new generation of nuclear energy density functionals and describing the correlations originating from restoration of broken symmetries and fluctuation of the quadrupole and octupole deformations. Recently, she has been involved in describing possible mechanisms of cluster formation in light nuclei. She has co-authored over 70 original scientific papers and 2 review papers with 7000 citations. In 2012 she received the Annual Croatian State Award for Science. She teaches Classical Mechanics and Quantum Physics at the Department of Physics, Faculty of Science, University of Zagreb.

# Information on the author

Antonio Bjelčić was born on 30th November 1994 in Zagreb, Republic of Croatia. In 2013 he completed his secondary education and enrolled in a research-oriented physics study programme at the Department of Physics, Faculty of Science, University of Zagreb. During the study of physics, in 2015 he enrolled in a parallel study of mathematics at the Mathematics Department, Faculty of Science, University of Zagreb. In 2018 under the mentorship of prof. dr. sc. Tamara Nikšić he completed the master's degree study of physics and undergraduate study of mathematics, both with 5.0 GPA. Same 2018 year, he enrolled in a graduate study of applied mathematics at the Mathematics Department, Faculty of Science, University of Zagreb and a Ph.D. study of theoretical nuclear physics at the Department of Physics, Faculty of Science, University of Zagreb, where he was employed as a research assistant. In 2020 under the mentorship of prof. dr. sc. Zlatko Drmač he completed the master's degree study of mathematics with 5.0 GPA. Faculty of Science honoured him with two awards for completing the study as the best student in class (one for mathematics, other for physics study). His fields of interests are theoretical nuclear physics and applied mathematics. More detailed resume is available at the following **link**.

**Publications:**


- A. Bjelčić, T. Nikšić, Comp. Phys. Comm. **253**, 107184 (2020).
- F. Mercier, A. Bjelčić, T. Nikšić, J.-P. Ebran, E. Khan, D. Vretenar, Phys. Rev. C **103**, 024303 (2021).
- Y. Zhang, A. Bjelčić, T. Nikšić, E. Litvinova, P. Ring, P. Schunck, Phys. Rev. C **105**, 044326 (2022).
- A. Bjelčić, T. Nikšić, Z. Drmač, Comp. Phys. Comm. **280**, 108477 (2022).